
**Universidade do Minho**
I3Bs - Instituto de Investigação em Biomateriais, Biodegradáveis e Biomiméticos

Alexandra Manuela Fernandes Brito

# Supramolecular assembly of carbohydrate amphiphiles for biomedical applications

Julho de 2020

Supramolecular assembly of carbohydrate amphiphiles for biomedical applications

Alexandra Manuela Fernandes Brito

UMinho | 2020

**Universidade do Minho**

I3Bs - Instituto de Investigação em Biomateriais, Biodegradáveis e Biomiméticos

Alexandra Manuela Fernandes Brito

# Supramolecular assembly of carbohydrate amphiphiles for biomedical applications

Tese de Doutoramento

Doutoramento em Engenharia de Tecidos, Medicina Regenerativa e Células Estaminais

Trabalho efetuado sob a orientação

**Doutora Iva Hristova Pashkuleva**

**Professor Doutor Rui Luís Gonçalves dos Reis**

Julho de 2020

## ACKNOWLEDGMENTS

Firstly, I would like to express my sincere gratitude to my advisor Dr Iva Pashkuleva. Thank you for your friendship, patience, motivation, immense knowledge, for believing in my ideas and give me the encouragement to pursued them. I could not have imagined having a better advisor and mentor for my PhD study and I'm sure this is a relationship that will endure for a long time. Благодаря ти!

I would like to deeply acknowledge the director of the 3B's Group and my co-advisor, Prof. Rui L. Reis, for the continuous support of my PhD study and related research, and for offering all the necessary means to carry out my work in 3B's and abroad.

I would like to acknowledge, Dr Ricardo Pires, that even though he was not an official advisor to this thesis, he was in all sense of the word an important supervisor for me throughout these four years. Thank you for all the hours you've spent with me in the lab, for believing in me and for your kinds words when things were not working as planned. I really appreciate your guidance and friendship.

I also acknowledge all the 3B's technicians for making our work easier every day in the lab, in particular, Liliana Gomes, Ana Araújo and Cláudia Costa. During this PhD I was lucky enough to visit two cutting-edge science research laboratories: Ulijn Lab and the Jason Lewis Lab. There, I met amazing people that believed in me, shared their knowledge and inspired me to be a better researcher. Thank you: Prof. Rein Ulijn, for allowing me to visit your lab and letting me learn from the leaders of the field. I thank you for your insightful comments and encouragement, but also for the hard questions which incented me to widen my research from various perspectives; Dr Jason Lewis, who provided me an opportunity to join his team, from whom I've learned a lot; Dr Patricia Ribeiro, you are an inspiration and a force to reckoned with, thank you for always push me to be the best that I can be. Thank you to all my co-authors, Diana Costa, Ramon Carball, Dhwanit Dave, Salma Kassem, Daniela Kroiss and Ayala Lampel, who believed in the work proposed and help me to obtain the best results. I would like to acknowledge the Portuguese Foundation for Science and Technology (BD/113794/2015; PTDC/BTM-MAT/28327/2017 CARDIOHEAL; M-ERA-NET2/0001/2016 INCIPIT), EU's H2020 program (Forecast 668983), Liga Portuguesa Contra o Cancro, and Fundação Luso Americana.

I thank my fellow 3B's PhD friends Barbara, Carla, Guedes and Casanova, for all the fun we have had in the last four years. Last but not least, I would like to acknowledge the most important people in my life: Luca, my best friend and soul mate, thank you; and my family, specially my mum and sisters, who taught me how to be independent, kind and to fight for what is right, thank you.

## STATEMENT OF INTEGRITY

I hereby declare having conducted this academic work with integrity. I confirm that I have not used plagiarism or any form of undue use of information or falsification of results along the process leading to its elaboration.

I further declare that I have fully acknowledged the Code of Ethical Conduct of the University of Minho.

## ABSTRACT

Carbohydrates are involved in all essential processes within the life cycle of cells and organisms - they exert their bioactivities *via* simultaneous multivalent non-covalent interactions with other biomolecules. Supramolecular systems, therefore, provide the ideal means to generate polyvalent architectures for studying and modulating these interactions: the inherent reversibility of the self-assembling process and the translation of monomers into polymers provides spatiotemporal control over ligand density and assembly architecture. This thesis demonstrates the versatility of simple carbohydrate amphiphiles as molecular building blocks for the assembly of biofunctional materials using different supramolecular approaches. **Biocatalytic self-assembly** (BSA) uses an enzyme transformation of the amphiphile as a trigger of the assembly process and was explored for the formation of chiral supramolecular structures (Chapter III) and as a therapeutical approach for cancer management (Chapters IV and V). A simple monosaccharide has five chiral centers in its cyclic form and five carbons at which an enzyme sensitive moiety can be introduced. In Chapter III, we show that the choice of the regioisomer influences the chirality of the assembled structure. In Chapters IV and V, we demonstrate that introducing carbohydrate moiety in the molecular design of the amphiphile allows the use of a single molecule to target simultaneously different features of cancer metabolism: the alkaline phosphatase overexpression that triggers the *in situ* BSA and the Warburg effect, associated with the overexpression of glucose transporters. In Chapter VI, we explored the possibility to create nanostructures with increasing complexity and chemical diversity, without compromising the function of the individual building blocks: **co-assembly** of simple peptide and carbohydrate amphiphiles was used to generate minimalistic proteoglycan mimics. Finally, the self-assembly of short glycopeptides was studied in Chapter VII as a **reductionist approach** towards understanding the role of glycosylation in protein folding and aggregation. These minimalistic models provide better understanding about the role of amino acids sequence and hydration in aggregates' formation and stability and, thus about the mechanism of the process at molecular level. Altogether, the results presented in this thesis manifest the multifarious utility of supramolecular carbohydrate systems in understanding and manipulating different physiological and pathological processes.



**Keywords:** carbohydrate amphiphiles; minimalistic models; supramolecular chemistry; biocatalytic self-assembly; co-assembly

## RESUMO

Os carboidratos estão envolvidos em processos essenciais no ciclo de vida das células e organismos – estes exercem as suas bioatividades com outras biomoléculas, por meio de interações simultanemamente multivalentes e não covalentes. Sistemas supramoleculares, representam meios ideais para criar arquiteturas polivalentes no estudo e modulação destas interações: a reversibilidade inerente do processo de **automontagem** e a tradução de monômeros em polímeros permite um controlo espaço-temporal sobre a densidade dos ligantes e a arquitetura de montagem. Esta tese demonstra a versatilidade de simples carboidratos anfifílicos como blocos de construção moleculares para a montagem de materiais biofuncionais usando diferentes abordagens supramoleculares. A **automontagem biocatalítica** (ASC) utiliza a transformação enzimática do anfifílico para desencadear o processo de montagem e foi explorada para a formação de estruturas supramoleculares quirais (Capítulo III) e como uma abordagem terapêutica para o tratamento do cancro (Capítulos IV e V). Um monossacarídeo simples possui cinco centros quirais na forma cíclica e cinco carbonos nos quais oide ser introduzido um grupo sensível à enzima. No capítulo III, mostramos que a escolha do regioisômero influencia a quiralidade da estrutura formada. Nos capítulos IV e V, demonstramos que a introdução de um carboidrato no desenho molecular do anfifílico permite atingir diferentes características do metabolismo do cancro simultaneamente: a sobrerexpressão da fosfatase alcalina que desencadeia a ASC *in situ* e o efeito Warburg, associada à sobrerexpressão dos transportadores de glucose. No Capítulo VI, exploramos a possibilidade de criar nanoestruturas com maior complexidade e diversidade química, sem comprometer a função individual dos blocos de construção: a co-montagem de simples peptidos e carboidratos anfifilos foi usada para gerar imitações minimalistas de proteoglicanos. Finalmente, a automontagem de glicopéptidos curtos foi estudada no Capítulo VII como uma **abordagem minimalista** para compreender o papel da glicosilação na conformação e agregação de proteínas. Estes modelos minimalistas conseguem explicar melhor o papel da sequência e da hidratação dos aminoácidos na estabilidade dos agregados formados e, deste modo, explicar o mecanismo do processo a nível molecular. No total, os resultados apresentados nesta tese demonstram a vantagem múltipla do uso de sistemas supramoleculares de carboidratos na compreensão e manipulação de diferentes processos fisiológicos e patológicos.



**Palavras chave:** carboidratos anfifílicos; modelos minimalistas; química supramolecular; auto-montagem biocatalitica; co-montagem.

# TABLE OF CONTENTS

# LIST OF ABBREVIATIONS

## A

Abs – Absorbance

ABTS – 2,2'-azino-bis(3-ethylbenzthiazoline-6-sulphonic acid

AFM - Atomic Force Microscopy

Akt – Protein kinase

ALP – Alkaline phosphatase

α-MEM – Alpha-Minimum Essential Medium

ANOVA – Analysis of variance

APTES - 3-Aminopropyl)triethoxysilane

ATB – Antibiotic/Antimycotic

ATP – Adenosine triphosphate

Au – Gold

## B

Basal – Basal medium

BSA – Biocatalytic self-assembly

BCA – Bicinchoninic acid assay

b-FGF – Basic fibroblast growth factor

BM – Basal medium

BMP2 – Bone morphogenic protein-2

## C

CCI – Carbohydrate-carbohydrate interactions

cDNA – Complementary DNA

CPI – Carbohydrate-protein interactions

## D

DAB – 3, 3 -diaminobenzidine

DAPI – 4,6-diamidino-2-phenylindole

DCM - Dicholoromethane

DIPEA - N,N-Diisopropylethylamine

DMB – Dimethylmethylene blue

DMF - Dimethylformamide

DMEM – Dulbecco's modified Eagle's medium.

DNA – Deoxyribonucleic acid

DOC - Sodium deoxycholate

DODT - 3,6-Dioxa-1,8-octane-dithiol

dsDNA – Double strained DNA

## E

E – Elastic modulus

ECM – Extracellular matrix

E-coli – Escherichia coli

EDC -1-Ethyl-3-(3-dimethylaminopropyl)carbodiimide

EDS – Energy dispersive X-ray spectroscopy

EGTA - Ethylene glycol tetraacetic acid

ELISA – Enzyme-linked immunosorbent assay

EGF – Epidermal growth factor

EVs – Extracellular vesicles

## F

FBS – Fetal bovine serum

FDA – U.S. Food and Drug Administration

Fmoc - Fluorenylmethyloxycarbonyl

FTIR - Fourier transform infrared spectroscopy

## G

GAPDH – Glyceraldehydes-3-phosphate-dehygrogenase

GAG – Glycosaminoglycan

GBP - Glycosaminoglycan-binding proteins

Glc - Glucose

GLUT – Glucose transporter

GFs – Growth factors

GPC – Gel permeation chromatography

## H

hASCs – Human adipose stem cells

hBM-MSCs – Human bone marrow-derived mesenchymal stem cells

HBTU - N,N,N′,N′-Tetramethyl-O-(1H-benzotriazol-1-yl)uronium hexafluorophosphate

HPLC – High Perfomance Liquid Chromatography

## I

IAD - iodoacetamide

$IC_{50}$ - Half maximal inhibitory concentration

ICC - Immunocytochemistry

Ig – Immunoglobulin

IGF – Insulin-like growth factor

## L

LC-MS – Liquid chromatography and mass spectrometry

## M

MMP - Metalloproteinases

mRNA – Messenger RNA

MTS–3-(4,5-dimethylthiazol-2-yl)-5-(3-carboxymethoxyphenyl)-2-(4-sulfophenyl)-2H-tetrazolium

## N

NADPH – Nicotinamide adenine dinucleotide phosphate

NADH – Nicotinamide adenine dinucleotide

NBDG - 2-deoxy-2-((7-nitro-2,1,3-benzoxadiazol-4-yl)amino)-

NHS – N-hydroxysuccinimide

## O

OD – Optical density

Osteo – Standard osteogenic differentiation medium

## P

PA – Peptide amphiphile

PATH – Doctoral Program on Advanced Therapies for Health

PET – Positron Emission Tomography

PBS – Phosphate-buffered saline

PCR – Polymerase chain reaction

pDNA – Plasmid Deoxyribonucleic acid

PMSF - Phenylmethanesulfonyl

## R

RGD – Arginine-glycine-aspartic acid

RNA – Ribonucleic acid

rNGF – Recombinant nerve growth factor

RPM – Rotations per minute

RT – Room temperature

RT-PCR – Real-time polymerase chain reaction

S

SA – Self-assembly

SD – Standard deviation

SDS - Sodium dodecyl sulfate

SEM – Scanning Electron Microscopy

SPSS – Statistical Package for the Social Sciences

sulfo-NHS – Sulfo-N-hydroxysuccinimide

T

2D – Two-dimensional

3D – Three-dimensional

TERM – Tissue Engineering and Regenerative Medicine

TEM - Transmission electron microscopy

TIS - Triisopropylsilane

U

UV – Ultraviolet light

UV-O – Ultraviolet-ozone

# LIST OF EQUATIONS

## LIST OF FIGURES

## LIST OF SUPPLEMENTARY FIGURES

## LIST OF SCHEMES

## LIST OF TABLES

## LIST OF SUPPLEMENTARY TABLES

## SHORT *CURRICULUM VITAE*

Alexandra Brito obtained a degree in Chemistry in 2010 at the University of Minho. During her bachelor studies, she also was awarded a Research integration grant by the Portuguese Foundation for Science and Technology (FCT), with a duration of a year, UMINHO/BII/058/2009, under the supervision of Dr Maria Alice Carvalho. In her graduation year, she visits the Faculty of Chemical Technology of the University of Pardubice in the Czech Republic, under the Erasmus Program, where she concluded her bachelor thesis under the supervision of Ales Imramovsky. In the same year, she enrolled in a Master degree in Medicinal Chemistry, at the University of Minho, which she finished in 2012. In the same year she worked as a researcher in the FCT projects: PTDC/QEQ-MED/1671/2012, under the supervision of Dr Maria José Alves and PTDC/CTM-NAN/119184/2010, under the supervision of Prof. Dr Fernanda Proença, in the Chemistry Department of the University of Minho. In 2013, she spent six months as a visiting researcher in the Leiden University Medical Center, in the frame of Leonardo da Vinci program, under the supervision of Dr Tom Van Wezel and Prof Dr Hans Morreau. She also possesses a post-graduation in Health of Science by the School of Medicine at the University of Minho. Since that, Alexandra is a PhD student at 3B's Research Group on Tissue Engineering, Regenerative Medicine and Stem Cells Doctoral Program, under the supervision of Dr Iva Pashkuleva and Prof Rui L. Reis and supported by FCT scholarship (2015-2019), and by the Portuguese Cancer League (2020), in the scope of her PhD studies, she visited, for one year, the Advanced Science Research Center at the City University of New York, under the supervision of Dr Rein Ulijn and the Department of Radiology at Memorial Sloan Kettering Cancer Center, under the supervision of Dr Jason Lewis, with financial support at Fundação Luso-Americana. During her PhD, Alexandra has been involved as a researcher in several research projects, namely in FCT projects: PTDC/BTM-MAT/28327/2017 and PTDC/NAN-MAT/28468/2017; in the Twinning project "Chem2Nature" and, more recently, in the H2020 funded ERA Chairs project "Forecast". Alexandra is a member of the European Society of Biomaterials and American Chemical Society and is an ambassador of the European Association of Cancer Research. She is a founding member of the PhDynamics Group from 3B's Research Group (2018).

She is author and co-author of 9 full-length papers published in international peer-reviewed scientific journals (5 published and 4 submitted), 1 book chapter, 3 published conference abstract, 13 oral communications, 18 poster presentations.

## LIST OF PUBLICATIONS

The work performed during the PhD period resulted in the publications listed below.

### Papers in international scientific journals with referees (as first author)

1. **Brito, Alexandra;** Kassem, Salma; Reis, Rui L.; Ulijn, Rein V.; Pires, Ricardo; Pashkuleva, Iva; "Design of Supramolecular Biomaterials Based on Carbohydrate Amphiphiles", submitted.
2. **Brito, Alexandra;** Reis, Rui L.; Ulijn, Rein V.; Pires, Ricardo A.; Pashkuleva, Iva: "Helical nanofibers with opposite handedness generated by biocatalytic self-assembly of aromatic carbohydrate amphiphiles", submitted.
3. **Brito, Alexandra;** Pereira, Patricia MR; Costa, Diana Soares da; Reis, Rui L.; Ulijn, Rein V.; Lewis, Jason S.; Pires, Ricardo A.; Pashkuleva, Iva: "Inhibiting cancer metabolism by aromatic carbohydrate amphiphiles that act as antagonists of the glucose transporter GLUT1" Chemical Science, 2020, 11, 3737-3744.
4. **Brito, Alexandra;** Pereira, Patricia MR; Reis, Rui L.; Ulijn, Rein V.; Lewis, Jason S.; Pires, Ricardo A.; Pashkuleva, Iva: "Aromatic Carbohydrate Amphiphile Disrupts Efficiently Cancer Spheroids without Following Relapse", submitted.
5. **Brito, Alexandra;** Abul-Haija, Yousef M.; Costa, Diana S.; Novoa-Carballal, Ramon; Reis, Rui L.; Ulijn, Rein V.; Pires, Ricardo A.; Pashkuleva, Iva: "Minimalistic Supramolecular Proteoglycan Mimics by Co-assembly of Aromatic Peptide and Carbohydrate Amphiphiles", Chemical Science, 2019, 10, 2385-2390.
6. **Brito, Alexandra;** Dave, Dhwanit; Lampel, Ayala; Krois, Daniela; Reis, Rui L.; Tutle, Tell; Ulijn, Rein V.; Pires, Ricardo A.; Pashkuleva, Iva: "Effect of serine and threonine on the aggregation of short peptides and glycopeptides", submitted

### Book Chapter

**Brito**, **Alexandra;** Ries, Rui L.; Pires, Ricardo A.; Pashkuleva, Iva: "Sweet building blocks for self-assembling biomaterials with molecular recognition", Self-assembling Biomaterials- Molecular Design, Characterization and Application in Biology and Medicine, Eds. Azevedo H. S., and da Silva R. M. P., Woodhead Publishing, 2018, pp 79-94

**Conference oral presentations (as first author speaker)**

1. **Brito, Alexandra;** Pereira, Patricia MR; Costa, Diana Soares da; Reis, Rui L.; Ulijn, Rein V.; Lewis, Jason S.; Pires, Ricardo A.; Pashkuleva, Iva: Glucose amphiphiles as metabolic inhibitors in cancer, FoReCaST, Porto, Portugal, July 2019.

2. **Brito, Alexandra;** Reis, Rui L.; Ulijn, Rein V.; Pires, Ricardo A.; Pashkuleva, Iva: Biocatlytic self-assembly of supramolecular gels is controlled by the choice of the amphiphile regioisomer, European Society of Biomaterials, Dresden, Germany, September 2019.

3. **Brito, Alexandra;** Reis, Rui L.; Ulijn, Rein V.; Pires, Ricardo A.; Pashkuleva, Iva: Supramolecular hydrogels formed by a biocatalytic self-assembly are controlled by the choice of the amphiphile regio-isomer, 1st Discoveries Forum of Regenerative Medicine, Porto, Portugal, September 2019.

4. **Brito, Alexandra;** Pereira, Patricia MR; Costa, Diana Soares da; Reis, Rui L.; Ulijn, Rein V.; Lewis, Jason S.; Pires, Ricardo A.; Pashkuleva, Iva: Carbohydrate analogue as a metabolic inhibitor for cancer cells, 13th International Meeting of the Portuguese Carbohydrate Group – GLUPOR 13, Porto, Portugal, September 2019.

5. **Brito, Alexandra;** Costa, Diana Soares da; Carvalho, Andreia; Reis, Rui L.; Ulijn, Rein V.; Pires, Ricardo A.; Pashkuleva, Iva: Short carbohydrate amphiphiles as smart therapeutics targetting cancer. 256th ACS National Meeting & Exposition: Nanoscience, nanotechnology and beyond, Boston MA, USA, August 2018, ABSTRACTS OF PAPERS OF THE AMERICAN CHEMICAL SOCIETY, vol. 256, pp. 112 - CARB, 2018.

6. **Brito, Alexandra;** Costa, Diana S.; Novoa-Carballal, Ramon; Reis, Rui L.; Abul-Haija, Yousef M.; Ulijn, Rein V.; Pires, Ricardo A.; Pashkuleva, Iva: Sugar coated supramolecular nanofibers as minimalistic proteoglycan mimics, Chem2Nature Workshop: Internation Symposium on Bioinspired Macromolecules Systems, Aveiro, Portugal, November 2017.

7. **Brito, Alexandra;** Abul-Haija, Yousef M.; Costa, Diana S.; Novoa-Carballal, Ramon; Reis, Rui L.; Ulijn, Rein V.; Pires, Ricardo A.; Pashkuleva, Iva: Supramolecular hydrogels based on the co-assembly of simple carbohydrates and peptides amphiphiles for biological applications, 12th Meeting of the Carbohydrates Group, September 2017, Aveiro, Portugal.

8. **Brito, Alexandra;** Costa, Diana Soares da; Carvalho, Andreia; Reis, Rui L.; Ulijn, Rein V.; Pires, Ricardo A.; Pashkuleva, Iva: Carbohydrate nanonets for cancer theranostics. Chem2Nature Second School Conference, Porto, Portugal, July 2017.

9. **Brito, Alexandra;** Costa, Diana S.; Novoa-Carballal, Ramon; Reis, Rui L.; Ulijn, Rein V.; Pires, Ricardo A.; Pashkuleva, Iva: Supramolecular hydrogels with tuned mechanical properties for tissue engineering, TERM STEM Conference, October 2016, Guimarães, Portugal.

**Invited talk**

1. **Brito, Alexandra;** Reis, Rui L.; Pires, Ricardo A.; Pashkuleva, Iva: Depriving cancer glycolysis by aromatic N-glucosides that act as GLUT1 antagonists and substrates for biocatalytic self-assembly, 2º Encontro Nacional de Jovens Investigadores em Oncologia, September 2020, Porto, Portugal.

**Conference oral presentations (non-speaker)**

2. Castro, Vânia I.; Gao, Yuting, **Brito, Alexandra**; Costa, Diana Soares da; Chen, Jie; Ulijn, Rein V.; Reis, Rui L.; Pashkuleva, Iva; Pires, Ricardo A.: Different energy inputs promotes helicity change in the supramolecular arrangement of carbohydrates, 1st Discoveries Forum on Regenerative and Precision Medicine, Porto, Portugal, September 2019.
3. Araújo, Ana Rita; **Brito**, **Alexandra**; Reis Rui L.; Pires, Ricardo A.: " Supramolecular inhibition of Aβ42 intermediates by GlcN analogues", 13th International Meeting of the Portuguese Carbohydrate Group – GLUPOR 13, Porto, Portugal, September 2019.
4. Castro, Vânia I.; Gao, Yuting, **Brito, Alexandra**; Costa, Diana Soares da; Chen, Jie; Ulijn, Rein V.; Reis, Rui L.; Pashkuleva, Iva; Pires, Ricardo A.: Carbohydrate stereoisomers self-assemble into supramolecular fibers with different helicity, 13th International Meeting of the Portuguese Carbohydrate Group – GLUPOR 13, Porto, Portugal, September 2019.
5. **Brito, Alexandra;** Abul-Haija, Yousef M.; Costa, Diana S.; Novoa-Carballal, Ramon; Reis, Rui L.; Ulijn, Rein V.; Pires, Ricardo A.; Pashkuleva, Iva: Co-assembly of peptide and carbohydrate amphiphiles to generate proteoglycan mimics, 256th ACS National Meeting & Exposition: Nanoscience, nanotechnology and beyond, Boston MA, USA, August 2018, ABSTRACTS OF PAPERS OF THE AMERICAN CHEMICAL SOCIETY, vol. 256, pp. 113 - CARB, 2018.

**Conference posters (as first author)**

1. **Brito, Alexandra;** Pereira, Patricia MR; Costa, Diana S.; Novoa-Carballal, Ramon; Reis, Rui L.; Lewis, Jason; Ulijn, Rein V.; Pires, Ricardo A.; Pashkuleva, Iva: Supramolecular assembly of carbohydrate amphiphiles for biomedical applications, Systems Chemistry Symposium 2020, Virtual Symposium, May 2020.

2. **Brito, Alexandra;** Pereira, Patricia MR; Reis, Rui L.; Ulijn, Rein V.; Lewis, Jason S.; Pires, Ricardo A.; Pashkuleva, Iva: Cancer spheroids are disrupted via a metabolic inhibition and a biocatalytic self-assembly process. TERM STEM, Braga, Portugal, November 2019.

3. **Brito, Alexandra;** Costa, Diana S.; Novoa-Carballal, Ramon; Reis, Rui L.; Abul-Haija, Yousef M.; Ulijn, Rein V.; Pires, Ricardo A.; Pashkuleva, Iva: Sugar coated supramolecular nanofibers as minimalistic proteoglycan mimics, Chem2Nature Workshop: Internation Symposium on Bioinspired Macromolecules Systems, Aveiro, Portugal, November 2017.

4. **Brito, Alexandra;** Costa, Diana Soares da; Carvalho, Andreia; Reis, Rui L.; Ulijn, Rein V.; Pires, Ricardo A.; Pashkuleva, Iva: Smart Carbohydrate Nanonets: appealing at the sweet side of cancer, FoReCaST Conference, Porto, Portugal, July 2017.

5. **Brito, Alexandra;** Costa, Diana S.; Novoa-Carballal, Ramon; Reis, Rui L.; Abul-Haija, Yousef M.; Ulijn, Rein V.; Pires, Ricardo A.; Pashkuleva, Iva: Biofunctional supramolecular hydrogels by co-assembly of simple carbohydrate and peptide amphiphiles, Annual TERMIS-EU, Davos, Switzerland, June 2017.

6. **Brito, Alexandra;** Costa, Diana S.; Novoa-Carballal, Ramon; Reis, Rui L.; Pires, Ricardo A.; Pashkuleva, Iva: "Supramolecular hydrogels with tuned mechanical properties for tissue engineering", GENE2SKIN Conference and TERM STEM, 2016.

7. **Brito, Alexandra;** Costa, Diana S.; Novoa-Carballal, Ramon; Reis, Rui L.; Pires, Ricardo A.; Pashkuleva, Iva: Synthesis of biofunctional supramolecular hydrogels by co-assembly of simple carbohydrate and peptide amphiphiles, Chem2Nature First School Conference, November 2016, Guimarães, Portugal.

**Conference posters (as co-author)**

1. Castro, Vânia IB; Gao, Yuting; **Brito, Alexandra**; Costa, Diana Soares da; Chen, Jie; Ulijn, Rein V.; Reis, Rui L.; Pashkuleva, Iva; Pires, Ricardo A.: Out of equilibrium assembly of carbohydrate amphiphiles as a modulator of the supramolecular helicity and gelation, FoReCast 2nd Workshop, 2019.

2. Gomes, Sandra F.; Brito, **Alexandra Brito; Caballero,** David; Costa, Diana Soares da; Brancato, Virginia; Kundu, Subhas C., Martins, Ana M.; Pashkuleva, Iva; Reis, Rui L.; Pires, Ricardo A.: Development of micropatterned supramolecular hydrogels for myocardium regeneration, Chem2Nature Final Conference, 2018.

3. Castro, Vânia IB; Gao, Yuting; **Brito, Alexandra**; Chen, Jie; Reis, Rui L.; Pashkuleva, Iva; Pires, Ricardo A.: Effect of stereochemistry on the assembly and properties of supramolecular structures made of short aromatic carbohydrate amphiphiles, Chem2Nature_Final Conference, 2018.

4. Gomes, Sandra F.; Brito, **Alexandra Brito; Caballero,** David; Costa, Diana Soares da; Brancato, Virginia; Kundu, Subhas C., Martins, Ana M.; Pashkuleva, Iva; Reis, Rui L.; Pires, Ricardo A.: Micropatterned supramolecular hydrogels promote cell alignment for myocardium regeneration, Chem2Nature, 2018.

**Awarded grants**

- Liga Portuguesa para o cancro scholarship, awarded for 12 months.
- Scholarship from Fundação Luso-Americana para o Desenvolvimento FLAD for an internship in the USA, award for 4 months.
- Ph.D. scholrship awarded by Fundação para Ciência e Tecnologia (PD/BD/113794/2015).

"*Let us fight for a world of reason, a world were science and progress will lead to all man's happiness*."

Charles Chaplin, in *The Great Dictator*.

# SECTION 1

# GENERAL INTRODUCTION

# Chapter I

# DESIGN OF SUPRAMOLECULAR BIOMATERIALS BASED ON CARBOHYDRATE AMPHIPHILES

## DESIGN OF SUPRAMOLECULAR BIOMATERIALS BASED ON CARBOHYDRATE AMPHIPHILES


### Abstract

After billions of years of evolution not a single live cell has emerged that does not cover itself with a dense code of glycans: carbohydrates are involved in all essential processes within the life cycle of cells and organisms. They exercise their bioactivities via simultaneous multivalent non-covalent interactions with other biomolecules such as proteins. Supramolecular polymers are ideal systems to generate polyvalent architectures for studying and modulating these interactions: the inherent reversibility of the self-assembling process and the translation of monomers into polymers provides control over ligand density and assembly architecture. We present briefly some recent approaches to develop such systems and to use them in different biomedical applications


---

*This chapter is based on the following publications:*

**Brito, Alexandra;** Kassem, Salma; Reis, Rui L.; Ulijn, Rein V.; Pires, Ricardo; Pashkuleva, Iva; "Design of supramolecular biomaterials based on carbohydrate amphiphiles*", submitted.*

**Brito, Alexandra;** Reis, Rui L.; Pires, Ricardo; Pashkuleva, Iva; "Sweet building blocks for self-assembling biomaterials with molecular recognition", Self-assembling Biomaterials- Molecular Design, Characterization and Application in Biology and Medicine, Eds. Azevedo H. S., and da Silva R. M. P., Woodhead Publishing, 2018, pp 79-94.

## I.1. INTRODUCTION

Carbohydrates are involved in numerous essential processes within the life cycle of cells and organisms – they are a source of energy; important metabolites; sustain the swelling pressure and mechanical properties of different tissues; and are also responsible for activating cascades of cellular events, ranging from cellular adhesion to differentiation and apoptosis. Their function is exerted mainly through simultaneous non-covalent interactions with their environment. Because of their structural diversity (Fig. I.1), carbohydrates can display huge number of ligand structures with induced fit and cooperativity that turn their multivalent interactions specific and selective. The incorporation of carbohydrates in biomedical systems increases the level of molecular complexity, thus, giving rise to an exclusive class of bioinformation coding materials that are not accessible using more conventional materials based on peptides, proteins and other polymers.

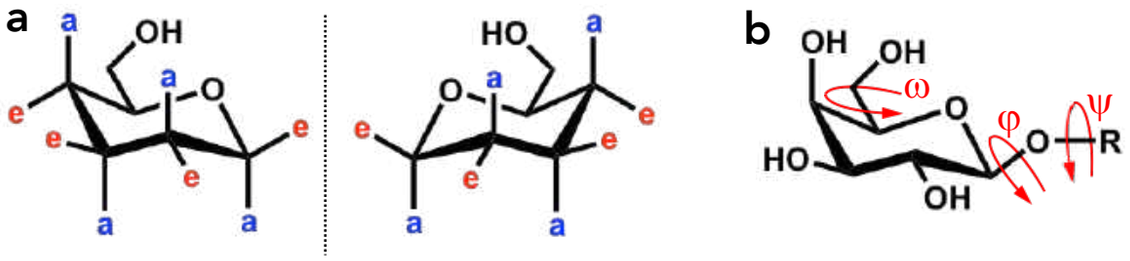


**Figure I.1. Structural diversity of carbohydrates is determined by (a) numerous isomers in which each hydroxyl group can be in either axial (a) or equatorial (e) position and (b) the induced fit set by the three dihedral angles (ω, φ, ψ).**

To capitalize on multivalency and the structural richness, supramolecular approaches are better suited than covalent synthesis for several reasons: they introduce a dynamic aspect to the system, offering the possibility of more complex communication with its environment through reversible formation, responsiveness and adaptability; they can generate larger functional and organized structures that would extend the multivalent interactions over longer distances; and their morphology can be tuned to match the targeted biointerface. In this chapter, we will present briefly the role of multivalency in carbohydrate bioactivity, then we will discuss the different building blocks and strategies employed in carbohydrate self-assembly and finally, we will highlight some of the recent biological applications of supramolecular carbohydrate systems.

## I.2. THE ROLE OF MULTIVALENCY IN CARBOHYDRATE AMPHIPHILES

Non-covalent interactions can be up to 100 times weaker than covalent bonds. To compensate the weakness of these interactions but preserve their reversibility, Nature has adopted the concept of multivalency - the ability of a substrate to form multiple individual bonds with a ligand to enhance binding affinity and ensure selectivity and specificity of recognition.[1] Simultaneous multiple bindings increase the binding contact surface resulting in an interaction that is much stronger and more selective than the individual bonds.

### I.2.1. Molecular basis of carbohydrate binding interactions

Carbohydrates interact with their environment through well-defined signature determined by their sequence and preferred three-dimensional conformation. Decades of crystallographic and NMR studies have identified the molecular interactions that govern carbohydrate binding and recognition in biological systems.[2] Each carbohydrate, ranging from simple monosaccharide to proteoglycans, has a unique imprint that can be recognized by other biomolecules.[3] The position and arrangement of the functional groups delimits hydrophilic and hydrophobic patches through which polar and non-polar interactions can respectively take place. Despite the structural diversity of the carbohydrate interactome, the nature of interactions at the molecular level remains the same: hydrogen-bonding is the main driving force while hydrophobic interactions and metal bridges balance and stabilize the complexes (Fig. I.2).

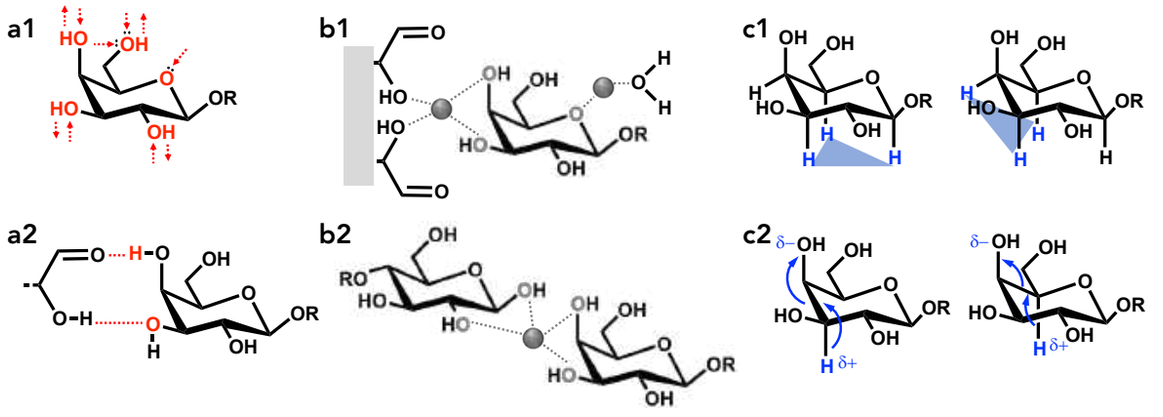


**Figure I.2. Schematic presentation of non-covalent interactions in which carbohydrates can be engaged: (a) hydrogen bonding can be either (a1) cooperative or (a2) bidentate; (b) complexation with cations, in which (b1) proteins amino acids, (b2) carbohydrates and/or (b1) water can also occupy coordination sites; and (c) hydrophobic CH-π stacking that**

**results from the London dispersion forces and stereoelectornic effects (electron-defficient CH bonds are formed via hyperconjugations as shown in c2).**

### I.2.1.1. Hydrogen bonding

Two types of hydrogen bonding have been identified in carbohydrate interactions: (i) cooperative hydrogen bonds in which the carbohydrate's hydroxyl groups act as both acceptor *via* the oxygen and donor through the hydrogen (red arrows in Fig. I.2a1); and (ii) bidentate hydrogen bonds (Fig. I.2a2) in which two adjacent hydroxyl groups of the carbohydrate bind to two different atoms of a planar polar amino-acid side chain (typically aspartate, glutamate, asparagine, glutamine or arginine).[4, 5] Cooperative hydrogen bonding occurs intramolecularly and/or in carbohydrate-carbohydrate interactions, while bidentate hydrogen bonds are mainly invovled in carbohydrate-protein interactions in which amide groups act as donors and the acidic side chains of aspartate and glutamate act as acceptors, thus providing a specific arrangement, selective for adjacent equatorial/equatorial or equatorial/axial hydroxyl groups. [*]

### I.2.1.2. Interactions with cations

The X-ray crystal structures of some lectins reveal the presence of divalent cations near the carbohydrate binding site. The metal ions either fix the positions of certain amino acids that interact with the carbohydrate or form bridges between the carbohydrate ligand and the binding pocket (Fig. I.2b1). Among different metals, calcium ions ($Ca^{2+}$) are the most common coordination centers with the carbohydrates hydroxyl groups forming the ligand, although the ring oxygen can also be part of the ligand, with the other coordination sites being occupied either by amino-acid residues or water molecules (Fig. I.2b1).[7] In carbohydrate-carbohydrate interactions, the coordination sites are all occupied by hydroxyl groups or water molecules (Fig. I.2b2). In complex carbohydrates, *e.g.* glycoconjugates, glycosaminoglycans, such coordination can result in formation of bridges between different carbohydrate chains - an indispensable feature in cell-cell adhesion, which increases the adhesion force. Cations can also compensate the negative charge of carbohydrates that contain acidic groups. Thus, the concentration

[*] In the biological milieu, water plays an important role in hydrogen bonds networks: the loss of bound water in protein binding pockets at the expense of carbohydrates comes with an entropic cost. For more details on this issue, the reader is referred to Lemieux's work on the role of water in carbohydrate biorecognition[6]

of the cations plays a crucial role not only in balancing the adhesive forces versus the charge repulsion, but also in modulating cell surface charge.

#### I.2.1.3. Hydrophobic interactions

Despite being highly polar and solvated molecules, carbohydrates can engage in hydrophobic interactions through non-polar patches created by the localization of several axial protons on the same face of the carbohydrate ring. Hydrogen bonds provide a structural framework that enables molecules approaching and van der Waals interactions. It is known for a long time that van der Waals forces contribute to the stability of carbohydrate-protein complexes, but only recently the contribution of CH-π interactions was demonstrated both experimentally and theoretically.[8-10] These studies showed that aromatic amino-acid residues can interact with different faces of the carbohydrate ring with a parallel stacking geometry (Fig. I.2c1). While London dispersion forces are the main attractive force of CH-π interactions, the weaker electrostatic interaction between the electron-rich aromatic ring and electron-defficient C–H bonds of the carbohydrate (Fig. I.2c2) controls the directionality of the bond. A comparison between different aromatic amino acids shows that all four tryptophan, tyrosine, phenylalanine and histidine engage in CH-π interactions with carbohydrates but there is a strong preference for tryptophan followed by tyrosine, phenylalanine and histidine.[9] This order reflects the electrostatic surface potential and electron-richness of their respective π-systems.

### I.2.2. Multivalent carbohydrate binding modes

A single occurrence of any of the above-mentioned interactions does not result in significant functional impartment of the carbohydrate. These interactions must be multiplied and organized in cooperative fashion to enhance and modulate the strength of binding and turn it biofunctional (Fig. I.3). Of note, multiple simultaneous interactions have unique collective properties that are qualitatively different than the simple arithmetic sum of the respective monovalent interactions. Multivalent ligands usually bind to their receptors in a sequential manner so that the entropic cost is paid in the initial binding. The entropic cost of subsequent interactions is therefore lower, resulting in favorable binding.[1]

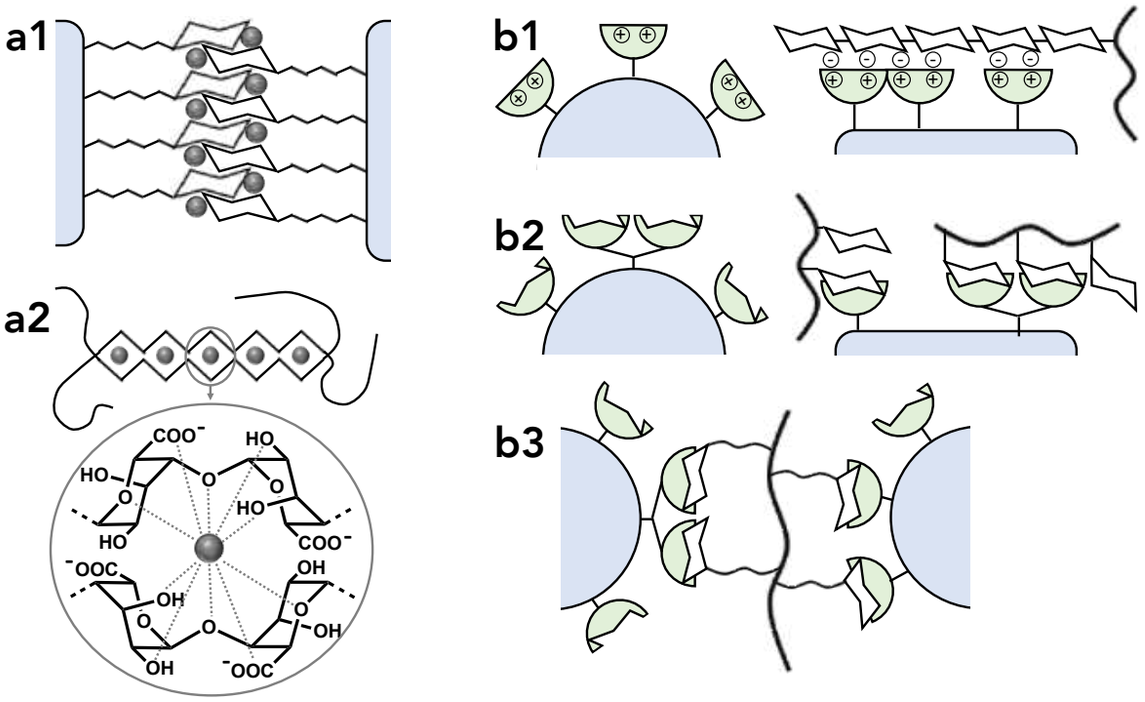


**Figure I.3. Examples of multivalent (a) carbohydrate-carbohydrate interactions that take place during (a1) cell-to-cell interactions or (a2) alginate chains in the presence of metal ions (green) and (b) protein-carbohydrate interactions between: (b1) glycan-binding proteins and glycosaminoglycans; (b2) lectins and glycoconjugates with multivalent carbohydrates presentation can promote lectin clustering; and (b3) multiple lectins and multivalent carbohydrate forming cross-linked lattices. Cells are presented in blue, receptors in light green and the metal ions in dark green.**

### I.2.2.1. Multivalent carbohydrate-carbohydrate interactions (CCI)

In biological systems, carbohydrate-carbohydrate interactions (CCI) call attention because of their involvment in cell-cell adhesion and recognition processes.[11, 12] The ultra weak CCI are advantageous during the first step of cell surface screening and together with their induced fit and high reactivity as compared with protein-protein interactions (*e.g.* integrines, cadherins) allow fine-tuning for primary connections between the cells' glycocalyx through the formation of low affinity and reversible bonds (Fig. I.3a1).[12, 13] These are then reinforced, if the fit is right, through multiple simultaneous and specific interactions, before irreversible processes can take place. In most biological systems bivalent ions, particularly $Ca^{2+}$, promote CCI by locking the carbohydrate chains in their complimentary arrangement to provide an optimal fit between cells and/or by crosslinking the carbohydrate chains from interacting cells. Such crosslinks might only be involved as a driving force in the initial cell-to-cell approaching or provide additional adhesion forces per binding site and formation of so-called carbohydrate zippers stems (Fig. I.3a2). The zippers

are usually formed by the systematic repetition of cells interactive sites and their adhesion strengths is within the piconewton range. While this binding mechanism is considered general for CCI, other binding modes may also occur, illustrating the tremendous value of multivalency in creating specificity and modulating binding forces.

#### I.2.2.2. Multivalent carbohydrate-protein interactions (CPI)

Most of the specific biological roles of carbohydrates are mediated by carbohydrate-protein interactions (CPI). If we exclude the glycan-specific antibodies, the proteins that interact with carbohydrates can be categorized into two major groups: lectins and glycosaminoglycan-binding proteins (GBP). Their monovalent interactions, *i.e.* protein singe binding site to monosaccharide, are generally weak (Kd in the micromolar range) but the binding affinities can be enhanced dramatically by adopting protein conformations that facilitate multivalent binding. The spatial arrangement of the binding sites can modulate the affinity of the interaction and thus allows selectivity. The carbohydrate density is also important because of the avidity effect but too high density can cause steric hindrance and compromise the selectivity.

Various binding modes exist and depend on the protein, the nature and complexity of carbohydrate, the environment and the particular function (Fig. I.3b). GBP interact with sulfated glycosaminoglycans *via* clusters of positively charged amino acids, *e.g.* Cardin–Weintraub sequences (Fig. I.3b1). On the other hand, lectins recognize specific carbohydrates termini and bind them into structurally defined pockets (Fig. I.3b2,3). Multivalent carbohydrates can either bind to subsites of single or multiple lectins. In the case of single lectins, the subsites are generally clustered to face the carbohydrate, facilitating face-to-face binding through multiple identical interactions. The clustering of receptor subsites increases the valency on the protein side thereby strengthening the interaction. This phenomenon is known as the "cluster glycoside effect" and the overall interaction can be stronger than the sum of the individual interactions in some cases. Lectins that are involved in signal transduction processes use different binding mode with cross-linked lattices between multiple lectins and one or more multivalent glycoconjugate (Fig. I.3b3). These cross-links create networks of non-covalent interactions that can be either linear, two or three-dimensional. Linear one-dimensional cross-links are soluble and have a high degree of flexibility. They result from interactions between bivalent carbohydrates and bivalent lectins, where each carbohydrate site is bound to a different lectin. More complex two and three-dimensional networks are

formed with carbohydrate ligands and proteins with higher valencies, often causing aggregation and precipitation.

## I.3. DESIGN OF CARBOHYDRATE SELF-ASSEMBLING BLOCKS

The biointeractions of carbohydrates showcase how cooperative supramolecular multivalent interactions can: (i) build specificity through spatial complementarity, and (ii) increase binding affinity through the multiplication of interaction sites. This understanding provides a vision on the potential that mimicking multivalency mechanisms could hold when designing carbohydrate systems for biomedical applications.

### I.3.1. General principles in the design of self-assembling building blocks

Self-assembly is a bottom-up approach by which dynamic multivalent systems can be generated by non-covalent (reversible) interactions. It is ubiquitously used by Nature to create complex structures whose biofunctionality is tailored by the generated (nano)morphology and the incorporated bioactive moiety. In biological self-assembled systems, carbohydrates are often conjugated to lipids, proteins or aromatic nitrogenous bases (Fig. I.4a-c). Such conjugation imparts the hydrophilic carbohydrates with amphiphilic properties and thus, enhances their self-assembling propensity. The diversity of the generated morphologies is striking (Fig. I.4d) and suggests that synthetic amphiphilic carbohydrate building blocks can be tuned to drive a structure-targeted assembly. Indeed, assembly of diverse synthetic analogues of natural glycoconjugates has shown that the size and structure of the linker[14-17] and the hydrophobic portion[16-20] affect the assembly, morphology and properties of the generated supramolecular systems. The main driving force of the assembly process depends on the structure of the hydrophobic component: CH-π interactions and aromatic staking prompt the assembly of aromatic amphiphiles[18, 21, 22], β-stacking usually propels the assembly of glycopeptides[23, 24] and hydrophobic forces forward the assembly of glycolipids[20]. Some linkers might enhance the aggregates stability by participating in supramolecular interactions as well.[16, 18] Finally, the carbohydrate component can also influence the assembly process usually by changing the solubility of the amphiphile in water.[25, 26] Additional functionalization of the carbohydrate with polar and charged groups such as sulfate and phosphate can be required for some amphiphiles to enhance their solubility.[21] Such functionalization can also introduce/change the repulsive Coulomb forces and thus,

affect the assembly.[21, 27] In supramolecular biomaterials, however, the carbohydrate is primary designed in function of a targeted biorecognition.[23, 24, 27-30]

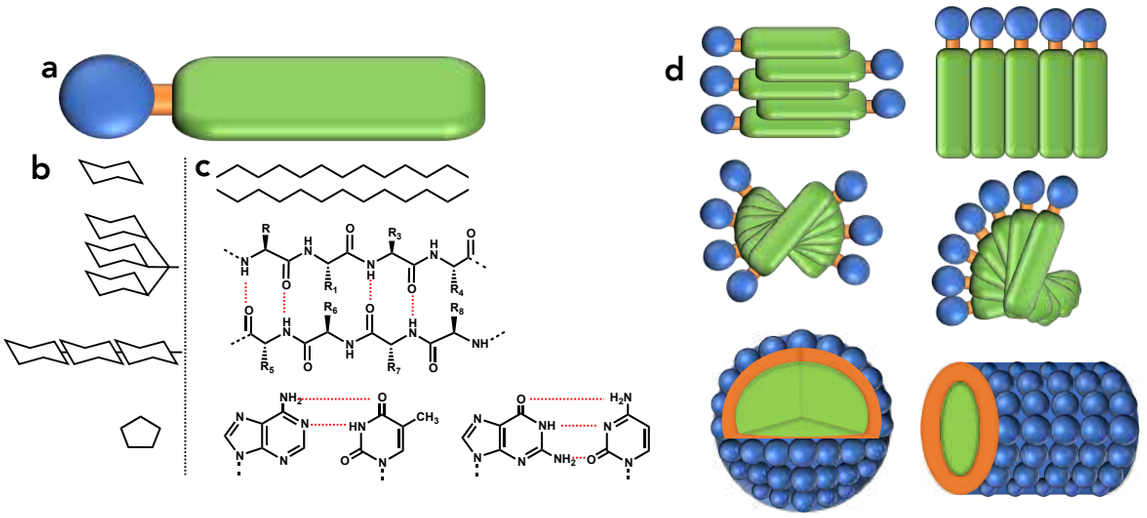


**Figure I.4. Schematic presentation of (a) general structure of carbohydrate amphiphile composed by hydrophilic carbohydrate moiety (blue), linker (orange, optional) and hydrophobic, usually self-assembling portion (green); (b, c) main structural components of natural carbohydrate amphiphiles; and (d) some of the modes by which these amphiphiles assemble. (b) The carbohydrate part can be simple six- (*e.g.* glycosphingolipids) or five- (*e.g.* nucleotides) carbon monosaccharide as well as linear (*e.g.* proteoglycans, mucines) or branched (*e.g.* glycosphingolipids, glycoproteins) oligosaccharide. (c) The hydrophobic portion can be made of lipids, proteins or nucleobases.**

### I.3.2. Types of carbohydrate building blocks for self-assembly

#### I.3.2.1. Glycopeptides

In biological systems, most proteins are glycosylated, *i.e.* covalently bound to carbohydrates, and form two main classes of bioactive molecules - glycoproteins and proteoglycans. Synthetic glycopeptides emerged as functional mimics of these molecules - they are simpler in composition but recapitulate some bioactivites of the natural components upon assembly. The design is usually based on amino acids sequence with known bioactivity and self-assembly propensity that is functionalized with a monosaccharide such as mannose[31], glucosamine[24, 30, 32, 33], or *N*-acetylglucosamine[23] to impart biorecognition and/or to change the properties (*e.g.* morphology, stability) of the peptide assemblies. The carbohydrate can be incorporated *via S*-[25, 34], *N*-[30, 32, 33, 35, 36], or *O*-[23, 24, 31, 37] glycosylation and can also include a linker[23, 31, 34, 35] between the carbohydrate and the peptide. In the case of short peptides, *e.g.* di- and tri-

peptides, the supramolecular interactions might not be strong enough to prompt assembly of stable structures and additional modification is required. The most used strategies in these cases are to insert additional aromatic segment(s) either as a part of the linker[23, 35] or at the peptide end of the amphiphile[30, 32, 36, 38]. Such modification introduces additional π-π stacking and enhances the self-assembly propensity of the amphiphile and can be also used for visualization. The targeted assembly of glycopeptides is usually unidirectional, *i.e.* leading to formation of nanofibers with peptide core and multivalent carbohydrate presentation on the shell - structures that mimic the native glycoproteins. The carbohydrate density can be tuned by co-assembly of glycosylated and non-glycosylated peptides to optimize the biointeractions and minimize the steric hindrance. Polymersomes and nanoparticles that mimic cell surface and extracellular vesicles are also of interest. They can be accessed by assembly of glycopeptide block copolymers.[39-41] In these supramolecular systems longer carbohydrate chains are exposed on the surface for biointeractions thus mimicking proteoglycans. To maintain the amphiphilic character of the copolymer, the peptide portion must be also extended allowing incorporation of longer biofunction coding sequences.[40]

### I.3.2.2. Nucleosides and nucleotides

The formation of double helix by nucleic acids is one of the most common examples given for supramolecular organization in biological systems. The process is driven by hydrogen bonding between specific Watson–Crick or Hoogsteen pairs of nucleobases. The nucleobases are *N*-glycosylated with ribose in RNA or 2-deoxyribose in DNA - a tiny structural difference that is crucial for the biorecognition of these molecules (*e.g.* by enzymes). Besides hydrogen bonding, nucleotides can participate in complexation with metals, π-stacking and electrostatic interaction *via* the phosphate group(s) (Fig. I.5a), which makes them versatile components for synthetic supramolecular biosystems.[42] Among the five natural nucleosides, guanosine (G) has attracted the attention of the carbohydrate community because of the recent data showing that Y RNA can be N-glycosylated at G.[43] This nucleoside is also of special interest for supramolecular chemists because of its self-complementarity and ability to form ribbons and ordered tetramers (G-quartets) that can further organize into hierarchical structures of higher order in the presence of metal ions (Fig. I.5b, c). Different metal ions can be used as a trigger of the self-assembly process to generate supramolecular structures with different morphology and gelation properties.[44-46]

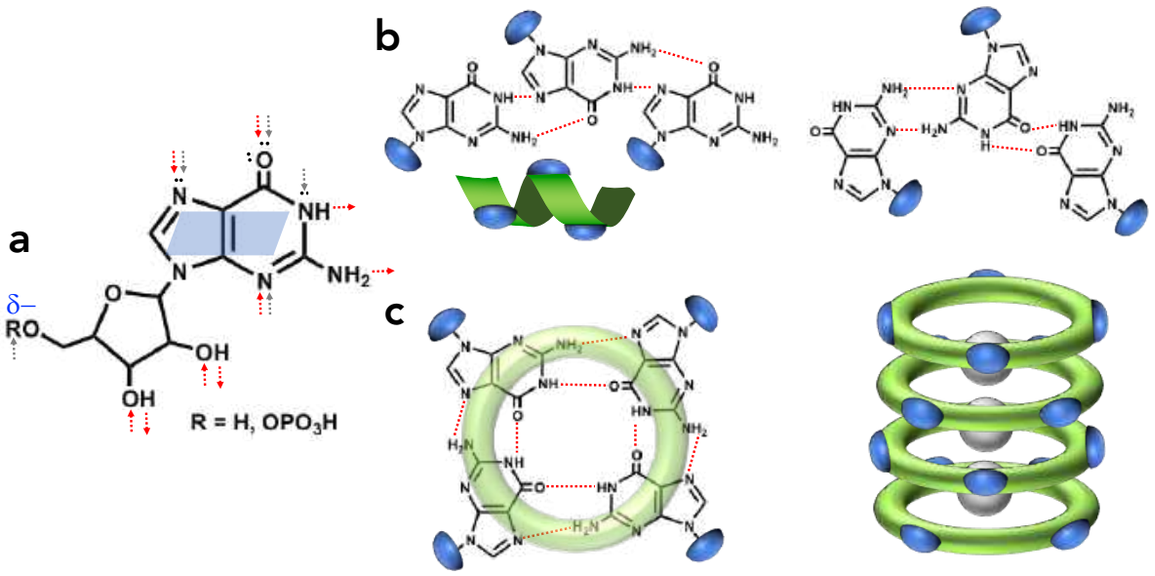


**Figure I.5. (a) Supramolecular interactions in which guanosine and its 5' monophosphate nucleotide can participate: hydrogen-bonding (red), complexation with metals (grey), π-stacking (light blue) and electrostatic interaction *via* the phosphate. These interactions result in formation of (b) supramolecular ribbons or (c) tetramers (G-quartet) in the presence of metal ions that can further stack in G-quadruplex.**

Nucleotides can be modified either at the pentose or at the nucleic acid to generate wide variety of amphiphiles.[47-51] The carbohydrate moieties in these amphiphiles contributes to the assembly process (mainly by hydrogen bonding) but surprisingly, there are not data on their involvement in any specific biorecognition.

### I.3.2.3. Glycolipids

The role of glycolipids in cell membrane structuring and cell-cell interactions has inspired the development of diverse amphiphiles that contain fatty chain(s) as a lipophilic component complementing hydrophilic carbohydrate(s) usually mono- or di-saccharide (Fig. I.6a). The driving force of their assembly is a microphase separation that results in formation of discrete regions for the lipophilic and hydrophilic components. While these amphiphiles seem structurally simple, they can form aggregates with various morphology such as micelles, twisted fibers, helical coils, nanotubes, among others. To assemble such variety of adaptive and functional systems, living organisms use fatty acids of different size (14 to 24 carbons) and saturation (0 to 6 unsaturated bonds).[52] Studies with synthetic glycolipids show that the

amphiphilic properties can be tuned by the length of the fatty acids, while their number (one or two) and/or saturation can change the packing parameter and thus, affect the morphology of the generated aggregate (Fig. I.6).[53-56] The fatty acids saturation is also important for permeability of the generated systems - a crucial parameter in the design of delivery systems. Unsaturated chains assemble in bilayers with enhanced water permeability and this effect is proportional to the number of the unsaturated bonds.[52, 54] When disaccharide is used instead monosaccharide as a polar component, the structure is stabilized by additional hydrogen bonding between the hydroxyl groups and thus, less flexible/permeable.[55] The bond between the carbohydrate and the fatty acid (α- or β-) and between the monosaccharides (1,4- or 1,6-) also influences the order of the system: more stable smectic A phase is formed by β-linked glycolipids and 1,4-linked disaccharides, for which the packing parameter is about 1 (Fig. I.6).[55]

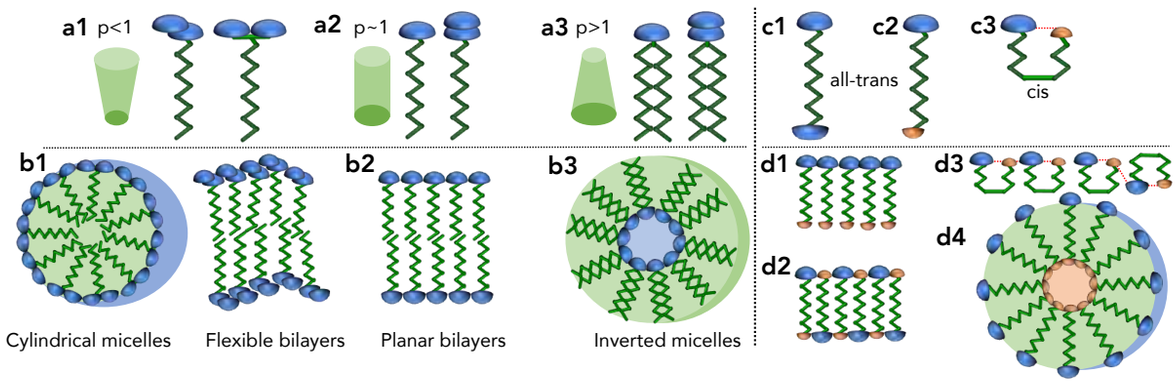


**Figure I.6. General structure of (a) glycolipids[55] and (b) their possible assemblies that can be predicted from the critical packing parameter (p). (c) Bolaamphiphiles can be (c1) symmetric and (c2, c3) asymmetric. The assembly of asymmetric ones is pH sensitive due to -COOH or -$NH_2$ groups (orange) that can participate in (c3) intramolecular and (d) intermolecular hydrogen bonding.**

Bolaamphiphiles can be considered as a subclass of glycolipids in which both ends of the lipid chain are functionalized with polar groups. Bolaamphiphiles can be symmetrical, *i.e.* bearing the same carbohydrate units at both termini[47, 57] or asymmetrical that have a carbohydrate moiety at one end and another polar group at the other one.[58-61] The role of the lipid length and saturation is similar as the described above but the presence of a second polar (and charged for asymmetrical amphiphiles) groups extends the assembly configurations, *e.g.* asymmetric bolaamphiphiles can form monolayers by parallel (Fig. I.6d1) or antiparallel (Fig. I.6d2) stacking that can further interact in head-to-head or head-to-tail

mode to form bilayers and more complex structures.[58, 59] The asymmetric bolaamphiphiles are of interest for biomaterials development (particularly as delivery systems) because of their pH sensitivity due to the second polar group that is usually COOH or $NH_2$ and can participate in intra- and inter- molecular hydrogen bonding with the carbohydrate (Fig. I.6c, d).[60, 61]

#### I.3.2.4. Other carbohydrate amphiphiles

Beside amphiphiles inspired by natural biomolecules, carbohydrates can be functionalized with synthetic hydrophobic portions structurally tailored to promote an assembly of a targeted morphology. The design of these amphiphiles can include different number of aromatic rings that promote assembly by π-π and/or CH-π stacking.[22, 29, 62, 63] Diblock copolymers obtained by functionalization of the carbohydrate reducing end with different hydrophobic polymers is another configuration. The main advantages of these amphiphiles are: (i) they can contain longer carbohydrate unit, which impart the assembled system with higher affinity towards its recognition and biointeractions; and (ii) the hydrophobic portion can be designed to be stimuli-responsive (*e.g.* light, pH).[27, 64-67]

## I.4. SUPRAMOLECULAR APPROACHES TO ASSEMBLE CARBOHYDRATE AMPHIPHILES

### I.4.1. Triggers of self-assembly in aqueous media

Self-assembly process represents disorder-order transition driven by the balance between repulsive and attractive forces of the involved entities. From a thermodynamic perspective, it can be described by the Gibbs free energy (ΔG, equation 1):

**Equation I.1: $\Delta G = \Delta H - T\Delta S$**

and will occur only if ΔG is negative, *i.e.* only if the energy gain associated with entropy (ΔS) decrease is compensated by an enthalpy (ΔH) decrease and below a critical temperature. In aqueous media, ΔG decrease depends on the supramolecular interactions between the amphiphiles but is also conditioned by the solvation dynamics and local water organization.[68, 69] Physical (*e.g.* temperature, light) and chemical (*e.g.* pH, ionic strength) factors that affect the balance between these interactions can result in different thermodynamic minima corresponding to different supramolecular organizations and biofunctionality.

Comprehensive understanding of the role of these factors on the dynamics and timescale of the assembly process is underway and will allow development of new materials in a predictable/targeted manner.

#### I.4.1.1. Temperature

Temperature is the most common physical trigger of self-assembly. In aqueous solutions and below a critical temperature, water molecules are organized in structured water around the hydrophobic portions preventing the supramolecular interactions between the amphiphile molecules. Heating above the critical temperature induces molecular mobility: the water molecules become disordered allowing approximation and induction of supramolecular ordering of the amphiphiles.[69] The balance disorder (water)/order (amphiphile) is important for maintaining the overall entropy positive and the temperature depends on the structure of the amphiphile in particular the ratio between the hydrophobic and hydrophilic portions.

Heating can be also applied when non-homogeneous, kinetically trapped arrested phases are formed and can interrupt the assembly of the system towards an equilibrium. In this case, the temperature is increased to disassemble the arrested phase and the formation of a new phase is controlled by the cooling rate. Transition between different minima is another process that can be manipulated by temperature changes. Because temperature affects both the thermodynamics and the kinetics of the system, the whole thermal history, *i.e.* the heating temperature and time, the cooling rate, the final temperature, and the time after cooling, is important for the assembly pathway and critical for the properties of the generated system.[70]

#### I.4.1.2. pH

Different pathologies (*e.g.* cancers, wound healing) are associated with pH changes. pH-triggered assembly/disassembly associated with morphological transition and differential diffusion kinetics is thus an attractive tool for management of such pathologies.[71] There are various molecular designs that rely on different pH sensitive processes. The most common approach includes functionalization of the amphiphile with basic/acidic functional group.[59, 60, 71] Protonation/deprotonation of such molecules is associated with re-balance of the supramolecular interactions or/and conformational changes (*e.g.* in asymmetric bolaamphiphiles with intramolecular hydrogen bonding, Fig. I.6c3). The result can be different. In some cases the shape of the assembly is preserved at different pH and only the diffusion coefficient is altered.[71]

Most often, however, different morphologies are generated due to an activation of new assembly regimen.[60] Another approach is based on cleavage of pH-sensitive linkages such as acetal.[72, 73] In this case, the amphiphiles assemble at neutral pH and degrade upon pH decrease, which may be useful for design of responsive drug delivery systems. pH change can also occur endogenously when pH sensitive groups are engaged in the supramolecular interactions triggering the assembly process. Such endogenous change can be applied for sequential assembly of multicomponent systems as demonstrated for aromatic amphiphiles of sorbitol functionalized with either acylhydrazide or carboxylic acid.[74] In this system, the assembly of the acylhydrazide decreases the pH, which in turn triggers the assembly of the carboxyl derivative.

#### I.4.1.3. Enzymes

Enzymes can also be used as a trigger of self-assembly. The process is known as enzyme-instructed or biocatalytic self-assembly (BSA).[29, 75] BSA is based on a transformation of enzyme-sensitive precursor into self-assembling molecule and thus is highly selective and sensitive: it depends on the enzyme and the precursor concentration as well as on the duration of the enzyme action. The rate of the enzymatic action controls the kinetics and the morphology of formed assembly. BSA can be applied *in situ* to trigger assembly in cells. Among different enzymes, phosphatases[29] and glycosydases[76, 77] have been selected as triggers because of their involvement in different pathologies. Some years ago, we proposed short aromatic amphiphile of glucosamine-6-phosphate as a BSA precursor.[29] Enzymatic removal of the phosphate group reduces its solubility and triggers formation of fibrillar structures that further organize into a supramolecular gel. BSA can be also used to trigger disassembly. Glycosidase-triggered drug release from amygdalin-fatty acid hydrogels can be manipulated by changing the enzyme concentration.[77] These approaches can be extended to other enzymes such as glycokinase and glycosyltransferase.

#### I.4.1.4. Light

Light is an attractive trigger for bioapplications because it is non-invasive and can be tuned by several means, namely wavelength, duration, and intensity. The amphiphiles include azobenzene (Fig. I.7a)[78, 79] or 2-butenedial (Fig. I.7b)[80, 81] as light-sensitive groups. The light irradiation triggers *trans* (visible light)/*cis* (UV light) isomerization and this conformational change induces rebalance of the supramolecular forces driving the amphiphiles assembly. Usually, sol-gel transition is promoted when wavelength within visible

region is used while UV-irradiation causes gel-sol transition. These transitions are reversible upon removal of the stimulus, which motivates the use of these systems as nanoprobes for biosensing and *in situ* cell imaging.

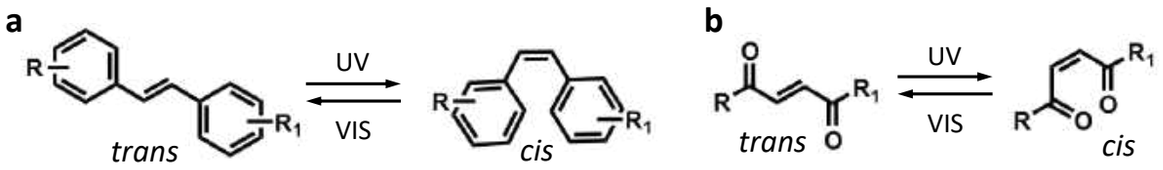


**Figure I.7. Light-sensitive groups incorporated in the structure of photo-responsive carbohydrate amphiphiles.**

### I.4.2. Multi-component systems

Self-assembly of two (or more) different building blocks is used to generate functional diversity. The co-assembly approaches applied to carbohydrates can be classified in two groups based on the used building blocks: (a) the components are able to self-assemble individually, but when mixed different systems are assembled either by co-assembly (components interact) or by assembly formed by discrete components[63, 74, 82, 83]; and (b) one of the components self-assembles and a non-assembling component is added to change the final assemblies.[21, 84-86] Under the first approach co-assembly can be promoted by using identical functional units that promote the self-assembly in the design of the amphiphiles, *e.g.* the components co-assemble by π-π stacking or β-sheet formation[21, 37, 82] and/or by charge complementarity between the co-assembled amphiphiles, *i.e.* by electrostatic interaction.[83] Recently, we have demonstrated that such approach is feasible for development of core-shell systems in which the peptide amphiphile assembles into a structural core while the carbohydrate amphiphile forms the functional shell of the nanofibers.[21] The main advantage of this assembly mode is its modularity - using independent peptide and carbohydrate blocks allows to generate structural diversity, *e.g.* different functional carbohydrate, different density by simple mixing of two solutions.

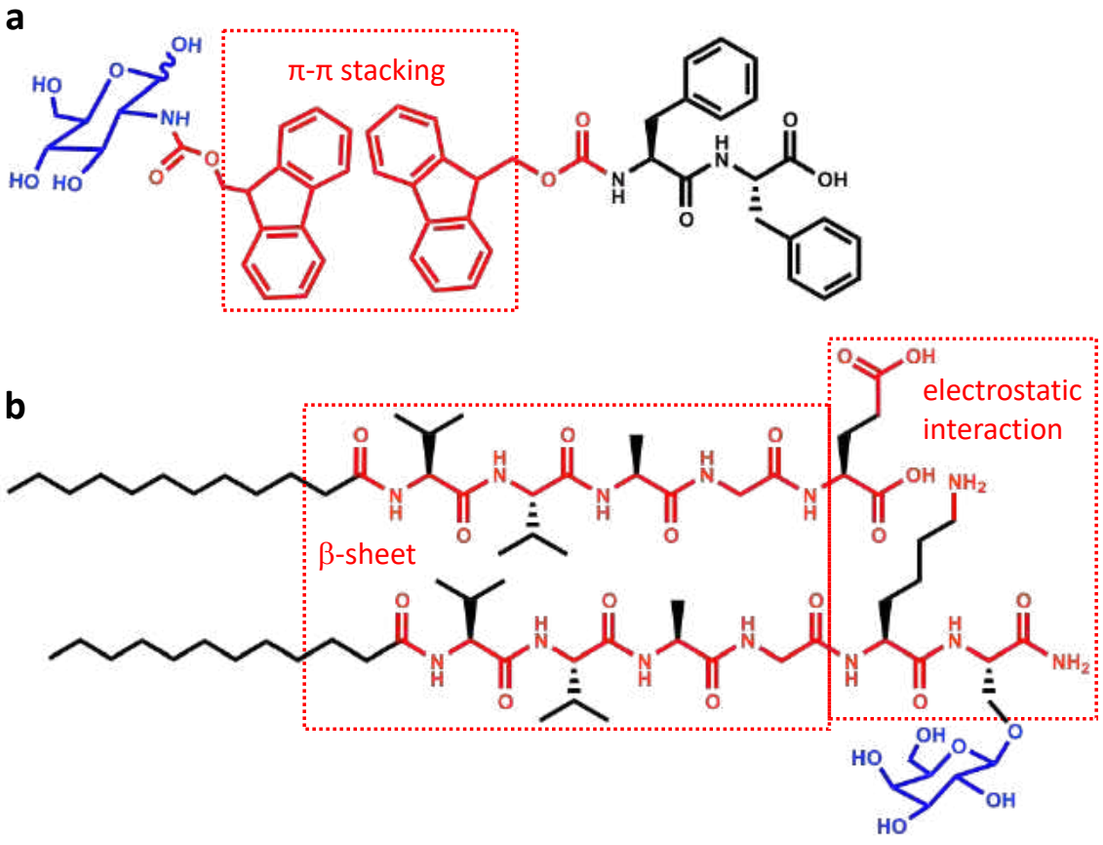


**Figure I.8. Examples of multicomponent systems with carbohydrate amphiphiles. Amphiphiles can (a, b) share the same functional units or/and (b) complementary charge that drives the co-assembly.**

In the second approach, bioactive carbohydrates, namely glycosaminoglycans (GAG, *e.g.* hyaluronan and heparin) are used as a non-assembling component and the assembly process is induced by the addition of a self-assembling peptide.[84-87] In most cases, an interfacial polyelectrolyte complexation between the negatively charged glycosaminoglycan and the positively charged peptide is the main driving force of the co-assembly process as demonstrated by the formation of a nanolayer at the interface between the solutions of the components.[84, 87, 88] Both sides of this layer have different properties and they depend on the concentration/viscosity of the used as well as on the order of adding (dropping peptide solution in GAG one or *vice versa*).

## I.5. BIOAPPLICATIONS OF CARBOHYDRATES SUPRAMOLECULAR SYSTEMS

### I.5.1. Mimics of extracellular matrix

The extracellular matrix (ECM) is three-dimensional, highly hydrated and dynamic assembly of macromolecules that provides structural support for cell adhesion and growing as well as biochemical information that control the cell fate.[89] Because glycoproteins are main components of the ECM, supramolecular carbohydrate interactions are central to ECM-cell communication. Mimicking the functions of glycoproteins is limited by the complex and challenging nature of synthetic glycochemistry, however self-assembling carbohydrate amphiphiles circumvent this issue by providing well-organized 3D matrices with surface exposed carbohydrate clusters emulating the multivalency and high density of ECM glycoproteins. This approach has been embraced by many in the field, with innovative variations in design elements. The first to explore this approach was Xu who proposed *de novo* glycoconjugate design that has three components: a self-assembling nucleobase (adenine), an integrin binding sequence (FRGD) and a glucosamine unit (Fig. I.9a).[30] *De novo* glycoconjugates have demonstrated their versatility in influencing cellular pathways through various mechanisms. In their rudimental form, they offer better cell-adhesion properties through CCI than non-carbohydrate containing ECM mimics and are known to enhance stem cell proliferation and differentiation. They can compete with native ECM proteins, offering a better anchoring point for cell adhesion. The morphology of the self-assembled structure has a direct effect on cell-cell interactions and organizations. Glycosylated nanoparticles, for instance, facilitate the formation of cellular spheroids from cell monolayers.[90] The morphogenesis is accompanied with imposed physical constraints that alter the accessibility of surface protein and molecular diffusion from the environment to the inside of the cellular cluster increasing the resistance to cytotoxic drugs.

One of the roles of ECM proteoglycans is to interact with soluble bioactive molecules secreted by cells, *e.g.* growth factors, cytokines, and regulate their stability, distribution and availability to cells. Several designs of carbohydrate amphiphiles have been proposed for development of supramolecular systems that mimic this ECM feature (Fig. I.9b-d).[21, 23, 24, 91, 92] These amphiphiles can be assembled alone (Fig. 9c-e)[23, 37, 91, 92] or co-assembled with peptide amphiphiles (Fig. I.9b, e)[21, 82, 83, 87] to generate nanofibers with surface-exposed carbohydrates. The generated hydrogels have nanofibrous structure with surface-exposed carbohydrates that protect and enhance the activity of different proteins by CPI.[21, 23, 91, 92]

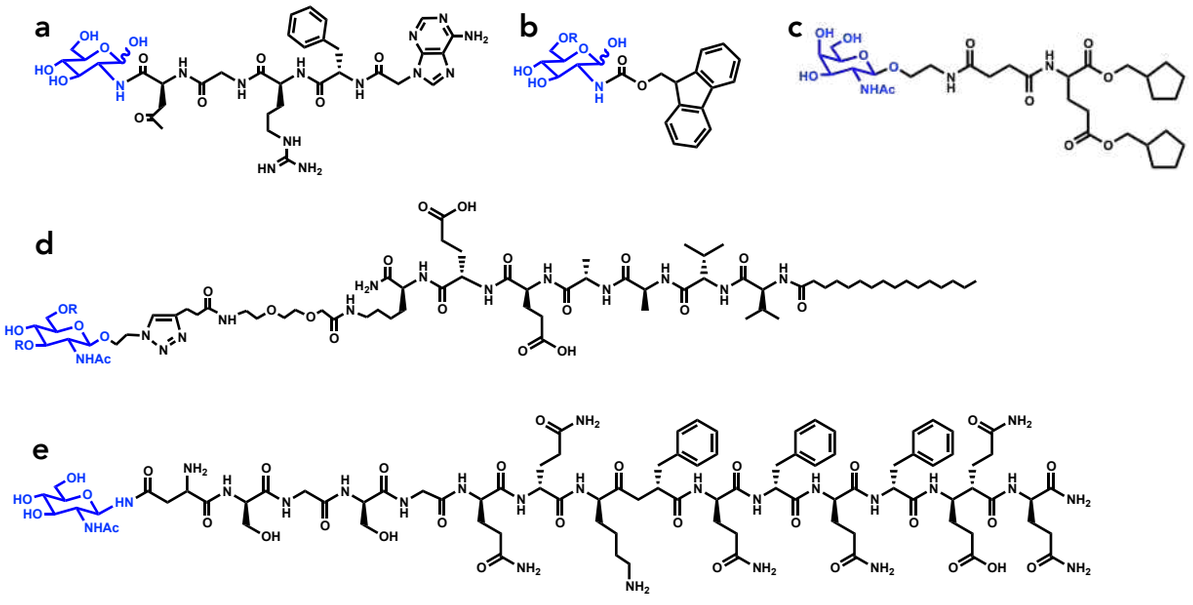


**Figure I.9. Different carbohydrate amphiphiles used to assemble structural and biofunctional mimics of extracellular matrix. R = H, $SO_3H$.**

These systems can be used as biosensors,[91-94] immunosuppressive materials[38] or in different tissue repair and engineering strategies.[21, 23, 83] Similar to heparin sulfate proteoglycans, sulfation of the carbohydrate unit can enhance significantly the biofunctionality of the system as shown for bone morphogenic protein-2 (BMP2)[23] and basic fibroblast growth factor (FGF2)[21], thus reducing significantly the protein dose needed for an efficient therapy. Co-assembly of glycosylated amphiphiles and their non-glycosylated analogues can be used to modulate the carbohydrate density on the surface of the assembled system, simply by varying the ratio of each component.[82] As discussed above, such density control is crucial for the bioactivity and selectivity of the system. The exact multivalent arrangement and distancing between exposed sugar moieties can also be tailored to specific protein binding by post-assembly functionalization of peptide nanostructures.[95]

Discrete cellular environments can be co-assembled from hyaluronan and peptide amphiphiles.[84, 85] These two components form hierarchically ordered macroscopic membranes or sacs that are semipermeable and allow exchange of nutrients and metabolites but cells are too big to cross them. The systems have the advantage that can be manipulated additionally, *e.g.* by sewing, micropatterning, which makes them versatile tools for tissue engineering and regenerative medicine.

### I.5.2. Systems with antimicrobial activity

Bacterial adhesion to the host cell is crucial step of an infection process that is mediated by carbohydrate-protein interactions. At this initial stage of the infection, bacteria adhesins/invasins bind to glycoconjugates, expressed on the eukaryotic cell surface. Moreover, some bacteria secret toxins (*e.g.* $AB_5$-type proteins) that facilitate the invasion process and bind to host cell also via their surface glycans. Multivalency is crucial in these processes as demonstrated by systematic studies using synthetic branched polymers and dendrimers functionalized with carbohydrates as inhibitors of these interactions. In unidirectional self-assembled systems, the glycosylation of nanofibers can also add to the hierarchical organization of the system by forming lateral carbohydrate-carbohydrate cross-links.[37] The nanofibers are thus able to align rather than intertwine *via* non-specific hydrophobic interactions, which generally leads to undesired aggregation, producing highly ordered supramolecular architectures. The multivalency and weakness of the interactions facilitates the sliding and repositioning of nanofibers to reach the most energetically favorable state of alignment. The interaction of glycosylated surfaces with surrounding water endows them with resistance to non-specific bacteria and proteins while maintaining their selectivity for specific lectins. This is due to the specific multivalent carbohydrate surface display, the density and arrangement of which can be modulated by different strategies for tailored binding.

Supramolecular multivalent antibacterials can be assembled by rod-coil amphiphiles (Fig. I.10) and their efficacy has been demonstrated for *Escherichia coli* (E. coli).[62, 96] Because the bacterial adhesin FimH has mannose-binding lectin domain, this carbohydrate has been a primary choice for amphiphile functionalization. The assembled systems exhibit multiple mannoses on their surface that interact and block the lectin. Of note, the supramolecular systems affect not only the protein-carbohydrate interactions but also inhibit the bacterial mobility by triggering their agglutination.[31, 63, 97] The agglutination depends on the shape and size of the assembled nanostructure that in turn can be controlled by the amphiphile design as discussed above: nanoribbons[31, 97] and long fibers[63] are more efficient agglutination promoters and introduction of a rigid segment into the amphiphiles facilitate the assembly of these nanostructures.[98]

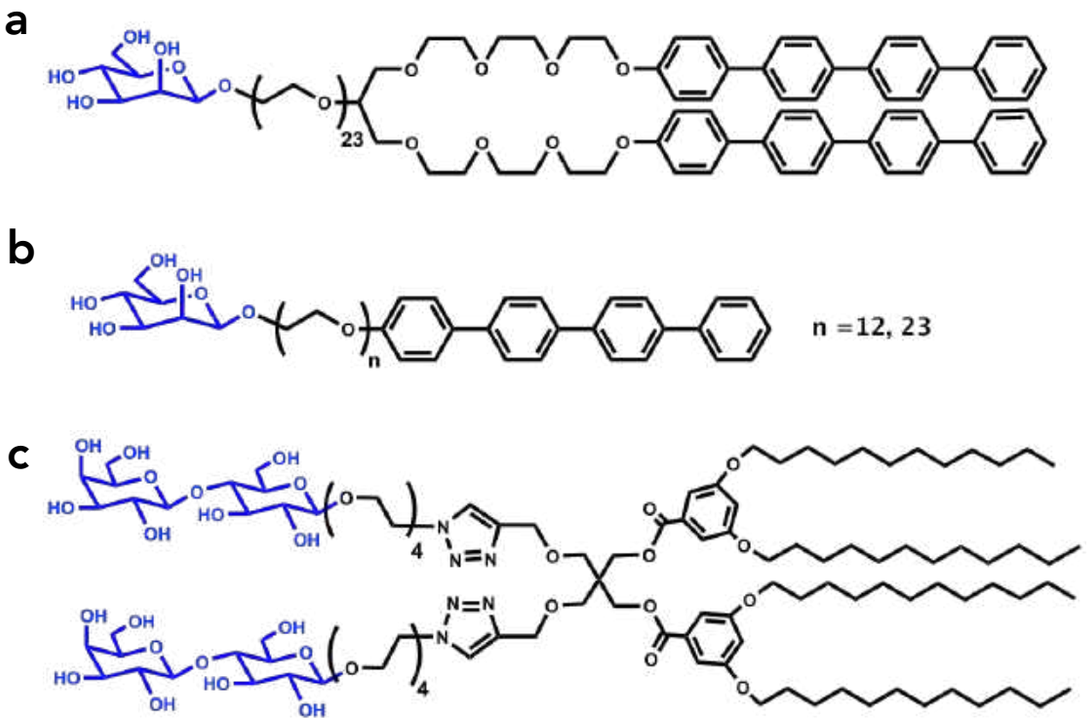


**Figure I.10. Rod-coil carbohydrate amphiphiles for assembly of multivalent antibacterial systems.**

### I.5.3. Cancer management

One of cancers hallmarks is their accelerated metabolism and higher glucose dependence as compared with the non-malignant cells. The metabolic alternations suggest that glucose antagonists must provide efficient tools for cancer management. Few years ago, we described a simple aromatic carbohydrate amphiphile, N-(fluorenylmethoxycarbonyl)-glucosamine-6-phosphate, as a chemotherapeutic agent.[29] This amphiphile deprive the glucose metabolism by interacting with glucose transporter 1 (GLUT1) and also by *in situ* assembly of a supramolecular net around the cancer cells (Fig. I.11).[28, 29] In aqueous environment the amphiphile assembles into micelles.[21] Alkaline phosphatase that is overexpressed in different cancers can cleave the amphiphile's phosphate group, thus triggering micelle-to-fiber transition. The result is formation of a discrete nanocage around cancer cells that acts as a physical barrier between these cells and their environment. The glucose units exposed on the surface of the fibers and can interact specifically with GLUT1 and to block them. The synergism between physical and biochemical deprivation of cancer metabolism turn the therapy selective and efficient.

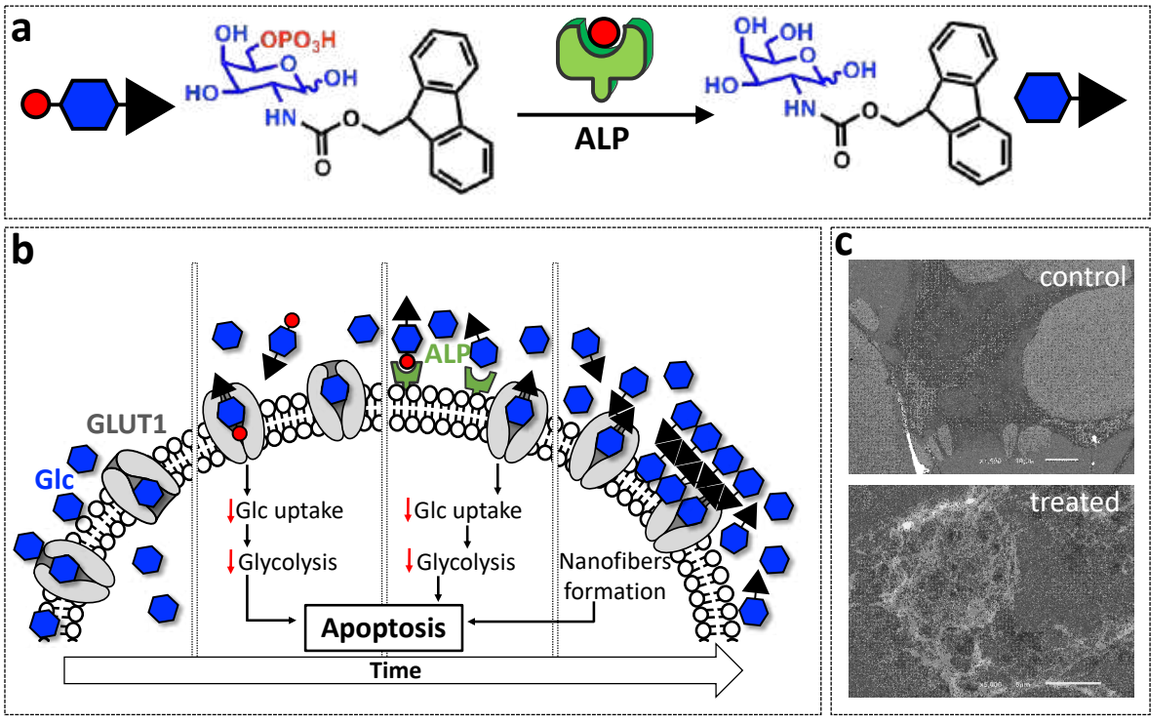


**Figure I.11. (a) Enzymatic transformation, (b) mechanism of action and (c) effect of N-(fluorenylmethoxycarbonyl)-glucosamine-6-phosphate on osteosarcoma like cells. Adapted from[28] published by the Royal Society of Chemistry and [29] published by American Chemical Society.**

## I.6. CONCLUSIONS AND FUTURE TRENDS

While the incorporation of carbohydrates within self-assembling building blocks seemed challenging some years ago, the boom that the fields of systems chemistry and glycochemistry have experienced lately has precipitated an interest in development of carbohydrate supramolecular systems with biomedical application. Nonetheless, most of the developed systems rely on the same principles used for structurally different building blocks, *e.g.* polymers and peptides, and do not explore unique carbohydrates features such as CCIs, chiral and topological abundance, multivalency. Although the cells are surrounded by complex polysaccharides in their native environment, most of the amphiphiles have simple (mono- and di-) saccharides as biofunctional units. Thus, new concepts that develop supramolecular assemblies from intricate biofunctional carbohydrates are yet to come and these should result in even better performing biomaterials. We opine that the full potential of carbohydrates in self-assembly can be only achieved if we introduce the principles regulating the glycome functions in the construction of supramolecular biomaterials.

## I.7. REFERENCES

1. Fasting C, Schalley CA, Weber M, Seitz O, Hecht S, Koksch B, et al. Multivalency as a Chemical Organization and Action Principle. Angew Chem Int Edit. 2012;51(42):10472-98.

2. Solis D, Bovin NV, Davis AP, Jimenez-Barbero J, Romero A, Roy R, et al. A guide into glycosciences: How chemistry, biochemistry and biology cooperate to crack the sugar code. Bba-Gen Subjects. 2015;1850(1):186-235.

3. McMahon CM, Isabella CR, Windsor IW, Kosma P, Raines RT, Kiessling LL. Stereoelectronic Effects Impact Glycan Recognition. J Am Chem Soc. 2020;142(5):2386-95.

4. de la Paz ML, Ellis G, Perez M, Perkins J, Jimenez-Barbero J, Vicent C. Carbohydrate hydrogen-bonding cooperativity - Intramolecular hydrogen bonds and their cooperative effect on intermolecular processes binding to a hydrogen-bond acceptor molecule. Eur J Org Chem. 2002;2002(5):840-55.

5. Gaiser OJ, Piotukh K, Ponnuswamy MN, Planas A, Borriss R, Heinemann U. Structural basis for the substrate specificity of a Bacillus 1,3-1,4-beta-Glucanase. J Mol Biol. 2006;357(4):1211-25.

6. Lemieux RU. How water provides the impetus for molecular recognition in aqueous solution. Accounts Chem Res. 1996;29(8):373-80.

7. Drickamer K. Ca2+-dependent sugar recognition by animal lectins. Biochem Soc T. 1996;24(1):146-50.

8. Fernandez MD, Canada FJ, Jimenez-Barbero J, Cuevas G. Molecular recognition of saccharides by proteins. Insights on the origin of the carbohydrate-aromatic interactions. J Am Chem Soc. 2005;127(20):7379-86.

9. Hudson KL, Bartlett GJ, Diehl RC, Agirre J, Gallagher T, Kiessling LL, et al. Carbohydrate-Aromatic Interactions in Proteins. J Am Chem Soc. 2015;137(48):15152-60.

10. Ramirez-Gualito K, Alonso-Rios R, Quiroz-Garcia B, Rojas-Aguilar A, Diaz D, Jimenez-Barbero J, et al. Enthalpic Nature of the CH/pi Interaction Involved in the Recognition of Carbohydrates by Aromatic Compounds, Confirmed by a Novel Interplay of NMR, Calorimetry, and Theoretical Calculations. J Am Chem Soc. 2009;131(50):18129-38.

11. Bucior I, Scheuring S, Engel A, Burger MM. Carbohydrate-carbohydrate interaction provides adhesion force and specificity for cellular recognition. J Cell Biol. 2004;165(4):529-37.

12. Hakomori S. Carbohydrate-to-carbohydrate interaction, through glycosynapse, as a basis of cell recognition and membrane organization. Glycoconjugate J. 2004;21(3-4):125-37.

13. Lai CH, Hutter J, Hsu CW, Tanaka H, Varela-Aramburu S, De Cola L, et al. Analysis of Carbohydrate-Carbohydrate Interactions Using Sugar-Functionalized Silicon Nanoparticles for Cell Imaging. Nano Lett. 2016;16(1):807-11.

14. Yan N, He G, Zhang HL, Ding LP, Fang Y. Glucose-Based Fluorescent Low-Molecular Mass Compounds: Creation of Simple and Versatile Supramolecular Gelators. Langmuir. 2010;26(8):5909-17.

15. Clemente MJ, Fitremann J, Mauzac M, Serrano JL, Oriol L. Synthesis and Characterization of Maltose-Based Amphiphiles as Supramolecular Hydrogelators. Langmuir. 2011;27(24):15236-47.

16. Mathiselvam M, Loganathan D, Varghese B. Synthesis and characterization of thiourea- and urea-linked glycolipids as low-molecular-weight hydrogelators. Rsc Adv. 2013;3(34):14528-42.

17. Goyal N, Cheuk S, Wang GJ. Synthesis and characterization of D-glucosamine-derived low molecular weight gelators. Tetrahedron. 2010;66(32):5962-71.

18. Huang YW, Wang JC, Wei ZX. Modulating supramolecular helicity and electrical conductivity of perylene dyes through an achiral alkyl chain. Chem Commun. 2014;50(61):8343-5.

19. Jung JH, Rim JA, Han WS, Lee SJ, Lee YJ, Cho EJ, et al. Hydrogel behavior of a sugar-based gelator by introduction of an unsaturated moiety as a hydrophobic group. Org Biomol Chem. 2006;4(10):2033-8.

20. Ono F, Watanabe H, Shinkai S. Structural optimization of super-gelators derived from naturally-occurring mannose and their morphological diversity. Rsc Adv. 2014;4(49):25940-7.

21. Brito A, Abul-Haija YM, da Costa DS, Novoa-Carballal R, Reis RL, Ulijn RV, et al. Minimalistic supramolecular proteoglycan mimics by co-assembly of aromatic peptide and carbohydrate amphiphiles. Chem Sci. 2019;10(8):2385-90.

22. Birchall LS, Roy S, Jayawarna V, Hughes M, Irvine E, Okorogheye GT, et al. Exploiting CH-pi interactions in supramolecular hydrogels of aromatic carbohydrate amphiphiles. Chem Sci. 2011;2(7):1349-55.

23. Lee SS, Fyrner T, Chen F, Alvarez Z, Sleep E, Chun DS, et al. Sulfated glycopeptide nanostructures for multipotent protein activation. Nat Nanotechnol. 2017;12(8):821-+.

24. Restuccia A, Tian YF, Collier JH, Hudalla GA. Self-Assembled Glycopeptide Nanofibers as Modulators of Galectin-1 Bioactivity. Cell Mol Bioeng. 2015;8(3):471-87.

25. Roytman R, Adler-Abramovich L, Kumar KSA, Kuan TC, Lin CC, Gazit E, et al. Exploring the self-assembly of glycopeptides using a diphenylalanine scaffold. Org Biomol Chem. 2011;9(16):5755-61.

26. Tsuzuki T, Kabumoto M, Arakawa H, Ikeda M. The effect of carbohydrate structures on the hydrogelation ability and morphology of self-assembled structures of peptide-carbohydrate conjugates in water. Org Biomol Chem. 2017;15(21):4595-600.

27. Carvalho AM, Teixeira R, Novoa-Carballal R, Pires RA, Reis RL, Pashkuleva I. Redox-Responsive Micellar Nanoparticles from Glycosaminoglycans for CD44 Targeted Drug Delivery. Biomacromolecules. 2018;19(7):2991-9.

28. Brito A, Pereira PMR, da Costa DS, Reis RL, Ulijn RV, Lewis JS, et al. Inhibiting cancer metabolism by aromatic carbohydrate amphiphiles that act as antagonists of the glucose transporter GLUT1. Chem Sci. 2020;11(14):3737-44.

29. Pires RA, Abul-Haija YM, Costa DS, Novoa-Carballal R, Reis RL, Ulijn RV, et al. Controlling Cancer Cell Fate Using Localized Biocatalytic Self-Assembly of an Aromatic Carbohydrate Amphiphile. J Am Chem Soc. 2015;137(2):576-9.

30. Du XW, Zhou J, Guvench O, Sangiorgi FO, Li XM, Zhou N, et al. Supramolecular Assemblies of a Conjugate of Nucleobase, Amino Acids, and Saccharide Act as Agonists for Proliferation of Embryonic Stem Cells and Development of Zygotes. Bioconjugate Chem. 2014;25(6):1031-5.

31. Lim YB, Park S, Lee E, Jeong H, Ryu JH, Lee MS. Glycoconjugate nanoribbons from the self-assembly of carbohydrate-peptide block molecules for controllable bacterial cell cluster formation. Biomacromolecules. 2007;8(5):1404-8.

32. Yuan D, Shi JF, Du XW, Zhou N, Xu B. Supramolecular Glycosylation Accelerates Proteolytic Degradation of Peptide Nanofibrils. J Am Chem Soc. 2015;137(32):10092-5.

33. Mahato M, Arora V, Pathak R, Gautam HK, Sharma AK. Fabrication of nanostructures through molecular self-assembly of small amphiphilic glyco-dehydropeptides. Mol Biosyst. 2012;8(6):1742-9.

34. Gour N, Purohit CS, Verma S, Puri R, Ganesh S. Mannosylated self-assembled structures for molecular confinement and gene delivery applications. Biochem Bioph Res Co. 2009;378(3):503-6.

35. Yang J, Du Q, Li L, Wang T, Feng Y, Nieh M-P, et al. Glycosyltransferase-Induced Morphology Transition of Glycopeptide Self-Assemblies with Proteoglycan Residues. ACS Macro Letters. 2020:929-36.

36. Yang ZM, Liang GL, Ma ML, Abbah AS, Lu WW, Xu B. D-glucosamine-based supramolecular hydrogels to improve wound healing. Chem Commun. 2007(8):843-5.

37. Restuccia A, Seroski DT, Kelley KL, O'Bryan CS, Kurian JJ, Knox KR, et al. Hierarchical self-assembly and emergent function of densely glycosylated peptide nanofibers. Commun Chem. 2019;2.

38. Zhao F, Heesters BA, Chiu I, Gao Y, Shi JF, Zhou N, et al. L-Rhamnose-containing supramolecular nanofibrils as potential immunosuppressive materials. Org Biomol Chem. 2014;12(35):6816-9.

39. Huang J, Bonduelle C, Thevenot J, Lecommandoux S, Heise A. Biologically Active Polymersomes from Amphiphilic Glycopeptides. J Am Chem Soc. 2012;134(1):119-22.

40. Xiao Y, Chinoy ZS, Pecastaings G, Bathany K, Garanger E, Lecommandoux S. Design of Polysaccharide-b-Elastin-Like Polypeptide Bioconjugates and Their Thermoresponsive Self-Assembly. Biomacromolecules. 2020;21(1):114-25.

41. Schatz C, Louguet S, Le Meins JF, Lecommandoux S. Polysaccharide-block-polypeptide Copolymer Vesicles: Towards Synthetic Viral Capsids. Angew Chem Int Edit. 2009;48(14):2572-5.

42. Sivakova S, Rowan SJ. Nucleobases as supramolecular motifs. Chem Soc Rev. 2005;34(1):9-21.

43. Flynn RA, Smith BAH, Johnson AG, Pedram K, George BM, Malaker SA, et al. Mammalian Y RNAs are modified at discrete guanosine residues with N-glycans. 2019.

44. Peters GM, Skala LP, Plank TN, Hyman BJ, Reddy GNM, Marsh A, et al. A G(4)center dot K+ Hydrogel Stabilized by an Anion. J Am Chem Soc. 2014;136(36):12596-9.

45. Dash J, Patil AJ, Das RN, Dowdall FL, Mann S. Supramolecular hydrogels derived from silver ion-mediated self-assembly of 5 '-guanosine monophosphate. Soft Matter. 2011;7(18):8120-6.

46. Adhikari B, Shah A, Kraatz HB. Self-assembly of guanosine and deoxy-guanosine into hydrogels: monovalent cation guided modulation of gelation, morphology and self-healing properties. J Mater Chem B. 2014;2(30):4802-10.

47. Iwaura R, Yoshida K, Masuda M, Yase K, Shimizu T. Spontaneous fiber formation and hydrogelation of nucleotide bolaamphiphiles. Chem Mater. 2002;14(7):3047-53.

48. Spada GP, Lena S, Masiero S, Pieraccini S, Surin M, Samori P. Guanosine-based hydrogen-bonded scaffolds: Controlling the assembly of oligothiophenes. Adv Mater. 2008;20(12):2433-+.

49. Du XW, Li JF, Gao Y, Kuang Y, Xu B. Catalytic dephosphorylation of adenosine monophosphate (AMP) to form supramolecular nanofibers/hydrogels. Chem Commun. 2012;48(15):2098-100.

50. Seela F, Pujari SS, Schafer AH. Hydrogelation and spontaneous fiber formation of 8-aza-7-deazaadenine nucleoside 'click' conjugates. Tetrahedron. 2011;67(38):7418-25.

51. Park SM, Kim BH. Ultrasound-triggered water gelation with a modified nucleoside. Soft Matter. 2008;4(10):1995-7.

52. Lopez M, Evangelista SE, Morales M, Lee S. Enthalpic Effects of Chain Length and Unsaturation on Water Permeability across Droplet Bilayers of Homologous Monoglycerides. Langmuir. 2017;33(4):900-12.

53. John G, Masuda M, Okada Y, Yase K, Shimizu T. Nanotube formation from renewable resources via coiled nanofibers. Adv Mater. 2001;13(10):715-8.

54. Sekhar KPC, Swain DK, Holey SA, Bojja S, Nayak RR. Unsaturation and Polar Head Effect on Gelation, Bioactive Release, and Cr/Cu Removal Ability of Glycolipids. Langmuir. 2020;36(12):3080-8.

55. von Minden HM, Brandenburg K, Seydel U, Koch MHJ, Garamus V, Willumeit R, et al. Thermotropic and lyotropic properties of long chain alkyl glycopyranosides. Part II. Disaccharide headgroups. Chem Phys Lipids. 2000;106(2):157-79.

56. Vill V, von Minden HM, Koch MHJ, Seydel U, Brandenburg K. Thermotropic and lyotropic properties of long chain alkyl glycopyranosides Part I: monosaccharide headgroups. Chem Phys Lipids. 2000;104(1):75-91.

57. Nasir MN, Crowet JM, Lins L, Akong FO, Haudrechy A, Bouquillon S, et al. Interactions of sugar-based bolaamphiphiles with biomimetic systems of plasma membranes. Biochimie. 2016;130:23-32.

58. Masuda M, Shimizu T. Lipid nanotubes and microtubes: Experimental evidence for unsymmetrical monolayer membrane formation from unsymmetrical bolaamphiphiles. Langmuir. 2004;20(14):5969-77.

59. Ghimire G, Moore MM, Leuschen R, Nagasaka S, Kameta N, Masuda M, et al. Influences of Hydrogen Bonding-Based Stabilization of Bolaamphiphile Layers on Molecular Diffusion within Organic Nanotubes Having Inner Carboxyl Groups. Langmuir. 2020;36(22):6145-53.

60. Baccile N, Babonneau F, Jestin J, Pehau-Arnaudet G, Van Bogaert I. Unusual, pH-Induced, Self-Assembly Of Sophorolipid Biosurfactants. Acs Nano. 2012;6(6):4763-76.

61. Baccile N, Selmane M, Le Griel P, Prevost S, Perez J, Stevens CV, et al. pH-Driven Self-Assembly of Acidic Microbial Glycolipids. Langmuir. 2016;32(25):6343-59.

62. Kim BS, Hong DJ, Bae J, Lee M. Controlled self-assembly of carbohydrate conjugate rod-coil amphiphiles for supramolecular multivalent ligands. J Am Chem Soc. 2005;127(46):16333-7.

63. Lee DW, Kim T, Park IS, Huang Z, Lee M. Multivalent Nanofibers of a Controlled Length: Regulation of Bacterial Cell Agglutination. J Am Chem Soc. 2012;134(36):14722-5.

64. Duan H, Donovan M, Hernandez F, Di Primo C, Garanger E, Schultze X, et al. Hyaluronic-Acid-Presenting Self-Assembled Nanoparticles Transform a Hyaluronidase HYAL1 Substrate into an Efficient and Selective Inhibitor. Angew Chem Int Ed Engl. 2020.

65. Novoa-Carballal R, Silva C, Moller S, Schnabelrauch M, Reis RL, Pashkuleva I. Tunable nano-carriers from clicked glycosaminoglycan block copolymers. J Mater Chem B. 2014;2(26):4177-84.

66. Silva C, Carretero A, da Costa DS, Reis RL, Novoa-Carballal R, Pashkuleva I. Design of protein delivery systems by mimicking extracellular mechanisms for protection of growth factors. Acta Biomaterialia. 2017;63:283-93.

67. Duan HH, Donovan M, Foucher A, Schultze X, Lecommandoux S. Multivalent and multifunctional polysaccharide-based particles for controlled receptor recognition. Scientific Reports. 2018;8.

68. Van Zee NJ, Adelizzi B, Mabesoone MFJ, Meng X, Aloi A, Zha RH, et al. Potential enthalpic energy of water in oils exploited to control supramolecular structure. Nature. 2018;558(7708):100-+.

69. Deshmukh SA, Solomon LA, Kamath G, Fry HC, Sankaranarayanan S. Water ordering controls the dynamic equilibrium of micelle-fibre formation in self-assembly of peptide amphiphiles. Nature Communications. 2016;7.

70. Draper ER, Adams DJ. Low-Molecular-Weight Gels: The State of the Art. Chem. 2017;3(3):390-410.

71. Ghimire G, Espinoza R, Xu H, Nasaka S, Kameta N, Masuda M, et al. Diffusion Behavior of Differently Charged Molecules in Self-Assembled Organic Nanotubes Studied Using Imaging Fluorescence Correlation Spectroscopy. Langmuir. 2019;35(24):7783-90.

72. Chen Q, Lv YX, Zhang DQ, Zhang GX, Liu CY, Zhu DB. Cysteine and pH-Responsive Hydrogel Based on a Saccharide Derivative with an Aldehyde Group. Langmuir. 2010;26(5):3165-8.

73. Goyal N, Mangunuru HPR, Parikh B, Shrestha S, Wang GJ. Synthesis and characterization of pH responsive D-glucosamine based molecular gelators. Beilstein J Org Chem. 2014;10:3111-21.

74. Piras CC, Smith DK. Sequential Assembly of Mutually Interactive Supramolecular Hydrogels and Fabrication of Multi-Domain Materials. Chem-Eur J. 2019;25(48):11318-26.

75. Yang ZM, Gu HW, Fu DG, Gao P, Lam JK, Xu B. Enzymatic formation of supramolecular hydrogels. Adv Mater. 2004;16(16):1440-+.

76. Ochi R, Kurotani K, Ikeda M, Kiyonaka S, Hamachi I. Supramolecular hydrogels based on bola-amphiphilic glycolipids showing color change in response to glycosidases. Chem Commun. 2013;49(21):2115-7.

77. Vemula PK, Li J, John G. Enzyme catalysis: Tool to make and break amygdalin hydrogelators from renewable resources: A delivery model for hydrophobic drugs. J Am Chem Soc. 2006;128(27):8932-8.

78. Ogawa Y, Yoshiyama C, Kitaoka T. Helical Assembly of Azobenzene-Conjugated Carbohydrate Hydrogelators with Specific Affinity for Lectins. Langmuir. 2012;28(9):4404-12.

79. Srinivas O, Mitra N, Surolia A, Jayaraman N. Photoswitchable cluster glycosides as tools to probe carbohydrate-protein interactions: synthesis and lectin-binding studies of azobenzene containing multivalent sugar ligands. Glycobiology. 2005;15(9):861-73.

80. Matsumoto S, Yamaguchi S, Ueno S, Komatsu H, Ikeda M, Ishizuka K, et al. Photo gel-sol/sol-gel transition and its patterning of a supramolecular hydrogel as stimuli-responsive biomaterials. Chem-Eur J. 2008;14(13):3977-86.

81. Matsumoto S, Yamaguchi S, Wada A, Matsui T, Ikeda M, Hamachi I. Photo-responsive gel droplet as a nano- or pico-litre container comprising a supramolecular hydrogel. Chem Commun. 2008(13):1545-7.

82. Restuccia A, Hudalla GA. Tuning carbohydrate density enhances protein binding and inhibition by glycosylated -sheet peptide nanofibers. Biomater Sci-Uk. 2018;6(9).

83. Yaylaci SU, Ekiz MS, Arslan E, Can N, Kilic E, Ozkan H, et al. Supramolecular GAG-like Self-Assembled Glycopeptide Nanofibers Induce Chondrogenesis and Cartilage Regeneration. Biomacromolecules. 2016;17(2):679-89.

84. Capito RM, Azevedo HS, Velichko YS, Mata A, Stupp SI. Self-assembly of large and small molecules into hierarchically ordered sacs and membranes. Science. 2008;319(5871):1812-6.

85. Mendes AC, Smith KH, Tejeda-Montes E, Engel E, Reis RL, Azevedo HS, et al. Co-Assembled and Microfabricated Bioactive Membranes. Adv Funct Mater. 2013;23(4):430-8.

86. Aviv M, Halperin-Sternfeld M, Grigoriants I, Buzhansky L, Mironi-Harpaz I, Seliktar D, et al. Improving the Mechanical Rigidity of Hyaluronic Acid by Integration of a Supramolecular Peptide Matrix. Acs Appl Mater Inter. 2018;10(49):41883-91.

87. Rajangam K, Behanna HA, Hui MJ, Han XQ, Hulvat JF, Lomasney JW, et al. Heparin binding nanostructures to promote growth of blood vessels. Nano Lett. 2006;6(9):2086-90.

88. Carretero A, da Costa DS, Reis RL, Pashkuleva I. Extracellular matrix-inspired assembly of glycosaminoglycan-collagen fibers. J Mater Chem B. 2017;5(17):3103-6.

89. Azevedo HS, Pashkuleva I. Biomimetic supramolecular designs for the controlled release of growth factors in bone regeneration. Advanced Drug Delivery Reviews. 2015;94:63-76.

90. Zhou J, Du XW, Chen XY, Xu B. Adaptive Multifunctional Supramolecular Assemblies of Glycopeptides Rapidly Enable Morphogenesis. Biochemistry. 2018;57(32):4867-79.

91. Yoshimura I, Miyahara Y, Kasagi N, Yamane H, Ojida A, Hamachi I. Molecular recognition in a supramolecular hydrogel to afford a semi-wet sensor chip. J Am Chem Soc. 2004;126(39):12204-5.

92. Kiyonaka S, Sada K, Yoshimura I, Shinkai S, Kato N, Hamachi I. Semi-wet peptide/protein array using supramolecular hydrogel. Nature Materials. 2004;3(1):58-64.

93. Koshi Y, Nakata E, Yamane H, Hamachi I. A fluorescent lectin array using supramolecular hydrogel for simple detection and pattern profiling for various glycoconjugates. J Am Chem Soc. 2006;128(32):10413-22.

94. Wada A, Tamaru S, Ikeda M, Hamachi I. MCM-Enzyme-Supramolecular Hydrogel Hybrid as a Fluorescence Sensing Material for Polyanions of Biological Significance. J Am Chem Soc. 2009;131(14):5321-30.

95. Battigelli A, Kim JH, Dehigaspitiya DC, Proulx C, Robertson EJ, Murray DJ, et al. Glycosylated Peptoid Nanosheets as a Multivalent Scaffold for Protein Recognition. Acs Nano. 2018;12(3):2455-65.

96. Kim BS, Yang WY, Ryu JH, Yoo YS, Lee M. Carbohydrate-coated nanocapsules from amphiphilic rod-coil molecule: binding to bacterial type 1 pili. Chem Commun. 2005(15):2035-7.

97. Lim YB, Park S, Lee E, Ryu JH, Yoon YR, Kim TH, et al. Tunable bacterial agglutination and motility inhibition by self-assembled glyco-nanoribbons. Chem-Asian J. 2007;2(11):1363-9.

98. Ryu JH, Lee E, Lim YB, Lee M. Carbohydrate-coated supramolecular structures: Transformation of nanofibers into spherical micelles triggered by guest encapsulation. J Am Chem Soc. 2007;129(15):4808-14

# SECTION 2

# EXPERIMENTAL DESIGN

# Chapter II

# Materials & Methods

# MATERIALS AND METHODS

## Overview

The aim of this chapter is to explain and describe the experimental procedures used in the thesis. We present briefly the basic principles behind the used instrumental techniques and the general methodologies for sample preparation and analysis. Each chapter of Section III: **Chapter III-VII** contains experimental section devoted to specific methodologies only used for that work.

## II.1. SYNTHESIS OF CARBOHYDRATES, CARBOHYDRATE AMPHIPHILES, PEPTIDES, PEPTIDE AMPHIPHILES AND GLYCOPEPTIDES

All commercial reagents were used without purification. The used solvents were analytical or HPLC grade.

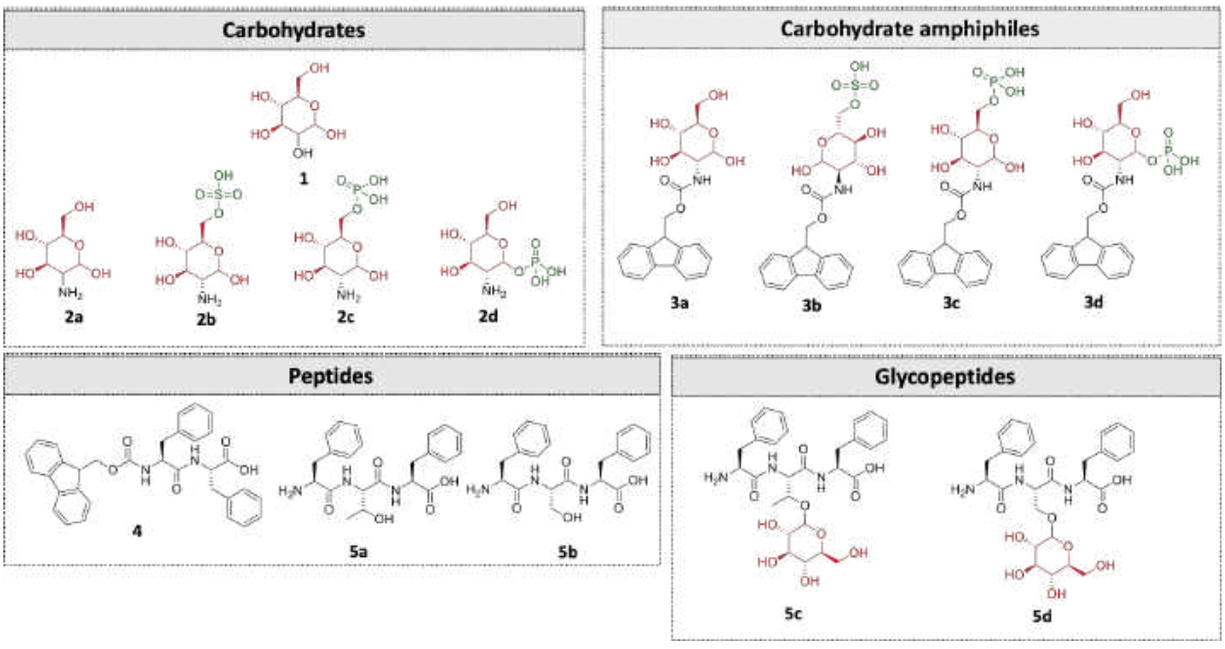


**Figure II.1. Compounds used throughout the thesis.**

### II.1.1. Synthesis and purification of carbohydrate amphiphiles

Aromatic carbohydrate amphiphiles (**3a-d**) were obtained from the respective glucosamines (2a-d) using previously reported one-step synthetic procedure (Scheme II.1).[1,2] Sodium salt of glucosamine 2a (Carbosynth, UK) or its derivatives 6-sulfate glucosamine 2b (Carbosynth, UK), 6-phosphate glucosamine **2c** (Carbosynth, UK) or 1-phosphate glucosamine **2d** (Sigma, Germany) were dissolved in water (30 g/L) in the presence of 2 eq. sodium hydrogen carbonate (Riedel-de Haen, Germany). The 9-fluorenylmethoxycarbonyl chloride (Fmoc-Cl, Sigma, Germany, 1.5-2 eq.) was dissolved in dioxane (Sigma, Germany) and added dropwise to the solution of the respective glucosamine. The reaction mixture was stirred at room temperature under nitrogen atmosphere during 48 hrs and then freeze-dried. The obtained white powder was dissolved in water and a liquid-liquid extraction with diethyl ether was applied to remove the unreacted Fmoc-Cl. The water phase was collected and column chromatography (70-230 and 230-400 mesh silica gel) was performed to remove any remaining Fmoc-Cl and to separate

the unreacted glucosamine from the product. The used eluent was ethyl actetate (EtOAc)/ methanol (MeOH)/ $H_2O$ (7/2/1) for the sulfate **3b** and EtOAc/MeOH/$H_2O$ (5/3/2) for the phosphate derivatives **3c, d**. The fractions containing the product (confirmed by thin layer chromatography, TLC) were joined and rotary evaporation was applied to remove the organic solvents, *i.e.* MeOH and EtOAc. The remaining aqueous solution was freeze-dried to obtain the purified **3a-d** as a white powder (Yield 3a: 76%, 3b: 70%, 3c: 81%, 3d: 86%). The purity of the samples was determined by high performance liquid chromatography (HPLC, KANUER, Germany) using a 250 mm x 4.6 mm reverse-phase C18 Atlantis column (Waters, UK), a flow of 1 mL/min, a UV detection wavelength at 280 nm and two eluents: A - $H_2O$ with 0.1% trifluoroacetic acid (TFA) and B - acetonitrile with 0.1% TFA. The HPLC runs comprised an initial step of 4 min under isocratic flow of 80% of eluent A and 20% of eluent B, followed by a gradient to 80% of B and 20% of eluent A for 31 min; this eluent composition (80% of B) was maintained for 5 min, followed by a gradient to 80% of A for 2 min and an isocratic elution (under 80% of A) during 4 min. Compounds **3a, c-d** were used in **chapter III**, **3a-c** in **chapter IV** and **VI** and compound **3c** in **chapter V**.

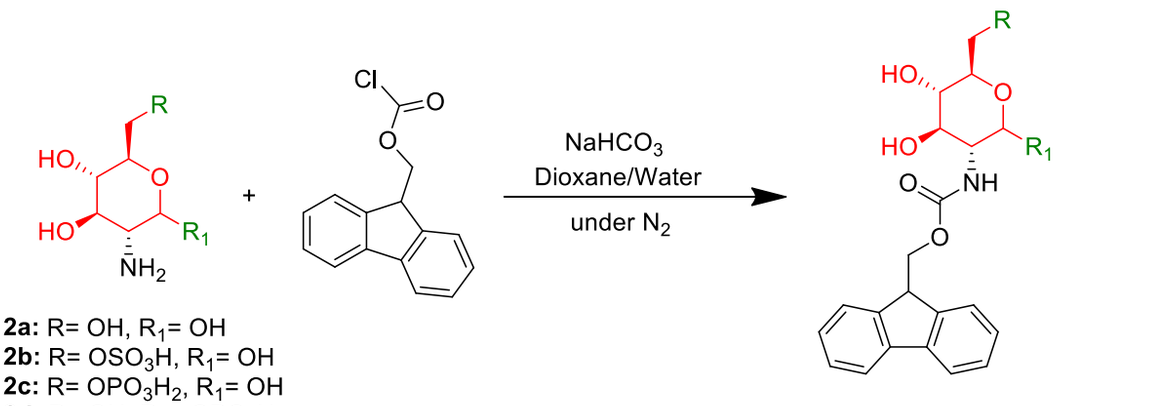


**2a:** R= OH, $R_1$= OH
**2b:** R= $OSO_3H$, $R_1$= OH
**2c:** R= $OPO_3H_2$, $R_1$= OH
**2d:** R= OH, $R_1$= $OPO_3H_2$

**3a:** R= OH, $R_1$= OH, η=76 %
**3b:** R= $OSO_3H$, $R_1$= OH, η= 70 %
**3c:** R= $OPO_3H_2$, $R_1$= OH, η= 81%
**3d:** R= OH, $R_1$= $OPO_3H_2$, η= 86%

**Scheme II.1. Synthesis of aromatic carbohydrate amphiphiles 3a-d.**

### II.1.2. Synthesis of the peptides and glycopeptides

Protected amino acids and amide resin were purchased from Novabiochem. N,N,N′,N′-Tetramethyl-O-(1H-benzotriazol-1-yl)uronium hexafluorophosphate (HBTU), N,N-Diisopropylethylamine (DIPEA), dimethylformamide (DMF), dicholoromethane (DCM), TFA, diethyl ether, and MeOH were purchased from Fisher Scientific. Piperidine, triisopropylsilane (TIS), 3,6-Dioxa-1,8-octane-dithiol (DODT)

and sodium methoxide were purchased from Sigma-Aldrich. Peptides **5a, b** and glycopeptides **5c, d** were synthesized following standard Fmoc protocol for solid phase peptide synthesis with DIPEA/HBTU activation.[3] Protected amino acids functionalized with peracetylated carbohydrates were used as building blocks for the glycopeptides synthesis (Scheme II.2). Peptides were cleaved with TFA/TIS/$H_2O$ (95:2.5:2.5) cocktail, precipitated with diethyl ether, dried, resuspended in $H_2O$, and freeze dried. Glycopeptides **5c, d** were further treated with sodium methoxide to remove the protecting acetyl groups from the carbohydrate moiety and precipitated in MeOH (Scheme II.2). Synthesized peptides and glycopeptides were purified by HPLC using a Macherey-Nagel C18 column of 250 mm length, 4.6 mm internal diameter and 3 μm particle size on Dionex P780 HPLC system. 50 μL of sample solution in water were diluted in 950 μL of a mixture $H_2O$:acetonitrile (50:50) containing 0.1% TFA. The mobile phase was $H_2O$:acetonitrile ramped from 20 to 80% for 20 min with a flow rate of 1mL $min^{-1}$. The peptides **5a, b** were detected using a UVD170U UV-Vis detector at 282 nm wavelength. Compounds **5a-d** were used in **chapter VII**.

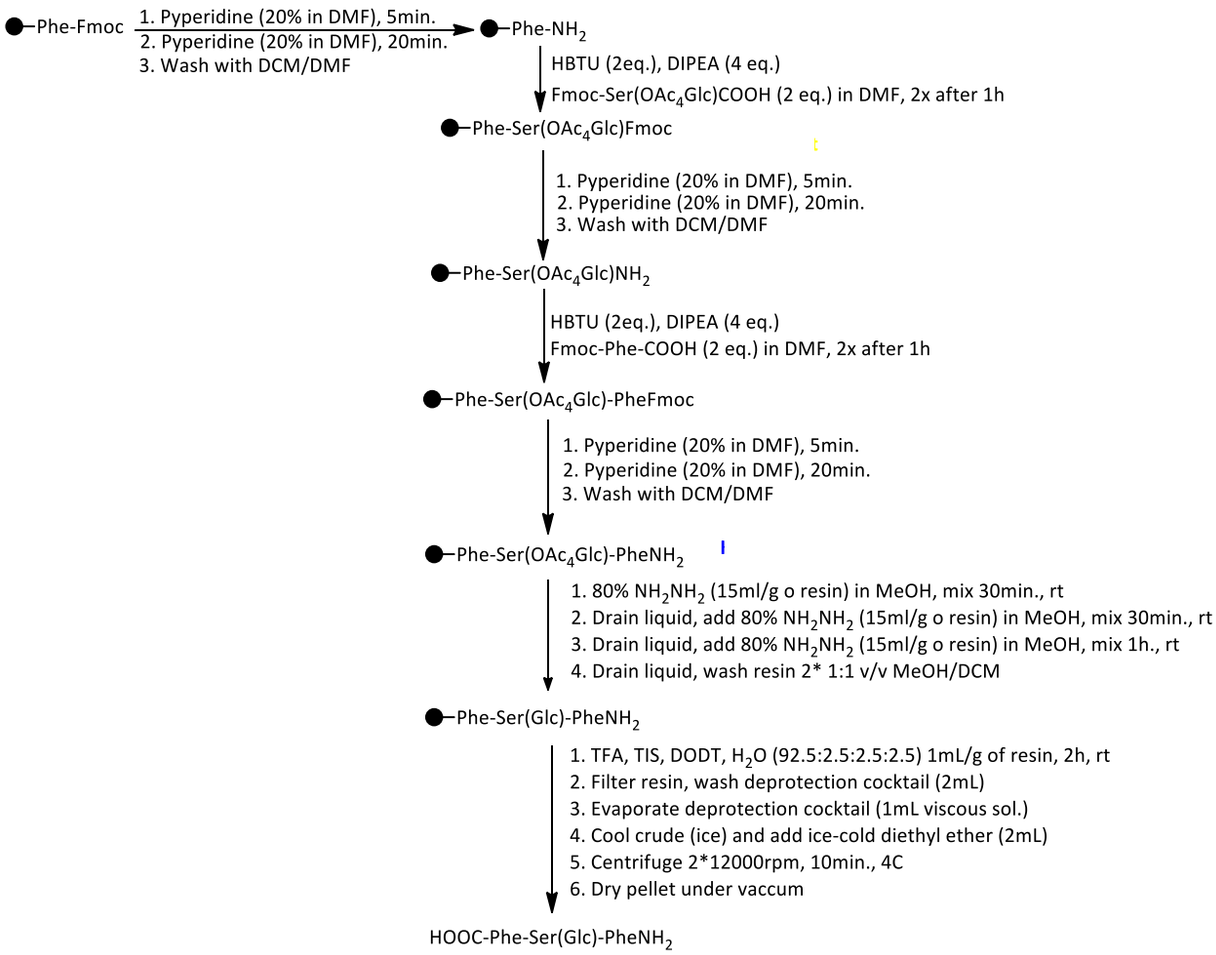


**Scheme II.2. Schematic presentation of the synthetic protocol used to obtain the glycopeptide 5c. The glycopeptide 5d and the peptides 5a, b were obtained following similar procedure.**

## II.2. CHARACTERIZATION OF THE OBTAINED COMPOUNDS

The structure and purity of the final products were confirmed by Electrospray ionization- mass spectrometry (ESI-MS) or Liquid chromatography-mass spectroscopy (LC-MS), Nuclear Magnetic Resonance (NMR) and High-Performance Liquid Chromatography (HPLC).

Identity and purity of all peptides and glycopeptides was confirmed by LC-ESI using Bruker's maXis-II ETD ESI-QqTOF instrument equipped with the Dionex Ulti-mate-3000 LC system. In the case of carbohydrate amphiphiles ESI-MS were acquired on a mass spectrometer Finnigan LXQ (Thermo Electron Corporation, USA) under negative-ion mode.

$^{1}H$ and $^{13}C$ NMR spectra were recorded on Bruker Avance III spectrometer (Bruker, Germany) at 25 °C in $D_2O$ or DMSO-$d_6$. The chemical shifts are reported in ppm ($\delta$ units) downfield to the solvent signal.

Duplicated signals observed for some protons and carbons correspond to the two carbohydrate anomeric forms. All compounds used in the following chapters have >95% purity.

### II.2.1. Carbohydrate amphiphiles

**Fmoc-glucosamine (Fmoc-Glc, 3a)**

$^{1}$H NMR (400 MHz, DMSO-$d_6$, 298 K): $\delta$ 7.89-7.82 (dd, 2H, J= 8Hz; 12Hz, H'6); 7.74-7.71 (dd, 2H, J= 8Hz; 12Hz, H'3); 7.42-7.37 (m, 2H, H'5); 7.35-7.28 (m, 2H, H'4), 6.44 (s, 1H, OH), 4.97 (d, 1H, H'1), 4,94 (s, 1H, OH); 4.71 (s, 1H, OH), 4.43 (d, 1H, H'1'), 4.59-4.21 (m, 2H, H'2 + H4); 3.87-3.32 (m, 5H)

$^{13}$C NMR (75 MHz, DMSO-$d_6$, 298 K): $\delta$ (duplicated signals are observed for some carbons; asterisks indicate those corresponding to the alpha anomer) 156.16; 143.92 139.41; 137.42; 128.91; 127.30; 124.20; 121.38; 120.03; 90.80; 74.73; 71.03; 70.17; 68.55; 61.16; 59.12; 56.39.

ESI-MS (m/z): $[M - Na]^+$ 424.39

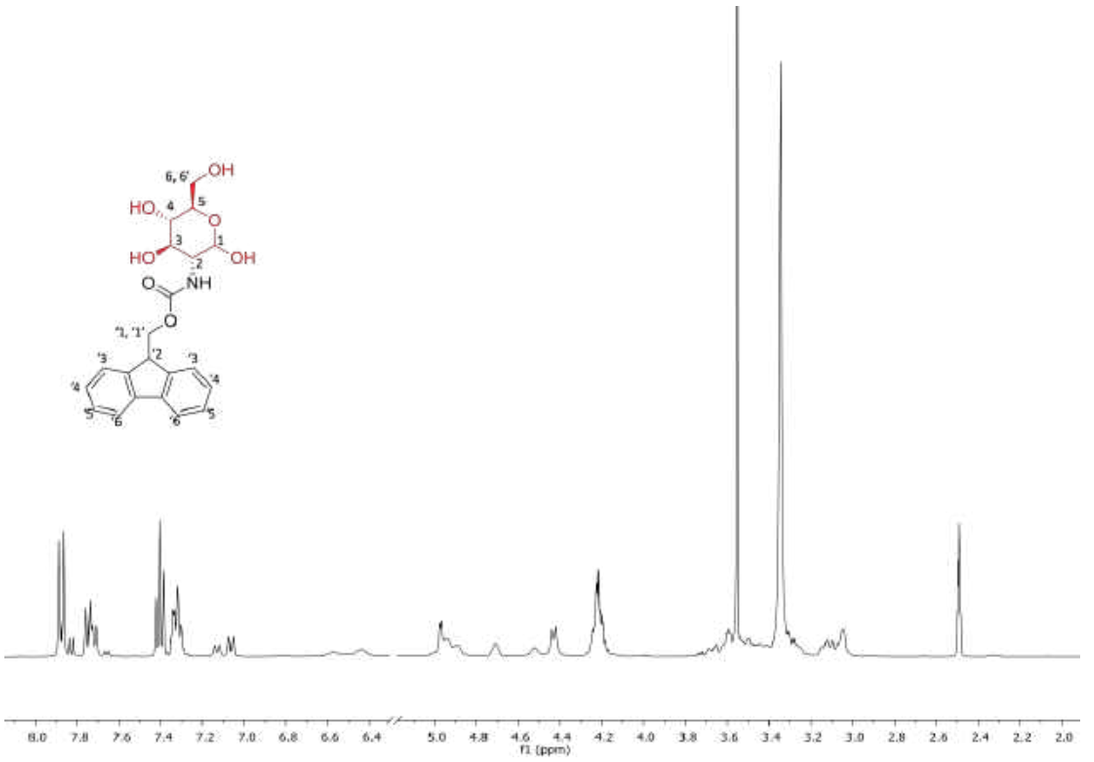


Figure II.2. $^{1}$H NMR (400 MHz, DMSO-$d_6$, 298 K) of Fmoc-Glc (3a).

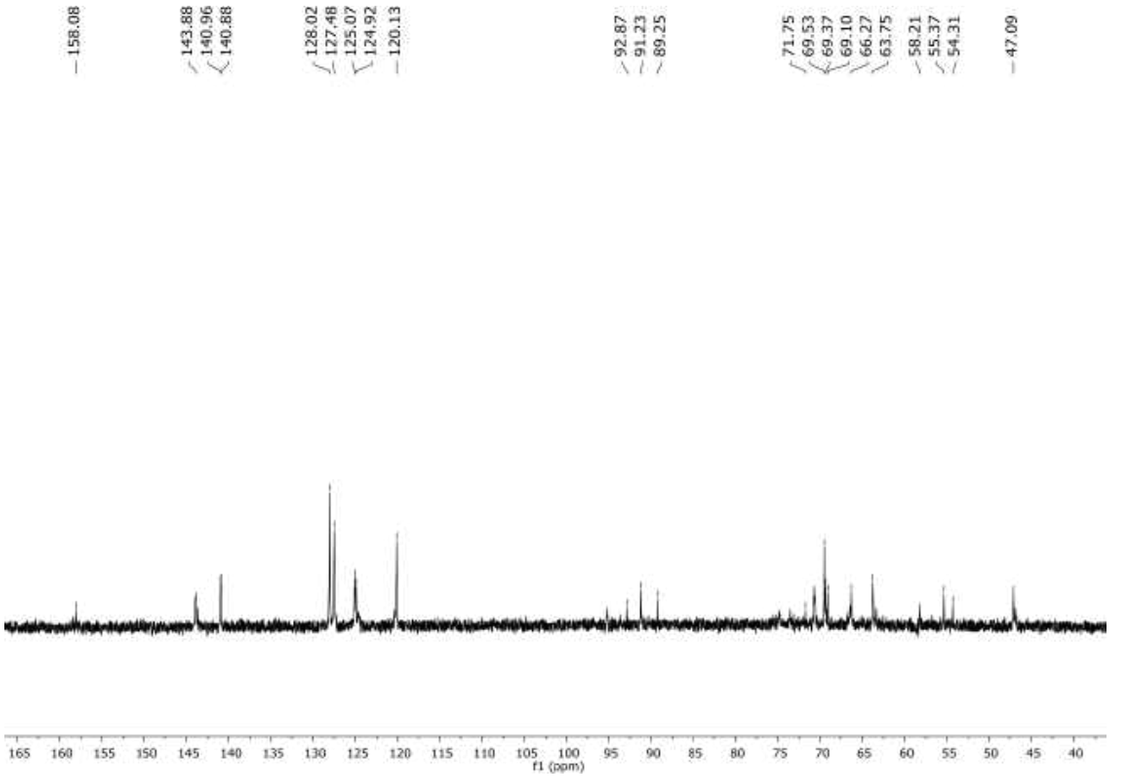


Figure II.3. $^{13}$C NMR (75 MHz, DMSO-$d_6$, 298 K) of Fmoc-Glc (3a).

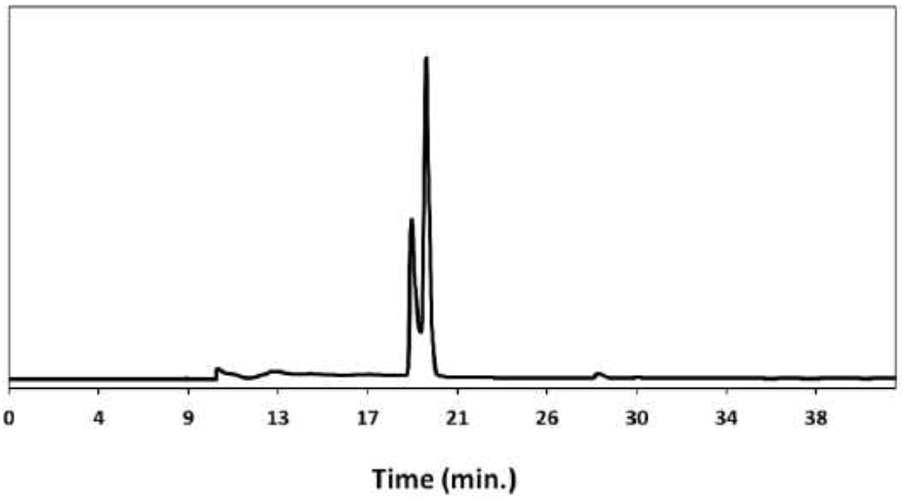


**Figure II.4. HPLC run of the purified Fmoc-Glc (3a), showing the two anomers.**

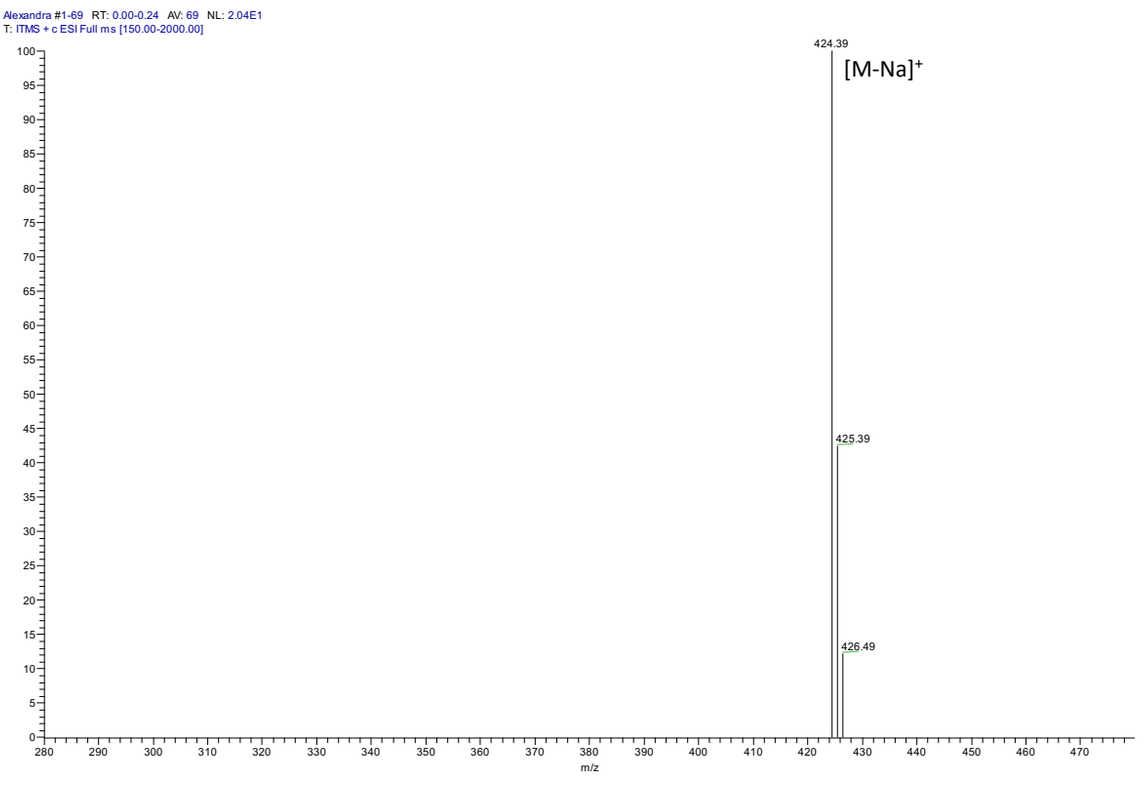


**Figure II.5. ESI-MS spectrum of Fmoc-Glc (3a).**

## Fmoc-glucosamine-6-O-sulfate (Fmoc-Glc6S, 3b)

$^{1}$H NMR (400 MHz, $D_2O$, 298 K): $\delta$ 7.91-7.86 (dd, 2H, J= 8Hz; 12Hz, H'6); 7.77-7.68 (dd, 2H, J= 8Hz; 12Hz, H'3); 7.52-7.49 (m, 2H, H'5); 4.45-7.43 (m, 2H, H'4), 5.06* (s, 1H), 4.99 (s, 1H), 4,69 (m, 1H,

H'1); 4.57 (m, 1H, H'1'), 4.31 (m, 2H, H6 + H6'), 4.01 (m, 1H, H2); 3.70 (m, 2H, H5 + H3). Asterisk indicates the alpha anomer.

$^{13}$C NMR (75 MHz, $D_2O$, 298 K): $\delta$ 158.04; 143.91; 140.92; 127.99; 127.45; 124.90; 120.11; 95.14; 91.22; 73.66; 70.84; 69.53; 67.13; 66.41; 62.51; 55.25.

ESI-MS (m/z): $[M - H]^-$ 480.13

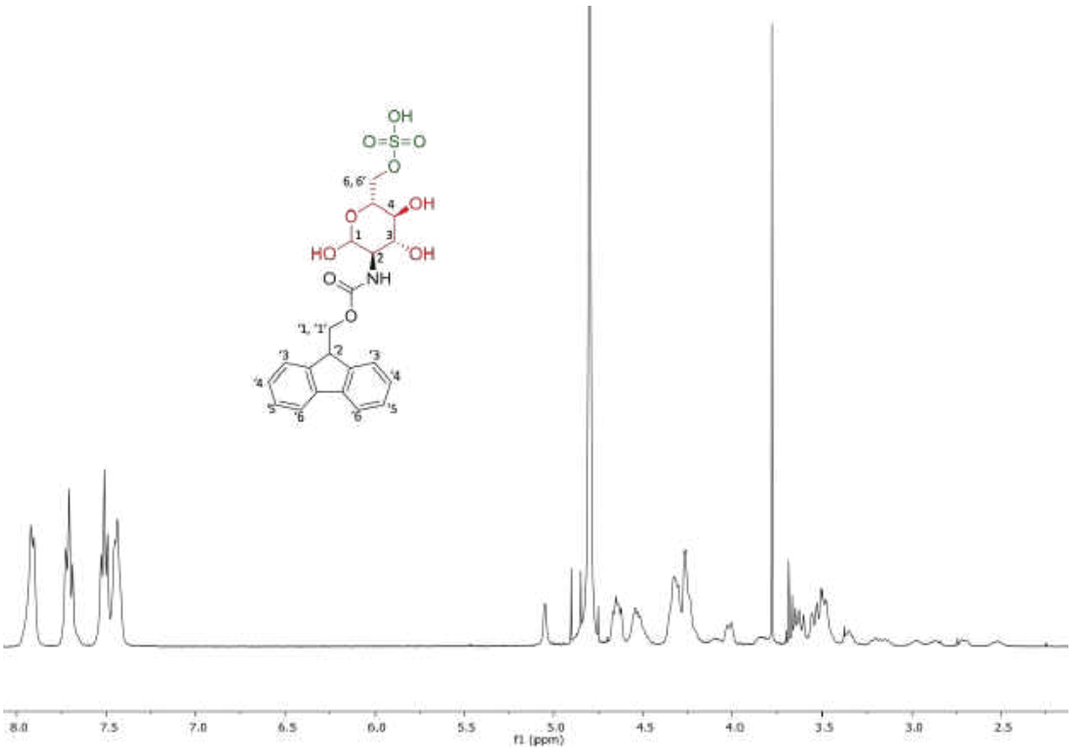


**Figure II.6. $^1$H NMR (400 MHz, D2O, 298 K) of purified Fmoc-Glc6S (3b).**

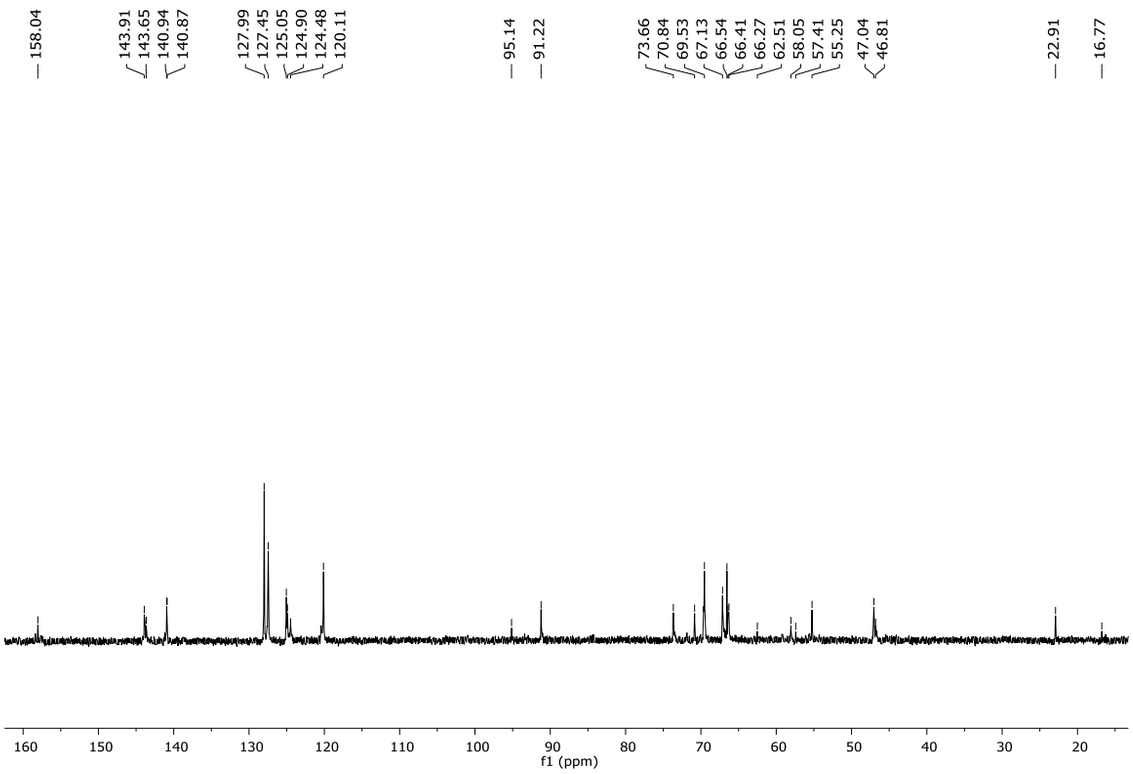


Figure II.7. $^{13}C$ NMR (75 MHz, $D_2O$, 298 K) of Fmoc-Glc6S (3b).

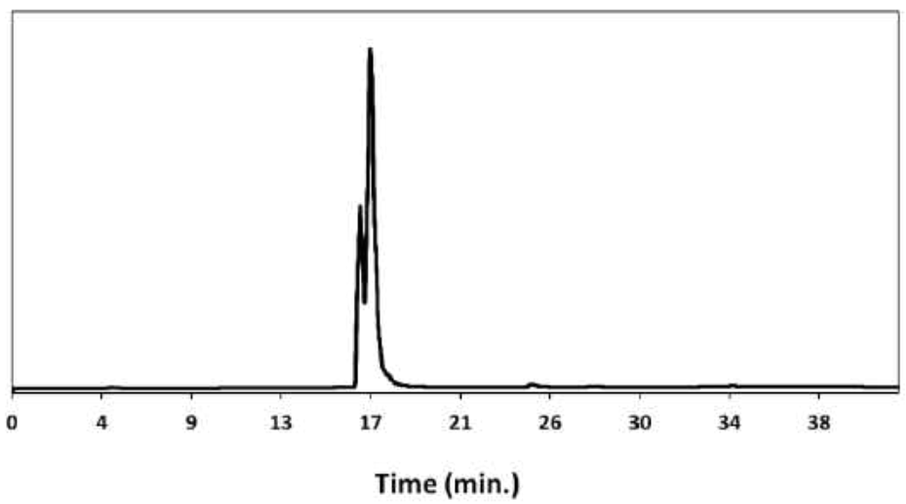


Figure II.8. HPLC run of the purified Fmoc-Glc6S (3b), showing the two anomers.

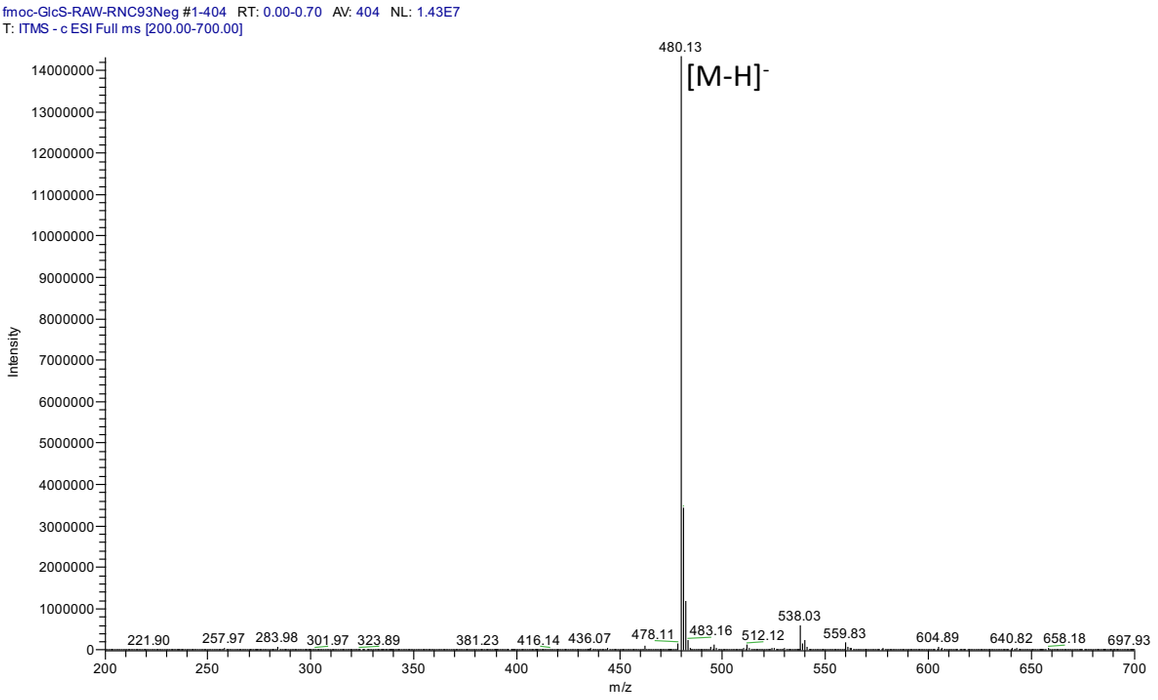


**Figure II.9. ESI-MS spectrum of Fmoc-Glc6S (3b).**

## Fmoc-glucosamine-6-O-phosphate (Fmoc-Glc6P, 3c)

$^{1}$H NMR (400 MHz, $D_2O$, 298 K): $\delta$ 7.94-7.93 (dd, 2H, J= 8Hz; 12Hz, H'6); 7.74-7.71 (dd, 2H, J= 8Hz; 12Hz, H'3); 7.54-7.52 (m, 2H, H'5); 7.51-7.45 (m, 2H, H'4), 5.26* (s, 1H), 5.05 (s, 1H), 4,55 (m, 1H, H'1); 4.33 (m, 1H, H'1'), 4.12 (m, 2H, H6 + H6'), 4.06 (m, 1H, H2); 3.52 (m, 2H, H5 + H3).

$^{13}$C NMR (75 MHz, $D_2O$, 298 K): $\delta$ 158.08; 143.88; 140.92; 128.02; 127.48; 124.99; 120.13; 91.23; 89.25; 71.75; 69.45; 69.10; 66.27; 63.25; 55.37.

ESI-MS (m/z): $[M - H]^-$ 480.08

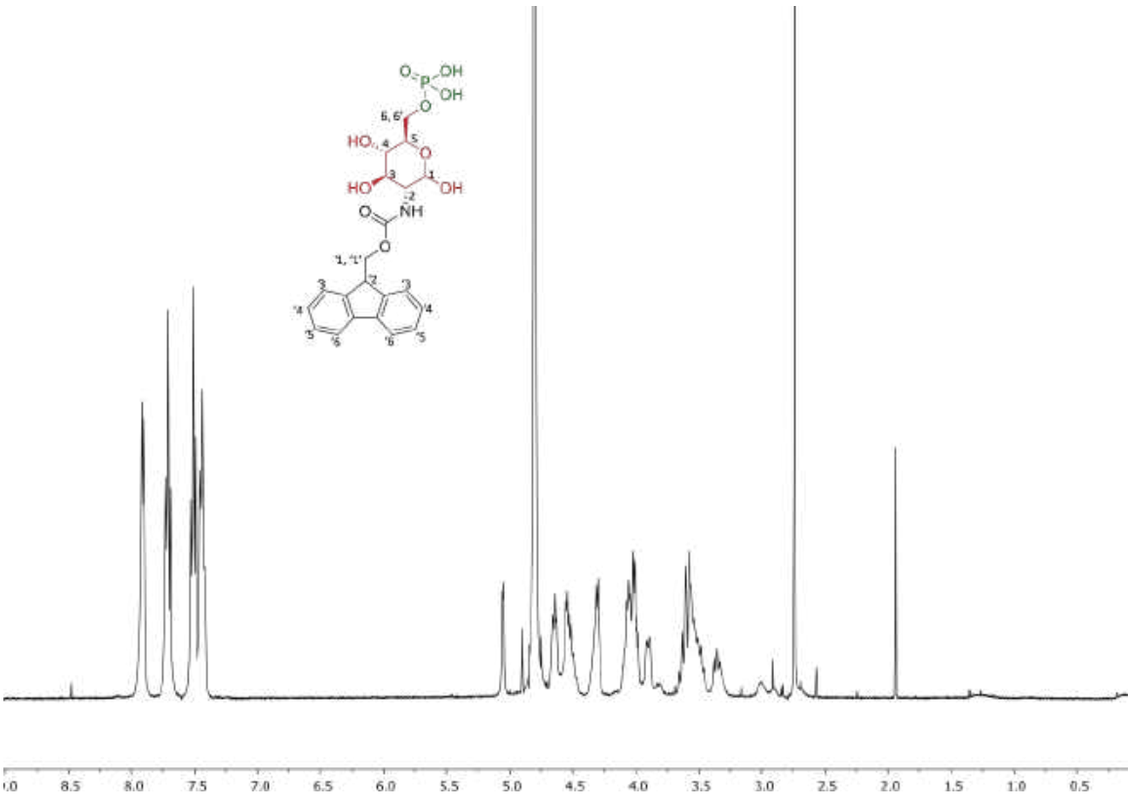


Figure II.10. $^{1}H$ NMR (400 MHz, $D_2O$, 298 K) of purified Fmoc-Glc6P (3c).

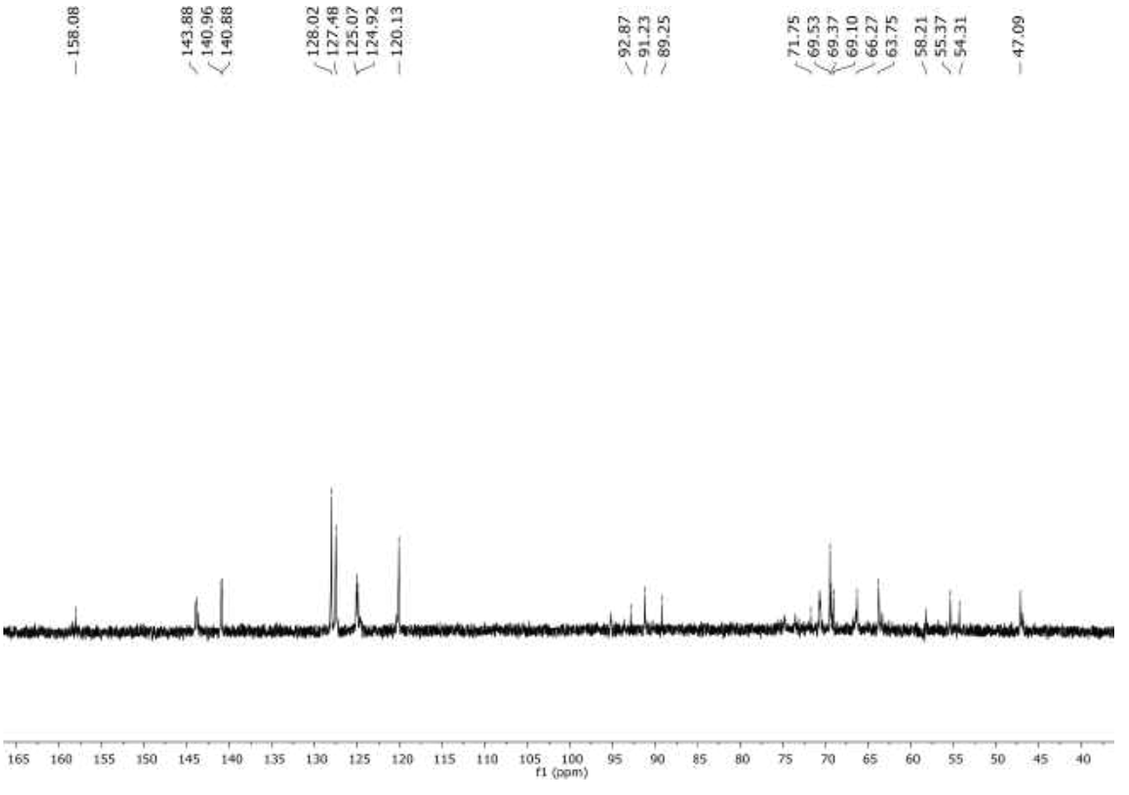


Figure II.11. $^{13}C$ NMR (75 MHz, D2O, 298 K) of Fmoc-Glc6P (3c).

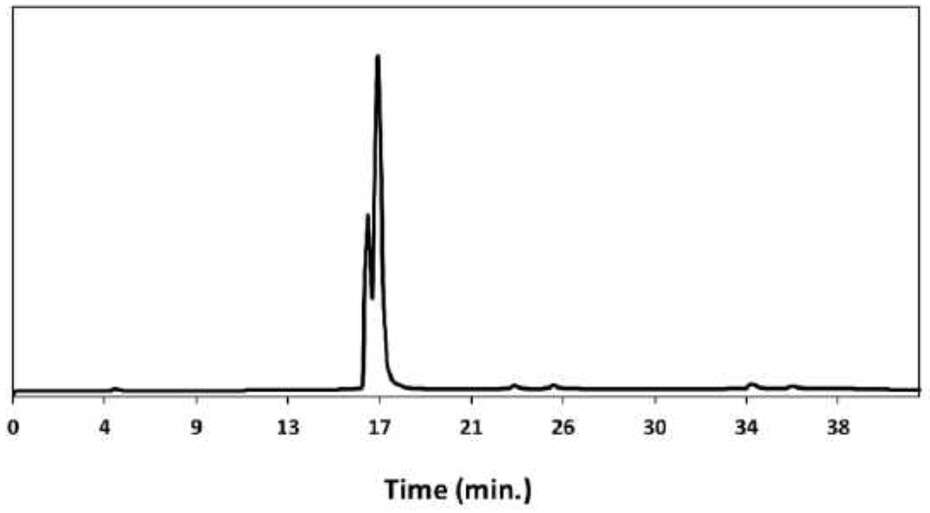


Figure II.12. HPLC run of the purified Fmoc-Glc6P (3c), showing the two anomers.

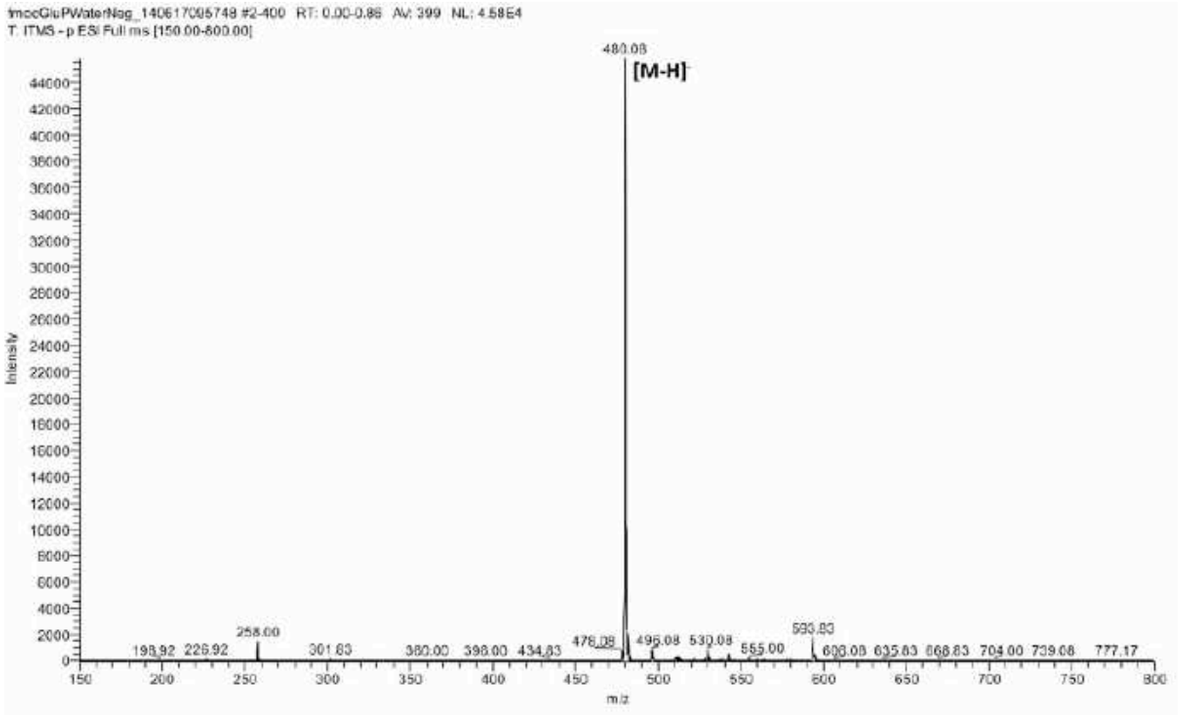


Figure II.13. ESI-MS spectrum of Fmoc-Glc6P (3c).

**Fmoc-glucosamine-1-phosphate (Fmoc-Glc1P, 3d)**

$^{1}$H NMR (400 MHz, $D_2O$, 298 K): $\delta$ 7.79 (dd, 2H, J= 8Hz; 12Hz, H'6); 7.60 (dd, 2H, J= 8Hz; 12Hz, H'3); 7.37 (m, 2H, H'5); 7.30 (m, 2H, H'4), 5.61 (s, 1H, H1), 5.29 (s, 1H, H3), 4.37-4.21 (m, 2H, H'1 + H´1´); 3.72-3.69 (m, 2H, H6 + H6´), 3.54 (m, 1H, H5), 3.46-3.39 (m, 1H, H2); 3.28-3.25 (m, 1H).

$^{13}$C NMR (75 MHz, $D_2O$): $\delta$ (duplicated signals are observed for some carbons) 133.03; 130.08; 128.70; 122.30; 94.09; 73.06; 72.20; 69.30; 65.04; 63.07; 58.06; 53.40; 49.03; 40.02.

ESI-MS (m/z): $[M - H]^-$ 482.12

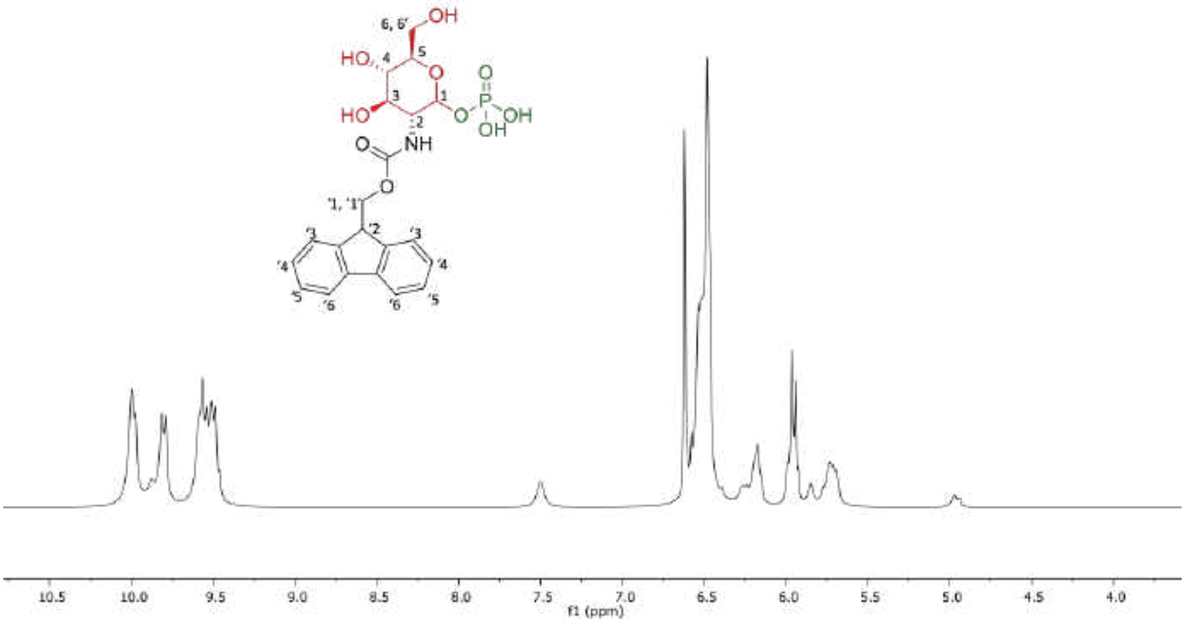


**Figure II.14. $^{1}$H NMR (400 MHz, D2O, 298 K) of purified Fmoc-Glc1P (3d).**

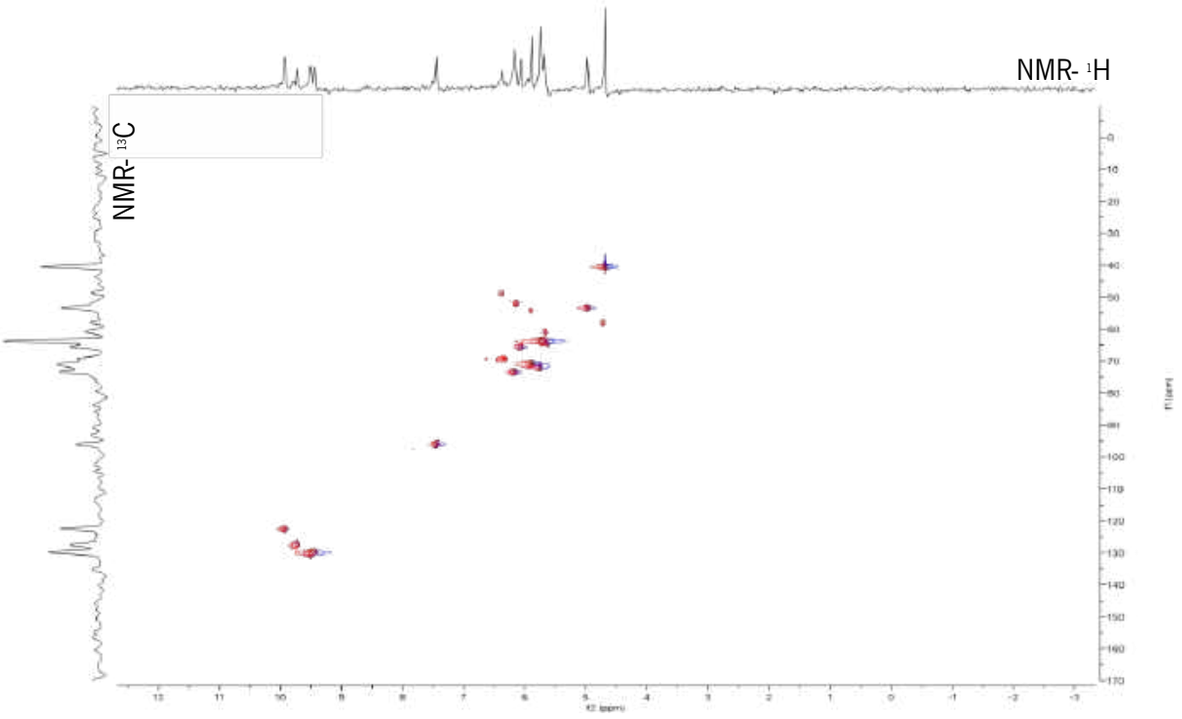


Figure II.15. HSQC-COSY spectra (400 MHz, $D_2O$, 298 K) of Fmoc-Glc1P (3d)

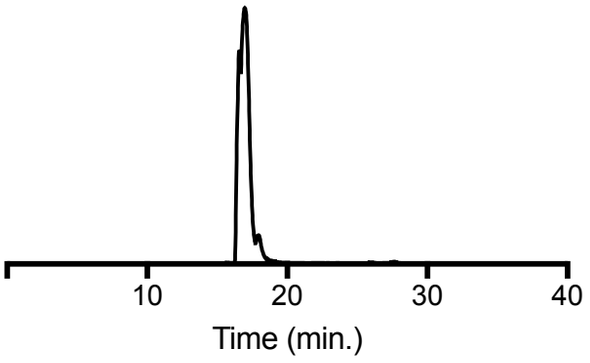


Figure II.16. HPLC spectrum of the purified Fmoc-Glc1P (3d).

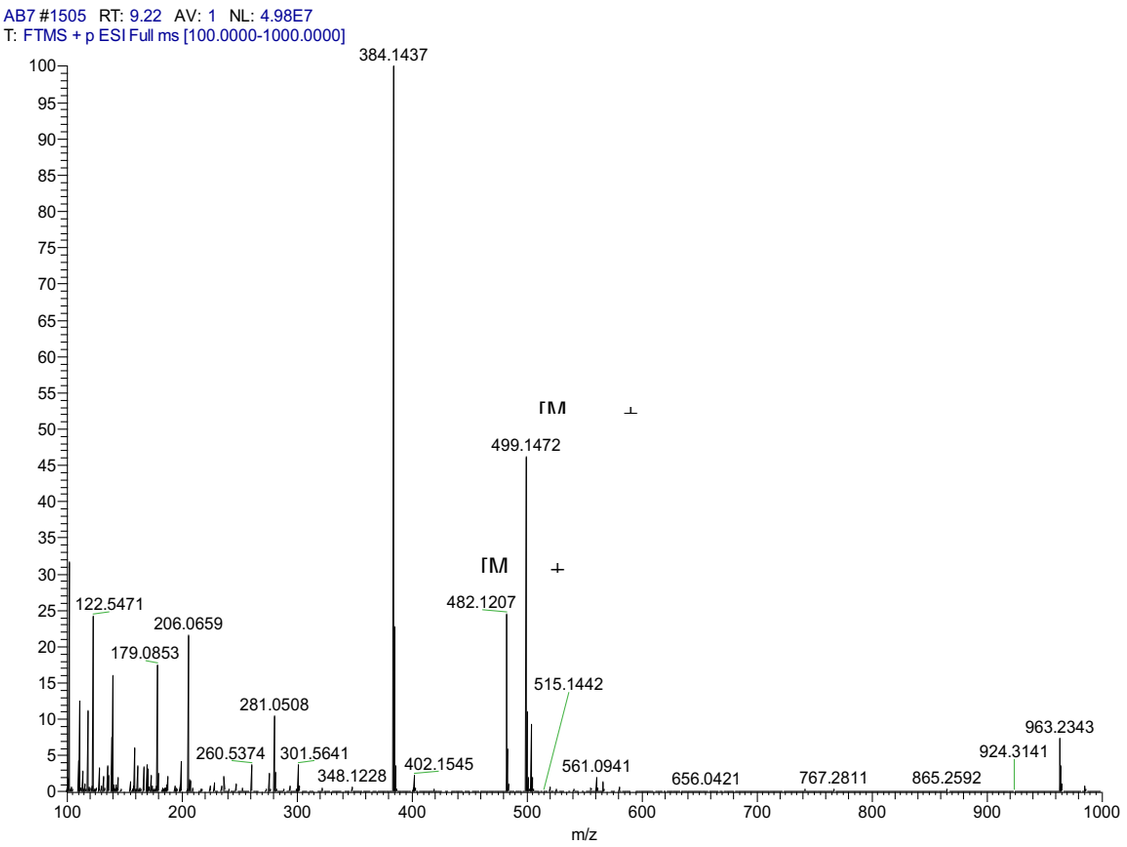


**Figure II.17. LC-MS spectrum of Fmoc-Glc1P (3d).**

## II.2.2. Peptides and glycopeptides

### Peptide FSF (5a)

$^{1}$H NMR (800 MHz, $D_2O$): $\delta$ 7.66 (H4, H5, H14, H17), 7.52 (H3, H7, H14, H18), 7.26 (H5, H15), 5.02 (H9), 4.93 (H12), 4.85 (H10), 4.76 (H1), 3.56- 3.53 (H2, H2'), 3.50- 3.48 (H13, H13').

$^{13}$C NMR (101 MHz, $D_2O$): $\delta$ 171.6, 174.7, 136.6, 128.6, 127.7, 125.9, 67.6, 62.7, 59.2 38.7, 36.5.

ESI-MS (m/z): [M - H]- 400.18.

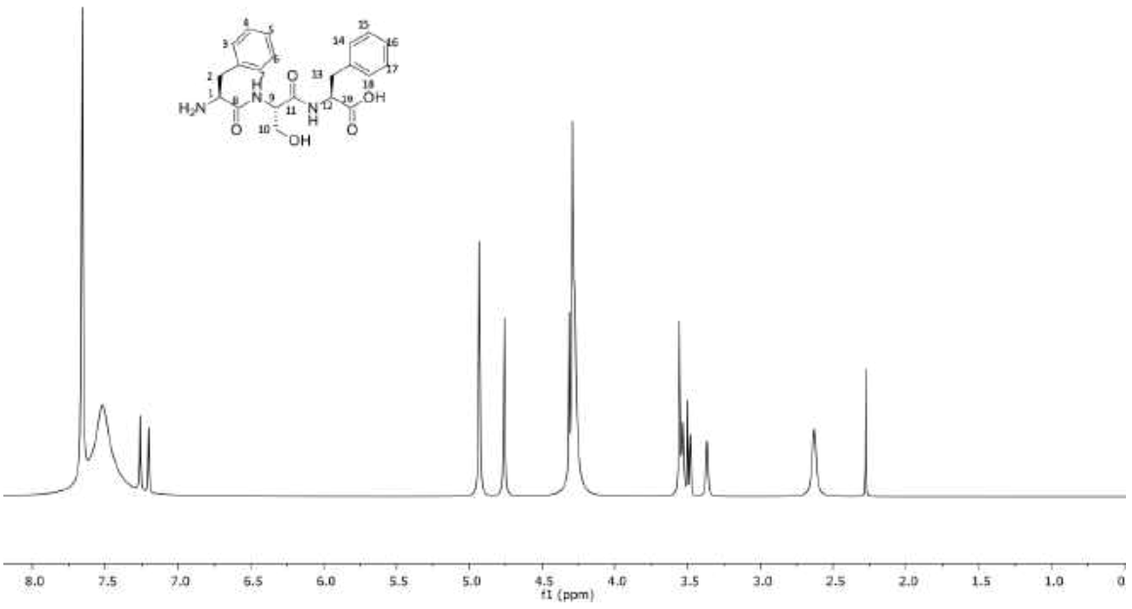


Figure II.18. $^{1}$H NMR spectrum (800 MHz, $D_2O$, 298 K) of FSF (5a).

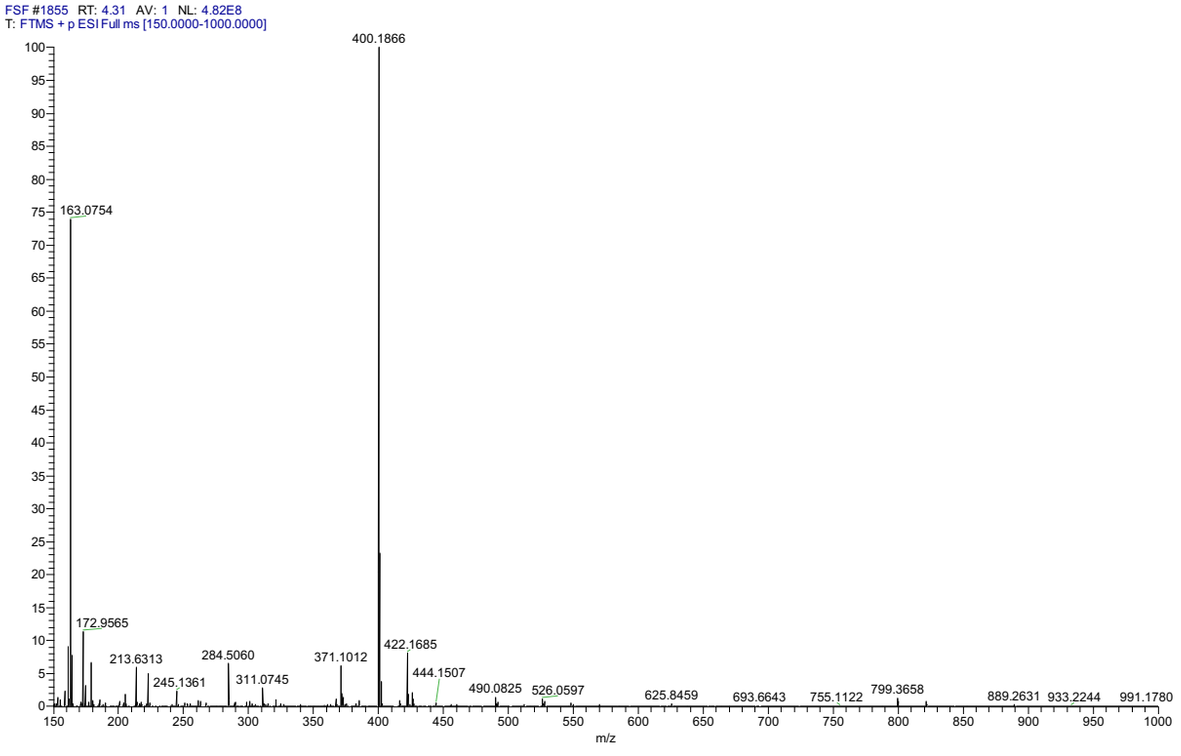


Figure II.19. ESI-MS spectrum of FSF (5a).

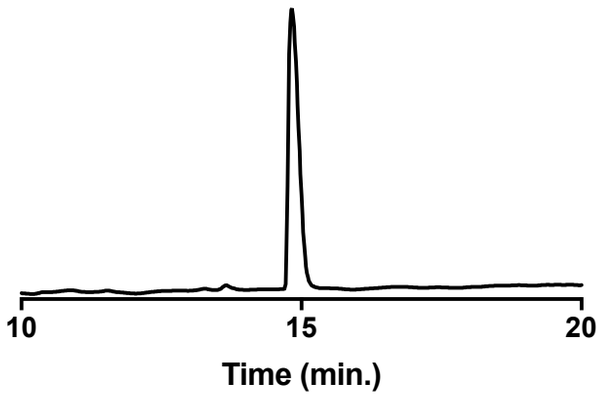


Figure II.20. HPLC spectrum of the purified FSF (5a).

### Peptide FTF (5b)

$^{1}$H NMR (800 MHz, $D_2O$): $\delta$ 7.20 (H4, H6, H14, H17), 7.14 (H3, H7, H14, H18), 6.85 (H5, H16), 4.83 (H12), 4.04 (H9), 3.88 (H10), 3.84 (H1), 3.78- 3.77 (H2, H2'), 3.75- 3.74 (H13, H13'), 3.06 (H20).

$^{13}$C NMR (101 MHz, $D_2O$): $\delta$ 171.7, 172.6, 136.6, 128.6, 127.7, 125.9, 67.5, 62.7, 59.2 38.7, 36.5.

ESI-MS (m/z): $[M - H]^-$ 414.20.

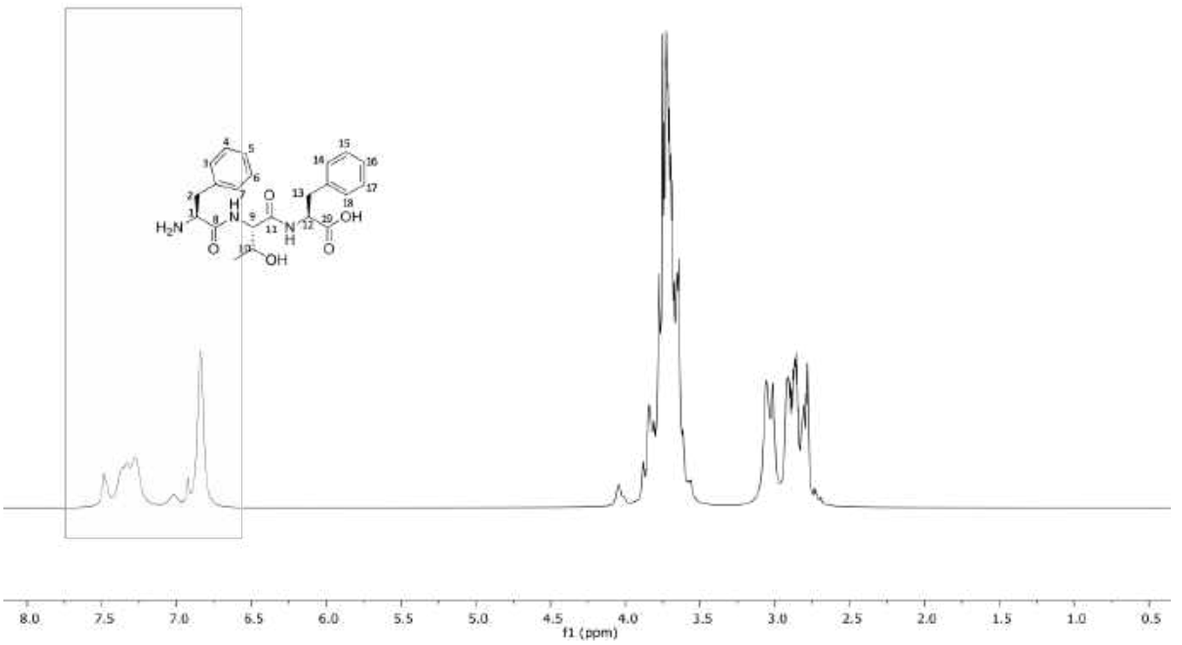


Figure II.21. $^{1}$H NMR spectrum (800 MHz, $D_2O$, 298 K) of FTF (5b).

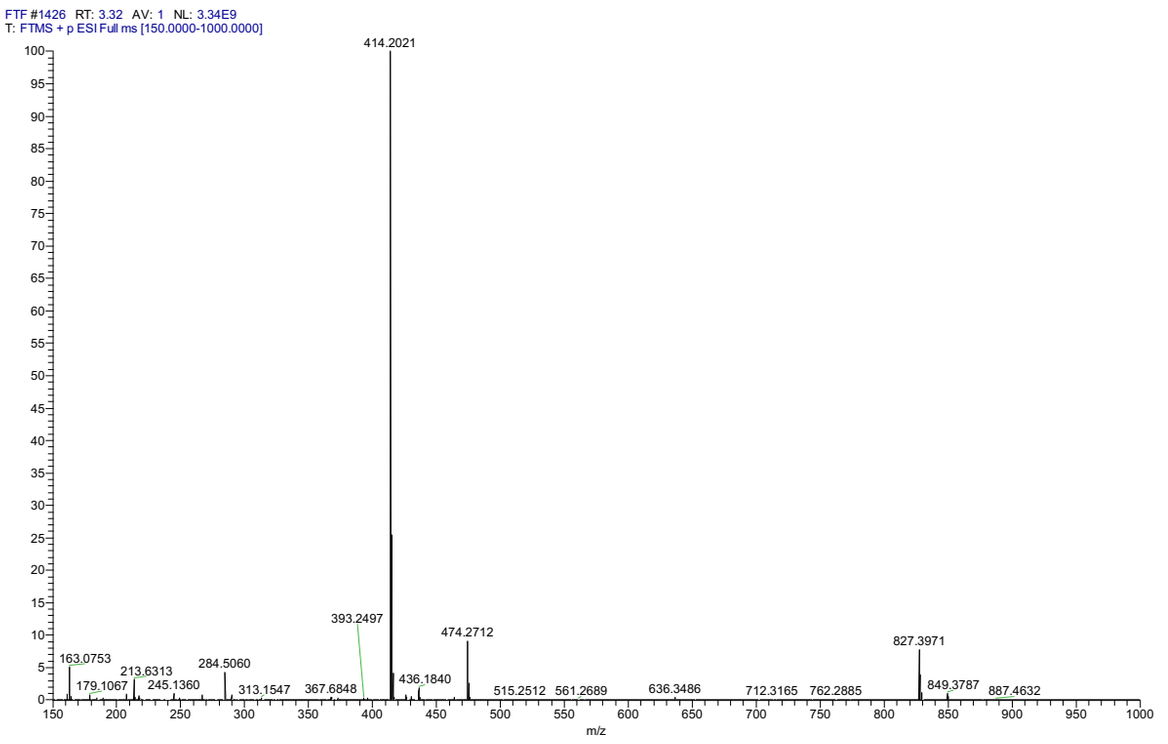


Figure II.22. ESI-MS spectrum of FTF (5b).

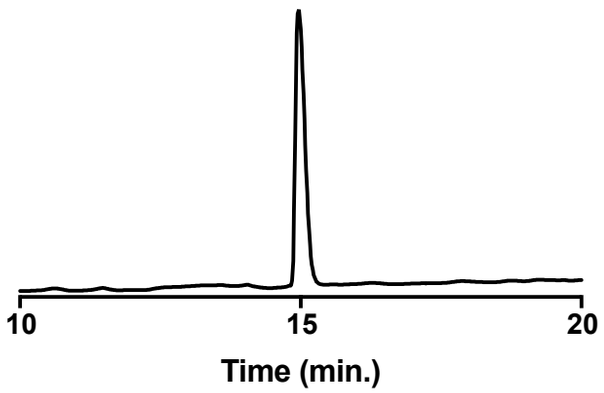


Figure II.23. HPLC spectrum of the purified FTF (5b).

### Glycopeptide FS(Glc)F (5c)

$^{1}$H NMR (400 MHz, $D_2O$): $\delta$ 7.50-7.48 (H4, H6), 7.46-7.45 (H3, H7), 7.44-7.43 (H5), 7.39-7.38 (H15, H17), 7.37-7.35 (H14, H18), 7.33-7.31 (H16), 5.76 (H21), 5.25 (H9), 4.53 (H12), 4.49 (H1), 3.86-3.75 (H26), 3.73 (H22), 3.72-3.70 (H10), 3.44-3.43 (H2), 3.39 (H23), 3.37 (H24), 3.30 (H25).

$^{13}$C NMR (101 MHz, $D_2O$): $\delta$ 171.7, 174.7, 129.60, 129.50, 129.26, 129.13, 129.01, 128.65, 128.59, 128.03, 127.30, 126.91, 126.73, 102.64, 102.41, 76.10, 75.66, 73.09, 69.68, 56.76, 56.36, 54.41, 53.24, 38.77, 38.56, 38.35, 38.13, 37.92, 23.47.

ESI-MS (m/z): $[M - H]^-$ 583.89.

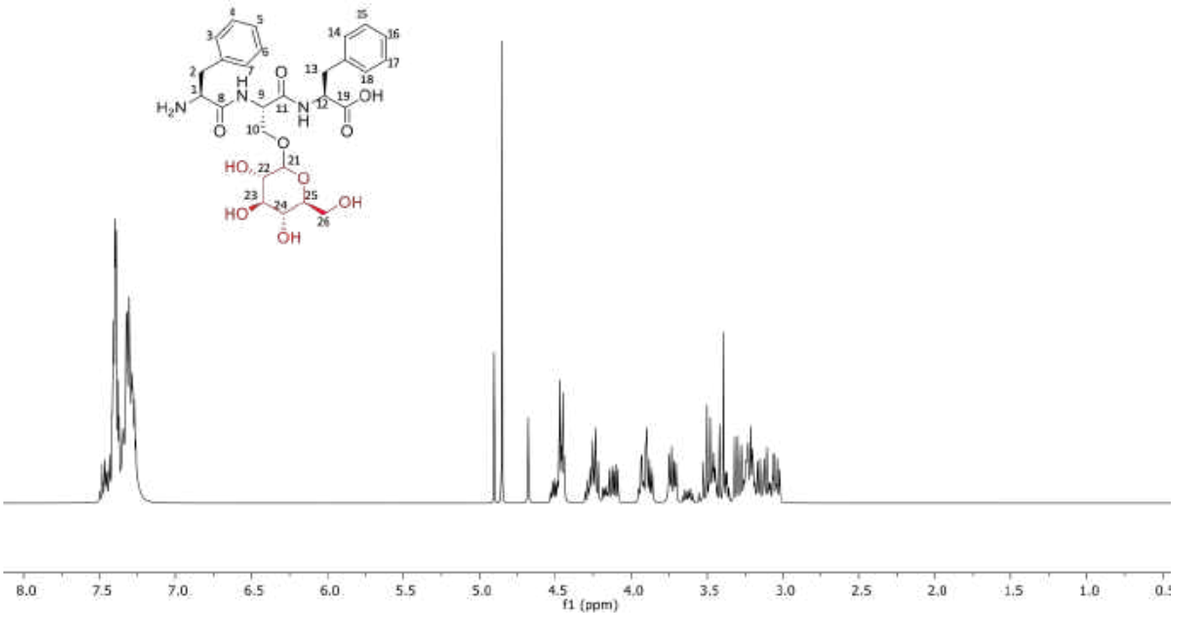


Figure II.24. $^{1}H$ NMR spectrum (800 MHz, $D_2O$, 298 K) of FS(Glc)F (5c).

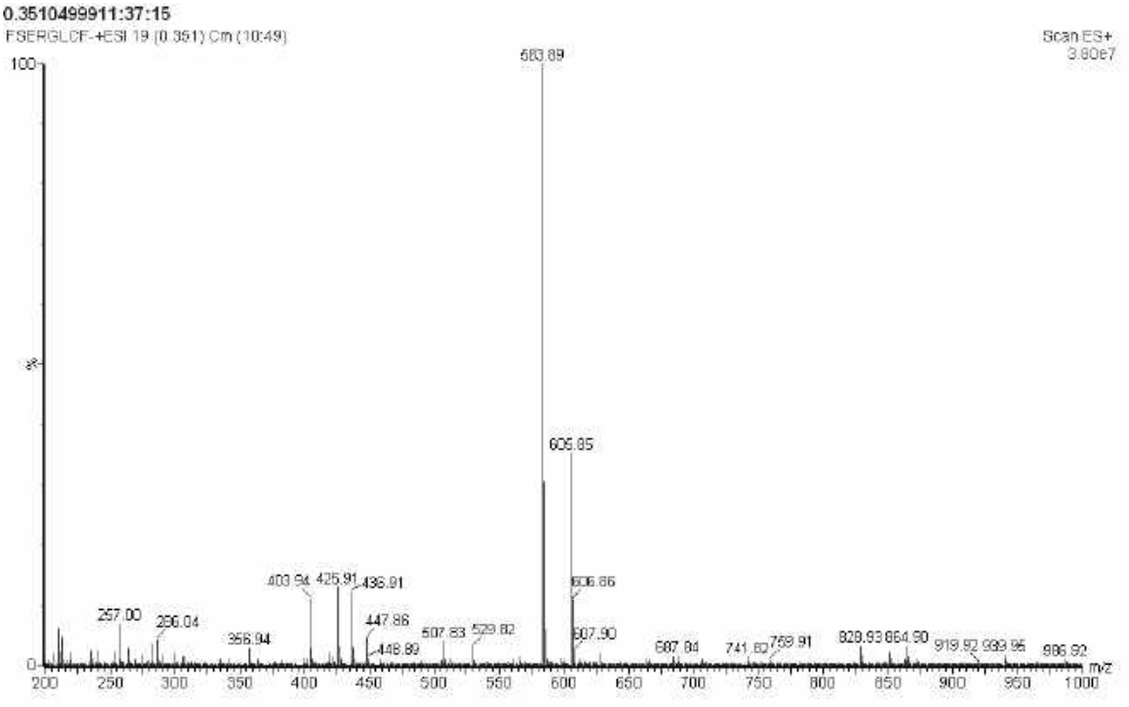


Figure II.25. ESI-MS spectrum of FS(Glc)F (5c).

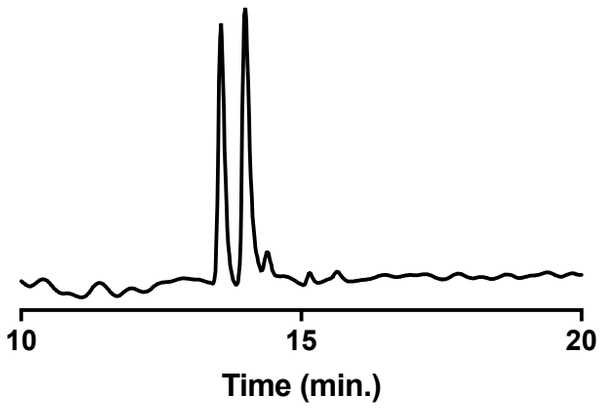


Figure 0.26. HPLC spectrum of the purified FS(Glc)F (5c).

### Glycopeptide FT(Glc)F (5d)

$^{1}$H NMR (700 MHz, $D_2O$): δ 7.28 (H4, H6), 7.24 (H3,H7), 7.14 (H5), 7.09 (H14, H16), 6.93 (H14, 17), 6.86 (H15), 5.33 (H21), 4.79 (H9), 4.00 (H12), 3.86 (H1), 3.85 (H10), 3.84-3.80 (H26), 3.77 (H23), 3.75 (H25), 3.71 (H24), 3.04-3.02 (H20).

$^{13}$C NMR (176 MHz, $D_2O$): δ 163.08, 117.14, 115.48, 72.15, 71.47, 69.35, 69.16, 23.05.

ESI-MS (m/z): $[M - H]^-$ 597.91.

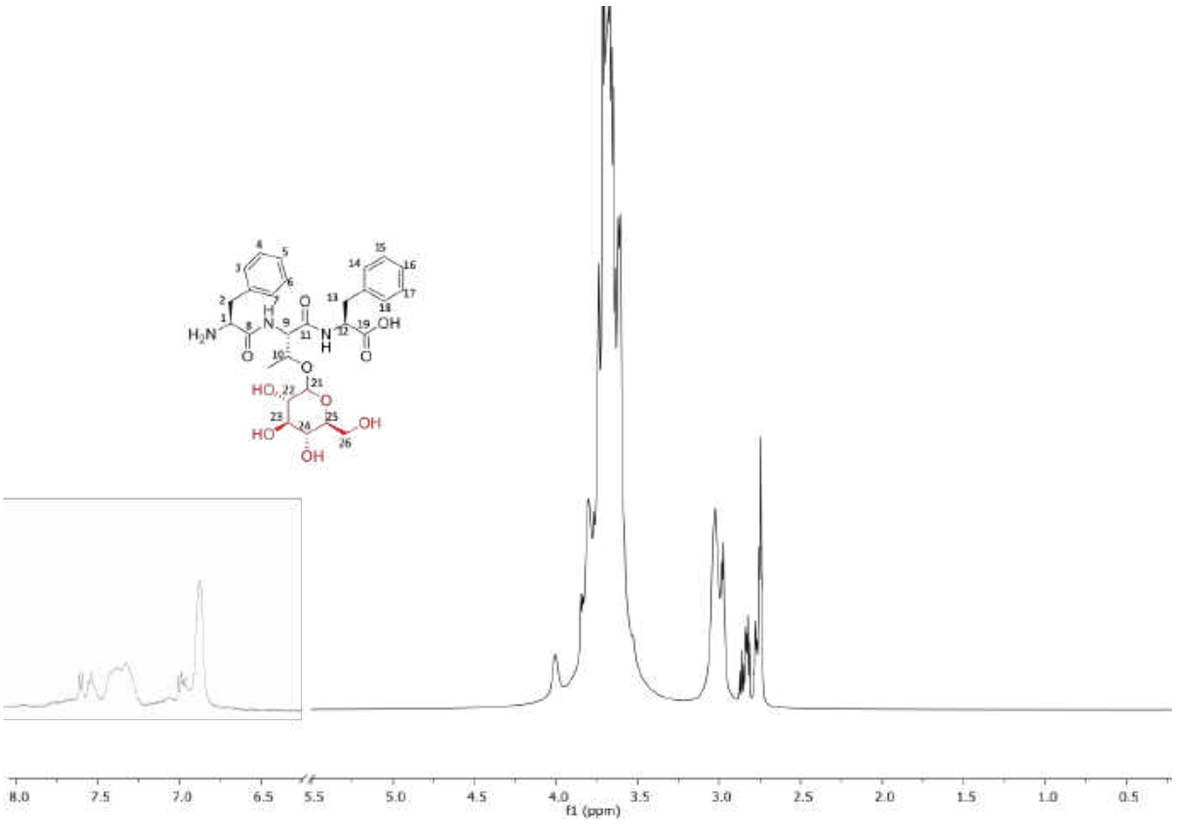


Figure II.27. $^{1}H$ NMR spectrum (800 MHz, $D_2O$, 298 K) of FT(Glc)F (5d).

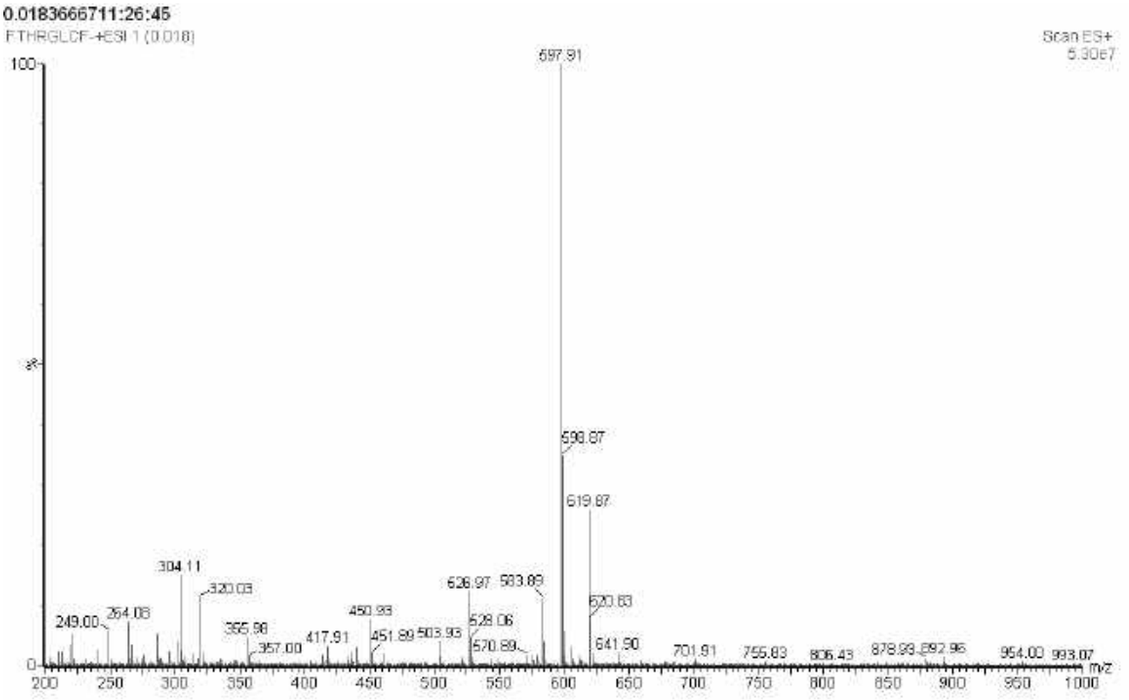


Figure II.28. ESI-MS spectrum of FT(Glc)F (5d).

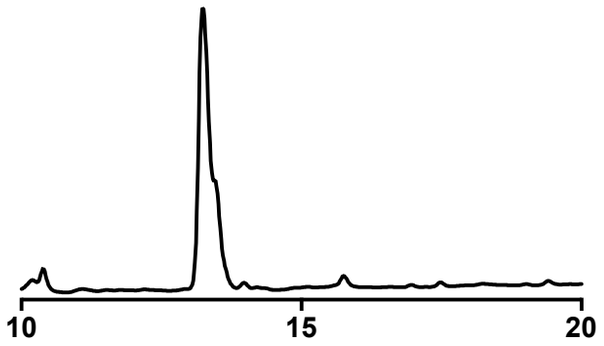


**Figure II.29. HPLC spectrum of the purified FT(Glc)F (5d).**

## II.3. SELF-ASSEMBLY OF CARBOHYDRATE AMPHIPHILES, PEPTIDES AND GLYCOPEPTIDES

In this thesis we used supramolecular assembly of carbohydrate derivatives to produce novel materials with unique properties. Self-assembly is the autonomous organization of components, herein molecules, into ordered structures or patterns without human intervention.[4] We used different types of self-assembly approaches (Scheme II.3) aiming to generate biofunctional materials with different properties suited to a targeted application. In all cases, the assembly was performed in water or aqueous media (*e.g.* cell culture media) under physiological conditions.

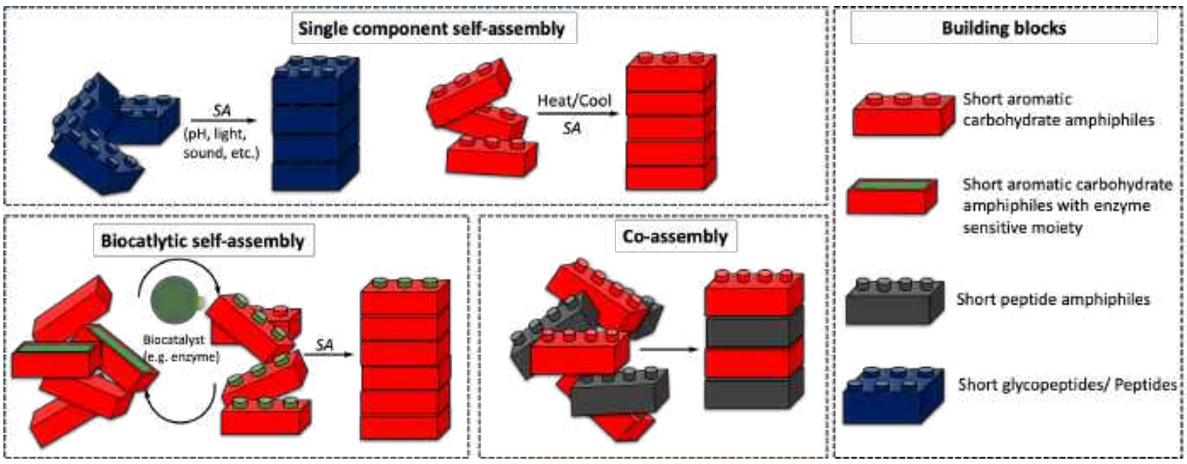


**Scheme II.3. Different types of self-assembly (SA) used in the thesis.**

### II.3.1. Single component self-assembly

Single component self-assembly refers to spontaneous and reversible organization of individual molecules into organized structures through non-covalent interactions. Different supramolecular interactions are involved in this process, *e.g.* hydrogen bonding, π– π stacking, van der Waals and CH-π interactions. These non-covalent interactions (weak and reversible) make the assembled structures responsive to external stimulus, *e.g.* pH, ionic strength. Some self-assembled system can further form gels via fibers thickening and aggregation (Scheme II.4).

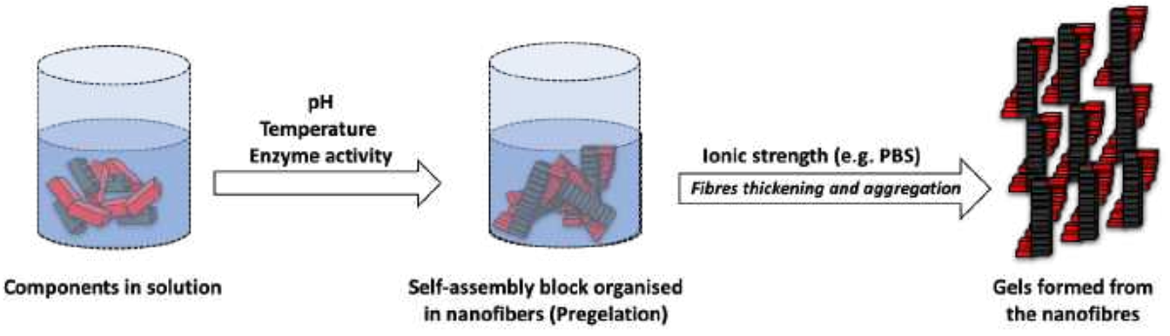


**Scheme II.4. Schematic presentation of single component self-assembly process with following gelation.**

Single component self-assembly process was used in **chapter VII**, where the self-assembly of tripeptides **5a, b** was compared with the assembly of the respective glycopeptides **5c, d.**

In **chapter III** and **V**, single component self-assembly of Fmoc-FF (**4**) triggered by heating was used as a control.

### II.3.2. Co-assembly of aromatic carbohydrate and peptide amphiphiles

Unlike self-assembly, co-assembly relies on the use of two (or more) different building-blocks to form ordered structures. It is used to generate functional diversity. The assembled structures can be categorized into three different groups (Scheme II.5): (a) the starting building blocks do not self-assemble, but when combined they assemble; (b) the components are able to self-assemble individually, which can lead to co-assemblies (components interact) or assemblies formed by single components; (c) one of the components self-assembles and a non-assembling component is added to change the final assemblies.[5]

Multicomponent co-assembly was used in **chapter VI** to functionalize peptide-based supramolecular system with carbohydrate moieties.

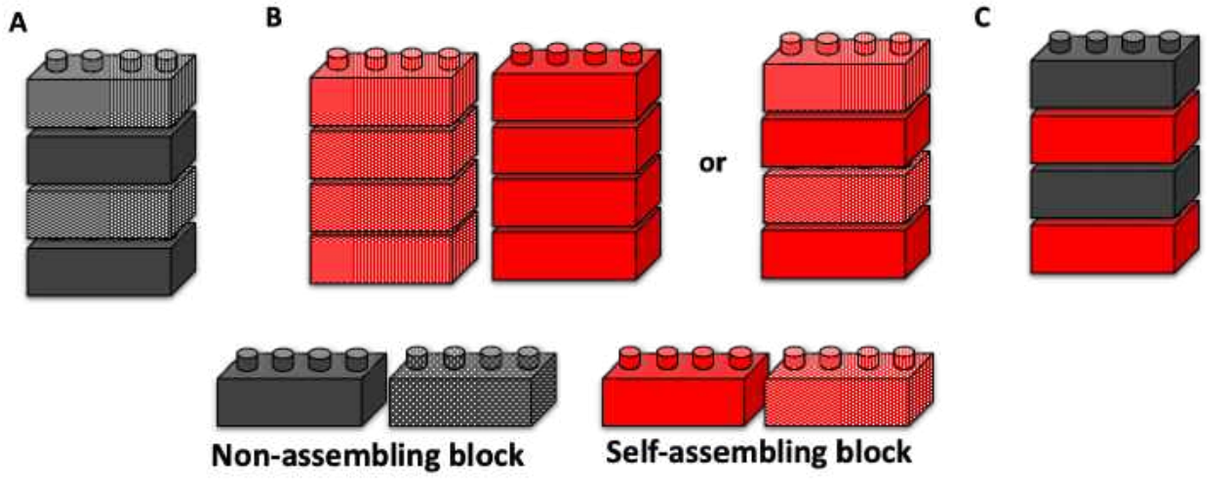


**Scheme II.5. Schematic presentation of two-component self-assembling systems for which (A) two non-assembling components are used; (B) two self-assembling components can form of self-sorting assembly of co-assembly; and (C) addition of non-assembling component can influence the properties of single component self-assemblies**

### II.3.3. Biocatalytic self-assembly (BSA)

In biocatalytic self-assembly precursors that are not able to self-assemble is converted into self-assembling block by an enzymatic transformation. This approach was used in **chapter III, IV** and **V**.

## II.4. CHARACTERIZATION OF THE OBTAINED SELF-ASSEMBLIES AT MOLECULAR LEVEL

### II.4.1. Circular dichroism (CD)

Asymmetric or chiral molecules have different optical properties. CD is an optical spectroscopy that measures the differential absorption of left versus right circularly polarized light by asymmetric molecules. This technique is commonly used to study secondary and tertiary protein structure. It can also give information on chiral organization of the supramolecular assemblies. CD spectra generally matches the UV–vis spectrum but the intensity of the CD signal (positive or negative) depends on the handedness of the supramolecular assemblies (Fig. II.30). In chapters III, VI and VII, CD was used to acquire information on the chirality of the self-assembled molecules. In addition, changes in CD as a function of the temperature, at characteristic wavelengths, was also used to determine the stability of the nanofibers formed in chapter VII.

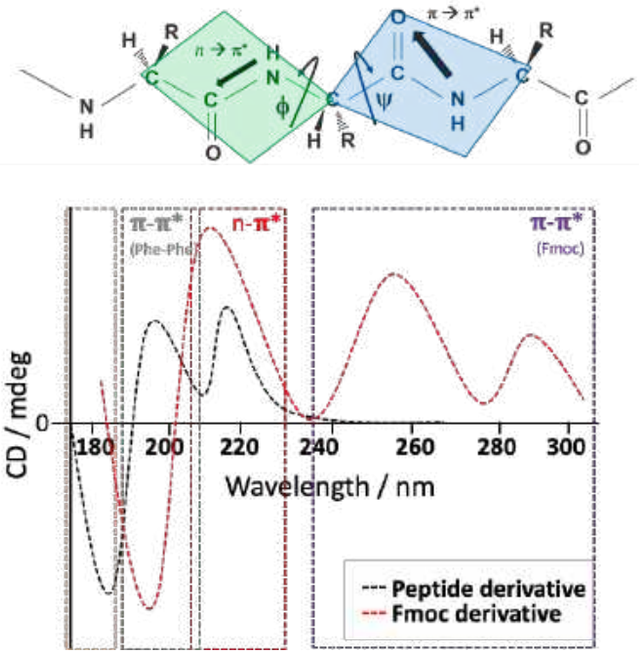


**Figure II.30. Typical CD spectra and characteristics signals of a peptide and its aromatic (Fmoc) derivative.**

**Sample preparation:**

*Solution:* In **chapter III, VI** and **VII**, 40 µL of each amphiphile(s) solution were analyzed using a cuvette of 1 mm pathlength. CD spectra were acquired at 37 °C on a Jasco J-810 spectrometer within the range

of 200-400 nm using a bandwidth of 1 nm. Each spectrum was obtained by accumulation of three acquisitions.

*Gel:* In **chapter VII**, 28 µl of each sample were pipetted into a 0.1 mm demountable quartz cuvette and spectra were measured on a JASCO J-1500 spectrometer with 2 s integration, a step size of 1 nm and a single acquisition with a slit width of 1nm. The temperature was maintained at 25 °C for all the measurements.

*Function of temperature:* Continuous ramp temperature measurements were performed for the stability studies in chapter VII. The samples (7.5-15 mM self-assembled glycopeptides and peptides in water) were added to a cuvette placed in a temperature-controlled module. Spectra were collected as a function of temperature starting from 25 °C and increasing to 90 °C (2 °C steps) and then decreasing back to 25 °C (5 °C steps) for a complete cycle.

### II.4.2. Fourier transform infrared spectroscopy (FTIR)

In supramolecular structures, FTIR can be used to confirm the presence of hydrogen bonding, *e.g.* FTIR amide I peaks (~1685 and ~1625 $cm^{-1}$) in peptide assemblies can indicate the formation of an extended β-sheet.[6] This technique was used in **chapter VI**.

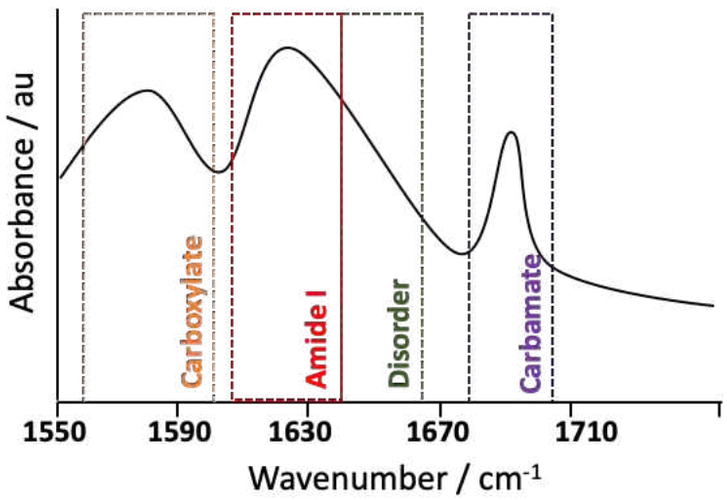


**Figure II.31. Typical FTIR spectra of Fmoc-peptide derivative with some characteristic absorption bands highlighted.**

**Samples preparation:** Spectra were acquired using a Bruker Vertex 70 spectrometer with a spectral resolution of 1 $cm^{-1}$. Measurements were performed in a standard IR cuvette (Harrick Scientific), in which the sample was placed between two $CaF_2$ windows (thickness, 2 mm) separated by a 25 µm PTFE

spacer. All sample manipulations were performed in a glove box to minimize interference from atmospheric water vapor. $D_2O$ (Sigma-Aldrich) was used as the solvent and 25 scans per sample were averaged to generate the final spectra.

### II.4.3. Fluorescence emission spectroscopy

Fluorescence emission spectroscopy give information on the interactions between aromatic groups (*e.g.* π-π stacking) in supramolecular systems assembled from aromatic amphiphiles.

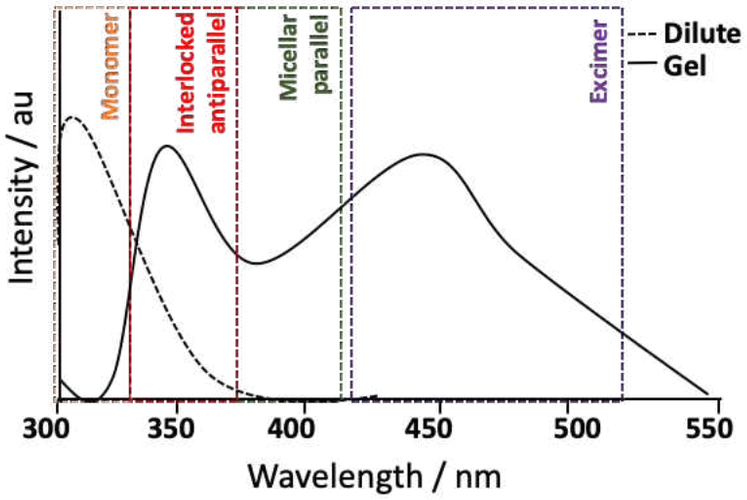


**Figure II.32. Typical fluorescence emission spectra for aromatic peptide amphiphiles with some characteristic emission bands highlighted.**

**Sample preparation:** In **chapter III** and **chapter VI**, a solution of the co-assemblies was dropped in a 10 mm cuvette. For gel analysis, a 1 mm cuvette was used and 20 µl of gel was added. Fluorescence emission spectra were recorded within the range 300-600 nm using a Jasco FP-6500 spectrofluorimeter. An excitation wavelength of 295 nm and a slit width of 3 nm was used. The data are presented as an average of three measurements.

### II.4.4. Wide-angle-X-ray Powder Diffraction (XRD)

Wide-angle X-ray powder diffraction (XRD) is a powerful method to understand molecular packing in the solid state, widely used to determine the atomic distances, intermolecular interactions, and the overall structure of any molecule at atomic resolution. This technique was used in **chapter VII**. The interplanar

spacings, *d*, of every single crystallographic phase can be determined by measuring the angles, θ, under which the constructively interfering X-rays leave the crystal (Scheme II.6). The long *d*-spacing obtained from XRD represents the longest repeat distance in the ordered structures by molecular self-assembly, which may provide insight into the packing of small molecules in either an extended or a bent conformation, contributing to the elucidation of the molecular organization of supramolecular nanostructures.[7,8]

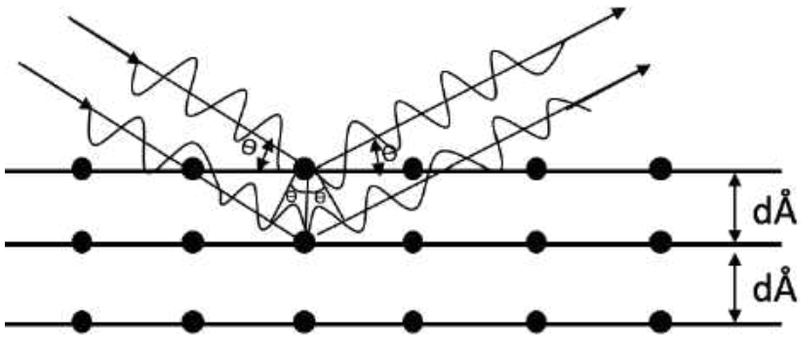


**Scheme II.6. Schematic representing of the diffraction of X-rays by crystal planes to determine lattice spacings by using the Bragg's law ($n\lambda = 2dsin\theta$), where *n* is an integer called the order of reflection, λ is the wavelength of x-rays, *d* is the characteristic spacing between the crystal planes of a given specimen and θ is the angle between the incident beam and the normal to the reflecting lattice plane.**

**Sample preparation:** Glycopeptides **5c, d** were dissolved in water to 65 mM stock concertation. Then, diluted to 40 mM final concentration and kept for 24 hrs at room temperature. The peptides **5a, d** were dissolved in water to 40 mM and kept for 24 hrs. The solutions that contained the assembled structures were freeze-dried and the obtained powder was placed on a quartz substrate. X-ray intensity data were recorded on a PANalytical X'Pert Pro Powder Diffraction instrument with an x-ray source of 3 kW and a wavelength of 1.5405 Å.

### II.4.5. Zeta Potential

Zeta potential is the difference in the electrokinetic potential between a dispersion medium and the stationary layer (Stern layer) of a fluid attached to a solid immersed in the medium (Scheme II.2.7). It is used as an indication of the surface charge of a solid immersed in a certain medium. We used zeta potential to obtain the surface charge of the fibers assembled in **chapter VI.**

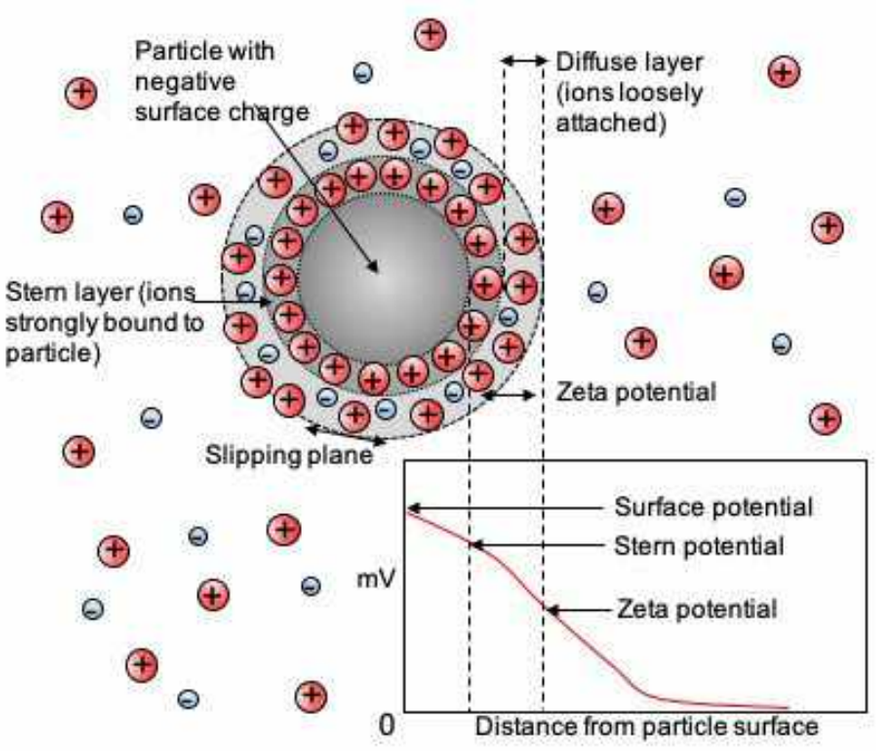


**Scheme II.7. Schematic presentation of the surface potential, Stern layer and zeta potential as a function of distance from a charged surface particle suspended in a dispersion medium.**

**Sample preparation:** The solutions containing co-assembled nanofibers were analyzed by dynamic light scattering (Nano ZS, Malvern Instruments, Malvern, UK). The measurements were performed after 24 hrs of sample preparation. The mobility of nanostructures was measured and was converted to zeta potential by the software.

## II.5. MICRO- AND MACROSCOPIC CHARACTERIZATION OF THE SUPRAMOLECULAR STRUCTURES

### II.5.1. Invert-vial test

Invert-vial test is an easy and fast assay that allows classification of a material as a solution, viscous liquid, half-gel, or solid-like gel. It was used in **chapters III-IV**.

### II.5.2. Oscillatory Rheology

Oscillatory rheology is used for characterization of viscoelastic materials. It determines the material response to an applied oscillatory stress and gives information about its elastic properties, such as G* (complex modulus), G′ (storage or elastic modulus), and G″ (loss modulus or viscosity). This information can be further used together with other characterization methods to conclude about the type, number, and strength of networks responsible for the hydrogelation.

**Sample preparation***:* In **chapter III, VI** and **VII**, the mechanical properties of the hydrogels were measured on a Kinexus Rheometer with an 8 mm/cone-plate geometry. The elastic (G') and viscous (G'') moduli of the hydrogels were recorded as a function of frequency between 0.01 and 10 Hz. A solvent trap was used to keep the sample hydrated and the temperature of the sample was maintained at 37 °C by an integrated temperature controller. In **chapter VII**, an Anton Paar MCR 302 rheometer was used to measure rheological properties with temperature controlled at 25 °C using a 10 mm vane geometry. Samples were prepared in a 10 mm mold and after 48h of assembly, the gels were transferred onto the stage for measurements. We start by performing amplitude sweeps at a constant frequency of 0.1 Hz from sheer strain 0.01-10 % to ensure the measurements to be taken in viscoelastic regime. In order to measure G' and G", frequency sweep was done at constant strain (0.01%) in the frequency range of 0.1-10 Hz. Replicates of three were done from each sample for frequency sweeps.

### II.5.3. Microscopy

#### II.5.3.1. Electron microscopy

Transmission electron microscopy (TEM) and scanning electron microscopy (SEM) microscopies use a beam of accelerated electrons as a source of illumination. SEM uses scattered electrons and scans only the sample surface. It can give insights on the sample morphology with a resolution of 20 nm. On the other hand, TEM uses transmitted electrons and give more details on the sample composition and morphology of the sample with higher resolution of about 1 nm. These techniques were used in **chapter III, V, VI** and **VII**.

**Sample preparation for TEM:** 5 µl of a sample solution was dropped onto a carbon-coated grid (Electron Microscopy Sciences) and left for 1 min. The excess of solution was removed with filter paper (blotting),

followed by staining with 5 µl of 2% (w/v) uranyl acetate solution for 30 sec. The excess staining was removed by blotting and the grid was left to dry in air at room temperature. Sample was then imaged in a FEI TITAN Halo TEM operating at 300 kV and images were recorded on a FEI CETA 16M camera.

**Sample preparation for SEM:** A drop of a solution of the self-assembled systems was deposited onto a silicon wafer and let dry at room temperature. The samples were then coated with platinum, using a Leica ACE600 sputter coater. After the coating samples were imaged using a FEI Helios Nanolab660 Dualbeam FIB-SEM, recorded at 5kV.

#### II.5.3.2. Atomic Force Microscopy (AFM)

AFM is a scanning probe microscopy with a high-resolution and potential to image hydrated samples in situ. It gives information about the morphology and the mechanical properties of the assemblies. This technique was used in **chapters III, IV, VI** and **VII**.

**Sample preparation:** When the sample was positively charged or neutral (assemblies of Fmoc-Glc **3a**, glycopeptides and peptides **5a-d**), fresh cleaved micas were used without functionalization. For the rest of the samples the mica sheet was functionalized with amine groups using 200 µL (3-Aminopropyl) triethoxysilane (APTES) for 30 min at room temperature to increase the affinity of the sample to the mica. A drop of the self-assembled sample was dropped on the mica sheet. All AFM images were acquired with a JPK Nanowizard 3, in air at room temperature. The morphological features and mechanical properties of the nanofibers were assessed under JPK quantitative imaging mode using RTESPA-525 probes (k~200 N/m, Bruker, Germany) calibrated by the contact free method. All approaching force curves were fitted using Hertz model to obtain the elastic modulus (E). The reported E is averaged over 30 measurements.

### II.6. BIOLOGICAL CHARACTERIZATION

The systems developed in this thesis were prepared to be used in a biological context. We used different type of cells and proteins in contact with the developed systems and evaluated the performance by several biological tests.

### II.6.1. *In vitro* cell culture

Human osteosarcoma SaOs2 and mammary gland/breast cancer MDA-MB-468, MCF-7 and HS587T cell lines were purchased from American Type Culture Collection (ATCC) and were used in **chapters IV** and **V**. The cell lines were authenticated at Memorial Sloan-Kettering Cancer Center (MSKCC) integrated genomics operation core using short tandem repeat analysis. The cells used in our experiments were mycoplasma free and had a passage number lower than 15. SaOs2 were cultured at 37 °C in a humidified 95/5 % air/$CO_2$ atmosphere using Dulbecco's modified Eagle's medium (DMEM) low glucose (Sigma) supplemented with 10% fetal bovine serum (FBS, Gibco, UK) and 1 % antibiotic/antimycotic (Gibco, UK) solution. MDA-MB-468 cells were cultured in DMEM high glucose (Sigma) and in the case of ATDC5 cells, DMEM-F12 (Sigma) was used. HS578T cells were cultured in Dulbecco´s Modified Eagle´s Medium (DMEM, Sigma or MSKCC media preparation core). MCF-7 cells were cultured in Eagle´s Minimum Essential Medium (EMEM; Corning, NY, USA or MSKCC media preparation core) with 1.5 g/L sodium bicarbonate, non-essential amino acids, L-glutamine and sodium pyruvate. Both culture media were supplemented with 10 % (v/v) of fetal bovine serum (Life Technologies, Carlsbad, CA, USA), 100 U/mL penicillin, 100 μg/mL streptomycin and 0.25 μg/mL amphotericin B (Sigma). The cultures were maintained at 37 °C in a 5 % $CO_2$ humidified atmosphere.

### II.6.2. Viability and proliferation assessment

#### II.6.2.1. Metabolic activity (MTS assay)

Cytotoxicity of the prepared compounds was tested by MTS assay (CellTiter 96® AQueous One Solution) following the supplier's instructions in **chapter IV**. The assay is based on the ability of mitochondrial dehydrogenase enzymes present in viable cells to convert the 3-(4,5-dimethylthiazol-2-yl)-5-(3-carboxymethoxyphenyl)-2- (4-sulphofenyl)-2H-tetrazolium (MTS) compound into a brown formazan product that is soluble in culture medium. The optical density (OD) was read at 490 nm on a multiwell microplate reader (Synergy HT, BioTek Instruments). The metabolic activity of cells cultured in the absence (control) and presence of the tested compounds is compared and used as a measure for the cytotoxicity.

### II.6.2.2. Viability assay (alamarBlue)

In **chapter IV**, cells in exponential growth phase were seeded in 96 well plate at a density of 50 000 cells/cm$^2$ and incubated overnight at 37 °C and 5 % $CO_2$. alamarBlue Cell Viability Reagent is based on an active and non-toxic compound, resazurin, that is cell permeable and reduced to resorufin, in viable cells giving a red fluorescent color, as a cell health indicator. The culture medium was then removed and replaced by medium without FBS containing the compound to be tested at different concentrations. The cells were incubated at 37 °C and 5 % $CO_2$ for 24 hrs. After this time, cells were washed with PBS and 10 µL of alamar blue were added to each well. The cells were incubated again for 3 hrs at 37 °C and 5 % $CO_2$. The fluorescence with an excitation wavelength at 530-560 nm and emission wavelength at 590 nm was then measured in a microplate reader (SYNERGY HT, Manufacturer Biotek). Medium with the tested compound(s) but without cells was used as a negative control. Untreated cells were used as positive control. The viability was calculated according to the manufacturer's instructions.[9]

**Viability assay (live/dead):** Viability of cells seeded or encapsulated in supramolecular gels (Chapter VI) or cells after treatment with N-glucosides (**chapter IV** and **V**), calcein- AM and propidium iodide (PI) dyes were used. Calcein-AM is a membrane-permeant dye, which gives a green signal in the cytoplasm, when is hydrolyzed by endogenous esterase into the highly negatively charged calcein*, i.e.* it stains the live cells. On the other hand, propidum iodide stains dead cells in red by permeating the cell membrane and binding to the DNA of dead cells. Briefly, at specific time points, the culture medium from the samples was removed and PBS containing 0.2 % (v/v) of Calcein-AM and 0.1 % (v/v) of PI was added to each well. Afterwards, samples were then incubated at 37 °C for 30 min protected from light. Afterward, samples were washed three times with PBS and immediately visualized in the dark by confocal microscopy (Leica TCS SP8). The cell viability was quantified with CellProfiler image analysis software (version 3.0) using the confocal images (at least three per sample) of a live/dead staining. Live cells (green signal) and dead cells (red signal) were separated from the background using Otsu threshold method and the clumped cells were separated by shape. Cells that were stained simultaneously in green and red were counted as death cells. The cell viability is presented as percentage of live cells from the total of number of cells.

#### II.6.2.3. Proliferation assay

Quantification of cell proliferation was performed with Quan-iTTM PicoGreen® dsDNA assay kit (Molecular Probes/Invitrogen) after cell lysis following the manufacturer's instructions and by the Ki-67 immunohistochemistry (rabbit monoclonal antibody, Abcam). For the Ki-67 immunohistochemistry, cells were fixed in 1 % formalin for 3 min, permeabilized with 0.2 % TritonX-100 for 5 min and blocked in 3 % bovine serum albumin in PBS at room temperature for 30 min. Ki-67 antibody incubation was performed overnight at 4 °C. Nuclei were counterstained with 1 μg/mL 4,6-diamidino-2-phenyl (DAPI, Sigma) for 30 min. Samples were washed with PBS, mounted with Vectashield® (Vector) in glass slides and observed under a laser scanning confocal microscopy (Leica, TCS SP8).

#### II.6.2.4. Cytocompatibility of the supramolecular gels

The cytocompatibility was evaluated by two different protocols using 2D cell seeding or 3D cell encapsulation. Cells were cultured (5% $CO_2$ incubator at 37 °C) on tissue culture polystyrene (TCPS) using the recommended medium supplemented with 10% fetal bovine serum and 1% Antibiotic/Antimycotic. Upon reaching confluence, the cells were detached from the TCPS with TrypLe (ThermoFisher Sci), centrifuged, and resuspended in the respective medium.

*2D cell seeding:* The cell media and pregelation solutions were heated (water bath) to 37 °C. The gels were formed as described in II.3.2. After gelation the DMEM was replaced by the medium specific for the respective cell line supplemented with 10 % fetal bovine serum and 1 % Antibiotic/ Antimycotic. The medium was exchanged 3 times during 24 hrs and then the top medium from the insert was replaced with a cell suspension at a concentration of $10^5$ cells/gel. The medium was changed after 24 hrs of culture and after more 24 hrs of culture, gels were washed with PBS and incubated with Calcein-AM (Life Technologies) and Ethidium Homodimer-1 (EthE-1, Sigma) in PBS for 10 min. The samples were washed and observed using confocal laser scanning microscope (Leica TCS SP8) with 488 nm (green, Calcein AM) and 633 nm lasers (red, EthE-1).

*3D cell culture:* Pregelation solution (500 μL) was pipetted into transwell cell culture insert, placed into 12 wells culture plate and 1.5 mL of the respective cell culture medium was added in the well (*i.e.* no medium was added directly to the pregelation solution). The plate was placed in an incubator (5 % $CO_2$, 37 °C) for 15 min. After this period, the pregelation solution in the insert was mixed (pipetting up and down several times) and the media from the plate was replaced. This process was repeated 3 times. Cell

suspension (150 µL, $2.5\times10^5$ cells/gel) was then added into the insert (pipetting up and down several times to mix well) and the plate was incubated again. After gelation (2 hrs) the media from the bottom of the insert was replaced and 200 µL of fresh medium was added on top of the gel. The medium was exchanged after 24 hrs of culture. After 48 hrs in culture, the gels were processed as described above for the 2D culture.

#### II.6.2.5. Real-Time Polymerase Chain Reaction

Real Time Polymerase Chain Reaction is an amplification technique for cloning specific or targeted parts of DNA sequence to generate thousands or millions copies of the DNA of interest. It was used to evaluate the expression of GLUT1-GLUT4 genes (**chapter IV**). The whole procedure consists on: extraction of RNA, cDNA production from the extracted RNA and real-time quantification of the amplification of specific sequences using specific primers.

**Sample preparation**: Total RNA extraction was performed using TRIzol ® reagent. Chloroform was added to the cell extract and centrifuged at 12 000 g for 10 min. The aqueous phase was separated from the organic one and the RNA was recovered from it by precipitation with isopropyl alcohol. One µg of total RNA was transcribed to cDNA (cDNA quantification kit). RT-PCR analysis of the samples was performed in triplicate. Oligonucleotide primer pairs were used to detect the presence of mRNAs encoding members of the GLUT family (*SLC2A*) in different cell lines by real time RT-PCR. Fragments were analyzed by agarose gel electrophoresis. The oligonucleotides sequences are presented below.

| Oligo name | Sequence (5' → 3') | Tm (°C) | MW (g/mol) |
|---|---|---|---|
| HsGlut1Fwd | TCCACGAGCATCTTGAGA | 56.7 | 5773 |
| HsGlut1Rev | ATACTGGAAGCACATGCCC | 56.7 | 5782 |
| HsGlut2Fwd | CACTGATGCTGCATGTGGC | 58.8 | 5820 |
| HsGlut2Rev | ATGTGAACAGGGTAAAGGCC | 57.3 | 6215 |
| HsGlut3Fwd | TTCAAGAGCCCATCTATGCC | 57.3 | 6037 |
| HsGlut3Rev | GGTCTCAGGGACTTTGAAGA | 57.3 | 6197 |
| HsGlut4Fwd | GGCATGTGTGGCTGTGCCATC | 63.7 | 6469 |
| HsGlut4Rev | GGGTTTCACCTCCTGCTCTAA | 59.8 | 6348 |
| Hs18SFwd | CCCCTCGATGCTCTTAGCTG | 57.3 | 6116 |
| Hs18SRev | CCCATCACGAATGGGGTTCA | 57.3 | 6135 |

### II.6.3. Protein Expression

Western blotting (WB), also called immunoblotting, is widely used to identify and quantify protein expression in a cell or tissue extract. The proteins are separated based on molecular weight through gel electrophoresis. These results are then transferred to a membrane which is incubated with labelled antibodies specific to the protein of interest. Although WB shares some basic principles with immunocytochemistry (ICC), *i.e.* relies on the specific binding of an antibody to the protein of interest, WB is more sensitive. However, WB is also destructive technique whilst ICC maintain the studied tissue intact.

#### II.6.3.1. Western Blot analysis

Whole protein extracts were prepared by washing cells twice with ice-cold PBS and harvesting with radioimmunoprecipitation assay buffer (RIPA buffer: 150 mM NaCl, 50 mM Tris-HCl, pH 7.5, 5 mM ethylene glycol tetraacetic acid (EGTA), 1% Triton X-100, 0.5% sodium deoxycholate (DOC), 0.1% sodium dodecyl sulfate (SDS), 2 mM phenylmethanesulfonyl (PMSF), 2 mM iodoacetamide (IAD)) and 1X protease inhibitor cocktail (Roche, Indianapolis, IN, USA). After centrifugation at 16,000 g for 10 min at 4 °C, supernatants were collected and used for protein quantification with Pierce BCA Protein Assay Kit (Thermo Fisher Scientific) following the manufacturer's instructions. Absorbance at 562 nm was measured on a multiwell microplate reader (Synergy HT, BioTek Instruments). Quantification was followed by denaturation of the sample with Laemmli buffer. WB analysis was performed by loading 40 μg proteins per lane on 4-12% Bis-Tris Protein Gels (Novex). After electrophoresis and transfer to nitrocellulose membranes (Thermo Fischer Scientific), the membranes were incubated in 5% (m/v) bovine serum albumin in Tris-buffered saline-Tween (TBS-T, Cell Signalling Technology) and probed with the respective antibody (rabbit anti-GLUT1 1:1,000 (rabbit polyclonal, Merck-Millipore, Watford, UK) and mouse anti β-actin 1:20,000, Sigma). After washing, the membranes were incubated with labelled secondary antibody (IRDye®800CW anti-Rabbit or anti-Mouse IgG 1:15,000 (LI-COR Biosciences) and imaged on the Odyssey Infrared Imaging System (LI-COR Biosciences). Densitometric analysis was performed with ImageJ software.

### II.6.3.2. Immunocytochemistry (ICC)

The principle of immunostaining is the use of antibodies to target specific protein or antigen in cells. Briefly, the initial step comprises the cells' fixation, usually with 10 % formalin, and submitted to a permeabilization step (when the target protein is intracellular). Cells are then incubated with a primary antibody, diluted accordingly to each antibody specifications, in 1 % Bovine serum albumin in PBS, overnight at 4 °C. Afterwards, cells are incubated, in an appropriate dilution, the fluorochrome-conjugated secondary antibody in 1 % Bovine serum albumin (if the initial antibody is fluorescent-labeled there is no need for this step), 1h at room temperature. Cells are washed and then imaged under a fluorescent microscope.

**Immunofluorescence analysis of glucose transporter 1 (GLUT1):** Anti-Glucose transporter GLUT1 (rabbit polyclonal antibody) was purchased from Abcam®. Cells were fixed in 1 % formalin for 3 min, permeabilized with 0.2 % TritonX-100 for 5 min and blocked in 3% bovine serum albumin in phosphate buffered saline (PBS) at room temperature for 30 min. Cells were incubated with the primary anti-GLUT1 antibody overnight at 4 °C. After washing, secondary antibody incubation was performed with an anti-rabbit IgG Alexa-Fluor-488 for 30 min. at room temperature. Phalloidin–Tetramethylrhodamine (TRITC) conjugate was used (1:200 in PBS for 30 min, Sigma) to assess cytoskeleton organization. Nuclei were counterstained with 1 μg/mL 4,6-4,6-diamidino-2-phenyl (DAPI, Sigma) for 30 min. The cells were washed with PBS, mounted with Vectashield® (Vector) in glass slides and observed under an Imager Z1 fluorescence microscope (Zeiss) and photographed using an Axio Cam MRm (Zeiss).

## II.7. REFERENCES

1. Birchall LS, Roy S, Jayawarna V, Hughes M, Irvine E, Okorogheye GT, et al. Exploiting CH-π interactions in supramolecular hydrogels of aromatic carbohydrate amphiphiles. Chemical Science. 2011;2(7):1349-55.

2. Brito A, Abul-Haija YM, da Costa DS, Novoa-Carballal R, Reis RL, Ulijn R, et al. Minimalistic Supramolecular Proteoglycan Mimics by Co-assembly of Aromatic Peptide and Carbohydrate Amphiphiles. Chemical Science. 2019.

3. Palomo JMJRA. Solid-phase peptide synthesis: an overview focused on the preparation of biologically relevant peptides. 2014;4(62):32658-72.

4. Whitesides GM, Grzybowski B. Self-assembly at all scales. Science. 2002;295(5564):2418-21.

5. Buerkle LE, Rowan SJ. Supramolecular gels formed from multi-component low molecular weight species. Chemical Society Reviews. 2012;41(18):6089-102.

6. Barth A, Zscherp C. What vibrations tell us about proteins. Q Rev Biophys. 2002;35(4):369-430.

7. Alexander L, Klug HPJAC. Basic aspects of X-ray absorption in quantitative diffraction analysis of powder mixtures. 1948;20(10):886-9.

8. Aitipamula S, Vangala VR. X-Ray Crystallography and its Role in Understanding the Physicochemical Properties of Pharmaceutical Cocrystals. Journal of the Indian Institute of Science. 2017;97(2):227-43.

9. Sebaugh JL. Guidelines for accurate EC50/IC50 estimation. Pharmaceutical Statistics. 2011;10(2):128-34

# SECTION 3

# EXPERIMENTAL STUDIES

# Chapter III

# HELICAL NANOFIBERS WITH OPPOSITE HANDENESS GENERATED BY BIOCATALYTIC SELF-ASSEMBLY OF AROMATIC CARBOHYDRATE AMPHIPHILES

## HELICAL NANOFIBERS WITH OPPOSITE HANDEDNESS GENERATED BY BIOCATALYTIC SELF-ASSEMBLY OF AROMATIC CARBOHYDRATE AMPHIPHILES


### Abstract

We report on biocatalytic self-assembly of supramolecular helical fibers from aromatic carbohydrate amphiphiles. Alkaline phosphatase is used to trigger the self-assembly of Fmoc-glucosamine-1-phosphate and Fmoc-glucosamine-6-phosphate. The enzymatic dephosphorylation rate is dictated by the regioisomer used and causes micelle-to-fiber transition and gelation. Remarkably, the two regioisomers assemble in helical fibers with opposite chirality and the moduli of the generated gels depend on the used isomer.


---


*This chapter is based on the publication:*

**Brito, Alexandra;** Reis, Rui L.; Ulijn, Rein V.; Pires, Ricardo A.; Pashkuleva, Iva: **"**Helical nanofibers with opposite handedness generated by biocatalytic self-assembly of aromatic carbohydrate amphiphiles", *submitted.*

## III.1. INTRODUCTION

Biocatalytic self-assembly (BSA) is a dynamic process, in which precursors of self-assembling amphiphiles serve as enzyme substrates so that the enzymatic reaction can be used to control the kinetics of the assembly process.[1, 2] The concept was introduced by Xu *et al.* in the early 2000's[1] and since then it has been intensively exploited in the development of supramolecular materials[3, 4], responsive drug delivery systems[5-7], cancer therapeutics[8-11], among others. Compared to conventional self-assembly, which is typically triggered by bulk changes in environmental conditions (T, pH, ionic strength, solvent polarity), BSA has two main advantages: (i) selectivity imposed by the involvement of the enzymatic transformation and (ii) ability to tightly control kinetics and consequent structure growth in space and time. The versatility of BSA is demonstrated by the possibility to access a variety of architectures that represent equilibrium[3] or kinetic products[12], as well as transient supramolecular structures[13]. Phosphatases[11, 14] and metalloproteinases (MMPs)[5, 6, 15] are the most frequently used BSA triggers in biomedical contexts because of their relevance to different pathologies. Different modes of action have been demonstrated, including supramolecular disassembly[5], assembly[1, 14] or reorganization[2, 15] due to enzyme-catalysed changes in amphiphilicity through peptide or phosphate ester hydrolysis. As is relevant to any enzymatic process, BSA kinetics and conversion yields are dependent on the concentration of both enzyme and substrate.[1, 8, 14] A number of the substrate's structural features have been manipulated to control the enzymatic transformation, including the number of enzyme sensitive moieties in the precursor, to control the kinetics[8]; chemical nature of the precursor, typically this would be the amino acid sequence[4, 15] which dictates the self-assembly propensity of the reaction product; and chirality of the building blocks [16-18], which impacts kinetics and supramolecular chirality of the structures formed.

Previously, we have introduced a phosphorylated carbohydrate amphiphile as a substrate for BSA and showed that alkaline phosphatase (ALP) can trigger the formation of supramolecular fibers and hydrogels through the formation of intermolecular CH-$\pi$ stacking.[14] Carbohydrates provide a rich library of water soluble, chiral building blocks: a simple monosaccharide has five chiral centers in its cyclic form and five carbons at which the enzyme sensitive moiety can be introduced. We hypothesized that such structural wealth can be exploited under BSA conditions and will have great impact on the kinetics of enzyme transformation of the carbohydrate substrate and the subsequent self-assembly. Such systems would extend the possibility to tailor the

properties of supramolecular biomaterials beyond amino acids sequence and stereochemistry - using carbohydrate isomers we can diversify the materials at functional and structural level, inspired by biological control of structure and function through glycosylation.

Herein, we compared two carbohydrate regioisomers (Fig. III.1a), *i.e.* Fmoc-glucosamine-1-phosphate (FGlc1P, **3d**) and Fmoc-glucosamine-6-phosphate (FGlc6P, **3c**), as substrates for BSA triggered by ALP. We also used the non-phosphorylated carbohydrate amphiphile, Fmoc-glucosamine (FGlc, **3a**), for comparative purposes and assembled it by sequential heating and cooling as previously described.[19]

## III.2. MATERIALS AND METHODS

### III.2.1. Biocatalytic self-assembly

The substrate (FGlc1P or FGlc6P) was dissolved in PBS (pH 7.4). We have tested 3 different concentrations, namely 10, 15 and 20 mM. Different amount of alkaline phosphatase (ALP) was added to the solution of the substrate and kept at 25°C, for 48 h. Aliquots of these solutions were taken at predetermined time points and analyzed by LC-MS. For comparative purposes, we also prepared gels of FGlc by heating-cooling using the same concentrations, i.e. 10, 15 and 20 mM. FGlc was dissolved in PBS upon heating (90 °C) until full solubilization. Gels were obtained upon cooling of these solution to room temperature. The formation of the gels was confirmed by the inverted vial test. The reported characterization data were obtained after 48 hrs unless otherwise mentioned.

### III.2.2. Circular dichroism (CD)

About 20 µl of Fmoc-glucosamine gels (in the case of FGlc1P 20 µl of the solution was pipetted) was mount to a 0.1 mm demountable quartz cuvette and spectra were measured on a JASCO J-1500 spectrometer with 2s integration, a step size of 1 nm and a single acquisition with a slit width of 1 nm. For all measurements the temperature was maintained at 20 °C.

### III.2.3. Rheometry

An Anton Paar MCR 302 rheometer with temperature controller set at 25 °C and a 10 mm vane geometry was used to measure the mechanical properties of the obtained gels. Gels were prepared in a 10 mm mold (48 hrs of assembly) and transferred onto the stage for measurements. Initially, amplitude sweeps at a constant frequency of 0.1 Hz from sheer strain 0.01-10 % were performed to ensure that the measurements are in viscoelastic regime. To determine G' and G", frequency sweep was done at constant strain (0.01%) in the frequency range of 0.1-10 Hz. Three replicates were done from each sample.

### III.2.4. Scanning electron microscopy (SEM)

A ~ 20 μL drop of the self-assembled systems was deposit onto a silicon wafer and let dry at room temperature. The dry samples were coated by a platinum using a Leica ACE600 sputter coater. The coated samples were imaged using a FEI Helios Nanolab660 Dualbeam FIB-SEM. Images were recorded at 5kV.

### III.2.5. Atomic Force Microscopy (AFM)

Fresh cleaved mica sheet was functionalized with 200 μL (3-Aminopropyl)triethoxysilane (APTES) for 30 min at room temperature. The functionalized mica was rinsed with deionized water and dry under nitrogen flow. A small drop of the assembled Fmoc derivatives was added, dried at room temperature and characterized with a JPK Nanowizard 3 in air at room temperature. The mechanical properties of the nanofibers were assessed under JPK quantitative imaging mode using RTESPA-525 probes (k~200 N/m, Bruker, Germany) calibrated by the contact free method. The obtained approaching force curves were fitted using Hertz model to attain the elastic modulus (E). The reported E is averaged over 40 measurements.

### III.2.6. Fluorescence spectroscopy

For gel spectra recording a 1 mm cuvette was used and approximately 20 μl of gel was added. Fluorescence emission spectra were recorded within the range 300-600 nm using a Jasco FP-6500

spectrofluorimeter. An excitation wavelength of 295 nm and a slit width of 3 nm was used. The data are presented as an average of three measurements.

## III.3. RESULTS AND DISCUSSION

The regioisomers were chosen because of the important biological functions of glucose-1-phosphate (Glc1P) and glucose-6-phosphate (Glc6P) in the cellular metabolism and glycan synthesis.

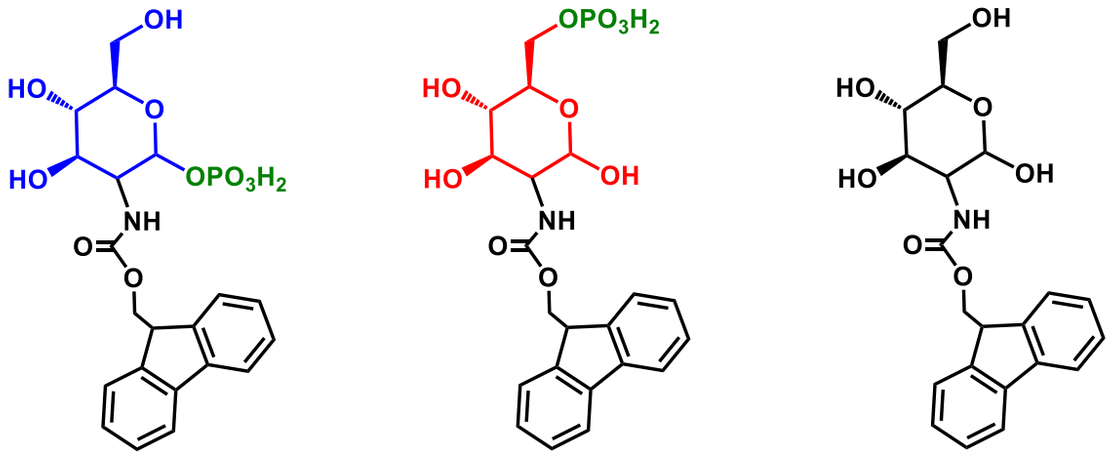


**Figure III.1.Chemical structure of the aromatic carbohydrate amphiphiles used in this study: (3d) Fmoc-D-glucosamine-1-phosphate (FGlc1P); (3c) Fmoc-D-glucosamine-6-phosphate (FGlc6P); and the control, (3a) Fmoc-D-glucosamine (FGlc).**

We assumed that the phosphate position will affect the dephosphorylation kinetics (Fig. III.2a) and thus modulate the nucleation and growth of supramolecular structures, which may give rise to different morphologies. The interactions of FGlc1P and FGlc6P with ALP were first assessed *in silico* by a computational molecular-docking process using the web-based SwissDock program using blind docking (Table III.1).[20-23] The obtained values for Gibbs free energy of the enzyme-substrate complexes ($\Delta G_{ES}$) were different for the two regioisomers: ~1.2-fold lower $\Delta G_{ES}$ was calculated for FGlc1P when compared to FGlc6P, indicating a higher stability of ALP/FGlc1P complex. Van der Waals interactions ($\Delta G_{vdw}$) have the greatest contribution (~1.8-fold higher) suggesting an involvement of additional π-π and CH-π interactions. The stability of the enzyme-substrate complex influences the reaction rate: weak binding of substrates to enzymes can be

advantageous, while excessive complex stability is considered a thermodynamic pit.[24] The computational results thus indicate faster conversion rate for FGlc6P.

**Table III.1. *In silico* predictions for the Gibbs free energy corresponding to the formation of enzyme-substrate complex ($\Delta G_{ES}$), *i.e.* the complex between ALP (E) and FGlc1P or FGlc6P. The results were obtained from top score models generated with SwissDock.**

| Substrate | $\Delta G_{ES}$ (kcal/mol) | $\Delta G_{vdw}$ (kcal/mol) | $\Delta G_{ligsolvnonpol}$ (kcal/mol) | $\Delta G_{ligsolvpol}$ (kcal/mol) |
|---|---|---|---|---|
| FGlc1P | -9.22 | -80.98 | 10.84 | -26.55 |
| FGlc6P | -7.55 | -44.20 | 10.82 | -25.22 |

$\Delta G_{vdw}$: Energy of Van der Waals interactions; $\Delta G_{ligsolvnonpol}$: Solvation energy due to non-polar interactions; $\Delta G_{ligsolvpol}$: Solvation energy due to polar interactions.

The conversion of the substrates FGlc1P and FGlc6P to the self-assembling FGlc was studied over time by LC-MS (Fig. III.2b). We confirmed the faster conversion rate of FGlc6P when compared to FGlc1P regardless of the amount of ALP used. When 50U of ALP (U is defined as the amount of ALP needed to dephosphorylate 1 μmol of 4-nitrophenyl phosphate per min at pH 9.8 at 37 °C) was used for dephosphorylation of 20 mM amphiphile, we observed similar rates for short reaction times (up to 3 h) but after this initial period the conversion of FGlc6P was on average 1.2-fold higher when compared to FGlc1P isomer. After 24 hrs, we achieved 94% conversion of FGlc6P, while the dephosphorylation of FGlc1P was 76%. This experimental result agrees with the docking data and presents direct evidence that the position of the phosphate group in the glucose ring modulates ALP kinetics.

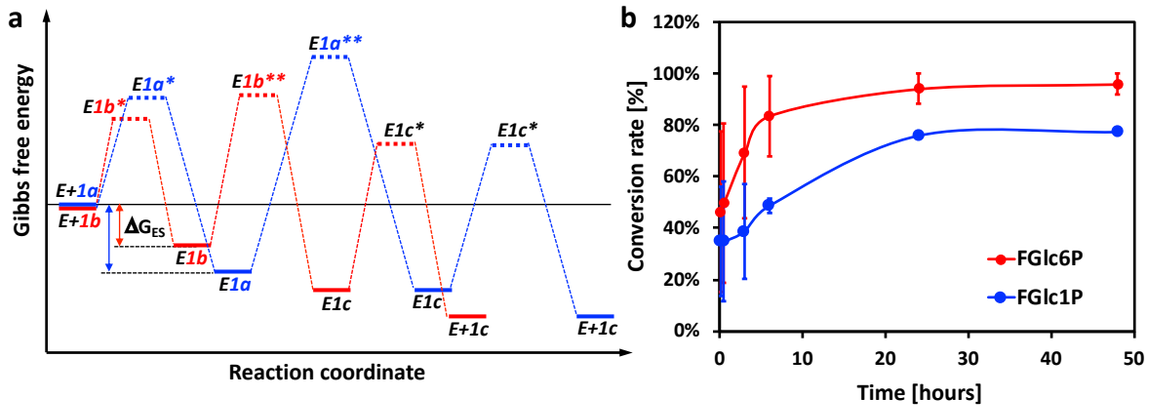


**Figure III.2. (a) Schematic presentation of the Gibbs free energy profile for the enzymatic (E) dephosphorylation of FGlc1P (3d) and FGlc6P (3c) to the product FGlc (3a) and (b) experimental data for the conversion rate obtained by LC-MS monitoring of dephosphorylation reaction of 20 mM 3c or 3d by 50U ALP.**

The influence of the phosphate position and the conversion rate on the self-assembly was also studied. FGlc1P and FGlc6P formed micellar aggregates with size of about 100 nm (Fig. III.3a) that upon excitation show a fluorenyl emission peak around 300 nm (Fig. III.3c). Upon addition of ALP, the intensity of this signal decreased and a red shift to approximately 320 nm was observed, indicating a supramolecular transformation. Additionally, a band at about 450 nm appeared showing the formation of extended long-range stacking interactions between the Fmoc moieties. Indeed, microscopy images showed formation of fibrillar structures (Fig. 3b). The morphology and the mechanical properties of these fibers differ from the ones obtained by the heating/cooling procedure: the enzyme triggered self-assembly resulted in formation of helical and weaker fibers as observed by scanning electron microscopy (SEM, Fig. III.3b1, b2) and atomic force microscopy (AFM, Fig. III.3e), while no helicity was observed for the fibers that were generated directly from FGlc (Fig. III.3b3). Moreover, the handedness of the fibers assembled upon dephosphorylation depended on the used regioisomer: FGlc1P forms left-handed (*M*) helixes, while FGlc6P assembles into right-handed (*P*) helical structure although the self-assembling block FGlc is the same in all cases.

Notably, the pitch of the obtained fibers is equal for both substrates (101 ± 10 nm for fibers obtained from FGlc1P and 104 ± 15 nm for the ones generated from FGlc6P) and equal to the size of the micelles assembled from the FGlc1P and FGlc6P. This result suggests that fiber formation occurs *via* micelle fusion[25] rather than by micelle disassembly followed by re-assembly

as previously described for short peptides under MMP triggered BSA[6]. We propose that phosphate groups stabilize the micelles by electrostatic repulsion and impair their spontaneous fusion (Fig. III.3f).[26] Dephosphorylation by ALP has two effects: it removes the surface charge stabilizing the micelles and decreases the solubility of the amphiphiles in water. Both effects cause an increase of the surface tension and thus, destabilize the micelles in water and trigger their fusion to diminish the free energy (Fig. III.2f). A similar mechanism was reported recently for polymerization induced self-assembly (PISA) of amphiphilic block copolymers in water: amino-functionalized amphiphiles assembled in polymersomes, while fusion and continuous unidirectional growth of tubesomes was observed for uncharged copolymers.[25]

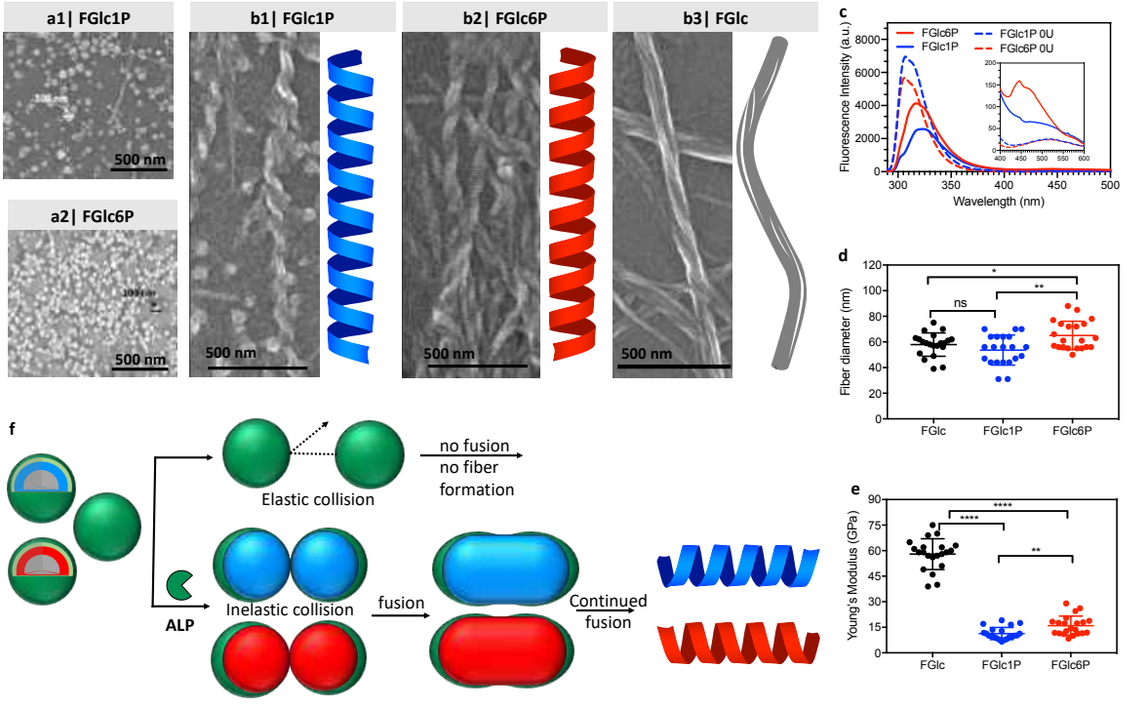


**Figure III.3. (a-b) Scanning electron microscopy images, (c-e) spectroscopic characterization and (f) schematic presentation showing changes of the assemblies upon dephosphorylation by alkaline phosphatase (ALP). Images of (a) micelles assembled by (a1) FGlc1P and (a2) FGlc6P; (b) fibers generated upon the addition of alkaline phosphatase (ALP, 50 U) to (b1) FGlc1P and (b2) FGlc6P or (b3) by heating/cooling of FGlc. (c) Fluorescence emission spectra (excitation at 280 nm) of FGlc6P and FGlc1P exposed to ALP (50 U) action. (d) Fibers' diameter and (e) mechanical properties determined by atomic force spectroscopy. In all cases the amphiphiles concentration was 20 mM. (f)**

**Proposed mechanism of fibers formation *via* micelles fusion: ALP action decreases the surface charge stabilizing the micelles and trigger their fusion to diminish the free energy.**

In PISA, the self-assembling blocks are generated *in situ* by polymerization and different kinetically trapped assemblies can be generated at different polymerization rates.[27] Similarly, in BSA different rate of the enzymatic transformation can induce formation of various structures corresponding to distinct local thermodynamic minima.[12] Herein, we demonstrate that fibers generated from FGlc (unphosphorylated amphiphiles) by heating/cooling process, differ from the ones obtained by BSA and although these structures are assembled from the same building block they correspond to different thermodynamic minima.

On the other hand, the fibers that were generated by BSA are supramolecular enantiomers, *i.e.* their thermodynamic stability is identical but the pathways for their assembly are energetically differentiated by using different substrate as starting points for the biocatalytic transformation (Fig. III.2a). C1 in glucose is an anomeric center and dephosphorylation at C1 can lead to formation of two anomers ($\alpha$ and $\beta$) that can further affect the assembly process. A previous study has shown that addition of monosaccharides to unfolded poly(m-ethynylpyridine) drives formation of folded structures *via* H-bonding and these structural changes depends on the used anomer.[28] Indeed, CD spectra showed different chirality for dephosphorylated FGlc1P and FGlc6P (Fig. III.4d) suggesting that the inverted handedness of BSA assembled fibers is induced by anomerization of FGlc1P upon dephosphorylation. A possible explanation for this anomerization can be the steric hindrance induced by the bulky Fmoc moiety that is in close proximity to the phosphate in FGlc1P.

The conversion of the substrates FGlc1P and FGlc6P to FGlc by ALP was accompanied by an increment of the solutions viscosity over the time, ultimately leading to formation of a gel (confirmed by the tube inversion test, Fig. III.4a). As expected, these gels were formed by entangled nanofibers (Fig. III.4b) and their properties were greatly affected by the used amphiphile and the assembly conditions (Fig. III.4c-e). All gels exhibited a viscoelastic response when an oscillatory shear was applied, with G' exceeding G'' by at least one order of magnitude and this behaviour is stable over the whole range of the tested frequencies. Gels formed by heating/cooling had the highest stiffness followed by the BSA generated gels obtained from FGlc6P that had 4-fold higher storage modulus when compared to the gels generated from FGlc1P. These results agree with previous studies showing that thermal treatment affects the balance between H-

bonding and aromatic stacking interactions that underpin the self-assembly and the gelation processes: temperatures above 333 K (herein we have used 363 K) are associated with the formation of more extensive π-stacking, less ordered H-bonding and result in stiffer gels.[29] The difference between FGlc6P and FGlc1P can be explained by their involvement in different H-bonding (*e.g.* OH group at the anomeric C1) due to the anomerization of FGlc1P upon dephosphorylation. As expected, the magnitude of this difference is smaller when compared to the gels generated by heating/cooling.

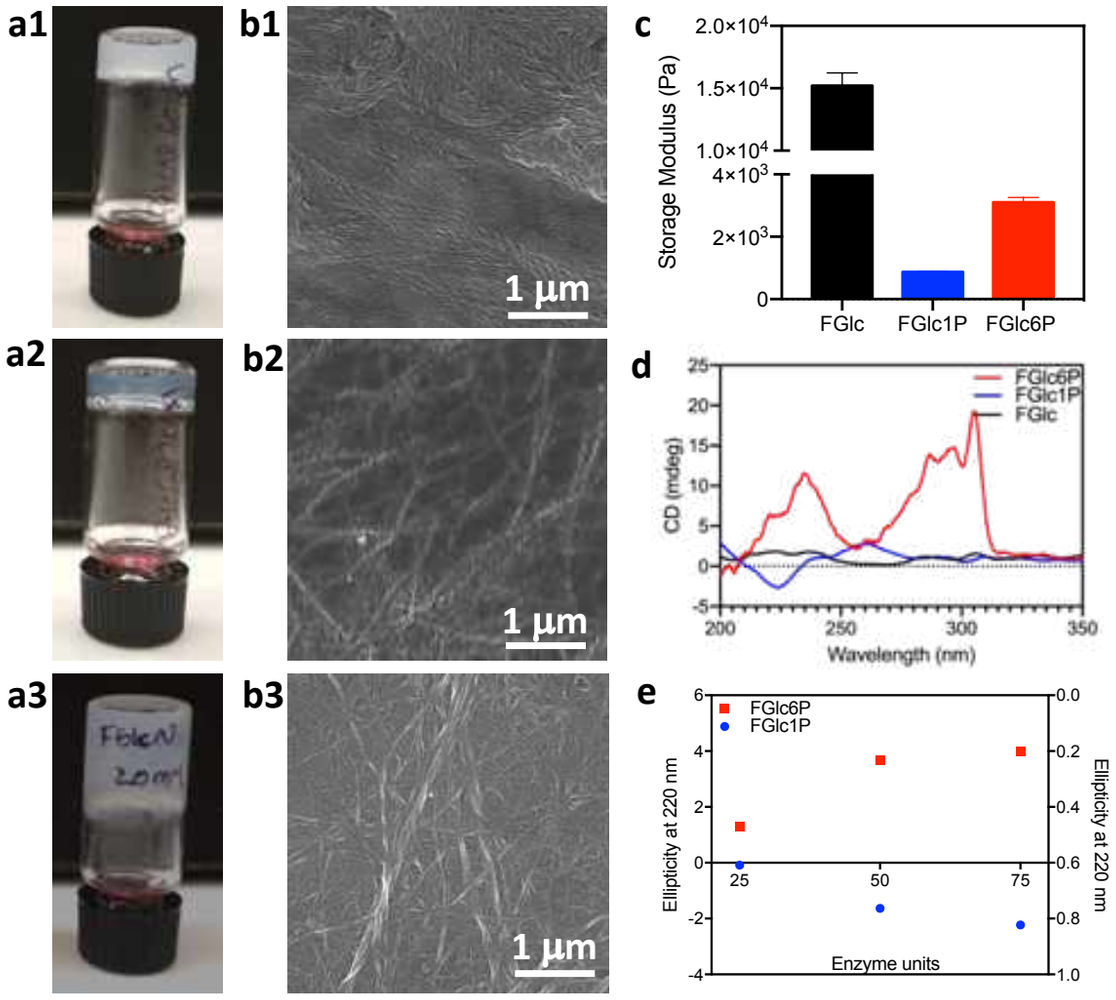


**Figure III.4. Characterization of the obtained hydrogels: (a) Macroscopic appearance of the gels obtained by BSA of (a1) FGlc1P, (a2) FGlc6P and (a3) heating/cooling of FGlc; (b) scanning electron microscopy images showing the structure of the gels formed by entangled nanofibers with different morphology for (b1) FGlc1P, (b2) FGlc6P and (b3) FGlc; (c) Storage modulus of the obtained gels; (d) circular dichroism spectra of the gels generated by BSA and heating/cooling**

**process; and (e) ellipticity change as a function of the amount of used enzyme for FGlc1P and FGlc6P transformation. The gels were generated from 20 mM FGlcX and 50 U of ALP, except for (e), where the amount of ALP was varied.**

Circular dichroism (CD) spectra of the phosphatase substrates FGlc1P and FGlc6P did not have any signal[26] but CD spectra of the BSA generated gels had signals at 220, 260 and 303 nm that are correlated with π-π* and n-π* transitions of the Fmoc chromophore (Fig. III.3d). The ellipticity increased with the concentration of ALP (Fig. III.3e) suggesting that the supramolecular order can be modulated by the enzyme concentration as previously shown.[12] The CD signal was negative when FGlc1P was used as a substrate and positive for FGlc6P substrate (Fig. 3e). In general, the gelator translates its chirality to the generated supramolecular structure.[30] However, presence of additives (e.g. proteins[31], hofmeister salts[32]), temperature[29] and other factors (pH, solvent)[30] that can affect the non-covalent interactions, such as H-bonding and π-stacking, can change the helicity as shown by CD analysis. Previously, we have shown that in BSA, the enzyme concentrations can be used as a mean to modulate the chirality: high enzyme concentrations lead to enhanced chirality due to restricted mobility of catalytic clusters that enforces formation of high-order sturctures.[12] Herein, we demonstrate that the substrate structural feature namely the position of the enzyme sensitive moiety can also affect the chirality of the supramolecular structure.

Our results indicate that in biological systems carbohydrates can be used to code biomolecular information not only in a sequence-dependent manner but also at stereochemical and mechano-transduction fashion: we showed that simple carbohydrate regioisomers are able to generate fibers with opposite chirality and different mechanical properties.

## III.4. SUPPLEMENTARY INFORMATION

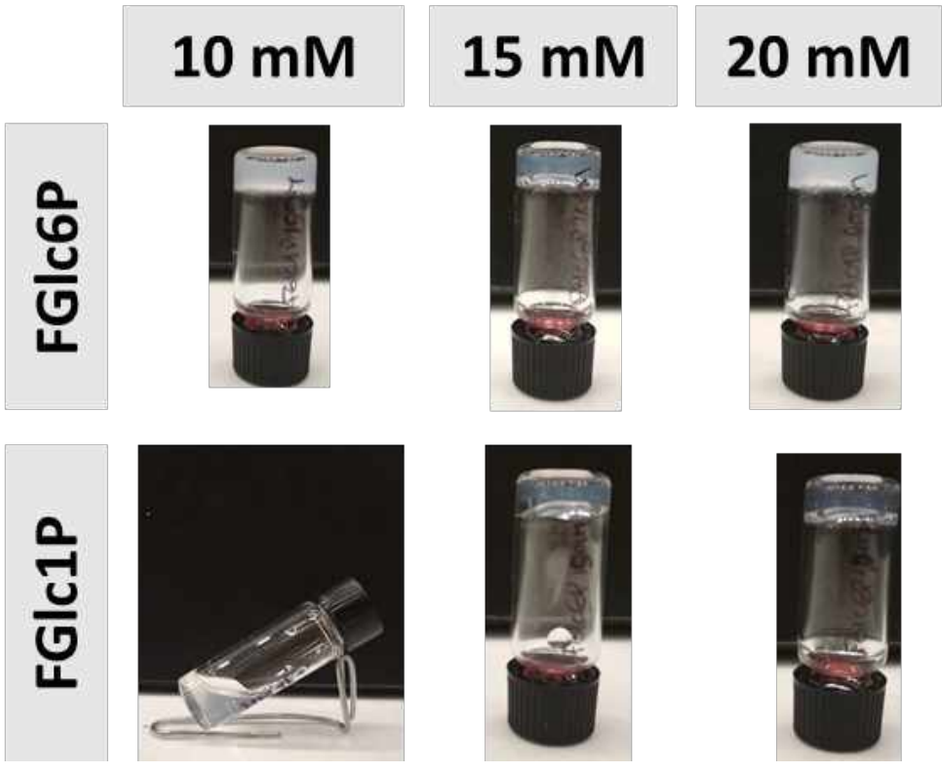


Supplementary Figure III.1. Images showing the inverted vial test for the gels obtained by alkaline phosphatase (50 units) conversion of FGlc1P and FGlc6P to FGlc.

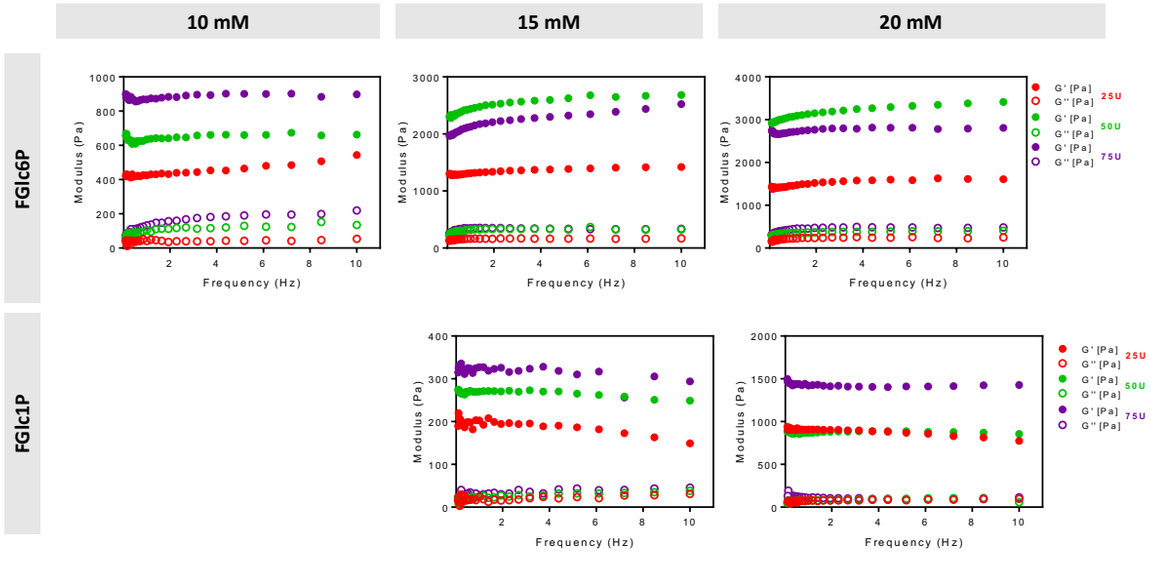


Supplementary Figure III.2. Rheology data illustrating the effect of carbohydrate amphiphiles (Fmoc-Glc6P and Fmoc-Glc1P) and enzyme concentration on gel stiffness.

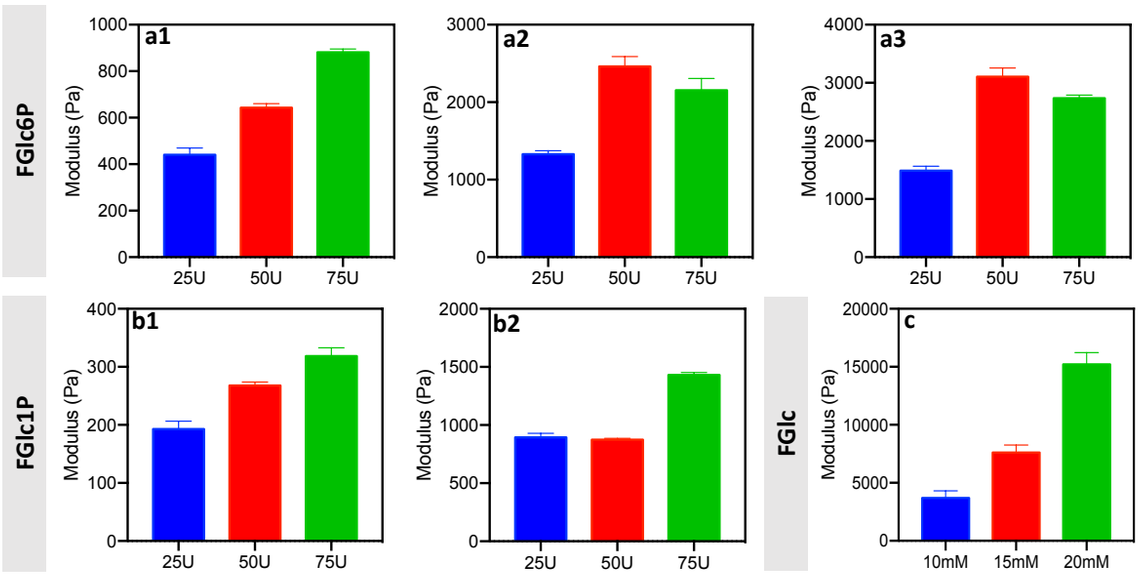


Supplementary Figure III.3. Mechanical properties of the gels obtained from: (a1) FGlc6P 10mM; (a2) FGlc6P 15 mM; (a3) FGlc6P 20 mM; (b1) FGlc1P 15 mM and (b2) FGlc1P 20 mM; (c) FGlc at different concentration. *No sustained gel was obtained from FGlc1P at 10 mM.

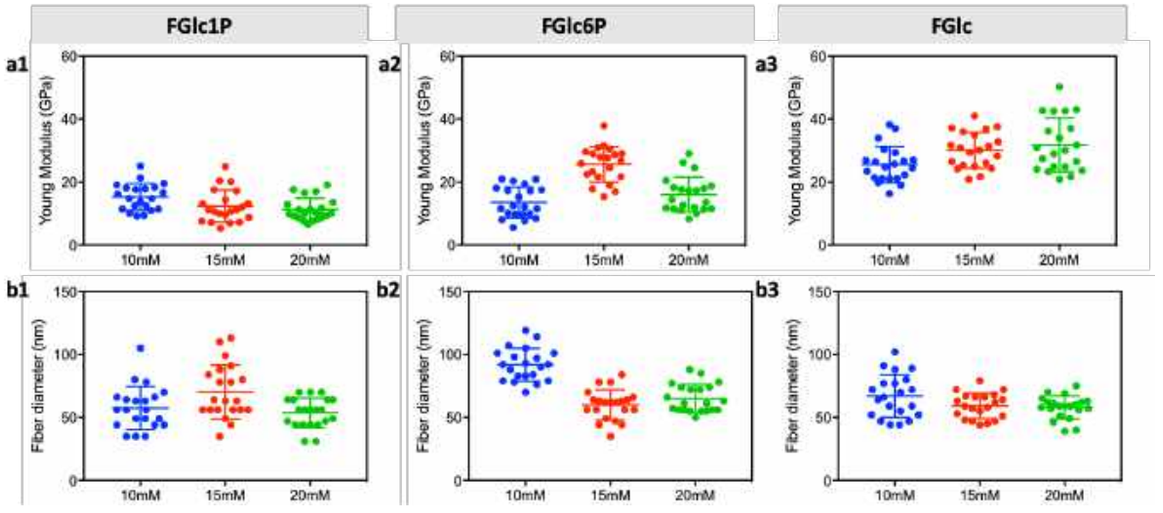


Supplementary Figure III.4. AFM measurements for (a1-a3) Young modulus and (b1-b3) fiber diameter of the single fibers generated by BSA using 50U of alkaline phosphatase and different substrate concentrations.

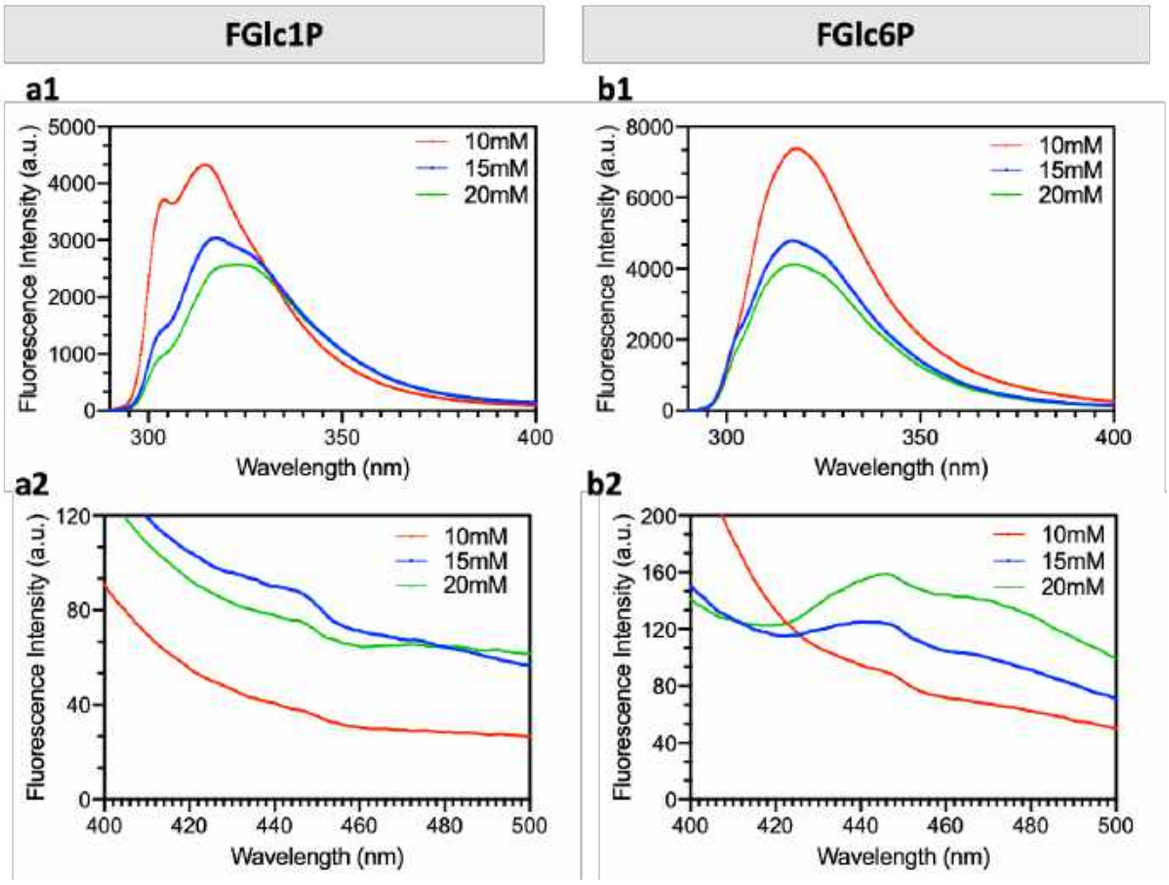


**Supplementary Figure III.5. (a1-a2) Fluorescence emission of FGlc1P (a1-a2) and FGlc6P (b1-b2) from 300-400 nm (a1, b1) and from 400-500 nm (a2, b2). The spectras was recorded for all gels at different concentration with addition of 50 U of ALP.**

## III.5. REFERENCES

1. Z. M. Yang and B. Xu, Chemical Communications, 2004, DOI: 10.1039/b408897b, 2424-2425.

2. J. K. Sahoo, C. G. Pappas, I. R. Sasselli, Y. M. Abul-Haija and R. V. Ulijn, Angew. Chem.-Int. Edit., 2017, 56, 6828-6832.

3. R. J. Williams, A. M. Smith, R. Collins, N. Hodson, A. K. Das and R. V. Ulijn, Nature Nanotechnology, 2009, 4, 19-24.

4. J. Son, D. Kalafatovic, M. Kumar, B. Yoo, M. A. Cornejo, M. Contel and R. V. Ulijn, Acs Nano, 2019, 13, 1555-1562.

5. R. W. Chakroun, A. Sneider, C. F. Anderson, F. Wang, P. H. Wu, D. Wirtz and H. Cui, Angew Chem Int Ed Engl, 2020, DOI: 10.1002/anie.201913087.

6. D. Kalafatovic, M. Nobis, N. Javid, P. Frederix, K. I. Anderson, B. R. Saunders and R. V. Ulijn, Biomaterials Science, 2015, 3, 246-249.

7. J. Gao, W. T. Zheng, D. L. Kong and Z. M. Yang, Soft Matter, 2011, 7, 10443-10448.

8. J. Zhou, X. W. Du and B. Xu, Angew. Chem.-Int. Edit., 2016, 55, 5770-5775.

9. X. W. Du, J. Zhou, J. Q. Wang, R. Zhou and B. Xu, ChemNanoMat, 2017, 3, 17-21.

10. X. W. Du, J. Zhou, H. N. Wang, J. F. Shi, Y. Kuang, W. Zeng, Z. M. Yang and B. Xu, Cell Death Dis., 2017, 8, 11.

11. Z. Q. Q. Feng, X. G. Han, H. M. Wang, T. T. Tang and B. Xu, Chem, 2019, 5, 2442-2449.

12. A. R. Hirst, S. Roy, M. Arora, A. K. Das, N. Hodson, P. Murray, S. Marshall, N. Javid, J. Sefcik, J. Boekhoven, J. H. van Esch, S. Santabarbara, N. T. Hunt and R. V. Ulijn, Nat Chem, 2010, 2, 1089-1094.

13. S. Debnath, S. Roy and R. V. Ulijn, Journal of the American Chemical Society, 2013, 135, 16789-16792.

14. R. A. Pires, Y. M. Abul-Haija, D. S. Costa, R. Novoa-Carballal, R. L. Reis, R. V. Ulijn and I. Pashkuleva, Journal of the American Chemical Society, 2015, 137, 576-579.

15. Y. J. Shi, Y. Hu, G. Ochbaum, R. Lin, R. Bitton, H. G. Cui and H. S. Azevedo, Chemical Communications, 2017, 53, 7037-7040.

16. J. Li, D. Bullara, X. W. Du, H. J. He, S. Sofou, I. G. Kevrekidis, I. R. Epstein and B. Xu, Acs Nano, 2018, 12, 3804-3815.

17. S. Marchesan, C. D. Easton, K. E. Styan, L. J. Waddington, F. Kushkaki, L. Goodall, K. M. McLean, J. S. Forsythe and P. G. Hartley, Nanoscale, 2014, 6, 5172-5180.

18. K. McAulay, B. Dietrich, H. Su, M. T. Scott, S. Rogers, Y. K. Al-Hilaly, H. G. Cui, L. C. Serpell, A. M. Seddon, E. R. Draper and D. J. Adams, Chemical Science, 2019, 10, 7801-7806.

19. L. S. Birchall, S. Roy, V. Jayawarna, M. Hughes, E. Irvine, G. T. Okorogheye, N. Saudi, E. De Santis, T. Tuttle, A. A. Edwards and R. V. Ulijn, Chemical Science, 2011, 2, 1349-1355.

20. A. Grosdidier, V. Zoete and O. Michielin, Proteins-Structure Function and Bioinformatics, 2007, 67, 1010-1025.

21. A. Grosdidier, V. Zoete and O. Michielin, Journal of Computational Chemistry, 2009, 30, 2021-2030.

22. A. Grosdidier, V. Zoete and O. Michielin, Nucleic Acids Research, 2011, 39, W270-W277.

23. A. Grosdidier, V. Zoete and O. Michielin, Journal of Computational Chemistry, 2011, 32, 2149-2159.

24. J. C. Aledo, C. Lobo and A. E. del Valle, Biochem Mol Biol Edu, 2003, 31, 234-236.

25. S. Varlas, R. Keogh, Y. J. Xie, S. L. Horswell, J. C. Foster and R. K. O'Reilly, Journal of the American Chemical Society, 2019, 141, 20234-20248.

26. A. Brito, Y. M. Abul-Haija, D. S. da Costa, R. Novoa-Carballal, R. L. Reis, R. V. Ulijn, R. A. Pires and I. Pashkuleva, Chemical Science, 2019, 10, 2385-2390.

27. J. T. Sun, C. Y. Hong and C. Y. Pan, Soft Matter, 2012, 8, 7753-7767.

28. M. Inouye, M. Waki and H. Abe, Journal of the American Chemical Society, 2004, 126, 2022-2027.

29. S. Debnath, S. Roy, Y. M. Abul-Haija, P. W. J. M. Frederix, S. M. Ramalhete, A. R. Hirst, N. Javid, N. T. Hunt, S. M. Kelly, J. Angulo, Y. Z. Khimyak and R. V. Ulijn, Chem-Eur J, 2019, 25, 7881-7887.

30. D. K. Smith, Chem Soc Rev, 2009, 38, 684-694.

31. N. Javid, S. Roy, M. Zelzer, Z. M. Yang, J. Sefcik and R. V. Ulijn, Biomacromolecules, 2013, 14, 4368-4376.

32. S. Roy, N. Javid, J. Sefcik, P. J. Halling and R. V. Ulijn, Langmuir, 2012, 28, 16664-16670.

# Chapter IV

# Inhibiting cancer metabolism by aromatic carbohydrate amphiphiles that act as antagonists of the glucose transporter GLUT1

## INHIBITING CANCER METABOLISM BY AROMATIC CARBOHYDRATE AMPHIPHILES THAT ACT AS ANTAGONISTS OF THE GLUCOSE TRANSPORTER GLUT1


### Abstract

We report on a series of aromatic N-glucosides that act as GLUT1 antagonists. Among these is a substrate for biocatalytic self-assembly and its product generated *in situ* by cancer cells overexpressing alkaline phosphatase. These compounds inhibit selectively the cancer metabolism *via* two coexistent mechanisms: by initial deprivation of the glucose uptake through competitive binding in the glucose binding pocket of GLUT1 and by formation of a sequestering nanoscale supramolecular network at the cell surface through localized (biocatalytic) self-assembly. We demonstrate that the expression of the cancer associated GLUT1 and alkaline phosphatase are crucial for the effectiveness of this combined approach: cancer cells that overexpress both proteins are prompter to cell death when compared to GLUT1 overexpressing cells. Overall, we showcase that the synergism between physical and biochemical deprivation of cancer metabolism is a powerful approach for development of effective anticancer therapies.


---


*This chapter is based on the publication:*

**Brito, Alexandra;** Pereira, Patricia M. R., Costa, Diana Soares da; Reis, Rui L.; Ulijn, Rein V.; Lewis, Jason S.; Pires, Ricardo A.; Pashkuleva, Iva: "Inhibiting cancer metabolism by aromatic carbohydrate amphiphiles that act as antagonists of the glucose transporter GLUT1", Chemical Science, 2020, **11**, 3737.

## IV.1. INTRODUCTION

Cancer is a major health problem for the modern society, causing 9.6 million deaths worldwide in 2018 and the 5-year prevalence was estimated to be 43.8 million.[1] These statistics shows that the conventional therapies are not sufficiently effective. There are two main reasons that limit the efficacy of existing treatments - the great complexity and consequent limited understanding of cancer cells, and their resistance to the currently used therapeutics.[2-4] Common strategies for targeting the inhibition of specific molecular pathways often have only a temporary success followed by a tumor relapse.[4] The use of a combined approach with several drugs can give rise to higher efficiency and avoidance of chemoresistance but so far, the results did not achieve the required efficacy.[2] Herein, we propose an alternative approach to cancer management that uses a single, multifunctional but yet specific molecule that targets a common cancer hallmark - their accelerated metabolism associated with a higher demand for nutrients and energy – *via* two synergistic pathways, namely by formation of a nanoscale supramolecular network around cancer cells and by the blockage of glucose transportation (Fig. IV.1).[4,5]

The altered cancer metabolism has inspired the development of various therapies.[6-11] Among them, biocatalytic self-assembly (BSA) has emerged as a biochemical approach that makes use of pathologically overexpressed enzymes (typically MMPs or phosphatases) to transform specifically designed precursors into self-assembling molecules and to trigger their assembly *in situ*, *i.e.* in close proximity of cancer cells.[2,6,12-20] Several studies suggested a mechanism that involves an initial internalization of the precursor by the cells, followed by intracellular enzymatic transformation and assembly that leads to cellular death.[6,21,22] Most of the described precursors are based on short self-assembling peptides that are functionalized with enzymatic sensitive moieties.[11,12,17,19,20,22] We recently demonstrated the use of a glucose derivative, N-fluorenylmethyloxycarbonyl-glucosamine-6-phosphate (FGlcP), as an alternative to peptide-based systems in phosphatase-triggered BSA cancer management.[7] For this system, we did not observe any intracellular assembly but formation of a nanoscale supramolecular network around osteosarcoma cells that overexpress membrane-bound alkaline phosphatase (ALP). The system proved to be effective in killing osteocarcoma cells. The amphiphile structure is based on glucose (Glc), which led us to hypothesize that FGlcP might act not only as a BSA precursor but also as an antagonist of the Glc transport, inhibiting aerobic glycolysis. Herein we investigate this hypothesis and demonstrate that a single compound, FGlcP, acts as an efficient cancer antimetabolite by concomitant blocking the glucose transporter 1 (GLUT1) *via* specific interactions with them and

formation of a nanonet serving not only as a physical barrier between the cancer cells and their environment, but also as a reservoir of GLUT inhibitor (Fig. IV.1).

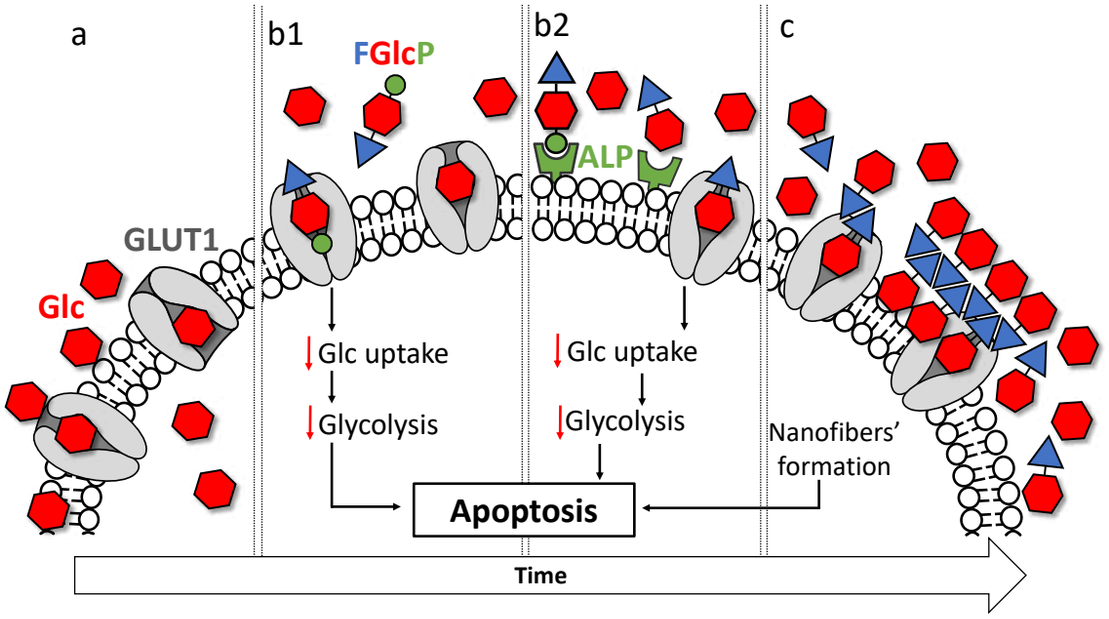


**Figure IV.1. Schematic presentation of the mechanism of action of N-fluorenylmethyloxycarbonyl-glucosamine-6-phosphate (FGlcP): (a) the increased glucose (Glc) metabolism is targeted via concomitant (b) blocking of the overexpressed glucose transporters (GLUT1) with (b1) FGlcP or/and (b2) its dephosphorylated analogue generated *in situ* and (c) formation of nanonet by self-assembly of this analogue.**

## IV.2. MATERIALS AND METHODS

### IV.2.1. Molecular docking

The identification of potential binding sites of **1a, 3a-c** to GLUT1 was performed by an automated molecular-docking procedure using the web-based SwissDock program.[26,43] The GLUT1 structure was uploaded from Protein Data Bank website, 4PYP (Crystal structure of the human glucose transporter GLUT1).[29] The structure of the tested ligands **1a, 3a-c** was uploaded in Mol2 format. The docking was performed using CHARMM Force Field with EADock DSS and default parameters, *i.e.* the whole target protein structure was considered.[26,27] The prediction of the binding modes and subsequent calculation were performed with UCSF Chimera software.[44]

### IV.2.2. Cell culture

SaOs2 human osteosarcoma and MDA-MB-468 mammary gland/breast cancer cell lines were purchased from American Type Culture Collection (ATCC). The cell lines were authenticated at Memorial Sloan-Kettering Cancer Center (MSKCC) integrated genomics operation core using short tandem repeat analysis. The cells used in our experiments were mycoplasma free and had a passage number lower than 15. SaOs2 were cultured at 37 °C in a humidified 95/5% air/$CO_2$ atmosphere using Dulbecco's modified Eagle's medium (DMEM) low glucose (Sigma) supplemented with 10% fetal bovine serum (FBS, Gibco, UK) and 1% antibiotic/antimycotic (Gibco, UK) solution. In the case of MDA-MB-468 cells, we used the same procedure but replaced DMEM low glucose with DMEM high glucose (Sigma).

### IV.2.3. Flow cytometry

SaOs2 and MDA-MB468 were detached with PBS/4mM EDTA. After centrifugation (250 *g*, 5 min) cells were re-suspended in PBS and incubated for 45 min at 4°C with rabbit anti-human GLUT1 antibodies and anti-human $\beta$-actin antibody, following manufacturer-recommended concentrations. Cells were subsequently washed with PBS, centrifuged, and incubated with secondary antibody alexa fluor 488 during 45 min at 4°C. Cells were washed again with PBS, centrifuged and fixated in 1% formalin in PBS. Data acquisition was performed on a FACS Calibur Flow Cytometer (BD Biosciences) and analyzed using the Flowing Software v2.5.1.

### IV.2.4. Supplementation of cell cultures with aromatic N-glucosides (3a-c)

All solutions were prepared just before the use. A concentration of 0.5 mM of the compounds **3b, 3c** was prepared by dissolving them in the corresponding cell culturing media and were supplemented to cell monolayers formed after 24 h of cell seeding. Due to the poor solubility in aqueous media, compound **3a** was dissolved in dimethyl sulfoxide (DMSO) at concentration of 1 M and then was diluted in the respective cell culture media to a final concentration of 0.5 mM. For all the experiments, the concentration of DMSO was kept under 0.005%.

### IV.2.5. Immunofluorescence analysis of glucose transporter 1 (GLUT1)

Anti-Glucose transporter GLUT1 (rabbit polyclonal antibody) was purchased from Abcam®. The cells were treated as described in chapter II of materials and methods and marked for GLUT1 (IgG Alexa-Fluor-488), cytoskeleton organization (Phalloidin–Tetramethylrhodamine (TRITC)) and nuclei (4,6-4,6-diamidino-2-phenyl (DAPI, Sigma). After mounting, the cells were observed under an Imager Z1 fluorescence microscope (Zeiss) and photographed using an Axio Cam MRm (Zeiss).

### IV.2.6. Real-Time Polymerase Chain Reaction

Total RNA extraction was performed using TRIzol ® reagent. Chloroform was added to the cell extract and centrifuged at 12 000 g for 10 min. The aqueous phase was separated from the organic one and the RNA was recovered from it by precipitation with isopropyl alcohol. One μg of total RNA was transcribed to cDNA (cDNA quantification kit). RT-PCR analysis of the samples was performed in triplicate. Oligonucleotide primer pairs were used to detect the presence of mRNAs encoding members of the GLUT family (*SLC2A*) in ATDC5, SaO2 and MDA-MB-468 cell lines by real time RT-PCR. Fragments were analyzed by agarose gel electrophoresis. The oligonucleotides sequences are presented below.

| Oligo name | Sequence (5' → 3') | Tm (°C) | MW (g/mol) |
|---|---|---|---|
| HsGlut1Fwd | TCCACGAGCATCTTGAGA | 56.7 | 5773 |
| HsGlut1Rev | ATACTGGAAGCACATGCCC | 56.7 | 5782 |
| HsGlut2Fwd | CACTGATGCTGCATGTGGC | 58.8 | 5820 |
| HsGlut2Rev | ATGTGAACAGGGTAAAGGCC | 57.3 | 6215 |
| HsGlut3Fwd | TTCAAGAGCCCATCTATGCC | 57.3 | 6037 |
| HsGlut3Rev | GGTCTCAGGGACTTTGAAGA | 57.3 | 6197 |
| HsGlut4Fwd | GGCATGTGTGGCTGTGCCATC | 63.7 | 6469 |
| HsGlut4Rev | GGGTTTCACCTCCTGCTCTAA | 59.8 | 6348 |
| Hs18SFwd | CCCCTCGATGCTCTTAGCTG | 57.3 | 6116 |
| Hs18SRev | CCCATCACGAATGGGGTTCA | 57.3 | 6135 |

### IV.2.7. Glucose uptake assay

NBDG was used as a direct method for visualization and quantification of Glc uptake following previously established protocols.[32,34] Briefly, cells (50 000 cells/$cm^2$) were seeded on tissue culture polystyrene coverslips. 24 h after seeding, the culture medium was removed and the cells were incubated with 0.02 mM NBDG for 30 min and then were washed with Krebs'–Ringer HEPES (KRH) buffer pH 7.4, containing the following (in mM): 136 NaCl, 20 HEPES, 4.7 KCl, 1.25 $MgSO_4$ and 1.25 $CaCl_2$. The samples were then analyzed under laser scanning confocal microscopy (Leica, TCS SP8).

### IV.2.8. Lactate production

Intra- and extracellular lactate production was assessed using the Lactate Assay Kit (Sigma-Aldrich, MAK064). SaOs2 or MDA-MB-468 cells were collected by scraping the wells and centrifuge at 2,000 g for 10 min at 4 °C. The supernatant was collected and used to quantify the extracellular lactate. The cell pellet was homogenized in 0.25 M metaphosphoric acid solution, in ice for 5 min followed by centrifugation (10,000 g for 5 min at 4 °C) and neutralization with 5 M potassium carbonate ($K_2CO_3$) solution. Additional centrifugation (10,000 g for 5 min at 4 °C) was performed to remove insoluble material and the supernatant was used to quantify the intracellular lactate. A master reaction mix containing 20 μL sample solution, 100 μL lactate assay buffer, 20 μL of lactate cofactor mixture and 20 μL fluorometric substrate was added, followed by addition of 40 μL of lactate dehydrogenase and reactions were incubated at RT for 20 min. Sample fluorescence was measured using an excitation wavelength of 530-540 nm and an emission wavelength of 585-595 nm, on a microplate reader.

### IV.2.9. Metabolic activity (MTS assay)

The complete procedure is described in **chapter II** (Materials and Methods). Cells metabolic activity was assessed by MTS (CellTiter 96® AQueous One Solution) following the supplier's instructions. The optical density (OD) was read at 490 nm on a multiwell microplate reader (Synergy HT, BioTek Instruments). The metabolic activity is presented as a ratio between the values obtained for the cells cultured in the presence of 0.5 mM of **3a-c** and the control (values obtained in the absence of the compounds).

### IV.2.10. Viability assay (alamarBlue)

The complete procedure is described in **chapter II** (Materials and Methods). Cells in exponential growth phase were seeded in 96 well plate at a density of 50,000 cells/$cm^2$ and incubated overnight at 37 °C and 5 % carbon dioxide ($CO_2$). The culture medium was then removed and replaced by medium without FBS containing **3a-c** with concentrations ranging from 3 mM – 0.125 mM. The cells were incubated at 37 °C and 5 % $CO_2$ for 24 h. After this time, 10 µL of alamar blue were added to each well. The cells were incubated again for 3 h at 37 °C and 5 % $CO_2$. The fluorescence with an excitation wavelength at 530-560 nm and emission wavelength at 590 nm was then measured in a microplate reader (SYNERGY HT, Manufacturer Biotek). Medium with **3a-c** but without cells was used as a negative control. Untreated cells were used as positive control. The viability and the $IC_{50}$ was calculated according to the manufacturer's instructions.[45]

### IV.2.11. Proliferation assay

The complete procedure is described in **chapter II** (Materials and Methods). Quantification of cell proliferation was performed with Quan-iT™ PicoGreen® dsDNA assay kit (Molecular Probes/Invitrogen) after cell lysis following the manufacturer's instructions. The effect of the **3a-c** on cell proliferation was also assessed by the Ki-67 immunohistochemistry (rabbit monoclonal antibody, Abcam). Briefly, cells were fixed in 1% formalin for 3 min, permeabilized with 0.2 % TritonX-100 for 5 min and blocked in 3% bovine serum albumin in PBS at room temperature for 30 min. Ki-67 antibody incubation was performed overnight at 4 °C. Nuclei were counterstained with 1 µg/mL 4,6-diamidino-2-phenyl (DAPI, Sigma) for 30 min. Samples were washed with PBS, mounted with Vectashield® (Vector) in glass slides and observed under a laser scanning confocal microscopy (Leica, TCS SP8).

### IV.2.12. NBDG fluorescence quantification

The pictures were recorded as described in glucose uptake experimental part. The green channel (NBDG) was converted to gray scale, then each image was divided in smaller images to optimize the threshold and separate the green signal from the background. Further, the area occupied by the green signal was then calculated by the Cell Profiler 3.0 Software.[46] For each condition 6 individual images were analyzed

and the total area occupied by the green signal was normalized by the total number of cells, in each picture.

### IV.2.13. Transfection assays

GLUT1 was depleted using a pool of three target-specific 19–25 nt siRNA (Santa Cruz Biotechnology).[47] Cancer cells were transfected upon 60–80% confluence with either SLC2A1-siRNA or scrambled (scr) siRNA (controls). Each transfection was performed for 5 h with 2.4 μM of siRNA in transfection medium (Santa Cruz) containing 0.5 μL/cm$^2$ of transfection reagent (Santa Cruz). After incubation with siRNA, a complete media was added for 24 h in the case of MDA-MB-468 and for 48 h for SaOs2 cultures.

### IV.2.14. Western Blot analysis.

The complete procedure is described in chapter II (Materials and Methods). Briefly, 40 μg of the isolated proteins was loaded per lane on 10% Bis-Tris Protein Gels (Novex), followed by electrophoresis. The gels were further transfer to nitrocellulose membranes (Thermo Fischer Scientific), the membranes were incubated in 5% (m/v) bovine serum albumin in Tris-buffered saline-Tween (TBS-T, Cell Signalling Technology) and probed with rabbit anti-GLUT1 1:1,000 (rabbit polyclonal, Merck-Millipore, Watford, UK) and mouse anti β-actin 1:20,000 (Sigma) antibodies. After washing, the membranes were incubated with IRDye®800CW anti-Rabbit or anti-Mouse IgG 1:15,000 (LI-COR Biosciences) and imaged on the Odyssey Infrared Imaging System (LI-COR Biosciences) followed by densitometric analysis with ImageJ software.

### IV.2.15. Biotin pull down of cell-surface proteins

Cells were washed twice with ice-cold PBS buffer containing 0.5 mM $MgCl_2$ and 1 mM $CaCl_2$. The cell monolayers were then incubated with 0.5 mg/mL of EZ-LINK Sulfo-Biotin (Thermo Fisher Scientific) for 30 min at 4 °C with gentle rotation. The reaction was stopped by washing twice with 100 mM glycine (Thermo Fisher Scientific) in PBS containing 0.5 mM magnesium chloride ($MgCl_2$) and 1 mM calcium chloride ($CaCl_2$). Cells were scrapped in RIPA buffer, lysates were centrifuged at 16,000 g for 10 min at 4 °C, and supernatants were collected and assayed for protein concentration using the Pierce BCA Protein Assay Kit. A volume of 500 μL of RIPA buffer containing an equal amount of proteins was incubated with NeutrAvidin Agarose Resins (Thermo Fisher Scientific) for 2 h at 4 °C with gentle rotation

and washed three times with RIPA buffer before suspension in Laemmli buffer. The total amount of the cell-surface protein content was loaded in the 4-12% Bis-Tris Protein Gels (Novex) as described in the previous sections. In the case of the total cell lysate, 40 μg were loaded and normalization was performed by analyzing the β-actin expression.

### IV.2.16. MDA-MB-468 tumor xenografts

All animals used in this work were treated according to the guidelines approved by the Research Animal Resource Center and Institutional Animal Care and Use Committee at Memorial Sloan Kettering Cancer Center, NY. The author PMRP has a Category C accreditation for animal research given from Federation of European Laboratory Animal Science (FELASA). We adhere to the animal research: reporting of *in vivo* experiments (ARRIVE) guidelines and to the guidelines for the welfare and use of animals in cancer research. Eight- to 10-weeks-old nu/nu female mice (Charles River Laboratories) were injected subcutaneously with 1 million of MDA-MB-468 cells, in a 150 μL cell suspension of a 1:1 (v/v) mixture of medium with reconstituted basement membrane (BD Matrigel, BD Biosciences). The tumor volume ($V/mm^3$) was estimated by external vernier caliper measurements of the longest axis, α/mm, and the axis perpendicular to the longest axis, b/mm. The tumors were assumed to be spheroidal and the volume was calculated in accordance with the equation $V = (4\pi/3) \times (\alpha/2)2 \times (b/2)$.

### IV.2.17. Small-Animal positron emission tomography (PET) Imaging

$^{18}$F-FDG (685 mCi/mmoL) was obtained from the Nuclear Pharmacy at Memorial Sloan Kettering Cancer Center on the morning of injection. **3c** was dissolved at 2 mM concentration in saline solution containing $^{18}$FDG (213 μCi-303 μCi). To improve tumor visualization, the mice were kept fasting overnight.[48] Animals were randomly divided into two groups (n= 3 mice per group): I) NC group, tail vein co-injection of saline plus $^{18}$F-FDG (200 – 205 μCi) and II) Block group, tail vein co-injection of **3c** (10 mg/kg) plus $^{18}$F-FDG (200 – 205 μCi). At 30 min post injection, mice were anesthetized with 1.5%–2% isoflurane (Baxter Healthcare) in an oxygen gas mixture 10 min before recording PET images. The dosage (200 – 205 μCi) and the time point (30 min) for $^{18}$F-FDG injection were determined according to a previous report and our preliminary studies.[49] All PET images were obtained on an Inveon PET/CT scanner (Siemens) and visualized using the AMIDE 1.0.4 software (http://amide.sourceforge.net).

### IV.2.18. Statistical analysis

Data are expressed as mean ± standard deviation. Data-set was first checked for a normal distribution using the Shapiro-Wilk normality test. Differences were analyzed by the Student t-test in the case of data with a normal distribution or by Mann-Whitney test for the sets that did not pass the normality test.

## IV.3. RESULTS

### IV.3.1. Molecular design and synthesis of aromatic N-glucosides

We designed and synthesized three derivatives (Fig. IV.2) of Glc (**1a**) aiming to establish reliable controls and to investigate the influence of different functional components (aromatic, glucose, charged groups) in the interactions with GLUT1. FGlcP (**3c**) is a BSA precursor that is transformed into the self-assembling molecule N-fluorenylmethyloxycarbonyl-glucosamine (FGlc, **3a**) upon phosphatase action (Fig. IV.1b2).[7] FGlc does not contain a charged group and thus, it has reduced solubility in aqueous media. Previously, we have shown that **3a** can self-assemble into nanofibers above a critical concentration that can be achieved upon heating or enzymatic action.[7,23,24] N-fluorenylmethyloxycarbonyl glucosamine-6-sulphate (FGlcS, **3b**) is an analogue of FGlcP, in which the phosphate group is replaced by a negatively charged sulphate. From a mechanistic point of view, the main difference between **3c** and **3b** is that the sulfate derivative is not susceptible to phosphatase transformation and the subsequent self-assembly, *i.e.* we hypothesize that it will act solely as GLUT1 antagonist.[24] All compounds were synthesized using a previously established procedure.[7,23,24]

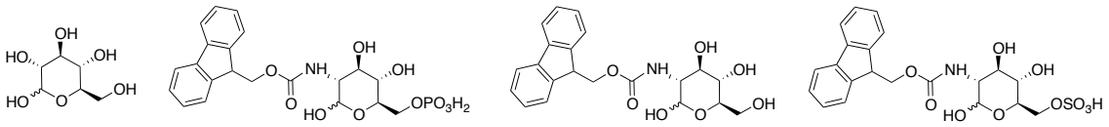

1a | Glc. 3c | FGlcP 3b | FGlc 3a | FGlcS

**Figure IV.2. Glucose (1a) and aromatic N-glucosides (3a-c) synthesized and used in this study.**

### IV.3.2. *In silico* analysis shows that 1a, 3a-c bind to GLUT1

Overexpression of GLUT1 has been associated with different tumor types.[9,10,25] We evaluated the differential interactions of the compounds **1a, 3a-c** with GLUT1 by a computational molecular-docking process using the web-based SwissDock program (Tables IV.1 and S IV.1).[26,27] The parameters were set for blind docking, *i.e.* we did not define *a priori* any specific region for binding. Docking studies with Glc (**1a**) were also carried out using these parameters to confirm the fidelity of the generated outputs by comparison with published data.[8,28,29] The results demonstrated spontaneous complexation between GLUT1 and all compounds **1a, 3a-c**: Gibbs free energy for all studied systems was negative ($\Delta G<0$) but the absolute values are larger for the amphiphiles **3a-c** when compared to **1a** (Table IV.1), indicating a higher affinity of these derivatives to the transporter. Van der Waals interactions ($\Delta G_{vdw}$) have the greatest contribution to this spontaneous process (InterFull values are the same as $\Delta G_{vdw}$) especially in the case of aromatic N-glucosides (**1a** vs **3a-c**) suggesting involvement of additional π-π and CH-π interactions due to the introduced Fmoc functionality.

**Table IV.1. *In silico* predictions for the binding energies involved in the interactions between GLUT1 and glucose (1a) or its derivatives (1b-d). The results were obtained from top score models generated with SwissDock**

| Comp | ΔG (kcal/mol) | $\Delta G_{vdw}$ (kcal/mol) | $\Delta G_{llgsolvnonpol}$ (kcal/mol) | $\Delta G_{llgsolvpol}$ (kcal/mol) |
|---|---|---|---|---|
| **1a** | -6.77 | -36.32 | 6.48 | -13.50 |
| **3c** | -10.09 | -68.89 | 10.36 | -24.31 |
| **3a** | -8.33 | -44.94 | 9.39 | -16.74 |

| | | | | |
|---|---|---|---|---|
| **3b** | -9.04 | -55.70 | 10.57 | -23.14 |

ΔG: Gibbs energy; $\Delta G_{vdw}$: Energy of Van der Waals interactions; $\Delta G_{ligsolvnonpol}$: Solvation energy due to non-polar interactions; $\Delta G_{ligsolvpol}$: Solvation energy due to polar interactions.

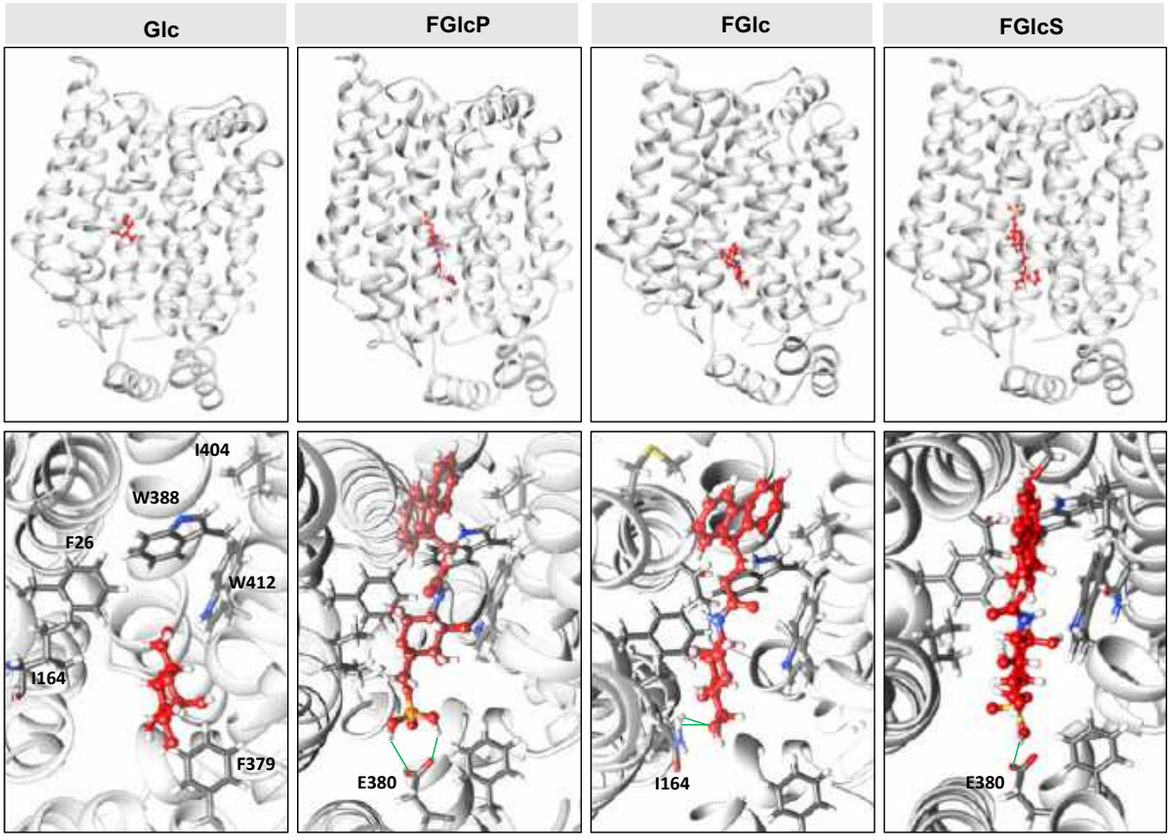


**Figure IV.3.** ***In silico*** **models for the interactions between the synthesized aromatic N-glucosides (3a-c, red) and GLUT1 (grey). The upper row shows top score clusters (with the lowest** ***FullFitness*****) of the full-size complex where the extracellular segment of GLUT1 is oriented upwards and the intracellular one downwards. The bottom row represents the magnification of the glucose-binding pocket in GLUT1. Hydrogen bonds are denotated with green lines.**

Modification with polar groups reduces additionally the $\Delta G_{vdw}$ (**3a** vs **3c** and **3b**) but also the solvation energy ($\Delta G_{ligsolvpol}$) evidencing formation of H-bonding between the GLUT1 and phosphate (**3c**) or sulfate (**3b**) groups. Of note, all compounds **1a, 3a-c** bind to the same pocket *via* interactions with amino acids that are crucial for the Glc complexation with GLUT1 (Fig. IV.3 and Table S IV.1).[8,28,29] Altogether the *in silico* data indicated that the studied compounds can deprive the Glc transport *via* competitive binding to GLUT1 and their antagonist activity follows the order: **3c** > **3b** > **3a**.

### IV.3.3. Selection of cancer cell lines

To test the effect of the aromatic carbohydrate amphiphiles we selected an osteosarcoma cell line (SaOs2) and a mammary gland/breast cancer cell line (MDA-MB-468) based on an initial search in the Cancer Cell Line Encyclopedia (CCLE) for cell lineages with high expression of solute carrier family 2 member 1 gene (*SLC2A1*) encoding GLUT1.[30,31] We confirmed the expression of GLUT1 in SaOs2 and MDA-MB-468 cancer cells at transcriptional and protein levels (Fig. S IV.1). PCR analysis demonstrated that the selected cell lines express the *SLC2A1* gene which codes GLUT1 (Fig. S IV.1a). Immunostaining confirmed the expression of GLUT1 for both cell lines (Fig. S1 IV.b) but flow cytometry analysis demonstrated 2-fold larger population of cells expressing GLUT1 in SaOs2 compared with MDA-MB-468 (Fig. S IV.1c). In addition, SaOs2 overexpress membrane-bound alkaline phosphatase that can trigger BSA on their surface while MDA-MB-468 present 3-fold less expression of this enzyme (Fig. S IV.1d).[7] These differences are important for the experimental design as they might enable us to distinguish the two possible mechanisms by which the amphiphiles can affect the metabolism of the cancer cells – BSA and inhibition of GLUT1 as well as any cooperative effect between these mechanisms.

### IV.3.4. Aromatic N-glucosides decrease Glc uptake by tumor cells

We used 2-(N-(7-nitrobenz-2-oxa-1,3-diazol-4-yl)amino)-2-deoxyglucose (NBDG) for visualization and quantification of the cells' glucose uptake in the presence and absence of compounds **3a-c**.[32,33] Initially, the rate of NBDG uptake was studied for different incubation periods and concentrations using previously established protocols.[32,34] A maximal fluorescence (indicating maximal NBDG uptake) was observed when cells were cultured in medium supplemented with 0.02 mM NBDG for 30 min, which were the conditions used below.

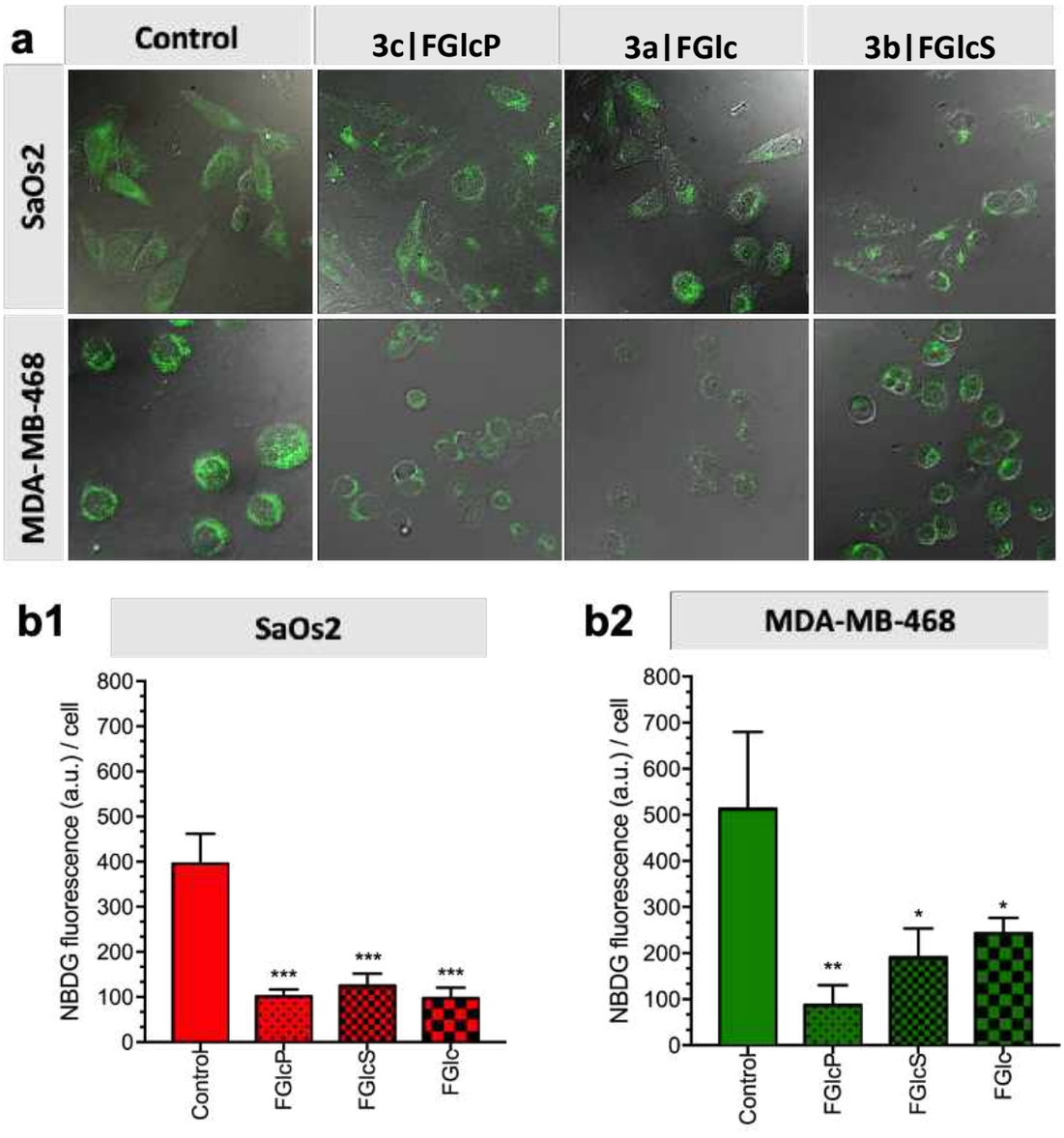


**Figure IV.4. Aromatic N-glucosides 3a-c block glucose uptake by tumor cells: (a) Representative fluorescent confocal scanning microscopy images showing uptake of 2-(N-(7-nitrobenz-2-oxa-1,3-diazol-4-yl)amino)-2-deoxyglucose (NBDG, green) by the SaOs2 and MDA-MB-468 cancer cells in the presence of aromatic N-glucosides 3a-c: cells were incubated with 0.02 mM of NBDG in the presence of 0.5 mM of the aromatic N-glucoside and visualized after 30 min; (b) NBDG uptake calculated from the fluorescence images; Statistics were calculated using the t-test *: $p < 0.05$; **: $p < 0.01$; *** $p < 0.001$.**

We designed a competitive assay in which the selected cell lines were incubated with NBDG in the presence of one of the compounds **3a-c**, *i.e.* conditions at which NBDG will compete with the aromatic N-glucosides for GLUT1. We observed that significantly less NBDG was taken up by both of the tested cell

lines (Fig. IV.4) suggesting that **3a-c** act as GLUT1 antagonists, in agreement with the *in silico* models. To demonstrate the whether this approach is applicable in clinically relevant scenario, we also performed molecular imaging with the clinically established fluorodeoxyglucose ($^{18}$F-FDG) positron emission tomography (PET). Our results showed that PET is suitable for monitoring the effect of the aromatic N-glucosides on the Glc distribution *in vivo* and we observed deprivation of the NBDG uptake at the tumor site upon supplementation with **3c** (Fig. S IV.2).

### IV.3.5. The effect of the aromatic N-glucosides is mediated by GLUT1

GLUT1 expression was quantified by Western blot analysis (Fig. IV.5a). We performed cell surface biotinylation to distinguish GLUT1 expressed at the cell surface and responsible for the Glc uptake from the total GLUT1 expression. The results demonstrated that cancer cells' incubation with aromatic N-glucosides significantly reduces the transporter expression on the cell surface but does not affect the total GLUT1 expression (Fig. IV.5a). These data agree with the formation of a strong complex between the aromatic N-glucosides and GLUT1 with consecutive blockage of the transporter (Fig. IV. 5d). Further confirmation of this mechanism of action was derived by *SLC2A1* knockdown. We used a pool of three target-specific nucleotides 19-25 (nt) small-interfering RNA (siRNA). A maximal *SLC2A1* suppression (> 50%) was observed 48 h after post-transfection for the SaOs2 cells (Fig. IV. 5b) and 24 h for the MDA-MB-468 (Fig. S IV.3). The transfected cells displayed a markedly decreased sensitivity to the compounds 1b-d confirming that their activity is mediated by GLUT1 (Fig. IV.5c).

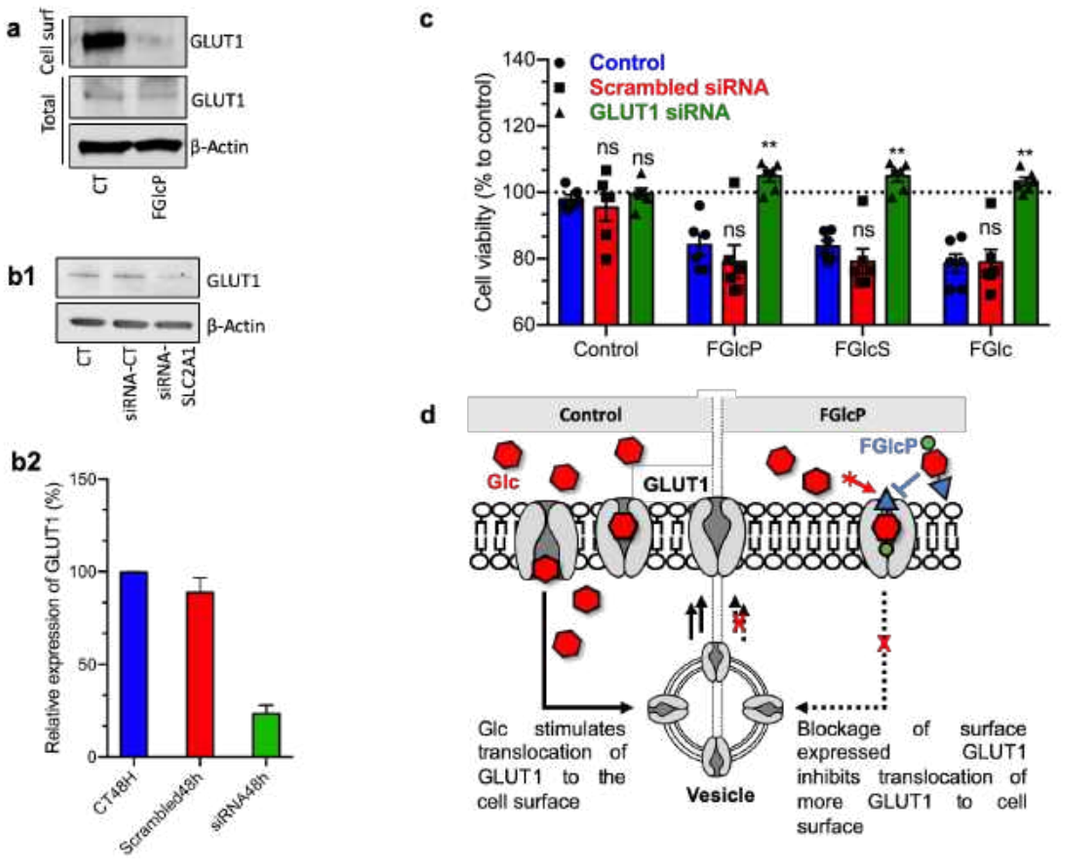


**Figure IV.5. Influence of GLUT1 expression on the effect of aromatic N-glucosides on SaOs2 viability. (a) Representative Western Blot analysis showing changes in GLUT1 expressed on the cell surface (extracts obtained by cell-surface biotinylation) and the total GLUT1 in SaOs2 cells without (CT) and with supplementation of 3c. (b1) Representative Western blot analysis and (b2) the respective densitometric analysis of GLUT1 expression by SaOs2 cells without transfection (CT) and after transfection with scrambled siRNA (siRNA-CT) or specific GLUT1 siRNA (siRNA-SLC2A1); (c) Cell viability of the transfected SaOs2 cells after incubation with 0.5 mM aromatic N-glucosides 3a-c for 1 h (quantification was performed after 24 hrs). (d) Schematic presentation of the GLUT1 transduction role. ns, non-significant; ** $p < 0.05$; *** $p < 0.001$; ns not statistically different. Data for MDA-MB-468 are provided in Fig. S IV.3.**

### IV.3.6. N-glucosides-mediated GLUT1 inhibition leads to cell death *via* an apoptotic mechanism

We observed that cancer cells incubated with the compounds **3a-c** have lower metabolic activity and cell proliferation, leading to an overall decrease in cell survival over time (Figs. IV.6a, S IV.4, S IV.5). Confirmation that this response is due to the GLUT1 inhibition and consecutive deprivation of the Glc uptake was obtained by quantification of the lactate production in the studied cells. Lactate is the last metabolite of glycolysis in cancer cells and indeed, its production was significantly inhibited (> 60%) by treatment with **3c** (Fig. IV.6b).

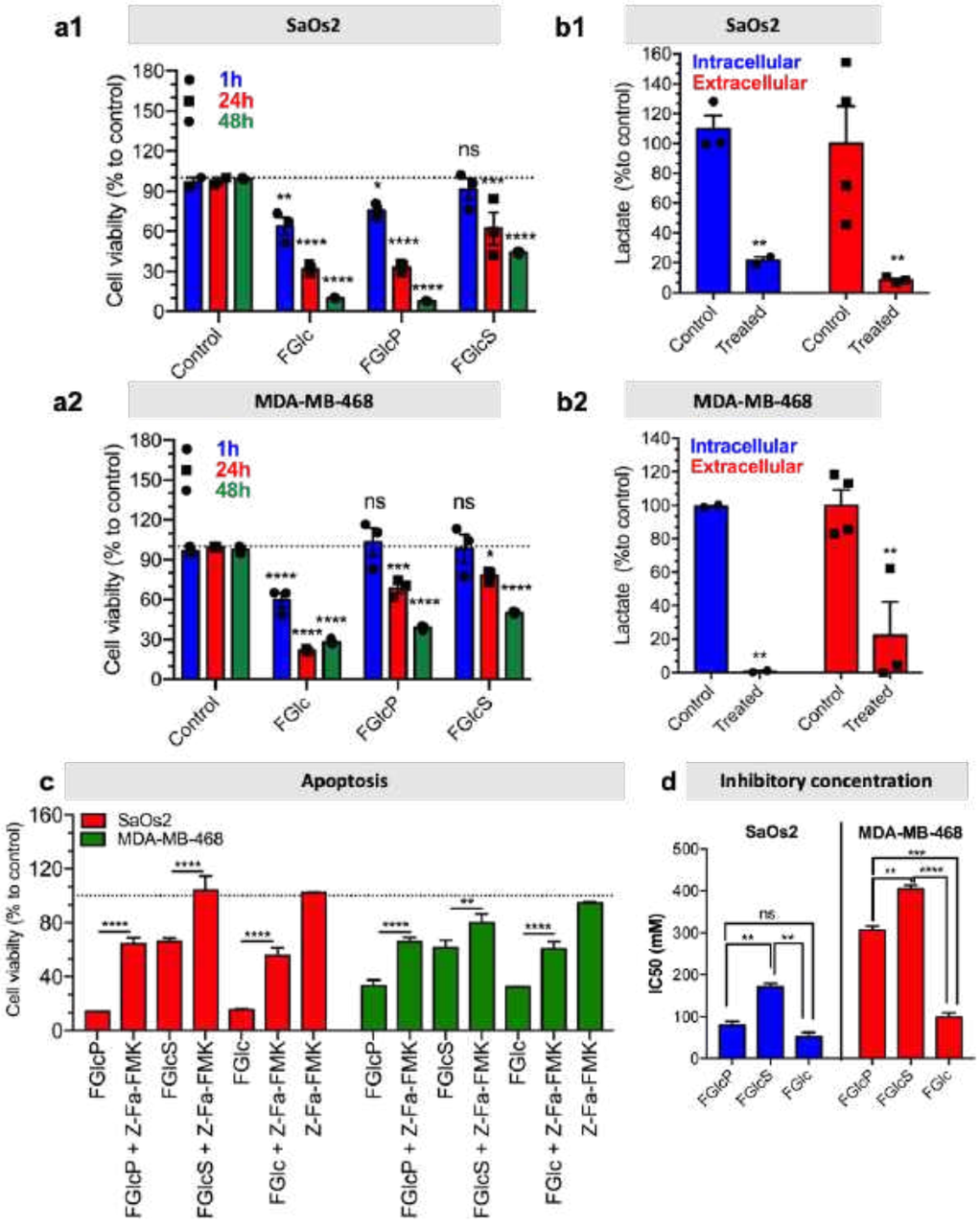


Figure IV.6. Aromatic N-glucosides deprive glycolysis and induce cell death. (a) Viability of SaOs2 (a1) and MDA-MB-468 (a2) cells after different incubation times with 0.5 mM 3a-c; (b) Intra- and extracellular lactate production by SaOs2 (b1) and MDA-MB-468 (b2) cells prior and after treatment with 3c; (c) Effect of the apoptosis inhibitor Z-Fa-FMK on cell viability (24 hrs) in the presence of the compounds 3a-c (0.5 mM); (d) Inhibitory concentrations of the studied N-glucosides determined for SaOs2 and MDA-MB-468 (24 hrs). All results are normalized to the control – cell culture without aromatic N-glucosides. ns: statistically non-significant difference; * $p < 0.05$; ** $p < 0.01$; *** $p < 0.001$; **** $p < 0.0001$.

We also investigated the type of cell death induced by this treatment. We studied the effect of 1b-d in a presence of an apoptosis (z-Fa-FMK) or a necroptosis (Nec-1) inhibitor.[35,36] We observed that Z-Fa-FMK rescues the SaOs2 and MDA-MB-468 cells treated by **3a-c** (Fig. IV.6c) while the addition of Nec-1 has no effect on cell survival (Fig. S IV.6). These results demonstrate that the aromatic N-glucosides activate apoptotic pathways in the cells overexpressing GLUT1. This result was also confirmed by the expression of the apoptosis-associated caspases 8 and 9.[37,38] Caspases are initially produced as inactive monomeric procaspases that require dimerization and often cleavage for activation.[38] We found that the apoptosis pathways are activated by cleavage of procaspase 8 (53 kDa) to shorter motifs (43 kDa, 18 kDa) and procaspase 9 (47 kDa) to oligomers of 25 kDa (Fig. S IV.7).

## IV.4. DISCUSSION

Cancer cells have a high energy demand that is associated with an increased glucose uptake (Warburg effect) and overexpression of glucose transporter proteins (GLUTs). The elevated consumption of Glc assures an immediate production of adenosine triphosphate, but also increases the availability of biosynthetic intermediates that support the highly proliferative nature of cancer cells.[39-41] As a result, cancer cells are very sensitive to Glc deprivation, which can prevent proliferation and induce cell death.[41] Glc is delivered inside cancer cells via the GLUTs, among which GLUT1 is upregulated in most of the solid tumours.[9,10,41] GLUTs are therefore suitable targets for the treatment of different types of cancers. Herein, we designed and synthetized several aromatic N-glucosides **3a-c** and investigated their potential to deprive the glycolysis in cancer cells. The molecular design of **3a-c** combines several functional elements: the aromatic Fmoc-functionality, which provides amphiphilic character and possibility for self-assembly *via* π-π interactions and the Glc portion that can participate in H-bonding and CH-π interactions and attribute GLUT antagonist characteristics are common features for all studied compounds. FGlc (1c) that contains only these two functional moieties has poor solubility in aqueous media (dimethyl sulfoxide at a concentration below 0.005% was used as a co-solvent). Thus, negatively charged polar group were incorporated within the structure of **3a** generating **3c** and **3b** aiming to improve their water solubility. The polar phosphate group of **3c** imparts also enzyme sensitivity: FGlcP (**3c**) is a BSA precursor that generates the self-assembling FGlc (**3a**) upon ALP action (Fig. IV.1b) causing cell death by formation of a pericellular supramolecular nanonet (Fig. IV.1c).[7,17]

*In silico* studies confirmed that all aromatic N-glucosides **3a-c** bind to the Glc pocket. The significant decrease in $\Delta G_{vdw}$ for these compounds when compared to Glc (**1a**) indicate that the aromatic

portion (Fmoc) can interact via CH-π and π-π interactions with the aromatic rings of *e.g.* Trp388 and Phe26 in the glucose-binding pocket causing conformational changes that can disturb the GLUT1 function (the inward opening, Fig. S IV.7).[28,29] On the other hand, the lower ΔG of the compounds **3a-c** indicates that even if the inward opening is not compromised, they might not be released because of the strong bonds formed with the GLUT1.

The effect of the aromatic N-glucosides on Glc transport was studied *in vitro* using two human cancer cell lines. Because SaOs2 cells express on their surface both ALP and GLUT1 proteins, it is challenging to distinguish the effect of BSA, triggered by ALP *versus* the GLUT1 antagonist effect of 1b-c. We and others previously demonstrated that BSA is a time and concentration (both enzyme and precursor) dependent process - short incubation times and low concentrations result in formation of very sparse and thus likely permeable supramolecular nanoscale network.[7,42] Thus, we have selected one additional human cell line, MDA-MB-468 that expresses 3-fold less ALP on their surface (Fig. S IV.1). We have also shortened the experimental time to 30 min and lowered the concentration of the aromatic N-glucosides to 0.5 mM (*versus* 7 hrs and 1 mM when the significant effect of BSA on cell viability was observed[7]) aiming to avoid BSA of **3c** and to determine the GLUT1 antagonist effect of the aromatic N-glucosides. At these conditions (30 min, 0.5 mM concentration of N-glucosides), we observed very similar response by the two cell lines: the compounds **3a-c** inhibit Glc transport (Fig. IV.4). This response was directly related with the GLUT1 expression: viability of SaOs2 and MDA-MB-468 with depleted GLUT1 was not affected by the aromatic N-glucosides. It is expected that the reduction of the Glc uptake will result in the translocation of more GLUT1 to the cell membrane.[41] Surprisingly, we observed exactly the opposite effect (Fig. IV.4a). The decrease of GLUT1 translocation to the membrane is indicative about the mechanism of action: GLUT1 proteins bind the aromatic N-glucosides but do not release them intracellularly, *i.e.* it is in a permanent ON mode and thus does not mediate correctly the need of Glc (Fig. IV.4, S IV.7b). As a result, cells do not respond to the Glc deprivation because they cannot sense it *via* GLUT1. Another indicative result about the mechanism of action is the obtained $IC_{50}$ values (Figs. IV.6d, S IV.4). Of note, these values were determined after 24 h of cells exposition to **3a-c**, *i.e.* conditions at which both mechanisms (BSA and blockage of GLUT1) are at play. Generally, lower $IC_{50}$ values were obtained at all conditions for SaOs2 cell as compared with MDA-MB-468, which can be explained by the higher surface expression of both ALP and GLUT1 by the osteosarcoma cell line when compared with the mammary gland one (Fig S IV.1). The lowest values were determined for the self-assembling FGlc (**3a**) either for SaOs2 or for MDA-MB-468 cells. A similarly low value was obtained for **3c** but only for SaOs2 cells showing that the precursor **3c** is already transformed by the ALP of SaOs2 into **3a** and a nanonet is

generated around SaOs2 cells.[7] Because MDA-MB-468 cells have lower expression of ALP this transformation does not occur and the $IC_{50}$ value of **3c** is 4-fold higher for these cells. **3b** that is solely involved in the GLUT1 blocking because does not self-assemble into nanofibers[24] and is not susceptible to BSA presented the highest $IC_{50}$ values for both cell lines. These results demonstrate that the formation of a nanonet around the cells not only sequesters them, but also add the inhibitory effect of the aromatic N-glucosides most probably by maintaining these compounds at high concentration in the pericellular space, *i.e.* close to GLUT1. In such scenario, the self-assembling **3a** has the greatest effect but its application can be hampered by the poor solubility in aqueous media. The precursor **3c** is an excellent alternative for tumors that overexpress phosphatases on their surface. Besides having the same activity as **3a**, it uses two molecular targets (ALP and GLUT1), thus enhancing its selectivity.

Our study demonstrated that the aromatic N-glucosides **3c** and **3b** have a potent anticancer activity, mainly due to their ability to inhibit Glc transportation and GLUT1 expression *via* two synergistic physical and biochemical mechanisms: formation of a supramolecular net around the cells and blockage of GLUT1.

## IV.5. SUPPLEMENTARY INFORMATION

**Supplementary Table IV.1. Complementary *in silico* data: *FullFitness* values for the top score positions and amino acids involved in the interactions between the compounds 1a, 3a-c and GLUT1 (located at a distance below 3.5 angstroms); in parentheses is the hydrogen bonding distance, when present.**

| Compound | Full fitness (Kcal/mol) | Interacting residues* (distance of hydrogen bonding) |
|---|---|---|
| **1a** | -1154.34 | Gly384 (1.42 Å), Gln282, Thr137, Asn288, TRp388, Glu380, Ser80, Ile164, Phe26, Asn411, Trp412, Phe379 |
| **3c** | -1310.01 | Trp388 (2.09Å), Glu38 (2.69Å, 1.83Å), Glu380, Phe379, Ile164, Thr137, Phe26, Gln282 |
| **3a** | -1167.94 | Gln161 (1.91Å), Gln282, Ile164, Phe26, Thr137, Val83, Ser80, Tyr28, Pro141, Gly138, Met142, Ala282. |
| **3b** | -1243.06 | Glu380 (1.86Å), Asn317 (2.38Å), Trp388, Thr137, Ile164, Phe26, Asn411, Phe379, Trp386, Leu160, Gln280, Thr28, Gln159, Gnl282. |

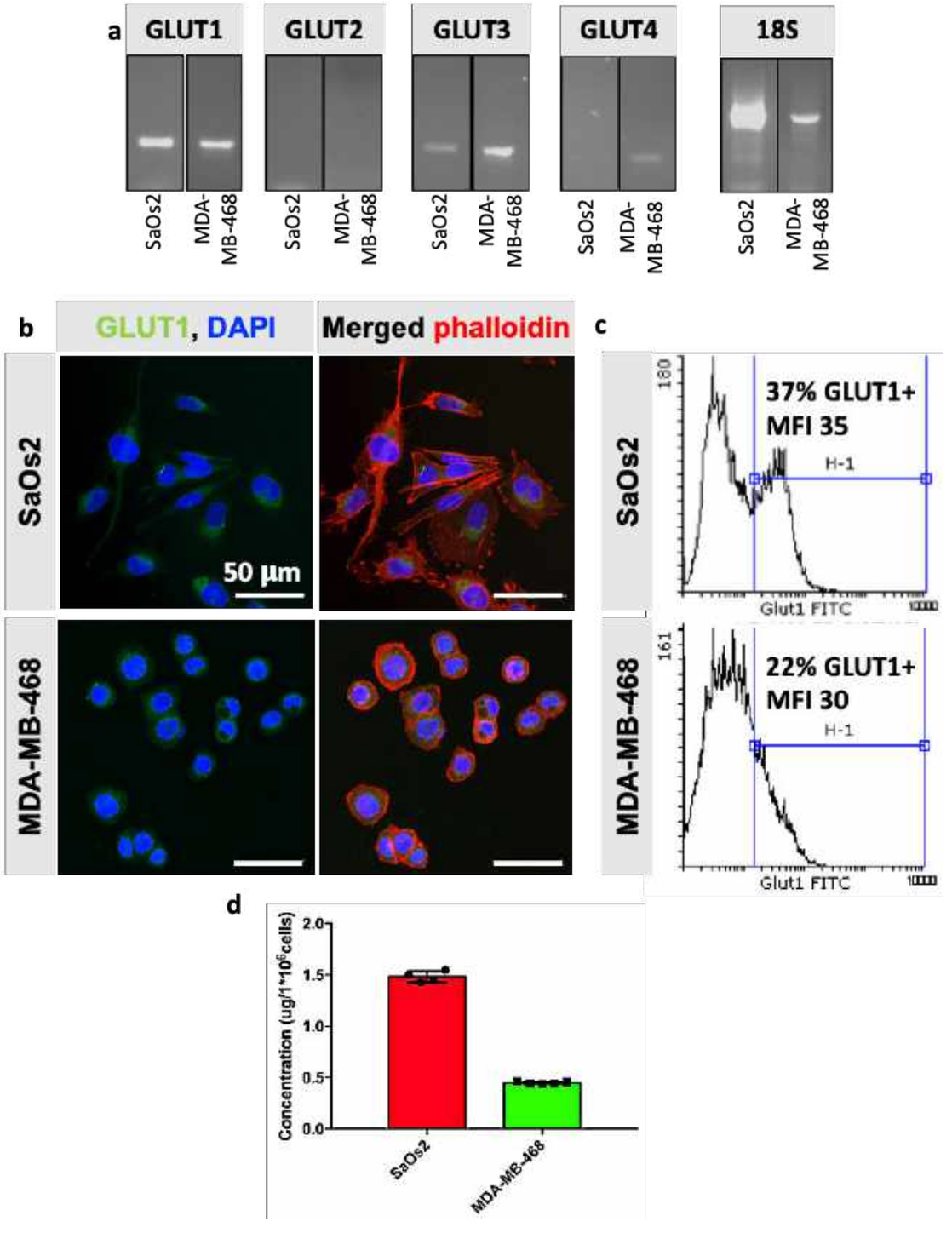


Supplementary Figure IV.1. Characterization of the selected cancer cell lines: (a) Agarose gel electrophoresis of the PCR products for *GLUT1-4* genes coding GLUT1-4, 18S is a housekeeping gene used as a control; (b) Confocal microscopy images visualizing the cytoskeletal organization (phalloidin, red), cells nuclei (DAPI, blue) and GLUT1 expression (green) in of SaOs2 and MDA-MB-468; (c) Flow cytometry data showing the percentage of GLUT1 positive cells from the total

cell population and the level of GLUT1 expression (mean fluorescent intensity, MFI); (d) Membranal alkaline phosphatase expressed by SaOs2 and MDA-MB-468.

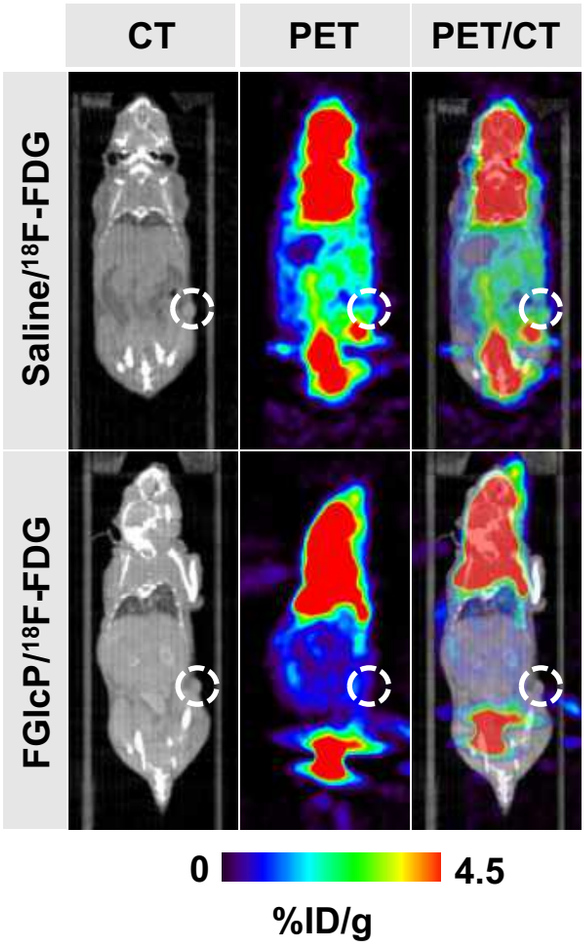


Supplementary Figure IV.2. Aromatic N-glucoside 3c deprives glucose uptake *in vivo*. Computed tomography (CT) and positron emission tomography (PET) of fluorodeoxyglucose ($^{18}$F-FDG) in nude mice bearing MDA-MB-468 tumor and administrated with an excess (2 mM) of compound 3c. Control mice were administrated with saline instead of compound 3c.

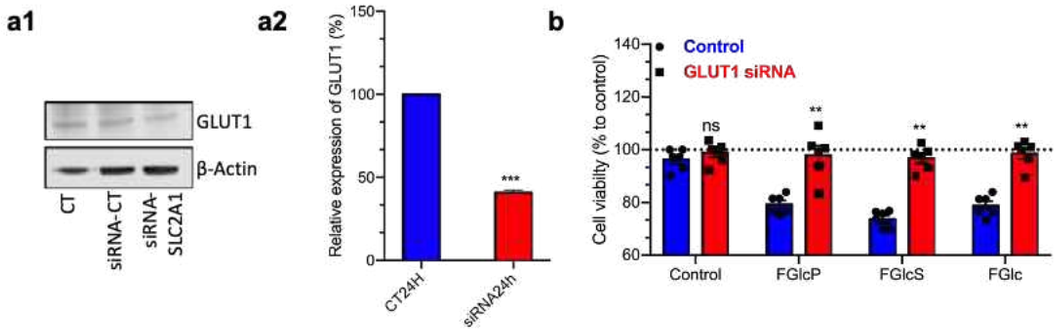


Supplementary Figure IV.3. Relation between GLUT1 expression and the effect of aromatic N-glucosides on MDA-MB-468 viability. (a1) Representative Western blot analysis and (a2) the respective densitometric analysis of GLUT1 expression by MDA-MB-468 cells without transfection (CT) and after transfection with specific siRNA (siRNA-*SLC2A1*); (b) Cell viability of the transfected SaOs2 cells in the presence of aromatic N-glucosides 3a-c. ns, non-significant; *: $p < 0.05$; **: $p < 0.01$; *** $p < 0.001$.

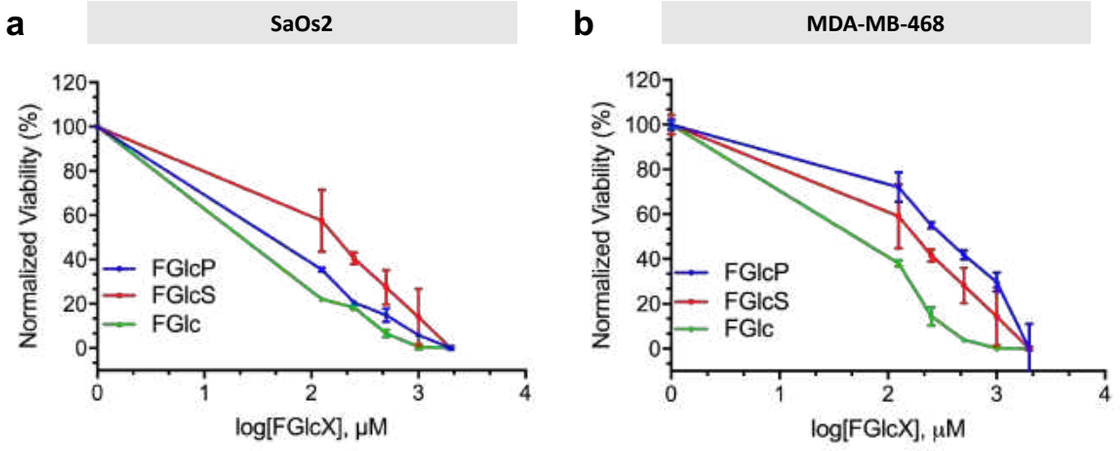


| | SaOs2 | MDA-MB-468 |
|---|---|---|
| 3c \| FGlcP | $IC_{50}$ = 79 μM<br>$R^2$ = 9.9 | $IC_{50}$ 307 μM<br>$R^2$ = 8.7 |
| 3a \| FGlc | $IC_{50}$ = 52 μM<br>$R^2$ = 9.8 | $IC_{50}$ = 99 μM<br>$R^2$ = 9.9 |
| 3b \| FGlcS | $IC_{50}$ = 171 μM<br>$R^2$ = 9.0 | $IC_{50}$ = 404 μM<br>$R^2$ = 9.5 |

Supplementary Figure IV.4. $IC_{50}$ plots and values for the aromatic N-glucosides 3a-c. (a) Viability of human osteosarcoma cell line SaOs2 in the presence of compounds 1b-d at different concentrations (24 hrs); (b) Viability of human breast cancer cell line MDA-MB-468 treated with aromatic N-glucosides at different concentrations (24 hrs); (c) $IC_{50}$ values

obtained from the plots. All results were normalized to the control – cells cultured in the absence of aromatic N-glucosides.

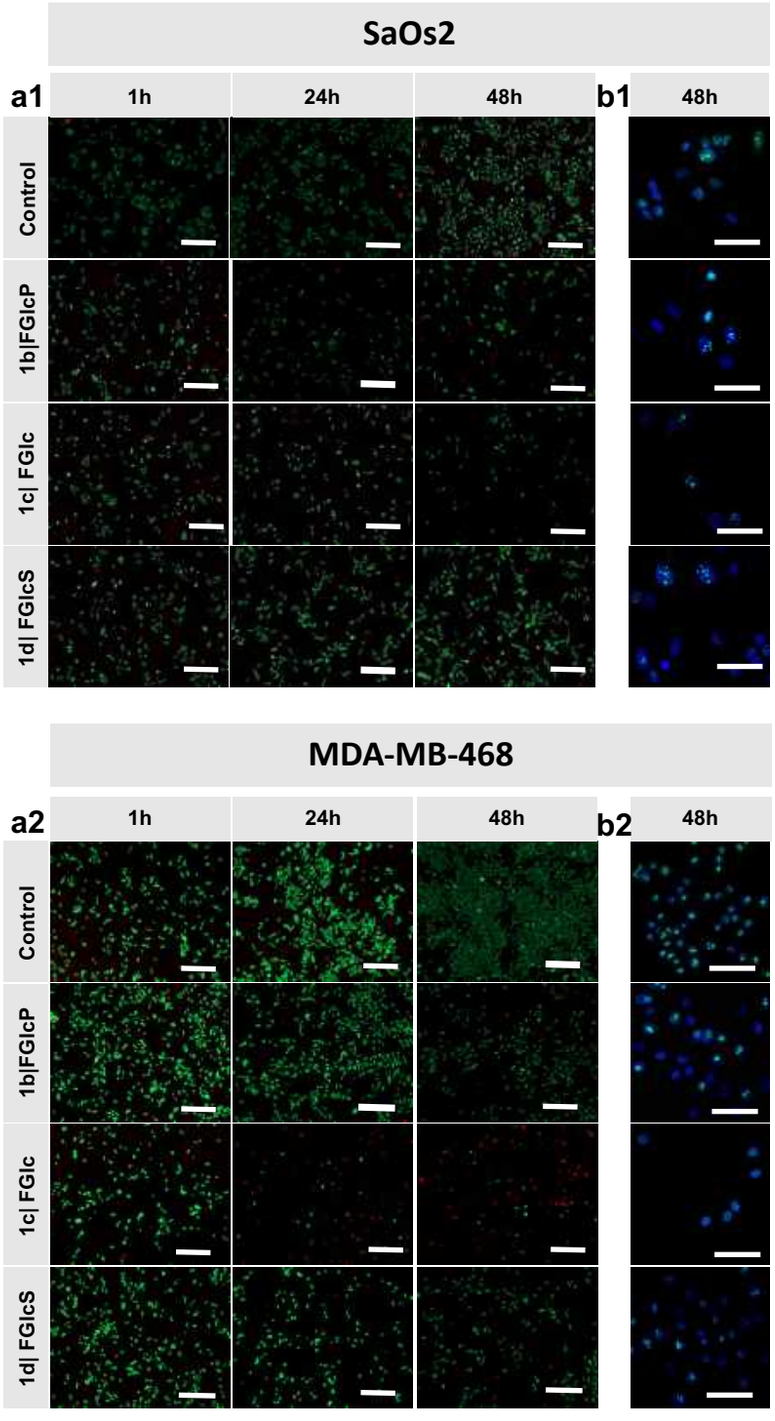


Supplementary Figure IV.5. Effect of the compounds 3a-c on the viability and proliferation of SaOs2 and MDA-MB-468: (a) Confocal laser scanning microscopy (CLSM) images of SaOs2 (a1) and MDA-MB-468 (a2) cells supplemented with 3a-c (0.5 mM) and stained with calcein AM (green) for live cells and propium iodide (red) for the dead ones. (b) CLSM

images of the studied cells stained with the proliferation marker Ki67 (light blue) and DAPI (dark blue) to visualize the nuclei.

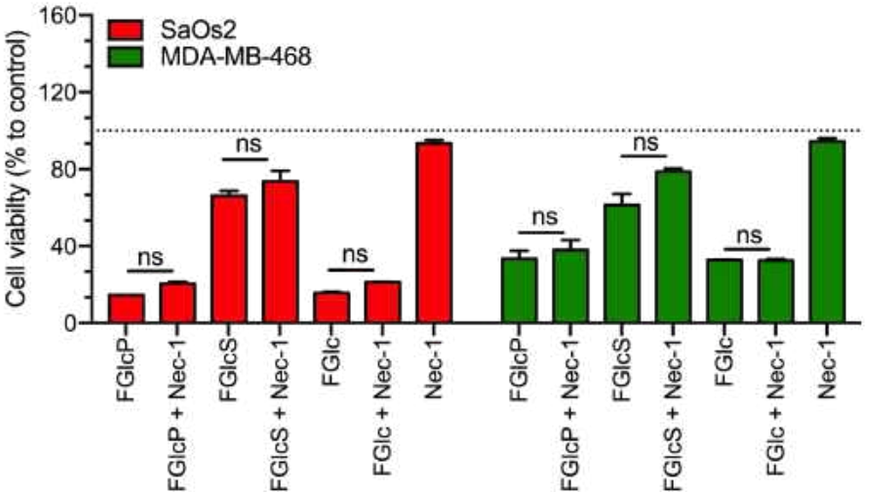


Supplementary Figure IV.6. Effect of the necroptosis inhibitor Nec-1 on cell viability: cells were cultured in the presence of the compounds 3a-c (0.5 mM) with or without the apoptosis inhibitor Z-Fa-FMK and the viability was determined after 24 hrs. The results are normalized to the control (cell culture without aromatic N-glucosides); ns: statistically non-significant difference.

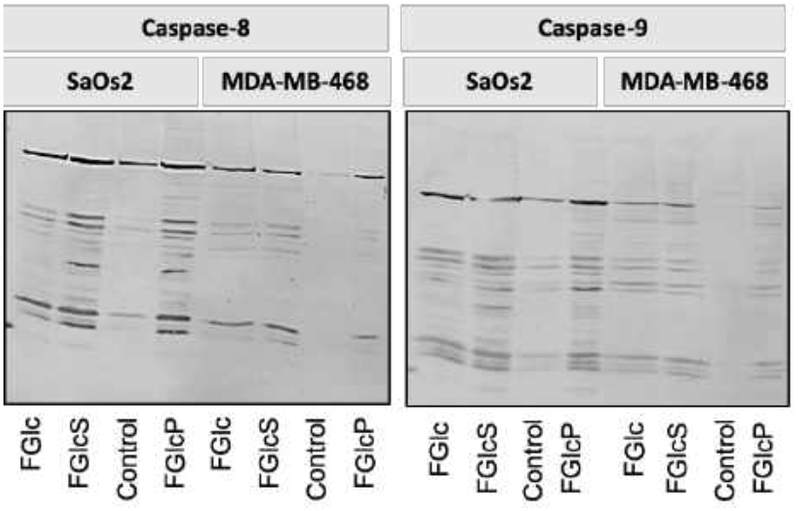


Supplementary Figure IV.7. Western blot analysis of initiators caspases 8 and 9 for SaOs2 and MDA-MB-468 cell lines in the presence and absence of compounds 3a-c.

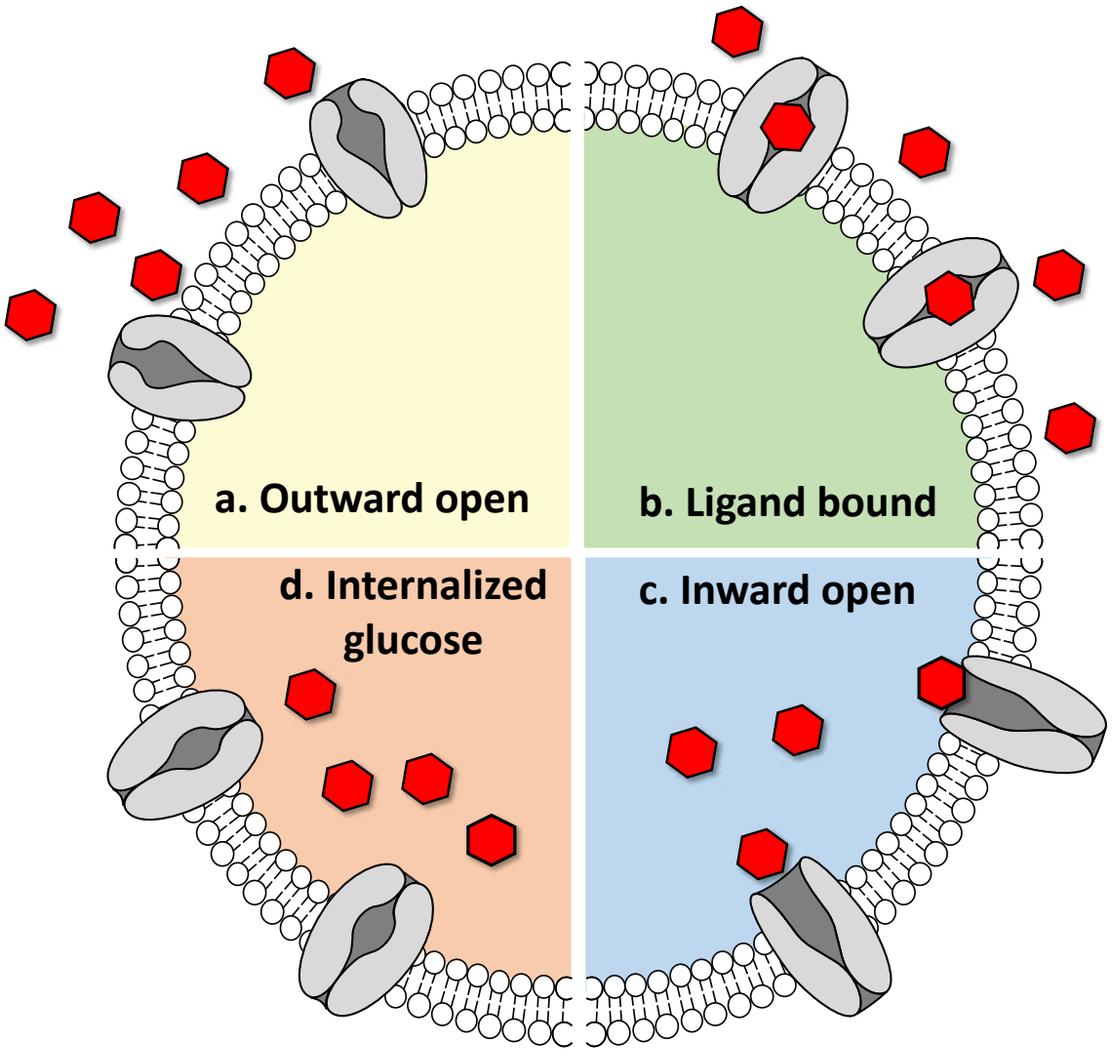


Supplementary Figure IV.8. Glucose (Glc) transport via GLUT1: (a) Glc is internalized via several residues of transmembrane segments 1, 4, 7 and 10 (here not shown in detail) that form the outward open conformation. (b) The primary substrate binding (ligand-bound) induces conformational changes. (c) The substrate is released from the inward open conformation as it is exposed to a low concentration environment. (d) The Glc release induces restauration of the initial GLUT1 conformation. When Glc is replaced by aromatic-N-glucosides either the rearrangement from ligand bond to inward open conformation of the release from the inward open conformation might be compromised.

## IV.6. REFERENCES:

1. (WHO) Who. Latest global cancer data: Cancer burden rises to 18.1 million new cases and 9.6 million cancer deaths in 2018. International Agency for research in cancer. 2018.

2. Zhou J, Xu B. Enzyme-Instructed Self-Assembly: A Multistep Process for Potential Cancer Therapy. Bioconjugate chemistry. 2015;26(6):987-99.

3. Pires RA, Abul-Haija YM, Reis RL, Ulijn RV, Pashkuleva I. Hydrogel Nanomaterials for Cancer Diagnosis and Therapy. Hydrogels: Design, Synthesis and Application in Drug Delivery and Regenerative Medicine. 2018:170.

4. Hanahan D, Weinberg RA. Hallmarks of Cancer: The Next Generation. Cell. 2011;144(5):646-74.

5. Cairns RA, Harris IS, Mak TW. Regulation of cancer cell metabolism. Nature Reviews Cancer. 2011;11(2):85-95.

6. Yang ZM, Xu KM, Guo ZF, Guo ZH, Xu B. Intracellular enzymatic formation of nanofibers results in hydrogelation and regulated cell death. Advanced Materials. 2007;19(20):3152-6.

7. Pires RA, Abul-Haija YM, Costa DS, Novoa-Carballal R, Reis RL, Ulijn RV, et al. Controlling Cancer Cell Fate Using Localized Biocatalytic Self-Assembly of an Aromatic Carbohydrate Amphiphile. Journal of the American Chemical Society. 2015;137(2):576-9.

8. Kapoor K, Finer-Moore JS, Pedersen BP, Caboni L, Waight A, Hillig RC, et al. Mechanism of inhibition of human glucose transporter GLUT1 is conserved between cytochalasin B and phenylalanine amides. Proceedings of the National Academy of Sciences of the United States of America. 2016;113(17):4711-6.

9. Chan DA, Sutphin PD, Nguyen P, Turcotte S, Lai EW, Banh A, et al. Targeting GLUT1 and the Warburg Effect in Renal Cell Carcinoma by Chemical Synthetic Lethality. Science Translational Medicine. 2011;3(94).

10. Granchi C, Fortunato S, Minutolo F. Anticancer agents interacting with membrane glucose transporters. Medchemcomm. 2016;7(9):1716-29.

11. Zhou J, Du XW, Yamagata N, Xu B. Enzyme-Instructed Self-Assembly of Small D-Peptides as a Multiple-Step Process for Selectively Killing Cancer Cells. Journal of the American Chemical Society. 2016;138(11):3813-23.

12. Feng ZQQ, Wang HM, Chen XY, Xu B. Self-Assembling Ability Determines the Activity of Enzyme-Instructed Self-Assembly for Inhibiting Cancer Cells. Journal of the American Chemical Society. 2017;139(43):15377-84.

13. Yao Q, Huang Z, Liu D, Chen J, Gao Y. Enzyme-Instructed Supramolecular Self-Assembly with Anticancer Activity. Advanced Materials. 2018.

14. Kalafatovic D, Nobis M, Javid N, Frederix PWJM, Anderson KI, Saunders BR, et al. MMP-9 triggered micelle-to-fibre transitions for slow release of doxorubicin. Biomater Sci-Uk. 2015;3(2):246-9.

15. Kalafatovic D, Nobis M, Son JY, Anderson KI, Ulijn RV. MMP-9 triggered self-assembly of doxorubicin nanofiber depots halts tumor growth. Biomaterials. 2016;98:192-202.

16. Son J, Kalafatovic D, Kumar M, Yoo B, Cornejo MA, Contel M, et al. Customizing Morphology, Size, and Response Kinetics of Matrix Metalloproteinase-Responsive Nanostructures by Systematic Peptide Design. Acs Nano. 2019;13(2):1555-62.

17. Kuang Y, Shi JF, Li J, Yuan D, Alberti KA, Xu QB, et al. Pericellular Hydrogel/Nanonets Inhibit Cancer Cells. Angew Chem Int Edit. 2014;53(31):8104-7.

18. Shi YJ, Hu Y, Ochbaum G, Lin R, Bitton R, Cui HG, et al. Enzymatic activation of cell-penetrating peptides in self-assembled nanostructures triggers fibre-to-micelle morphological transition. Chem Commun. 2017;53(52):7037-40.

19. Anderson CF, Cui HG. Protease-Sensitive Nanomaterials for Cancer Therapeutics and Imaging. Industrial & Engineering Chemistry Research. 2017;56(20):5761-77.

20. Cheetham AG, Lin YA, Lin R, Cui HG. Molecular design and synthesis of self-assembling camptothecin drug amphiphiles. Acta Pharmacologica Sinica. 2017;38(6):874-84.

21. Shi HB, Kwok RTK, Liu JZ, Xing BG, Tang BZ, Liu B. Real-Time Monitoring of Cell Apoptosis and Drug Screening Using Fluorescent Light-Up Probe with Aggregation-Induced Emission Characteristics. Journal of the American Chemical Society. 2012;134(43):17972-81.

22. Kuang Y, Xu B. Disruption of the Dynamics of Microtubules and Selective Inhibition of Glioblastoma Cells by Nanofibers of Small Hydrophobic Molecules. Angew Chem Int Edit. 2013;52(27):6944-8.

23. Grosdidier A, Zoete V, Michielin O. Fast docking using the CHARMM force field with EADock DSS. J Comput Chem. 2011;32(10):2149-59.

24. Grosdidier A, Zoete V, Michielin O. SwissDock, a protein-small molecule docking web service based on EADock DSS. Nucleic Acids Research. 2011;39:W270-W7.

25. Deng D, Xu C, Sun PC, Wu JP, Yan CY, Hu MX, et al. Crystal structure of the human glucose transporter GLUT1. Nature. 2014;510(7503):121-+.

26. Grosdidier A, Zoete V, Michielin O. EADock: docking of small molecules into protein active sites with a multiobjective evolutionary optimization. Proteins: Structure, Function, and Bioinformatics. 2007;67(4):1010-25.

27. Pettersen EF, Goddard TD, Huang CC, Couch GS, Greenblatt DM, Meng EC, et al. UCSF chimera - A visualization system for exploratory research and analysis. Journal of Computational Chemistry. 2004;25(13):1605-12.

28. Yamada K, Nakata M, Horimoto N, Saito M, Matsuoka H, Inagaki N. Measurement of glucose uptake and intracellular calcium concentration in single, living pancreatic beta-cells. Journal of Biological Chemistry. 2000;275(29):22278-83.

29. Yamada K, Saito M, Matsuoka H, Inagaki N. A real-time method of imaging glucose uptake in single, living mammalian cells. Nature Protocols. 2007;2(3):753-62.

30. Sebaugh JL. Guidelines for accurate EC50/IC50 estimation. Pharmaceutical Statistics. 2011;10(2):128-34.

31. McQuin C, Goodman A, Chernyshev V, Kamentsky L, Cimini BA, Karhohs KW, et al. CellProfiler 3.0: Next-generation image processing for biology. PLoS Biol. 2018;16(7):e2005970.

32. Pereira PMR, Silva S, Cavaleiro JAS, Ribeiro CAF, Tome JPC, Fernandes R. Galactodendritic Phthalocyanine Targets Carbohydrate-Binding Proteins Enhancing Photodynamic Therapy. Plos One. 2014;9(4).

33. Fueger BJ, Czernin J, Hildebrandt I, Tran C, Halpern BS, Stout D, et al. Impact of animal handling on the results of F-18-FDG PET studies in mice. Journal of Nuclear Medicine. 2006;47(6):999-1006.

34. Aft RL, Lewis JS, Zhang FJ, Kim J, Welch MJ. Enhancing targeted radiotherapy by copper(II)diacetyl-bis(N-4-methylthiosemicarbazone) using 2-deoxy-D-glucose. Cancer Research. 2003;63(17):5496-504.

35. Birchall LS, Roy S, Jayawarna V, Hughes M, Irvine E, Okorogheye GT, et al. Exploiting CH-pi interactions in supramolecular hydrogels of aromatic carbohydrate amphiphiles. Chemical Science. 2011;2(7):1349-55.

36. Brito A, Abul-Haija YM, da Costa DS, Novoa-Carballal R, Reis RL, Ulijn RV, et al. Minimalistic supramolecular proteoglycan mimics by co-assembly of aromatic peptide and carbohydrate amphiphiles. Chemical Science. 2019;10(8):2385-90.

37. Rastogi S, Banerjee S, Chellappan S, Simon GR. Glut-1 antibodies induce growth arrest and apoptosis in human cancer cell lines. Cancer Letters. 2007;257(2):244-51.

38. Deng D, Sun PC, Yan CY, Ke M, Jiang X, Xiong L, et al. Molecular basis of ligand recognition and transport by glucose transporters. Nature. 2015;526(7573):391-+.

39. Barretina J, Caponigro G, Stransky N, Venkatesan K, Margolin AA, Kim S, et al. The Cancer Cell Line Encyclopedia enables predictive modelling of anticancer drug sensitivity. Nature. 2012;483(7391):603-7.

40. Stransky N, Ghandi M, Kryukov GV, Garraway LA, Lehar J, Liu M, et al. Pharmacogenomic agreement between two cancer cell line data sets. Nature. 2015;528(7580):84-+.

41. Zou CH, Wang YJ, Shen ZF. 2-NBDG as a fluorescent indicator for direct glucose uptake measurement. Journal of Biochemical and Biophysical Methods. 2005;64(3):207-15.

42. Lopez-Hernandez FJ, Ortiz MA, Bayon Y, Piedrafita FJ. Z-FA-fmk inhibits effector caspases but not initiator caspases 8 and 10, and demonstrates that novel anticancer retinoid-related molecules induce apoptosis via the intrinsic pathway. Molecular Cancer Therapeutics. 2003;2(3):255-63.

43. Takahashi N, Duprez L, Grootjans S, Cauwels A, Nerinckx W, DuHadaway JB, et al. Necrostatin-1 analogues: critical issues on the specificity, activity and in vivo use in experimental disease models. Cell Death & Disease. 2012;3.

44. Wu YQ, Zhao D, Zhuang JN, Zhang FQ, Xu C. Caspase-8 and Caspase-9 Functioned Differently at Different Stages of the Cyclic Stretch-Induced Apoptosis in Human Periodontal Ligament Cells. PLoS One. 2016;11(12).

45. Pirnia F, Schneider E, Betticher DC, Borner MM. Mitomycin C induces apoptosis and caspase-8 and-9 processing through a caspase-3 and Fas-independent pathway. Cell Death and Differentiation. 2002;9(9):905-14.

46. Gatenby RA, Gillies RJ. Why do cancers have high aerobic glycolysis? Nature Reviews Cancer. 2004;4(11):891-9.

47. Hsu PP, Sabatini DM. Cancer cell metabolism: Warburg and beyond. Cell. 2008;134(5):703-7.

48. Macheda ML, Rogers S, Best JD. Molecular and cellular regulation of glucose transporter (GLUT) proteins in cancer. Journal of Cellular Physiology. 2005;202(3):654-62.

49. Zhou J, Du XW, Xu B. Regulating the Rate of Molecular Self-Assembly for Targeting Cancer Cells. Angew Chem Int Edit. 2016;55(19):5770-5

# Chapter V

# Aromatic Carbohydrate Amphiphile Disrupts Efficiently Cancer Spheroids without Following Relapse

## AROMATIC CARBOHYDRATE AMPHIPHILE DISRUPTS EFFICIENTLY CANCER SPHEROIDS WITHOUT FOLLOWING RELAPSE


### Abstract

Spheroids recapitulate the organization, heterogeneity and microenvironment of solid tumors. Herein, we targeted spatiotemporally the accelerated metabolism of proliferative cells located on the spheroid surface that ensure structure maintenance and/or growth. We demonstrate that phosphorylated carbohydrate amphiphile acts as a potent antimetabolite due to glycolysis inhibition and to in situ formation of supramolecular net around spheroid surface where alkaline phosphatase is overexpressed. The efficiency of the treatment is higher in spheroids as compared to the conventional 2D cultures because of the 2-fold higher expression of glucose transporter 1 (GLUT1). Moreover, treated spheroids do not undergo following relapse.


---


*This chapter is based on the publication:*

**Brito, Alexandra;** Pereira, Patricia M. R.; Reis, Rui L.; Ulijn, Rein V.; Lewis, Jason S.; Pires, Ricardo A.; Pashkuleva, Iva: **"**Aromatic Carbohydrate Amphiphile Disrupts Efficiently Cancer Spheroids without Following Relapse", submitted.

## V.1. INTRODUCTION

Biocatalytic self-assembly (BSA) combines the selectivity of an enzymatic conversion with the sensitivity and the precision of the supramolecular self-assembly.[1, 2] The approach has been applied to different pathologies, including cancers, where an overexpressed enzyme triggers *in situ* fiber formation by localized self-assembly leading to cell death or localized drug delivery through triggered disassembly of designed precursors.[1-6] BSA efficiency and *modus operandi* are usually demonstrated *in vitro* using two-dimensional (2D) cell cultures.[4, 7-9] While these cultures serve as suitable proof-of-concept model systems because of the high reproducibility and ease of handling, they do not recapitulate the complex tumor microenvironment: tumors are heterogeneous and complex organ-like structures, whose identity is dependent on the cell-to-cell contacts and alterations of the extracellular matrix.[10, 11] These characteristics are particularly relevant in BSA, where proteins present at the cell membrane are used as a trigger of the self-assembly process.

Herein, we developed a 3D tumor model using HS578T human breast cancer cells and studied BSA of the phosphorylated carbohydrate amphiphile, N-fluorenylmethyloxycarbonyl-glucosamine-6-phosphate (**3c**). This amphiphile can be transformed by alkaline phosphatase (ALP) overexpressed in some tumors, *e.g.* osteosarcoma, into the low molecular mass gelator N-fluorenylmethyloxycarbonyl-glucosamine (**3a**) that self-assembles into a nanoscale network (Scheme V.1b1) which sequesters and efficiently kills cancer cells.[4] Beyond the physical effect of creating a nanoscale network that acts as a barrier at the cell surface, there is also a specific chemical role for these glucose-based aromatic amphiphiles. The phosphorylated precursor **3c** and its dephosphorylated analogue **3a** contain a glucose moiety that interacts with glucose transporter 1 (GLUT1) (Scheme V.1b2), overexpressed in different cancers, thus, allowing double targeting, as we recently demonstrated.[12]

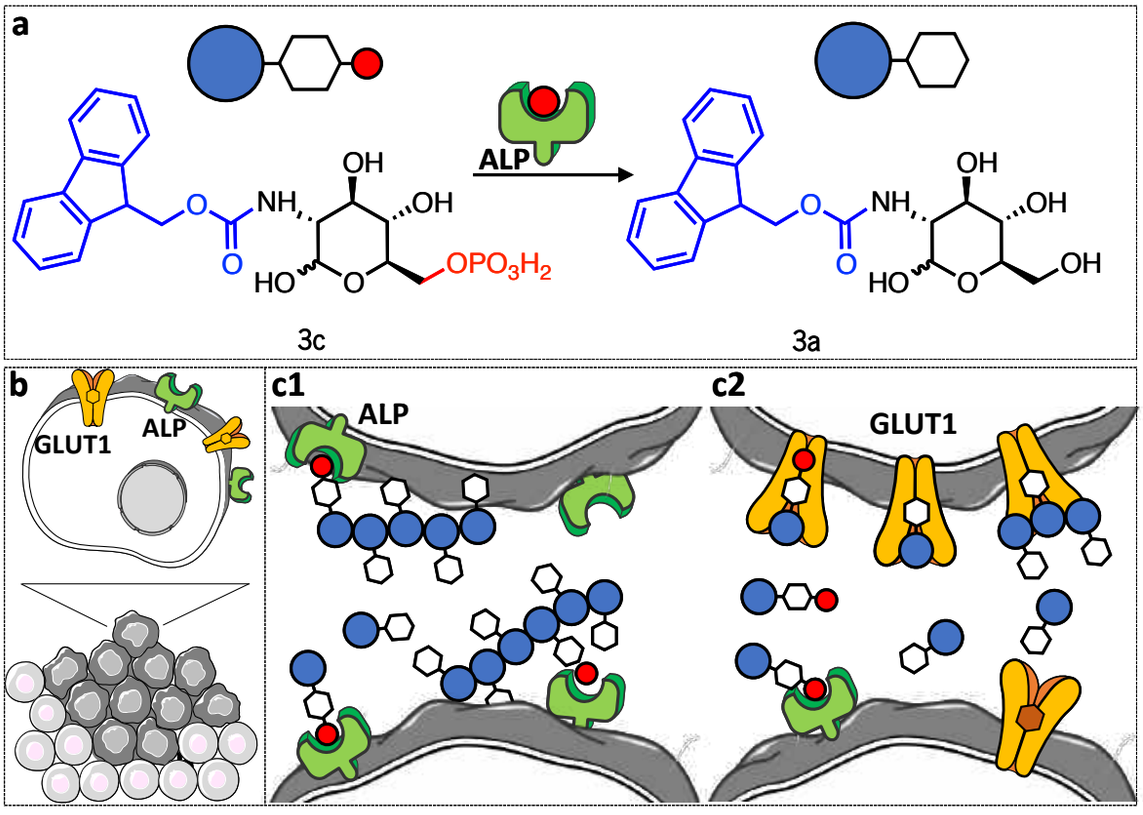


**Scheme V.1 (a) Schematic presentation of the enzymatic transformation of the phosphorylated precursor 3c to carbohydrate amphiphile 3a. (b) In tumors this transformation can trigger (c1) self-assembly on the tumor surface and (c2) blocking of the GLUT1 expressed by the proliferative cells on the tumor surface.**

## V.2. MATERIALS AND METHODS

### V.2.1. Monolayer (2D) cell cultures

SaOs2 osteosarcoma cells, MCF-7 and HS578T breast cancer cells were obtained from the American Type Culture Collection (ATCC, Manassas, VA, USA). SaOs2 and HS578T cells were cultured in Dulbecco´s Modified Eagle´s Medium (DMEM, Sigma or MSKCC media preparation core). MCF-7 cells were cultured in Eagle´s Minimum Essential Medium (EMEM; Corning, NY, USA or MSKCC media preparation core) with 1.5 g/L sodium bicarbonate, non-essential amino acids, L-glutamine and sodium pyruvate. Both culture media were supplemented with 10% (v/v) of fetal bovine serum (Life Technologies, Carlsbad, CA, USA), 100 U/mL penicillin, 100 µg/mL streptomycin and 0.25 µg/mL amphotericin B (Sigma). The cultures were maintained at 37 ℃ in a 5% CO2 humidified atmosphere.

### V.2.2. Spheroids formation and characterization

Spheroids were generated by growing cancer cell suspensions in agarose-coated 96 well plates.[11] The agarose prevented the cells from attaching to the bottom of the wells. Briefly, 150 μL/well of 1.5% (w/v in PBS) agarose solution (MP Biomedicals, Santa Ana, CA, USA) was added to the wells of a 96-well microplate. Cells (SaOs2, MCF-7 or HS578T with densities ranging from 2,500 to 20,000 cells per well) were then added and the microplate was hand-spun gently. Clusters of cancer cells were observed after 24 h of seeding, except for SaOs2 cells. Within the following 24 h the clusters formed spheroids for the HS578T cells, i.e. stable round aggregates which are not dislodged by pipetting. Images of clusters/aggregates/spheroids were obtained at 24, 48 and 72 h after cell culturing using the image analysis system consisting of Nikon Eclipse Ti fluorescent microscope and an Andor iXon EMCCD camera. The size of at least 6 spheroids was calculated for each cell line by measuring two orthogonal diameters (d1 and d2) using the line morphometry function. Volumes were calculated using equation V.1:

**Equation V.1: Volume = 4/3 πr^3**

where r=1/2×(d1+d2) is the geometric mean radius. Average cell number per spheroid was also determined at 24, 48 and 72 h after cell culturing by trypsinizing six different spheroids, mixing the cell suspension with Trypan blue (Sigma) and counting the number of total and viable cells, using a Vi-CELL XR, Cell Counter - Beckman Coulter.

### V.2.3. Treatment of spheroids and 2D flat cultures with 1

Monolayers and spheroids cultures were supplemented with 0.5 mM or 1 mM of compound **3c**, dissolved in media specific for each cell line. The supplemented culture was maintained for 48 h. The effect of the compound was assessed after additional 24 h to 72 h.

### V.2.4. Lactate dehydrogenase (LDH) assays

The cytotoxicity of **3c** was assessed using the CytoTox 96H Non-Radioactive cytotoxicity assay kit (Promega, USA) according to the manufacturer's instructions. Unlike other studies reporting the use of MTT for quantification spheroid viability, we were not able to apply this assay because the results were

neither reproducible nor consistent (data not shown). Therefore, we used CytoTox 96 Assay to quantify the LDH released from the spheroids as an indicator of cytotoxicity. Briefly, 50 μL of culture medium was collected from the well (96-well plate) containing cell spheroids and mixed with 50 μL of the CytoTox 96 Reagent in dark for 30 min at room temperature. Then 50 μL of stop solution was added to each well and the absorbance was recorded at 490 nm using a microplate reader (PowerWave HT Microplate Spectrophotometer). The average values of the culture medium background were subtracted from all values of experimental wells. The protein concentration was determined by Pierce BCA Protein Assay Kit after scrapping spheroid cultures in 1% (m/v) SDS solution in PBS (pH 7.0), and LDH activity was normalized to the protein concentration. The results were normalized to the maximal LDH release, which was determined by treating the control wells for 60 min with 1% Triton X-100 to lyse all cells.

### V.2.5. Transfection assay

GLUT1 was depleted using a pool of three target-specific 19–25 nt siRNA and CAV1 with a pool of 20–25 nt siRNA (Santa Cruz Biotechnology). Cancer cells were transfected with either SLC2A1-siRNA, siRNA-CAV1 or scrambled (scr) siRNA (controls). Each transfection was performed for 5 h with 2.4 μM of siRNA in transfection medium (Santa Cruz) containing 0.5 μL/cm2 of transfection reagent (Santa Cruz). After incubation with siRNA, complete media was added and the cells were incubated for 48 h. CAV1 and GLUT1 downregulation was assessed at 24 h, 48 h and 72 h post-transfection by Western Blotting.

### V.2.6. ALP inhibition

For alkaline phosphatase inhibition assays, we used the Pierce phosphatase inhibitor (Thermo Scientific) according to the manufacturer instruction (1 tablet per 10 mL of culture medium with FBS).

### V.2.7. Preparation of cell extracts and Western Blot

Scraped monolayer cells and spheroids cultured for 48 h were collected at 1,500 g for 5 min, washed twice with ice-cold PBS and whole protein lysates were extracted using RIPA buffer (150 mM NaCl, 50 mM Tris-HCl, pH 7.5, 5 mM ethylene glycol tetra-acetic acid, 1% Triton X- 100, 0.5% sodium deoxycholate, 0.1% SDS, 2 mM phenylmethanesulfonyl, 2 mM iodoaceta- mide, and 1x protease inhibitor cocktail (Roche, Indianapolis, IN, USA)). Cell extracts were centrifuged at 16,000 g for 10 min at 4 ℃. After

centrifugation, supernatants were used for protein quantification using the Pierce BCA Protein Assay Kit, followed by denaturation of the sample with Laemmli buffer. For the Western Blot analysis, 40 μg proteins were loaded per lane on sodium dodecyl sulphate-polyacrylamide gels (SDS-PAGE). Following electrophoresis and transfer to polyvinylidene fluoride membranes (Bio-Rad, Hercules, CA, USA), the blots were incubated in 5% (w/v) Bovine serum albumin in TBS-T (20 mM Tris, 150 mM NaCl, Tween 0.2%, pH 7.6). Membranes were then incubated with rabbit anti-GLUT1 1:1,000 (Thermo Fisher Scientific), rabbit anti- CAV1 1:1,000 (Thermo Fisher Scientific), rabbit anti-ALP 1:1,000 (Thermo Fisher Scientific) and rabbit anti-β-actin 1:1,000 (Thermo Fisher Scientific) antibodies. After washing, the membranes were incubated with IRDye 800CW anti- Rabbit IgG 1:15,000 (LI-COR Biosciences, Lincoln, NE, USA) and imaged on the Odyssey Infrared Imaging System (LI-COR Biosciences) followed by densitometric analysis.

### V.2.8. Immunofluorescence microscopy

Spheroids were grown for 48h and then treated as described above. Live-dead staining: after treatment, the spheroids were placed in a new 96 well plate without agarose and were stained with calcein AM (CA, 3 μM) and propidium iodide (PI, 3 μM) in 200 μL of phosphate-buffered saline (PBS). Imaging with a Leica TCS SP5 Confocal Laser Scanning Microscope was performed 3h after the staining. Immunolocalization: spheroids were placed in Optimal Cutting Temperature (OCT) mounting media and frozen immediately. After that, blocks were cut in sections of 10 μM. The sections were then dried at room temperature and fixed for 10 min with cold acetone. After washing with PBS, the spheroid was permeabilized with 0.25% v/v Triton X-100 in PBS with 0.02% w/v Bovine serum albumin in a humidified chamber and blocked with 10% v/v normal goat serum for 2h at room temperature. The spheroids were then incubated overnight at 4 °C with HIF-1α-488 (Abcam; 1:100), CAV1 (Abcam; 1:500), GLUT1 (Sigma-Aldrich, 1:100) or ALP (Abcam, 1:250). The spheroids were then rinsed with 0.02% Bovine serum albumin, 0.02% (w/v) sodium azide (NaN3) in PBS. Secondary fluorescent antibody Alexa Fluor 488 (Abcam, 1:1000) was applied for 1h at room temperature, except for HIF-1α-488, which is fluorescent-labeled. The spheroids were rinsed with 0.02% (w/v) NaN3 and were incubated with DAPI (Abcam, 1:1000) for 15 min at room temperature, followed by rinsing with 0.02% (w/v) NaN3. The spheroids were mounted in glycergel mounting medium and were imaged using a Leica TCS SP5 Confocal Laser Scanning Microscope. Sections were also submitted to MSKCC Molecular Cytology Core Facility for hematoxylin and eosin staining. In all experiments, untreated spheroids were used as controls and manipulated following the same protocols as for the treated ones.

### V.2.9. Scanning electron microscopy

The spheroids were placed onto a silica-wafer, dried at room temperature and imaged using high-resolution scanning electron microscopy (HRSEM, Auriga Compact, ZEISS) at 5kV after coating with 1nm of platinum.

### V.2.10. Statistical analysis

Statistical analyses were carried out using a statistical program (GraphPad Prism; GraphPad Software). Student's t-test was used to evaluate the effect of the treatment compared with the control. P- values were considered at the 5% level of significance to deduce inference of the significance of the data, were * $p < 0.01$; ** $p < 0.005$; *** $p < 0.001$; **** $p < 0.0001$.

## V.3. RESULTS AND DISCUSSION

We have selected three cell lines for spheroid formation, namely SaOs2 osteosarcoma, HS578T breast and MCF7 breast cancer cells because they all overexpress ALP, GLUT1 and caveolin 1 (CAV1) (Figure S V.1).[13] Our interests in GLUT1- and ALP-overexpressing cell lines is related to the affinity of compound **3c** for those proteins: **3c** can bind to GLUT1 because of the glucose moiety and can be transformed in the self-assembling **3a** upon ALP action (Scheme V.1c).[4, 12] In addition to GLUT1 and ALP, we also explored the contribution of CAV1 in carbohydrate amphiphile mediated BSA processes. CAV1 is the main structural protein of caveolae, the small pockets in the cell membrane that are known to modulate the glycolysis and to interact dynamically with ALP.[14, 15]

Formation of spheroids was studied by seeding the selected cell lines on agarose-coated well plates at different density (2,500-20,000 cells per well) and culture time (24 – 72 h).[11] Among the tested cells, only HS578T cells formed spheroids in a highly reproducible manner (Figures S V.2 and S V.3): 24 h after seeding, HS578T cells gathered into unstable aggregates, which were easily disrupted by mechanical force (*e.g.* pipetting). After 48 h, we observed formation of compact and stable spheroids composed by a shell of viable cells surrounding a necrotic core, which is typical for solid tumors (Figure V.1a).[10] Further compacting and a significant reduction in the

spheroid volume were observed in the following 24 h (Figure S V.3). We selected a cell density of 5,000 cells/well and 48 h of culture time for the spheroids' formation.

The structure of the spheroids (proliferative and quiescent cellular compartments) evidenced gradual deprivation of nutrients and oxygen from the surface to the bulk of the 3D structure. Such gradient is distinctive for solid tumors and is associated with specific genetic and metabolic changes. As an example, cells in the core are adapting to an anaerobic metabolism and produce large amount of lactate used as a source of energy.[16] This scenario is significantly different from 2D cultures where no competition for nutrients and oxygen exist and the population is homogeneous.

The comparison between HS578T monolayers and spheroids showed that both cultures expressed ALP, GLUT1 and CAV1 proteins (Figures V.1b and S V.1): ALP expression in spheroids was similar to that found in monolayers but both GLUT1 and CAV1 expression were found to be substantially different from that obtained for the 2D cell culture. In accordance with previous studies, we detected 3-fold lower CAV1 expression in spheroids when compared with monolayers.[17]

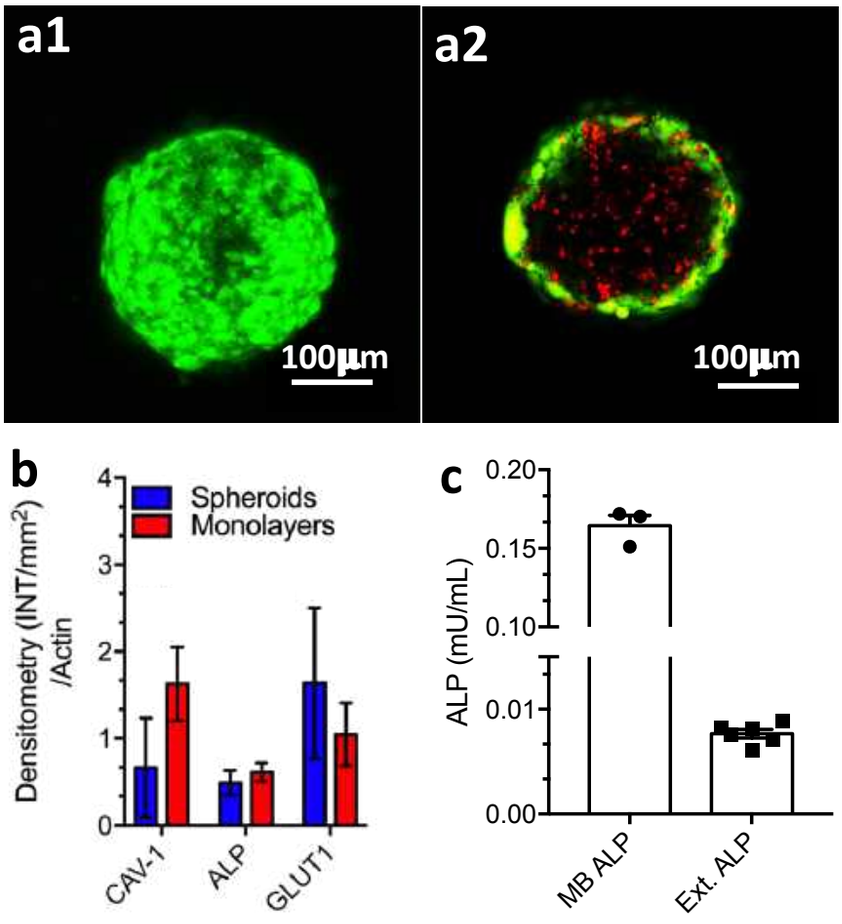


**Figure V.1. Characterization of the HS587T spheroids: (a) Representative confocal microscopy images of (a1) spheroid surface and (a2) core stained for live (green, calcein AM) and dead (red, propidium iodide) cells; (b) Densitometry quantification of Western-Blot analysis of ALP, CAV1, and GLUT1 expression by the 3D spheroids and 2D cell culture, normalized to the total β-actin protein content; (c) expression of membrane-bound (MB) and extracellular (Ext.) ALP in spheroids.**

On the other hand, a 2-fold increase in GLUT1 expression was observed when cells were cultured in spheroids. GLUT1 expression in spheroids and solid tumors is commonly higher than in the respective 2D cultures.[11, 18-20] This overexpression is associated with the survival mechanism(s) activated by the cells in the hostile tumor environment and correlates with aggressive, metastatic behavior.[18, 19] GLUT1 is therefore both prognostic marker and therapeutic target.

Among the heterogenous cell populations within the tumors, the proliferative cells on the surface are unique because they sustain the structure growth and provide an interface between the tumor and its environment. Thus, spatiotemporal targeting of the accelerated metabolism of

these cells provides a very efficient mean of isolating and destroying the tumors. The higher expression of GLUT1 is mainly due to high energy demands and we expected that the GLUT1 antagonist 1 will decelerate their metabolism crucial for tumor maintenance. On the other hand, these surface cells are not adapted to an anaerobic metabolism and the formation of ALP catalyzed BSA nanostructured network around the tumor will affect them further by deprivation of nutrients and oxygen.

The addition of **3c** to the spheroids resulted in their partial disintegration in a concentration and time-dependent manner (Figures V.2 and S V.4): the effect of **3c** on the spheroid morphology was visible after 48 h when 0.5 mM concentration was used and this time was shortened to 24 h upon a concentration increase to 1 mM. A closer look at the spheroids revealed the formation of a nanofibrous coating on the surface of the samples treated for 48 h, suggesting the occurrence of *in situ* BSA (Figure v.2b2). These nanostructures were absent in the control sample. Previously, we have observed a similar effect in 2D cultures of ALP overexpressing osteosarcomas SaOs2 that showed reduced metabolic activity at shorter culture time (1-7 h), which caused cell death at longer exposure (≥ 24 h) to **3c**.[4]

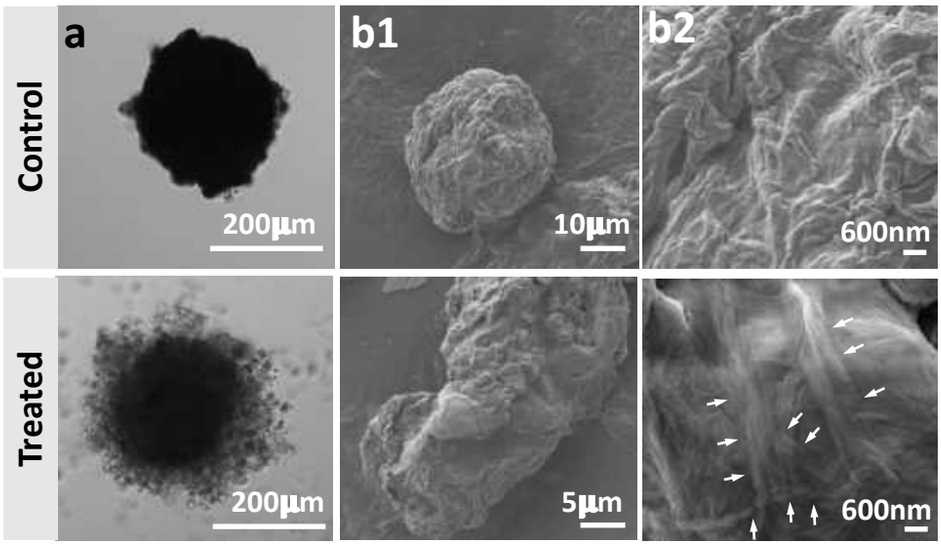


**Figure V.2. Effect of 3c on spheroid integrity and morphology: Representative (a) confocal microscopy and (b) high-resolution scanning electron microscopy images of untreated spheroids (control) and spheroids treated with 3c (1 mM, 48 h). White arrows indicate different fibers bundles.**

The morphological differences observed for the spheroids were accompanied by an increased release of lactate dehydrogenase (LDH) in the extracellular milieu of the treated

samples (Figure V.3a). This increase indicates compromised or damaged plasma membrane and is commonly used as a marker of necrotic cell death.[21] Indeed, histological staining of the spheroids with hematoxylin and eosin showed typical necrotic areas formed by cells without nuclei (Figure V.3b2, yellow circlers).[22] Live/dead staining also corroborated a significant increment of cell death in spheroids treated with **3c** (Figure V.3b1).

Confirmation of BSA involvement in cell death was done by quantification and inhibition of ALP that triggers the self-assembly process. We quantified both membrane-bound and extracellular ALP in the spheroids and found 20-fold higher values for the former form (Figure V.1c), suggesting its involvement in the BSA. Immunolocalization of membrane-bound ALP confirmed this result: the presence of **3c** increased the expression of ALP on the cell surface (Figure S5a). We then studied the inhibition of ALP using pierce phosphatase inhibitor.[4] The addition of the inhibitor rescued the cells and the spheroids had a similar shape and cell viability when compared to the control spheroids (Figure V.3c), manifesting a direct relationship between the ALP activity and the cytotoxicity of **3c**.

Glycolysis deprivation *via* blockage of GLUT1 by 1 and 2 was also studied as an additional contributor to cell death.[12] As noted, spheroids have a higher expression of GLUT1 as compared to the 2D cell culture (Figure V.1b). We knocked down GLUT1 expression in the spheroids by transfection with three target-specific siRNAs (Figure S V.6). Exposure of the transfected spheroids to 1 led to a reduction of the of LDH release, *i.e.* a significant decrease in the cytotoxicity of 1 (Figure V.3d). This result confirms that **3c** and/or its dephosphorylated analog **3a** interact with GLUT1 and the observed cytotoxicity is also mediated by this interaction.

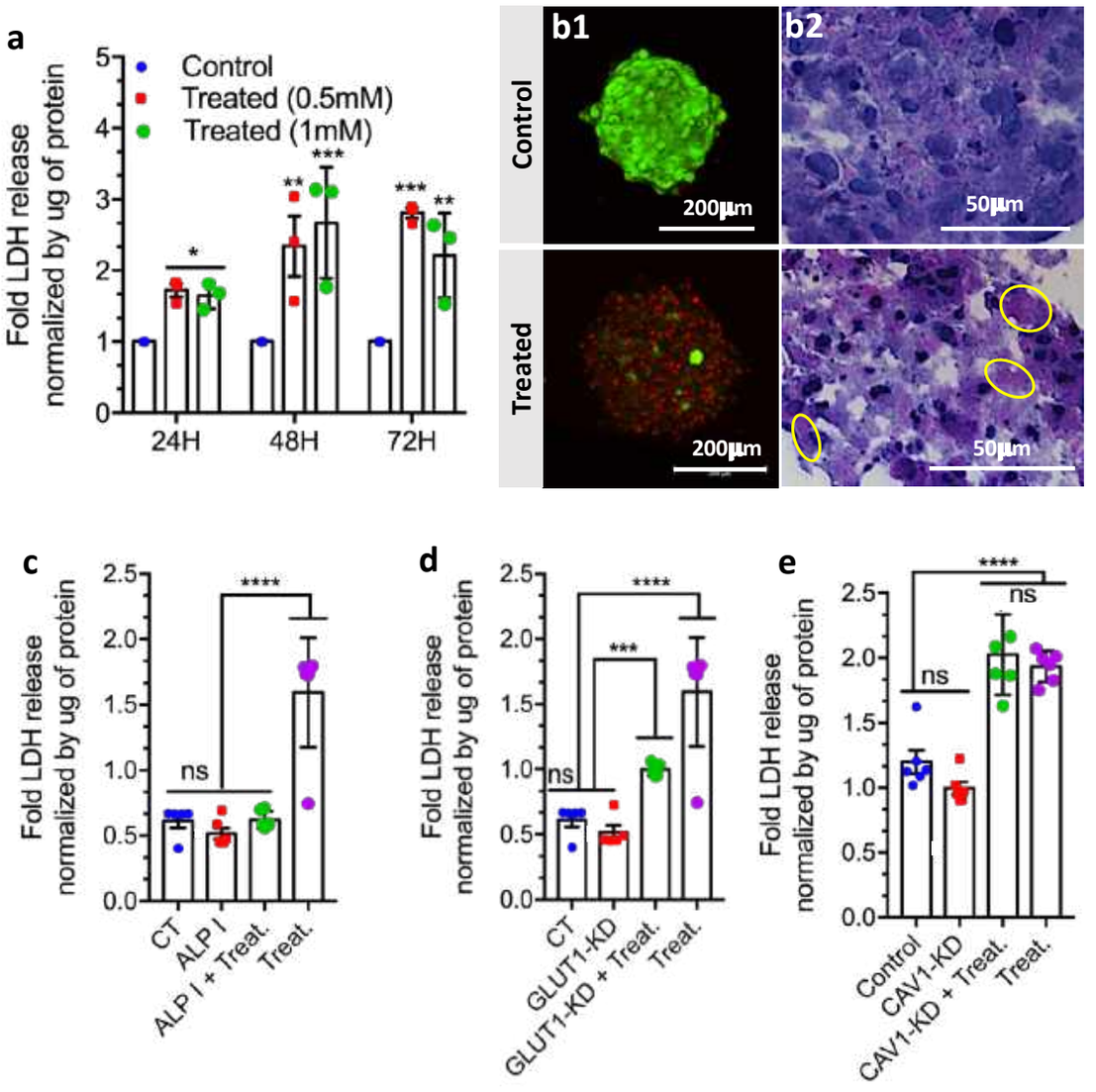


**Figure V.3. Effect of 3c on cell viability in HS578T spheroids: (a) Normalized LDH release as a function of time and concentration of 3c; (b) Cell death shown by microscopy images after (b1) live/dead and (b2) hematoxylin/eosin staining. LDH release of HS578T spheroids as a function of (c) ALP inhibition (I), (d) GLUT1 and (e) CAV1 knockdown (KD). The applied treatment (Treat.) was spheroid exposition to 3c (1 mM, 48 h). Statistics: ns (non-significant); * $p < 0.01$; ** $p < 0.005$; *** $p < 0.001$; **** $p < 0.0001$.**

Because ALP is present within caveolae and CAV1 is involved in glycolysis,[14] we also investigated possible interactions between this protein and **3c** in the spheroids. CAV1 protein was knocked down[23] (Figure S V.6) but its depletion did not affect the toxicity of **3c** (Figure V.3e), showing no direct participation of CAV1 in the necrotic pathway. Similar results (not shown) were obtained for 2D cultures with higher expression of CAV1.

A comparison of the effect of **3c** on spheroids (Figure V.3) and 2D cell culture (Figure S V.5) showed important differences: while cell death in 2D culture increases with increment of both the concentration of **3c** and the treatment time, in the 3D spheroids we observed a maximum effect of **3c** at lower concentration (*i.e.* 0.5 mM) and shorter treatment time (48 h). Further increase of the concentration of **3c** (*i.e.* to 1 mM) or extension of the treatment timeframe (72 h) did not induce additional cell death in the spheroids. This result indicates that either there is a higher sensitivity of the spheroids to **3c** or there is an inefficiency of the treatment at the studied conditions.

We, therefore, studied the possibility of recovery of the remaining live cells within the treated spheroid. Cancer recurrence and tumor relapse (usually in a more resistant form) caused by resistant cells within the tumors is one of the major hurdles in the development of efficient anti-cancer therapies. We re-plated the treated spheroid in an adherent well plate and confirmed that the cells were not able to recover from the effect of **3c**, supporting the efficacy of the treatment (Figure V.4b2). When untreated spheroid was re-plated, we observed formation of a dense spheroid (Figure V.4b1). Because ALP expression is similar for 2D cultures and 3D spheroids (Figure V.1b), we suggest that the observed higher sensitivity of the 3D tumor model to **3c** is due to the GLUT1 overexpression in spheroids. Thus, the use of the GLUT1 antagonist 1 as a substrate in a BSA anticancer therapeutic approach has two advantages. The first one is the enhanced efficacy: the high malignant potential of resistant cells is related to their ability to self-renew and form prone differentiated progeny that compose the bulk of the relapsed tumor - an energy-demanding process that depends on glucose uptake. In the presence of **3c**, some of these cells can survive, but their proliferative potential is significantly reduced due to the GLUT1 inhibition and deprivation of the glucose uptake. The second advantage is the selectivity: the overexpression of GLUT1 in solid tumors, and especially cells located at the surface makes it suitable target for a selective therapy.

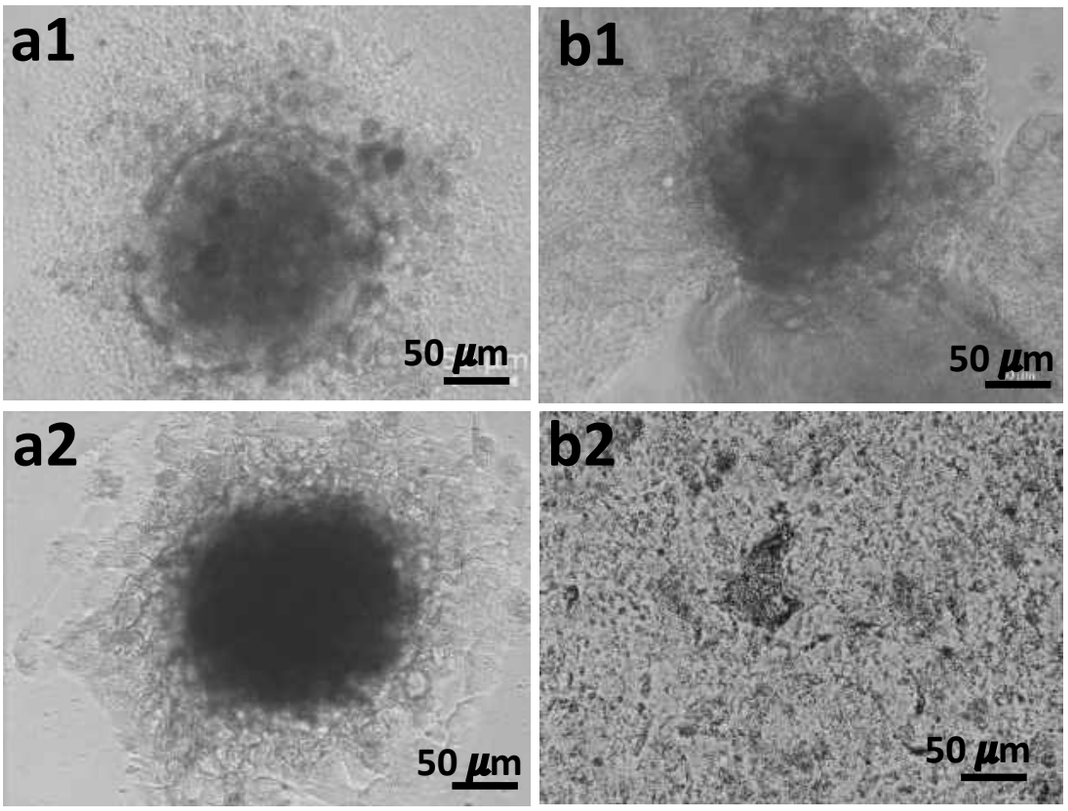


**Figure V.4. Spheroid relapse: representative transmitted-light microscope images of (a1) untreated spheroid (control) and (b1) spheroid exposed to 3c (1 mM, 48 h) that were (a2, b2) re-plated in adherent well plates for 48 h.**

We demonstrated that variable expression levels of the same proteins in 3D tumor models and 2D cell cultures can render dramatically different sensitivity to chemotherapies. We validated this observation by using carbohydrate amphiphile **3c** that participates simultaneously in two processes that are sensitive to the surface expression of two proteins, namely BSA triggered by membrane-bound ALP and glycolysis inhibition by blockage of GLUT1. Our data show that the combination of supramolecular chemistry with the manipulation of vital biochemical cascades is feasible approach to achieve efficient cancer therapies.

## V.4. SUPPLEMENTARY INFORMATION

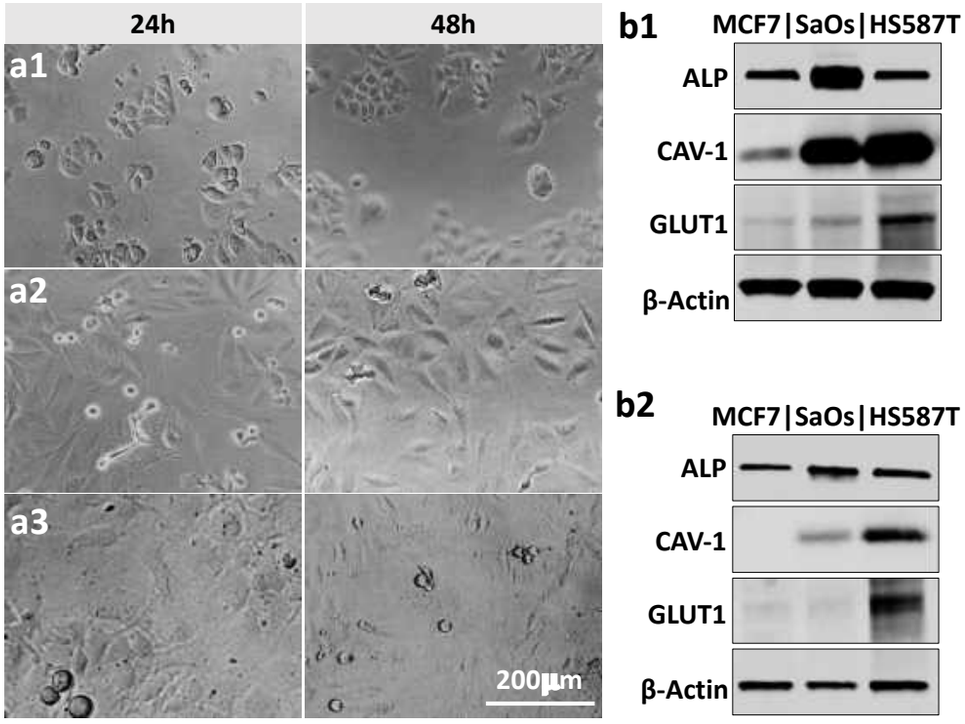


Supplementary Figure V.1. (a) Microscopy images of (a1) MCF7, (a2) SaOs2, and (a3) HS587T cells seeded on flat tissue culture plates for different time and (b) Western-Blot analysis of ALP, CAV-1, and GLUT1 expression by (b1) these cells and (b2) spheroids/aggregates made from them 48h after seeding. β-Actin was used to normalize the data in the densitometry analysis presented in Figure V.1 of the main manuscript.

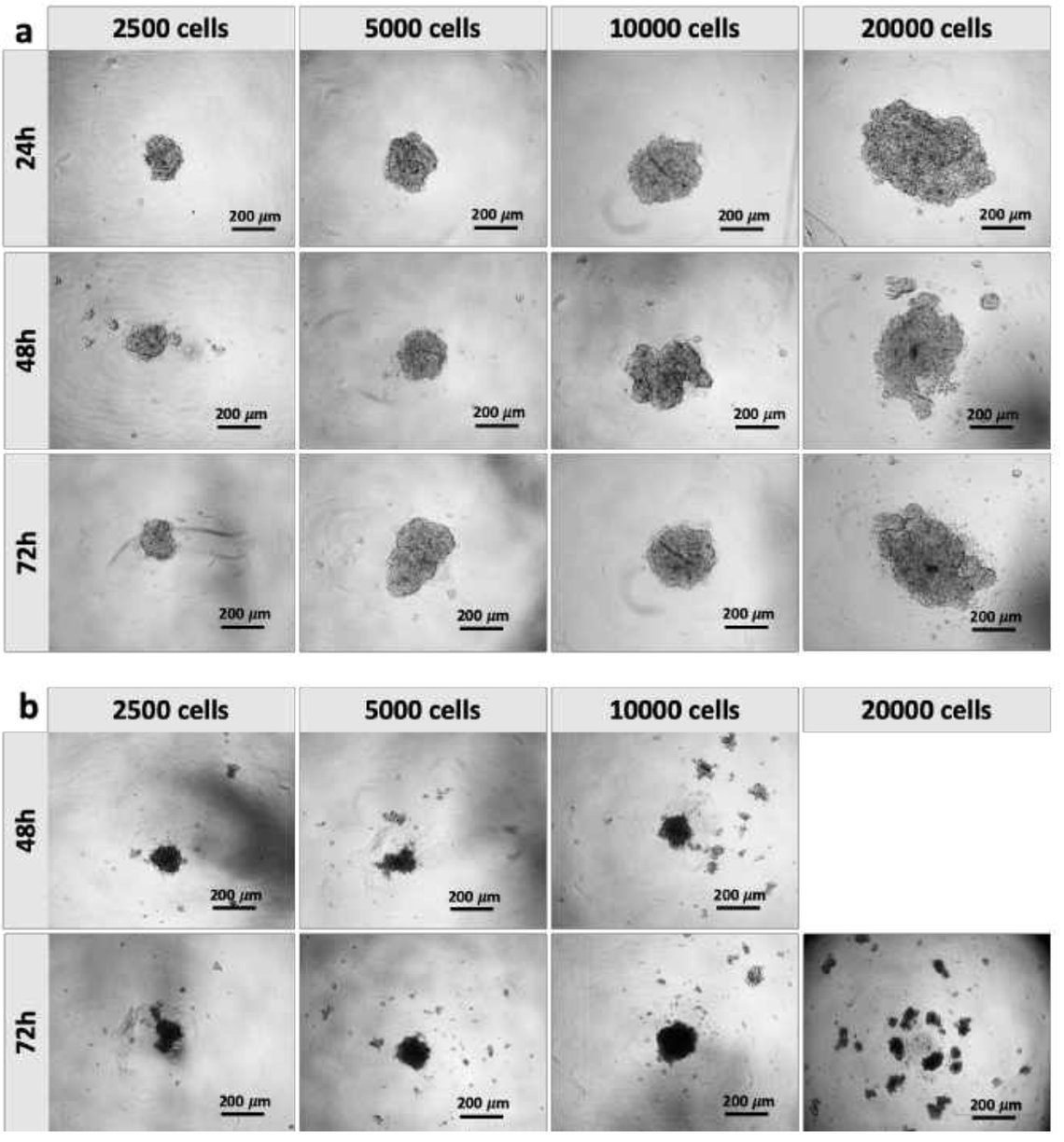


Supplementary Figure V.2. Ability of (a) MCF7 and (b) SaOs2 cells to form spheroids at different cell seeding (2500 – 20000 cells per well) and time (24 – 72h). No cells aggregate or spheroids were observed after 24h for SaOs2 cells.

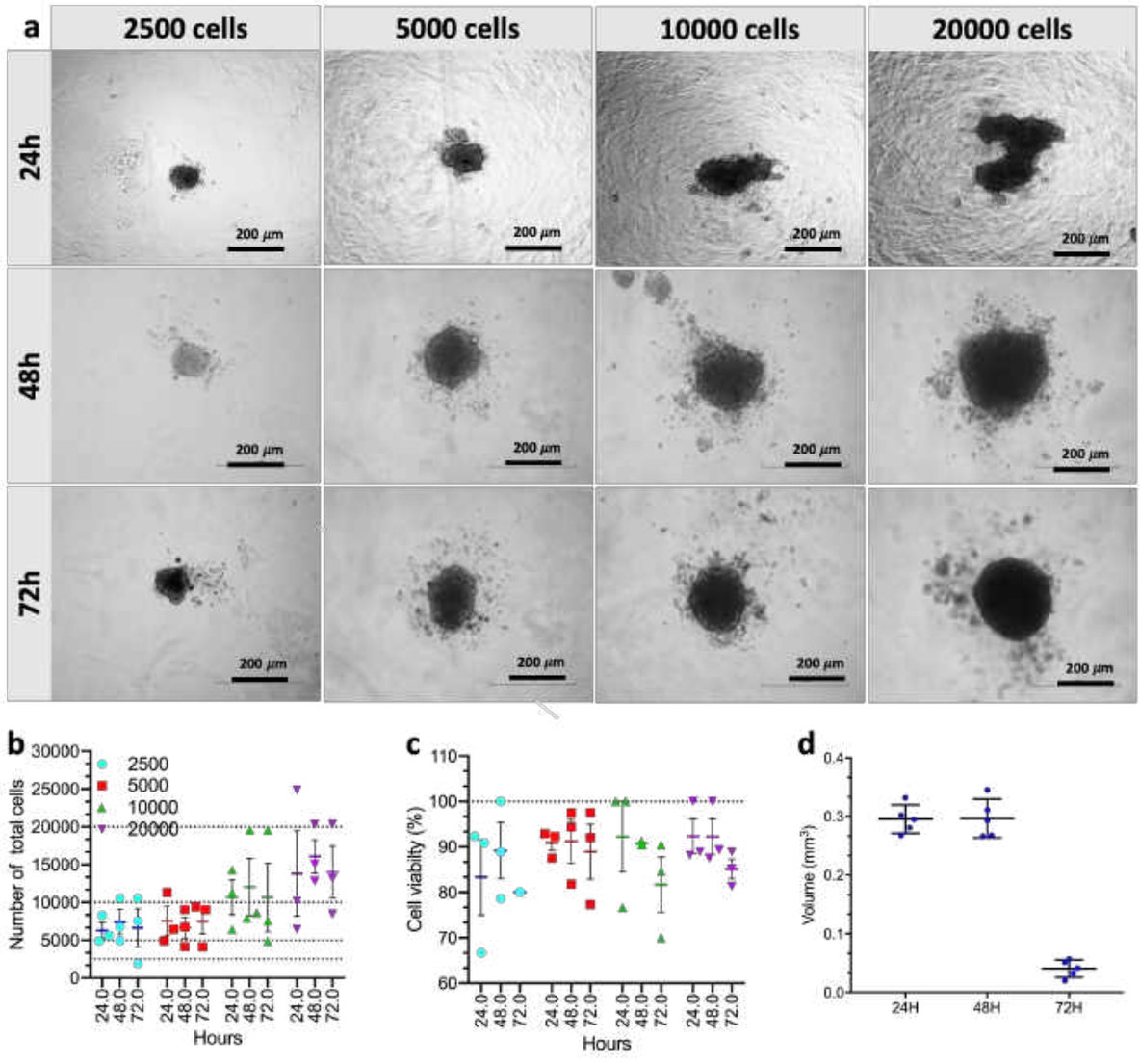


Supplementary Figure V.3. Effect of the conditions (seeding density and culture time) on the formation of spheroids by HS578T cells: (a) Representative optical microscopy images of the aggregates/spheroids; (b) Number of total HS578T cells forming the aggregates/spheroids and (c) their viability (obtained from the ratio between live cells and the total number of cells within the 3D cell structure) as a function of time; (d) volume of the spheroids generated at cell seeding density of 5000 cells/well.

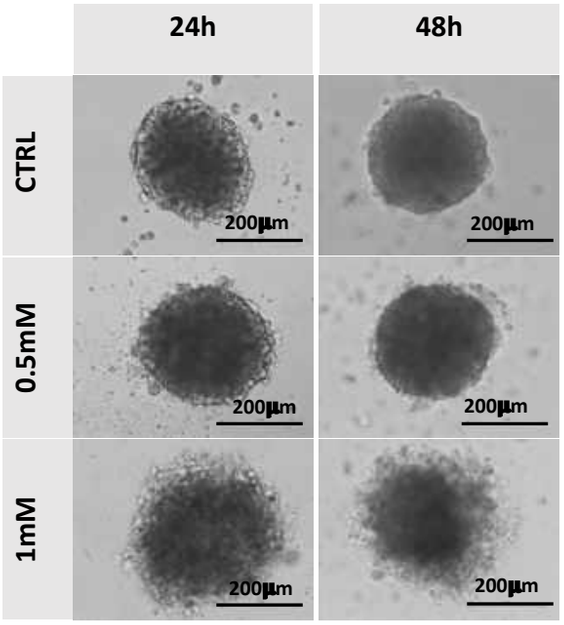


Supplementary Figure V.4. Light microscopy images of untreated spheroids (control, CTRL) and spheroids exposed to 3c at different concentration (0.5 and 1 mM) and for different time (24 and 48h).

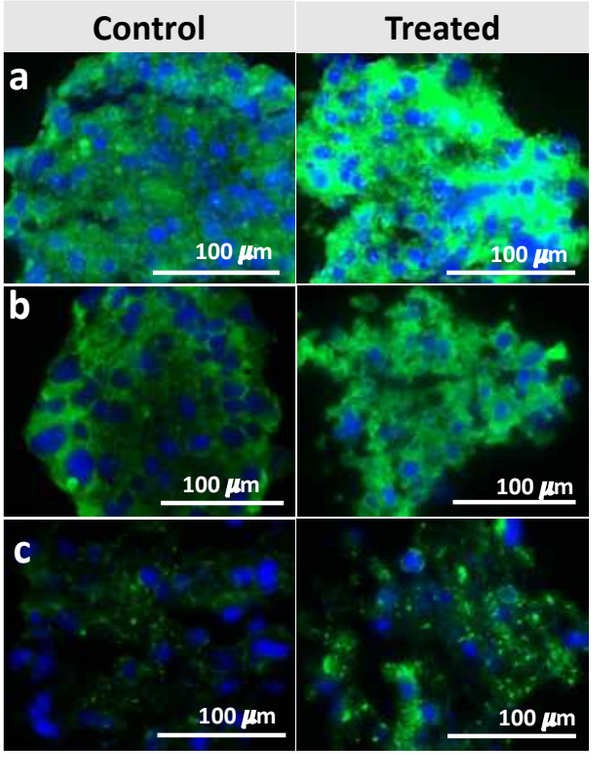


Supplementary Figure V.5. Immunolocalization of (a) ALP, (b) GLUT1, and (c) CAV1 showed by confocal microscopy images of untreated spheroids (control) and spheroids exposed to 3c (1mM, 48h).

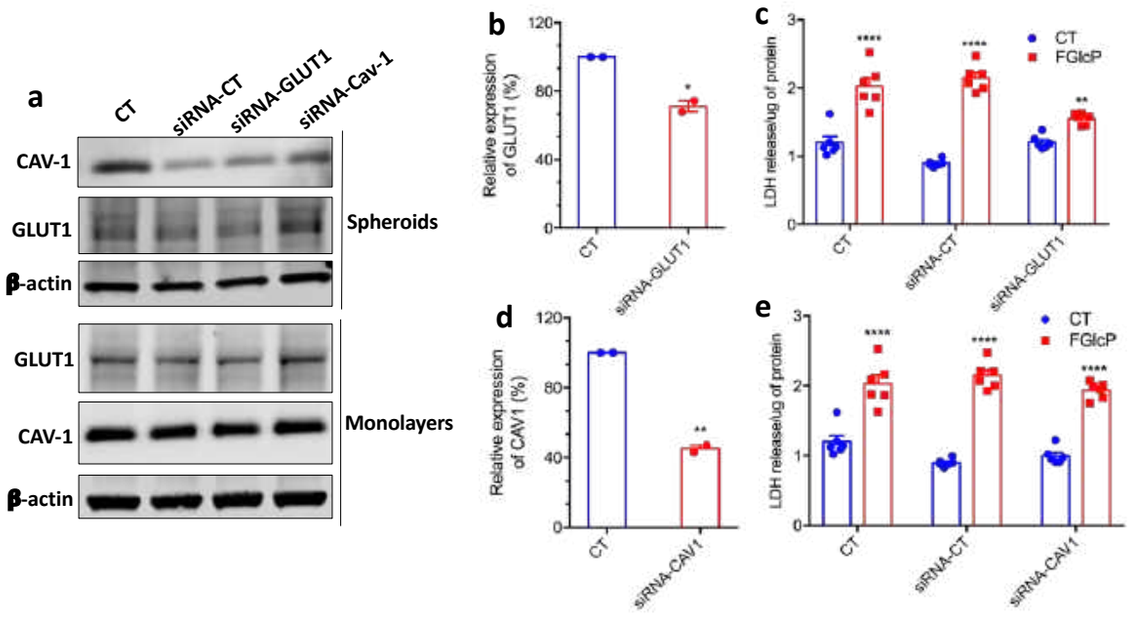


Supplementary Figure V.6. (a) Western Blot analysis and respective densitometry analysis showing the relative expression of (b) GLUT1 and (d) CAV1 in HS587T spheroids after depletion of the respective genes. Controls (CT) for the data presented on Figure V.3 in the main manuscript: effect of (c) GLUT1 and (e) CAV1 knockout on the cell viability determined by LDH release. siRNA-CT is abbreviation used for non-specific siRNA.

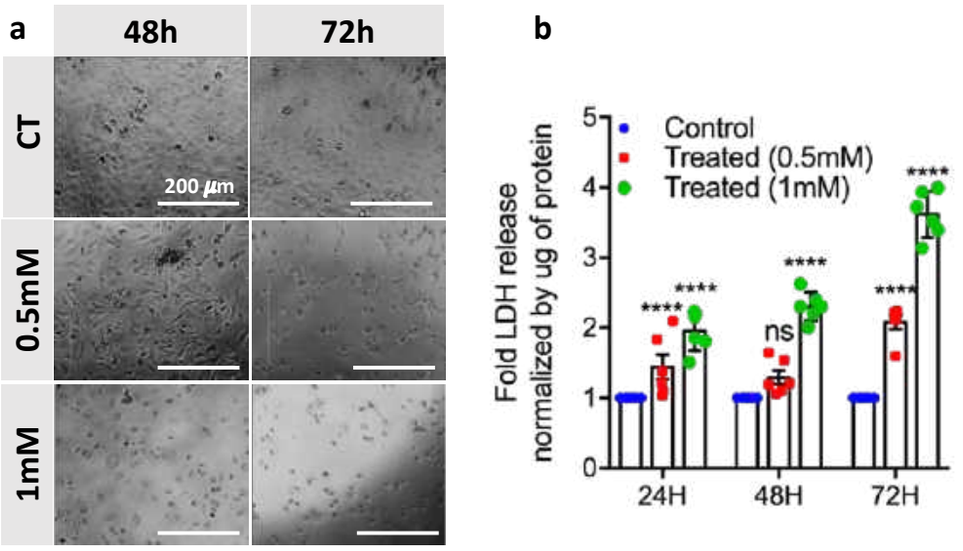


**Supplementary Figure V.7. (a) Representative images of the monolayers of HS578T cells supplemented with 3c (0 - 1mM) for different time (48-72h) and the respective (b) cell viability indicated by LDH release; * $p < 0.01$; ** $p < 0.005$; *** $p < 0.001$; **** $p < 0.0001$.**

## V.5. REFERENCES:

1. Pires RA, Abul-Haija YM, Reis RL, Ulijn RV, Pashkuleva I. Hydrogel Nanomaterials for Cancer Diagnosis and Therapy. In: Singh TRR, Laverty G, Donnelly R, editors. Hydrogels: Design, Synthesis and Application in Drug Delivery and Regenerative Medicine: CRC Press; 2018. p. 170-83.

2. Kim BJ, Xu B. Enzyme-Instructed Self-Assembly for Cancer Therapy and Imaging. Bioconjugate chemistry. 2020;31(3):492-500.

3. Anderson CF, Cui HG. Protease-Sensitive Nanomaterials for Cancer Therapeutics and Imaging. Industrial & Engineering Chemistry Research. 2017;56(20):5761-77.

4. Pires RA, Abul-Haija YM, Costa DS, Novoa-Carballal R, Reis RL, Ulijn RV, et al. Controlling Cancer Cell Fate Using Localized Biocatalytic Self-Assembly of an Aromatic Carbohydrate Amphiphile. Journal of the American Chemical Society. 2015;137(2):576-9.

5. Zhou J, Xu B. Enzyme-Instructed Self-Assembly: A Multistep Process for Potential Cancer Therapy. Bioconjugate chemistry. 2015;26(6):987-99.

6. Wang HM, Feng ZQQ, Xu B. Bioinspired assembly of small molecules in cell milieu. Chem Soc Rev. 2017;46(9):2421-36.

7. Li J, Bullara D, Du X, He H, Sofou S, Kevrekidis IG, et al. Kinetic Analysis of Nanostructures Formed by Enzyme-Instructed Intracellular Assemblies against Cancer Cells. ACS Nano. 2018;12(4):3804-15.

8. Zhou J, Du X, Yamagata N, Xu B. Enzyme-Instructed Self-Assembly of Small d-Peptides as a Multiple-Step Process for Selectively Killing Cancer Cells. J Am Chem Soc. 2016;138(11):3813-23.

9. Zhou ZQ, Xie X, Yi QK, Yin WC, Kadi AA, Li JB, et al. Enzyme-instructed self-assembly with photo-responses for the photo-regulation of cancer cells. Org Biomol Chem. 2017;15(33):6892-5.

10. Duval K, Grover H, Han LH, Mou Y, Pegoraro AF, Fredberg J, et al. Modeling Physiological Events in 2D vs. 3D Cell Culture. Physiology. 2017;32(4):266-77.

11. Pereira PMR, Berisha N, Bhupathiraju N, Fernandes R, Tome JPC, Drain CM. Cancer cell spheroids are a better screen for the photodynamic efficiency of glycosylated photosensitizers. Plos One. 2017;12(5).

12. Brito A, Pereira PMR, Soares da Costa D, Reis RL, Ulijn RV, Lewis JS, et al. Inhibiting cancer metabolism by aromatic carbohydrate amphiphiles that act as antagonists of the glucose transporter GLUT1. Chemical Science. 2020.

13. Barretina J, Caponigro G, Stransky N, Venkatesan K, Margolin AA, Kim S, et al. The Cancer Cell Line Encyclopedia enables predictive modelling of anticancer drug sensitivity. Nature. 2012;483(7391):603-7.

14. Nwosu ZC, Ebert MP, Dooley S, Meyer C. Caveolin-1 in the regulation of cell metabolism: a cancer perspective. Molecular Cancer. 2016;15.

15. Anderson RGW. The caveolae membrane system. Annual Review of Biochemistry. 1998;67:199-225.

16. Fasano A. Glucose Metabolism in Multicellular Spheroids, ATP Production and Effects of Acidity. In: Donofrio A, Cerrai P, Gandolfi A, editors. New Challenges for Cancer Systems Biomedicine. SIMAI Springer Series. 12012. p. 173-90.

17. Warnke E, Pietsch J, Wehland M, Bauer J, Infanger M, Gorog M, et al. Spheroid formation of human thyroid cancer cells under simulated microgravity: a possible role of CTGF and CAV1. Cell Communication and Signaling. 2014;12.

18. Amann T, Maegdefrau U, Hartmann A, Agaimy A, Marienhagen J, Weiss TS, et al. GLUT1 Expression Is Increased in Hepatocellular Carcinoma and Promotes Tumorigenesis. American Journal of Pathology. 2009;174(4):1544-52.

19. Osthus RC, Shim H, Kim S, Li Q, Reddy R, Mukherjee M, et al. Deregulation of glucose transporter 1 and glycolytic gene expression by c-Myc. Journal of Biological Chemistry. 2000;275(29):21797-800.

20. Longati P, Jia XH, Eimer J, Wagman A, Witt MR, Rehnmark S, et al. 3D pancreatic carcinoma spheroids induce a matrix-rich, chemoresistant phenotype offering a better model for drug testing. Bmc Cancer. 2013;13.

21. Chan FK, Moriwaki K, De Rosa MJ. Detection of necrosis by release of lactate dehydrogenase activity. Methods Mol Biol. 2013;979:65-70.

22. Gamrekelashvili J, Kruger C, von Wasielewski R, Hoffmann M, Huster KM, Busch DH, et al. Necrotic tumor cell death in vivo impairs tumor-specific immune responses. Journal of Immunology. 2007;178(3):1573-80.

23. Pereira PMR, Sharma SK, Carter LM, Edwards KJ, Pourat J, Ragupathi A, et al. Caveolin-1 mediates cellular distribution of HER2 and affects trastuzumab binding and therapeutic efficacy. Nature Communications. 2018;9

# Chapter VI

# Minimalistic Supramolecular Proteoglycan Mimics by Co-assembly of Aromatic Peptide and Carbohydrate Amphiphiles

# MINIMALISTIC SUPRAMOLECULAR PROTEOGLYCAN MIMICS BY CO-ASSEMBLY OF AROMATIC PEPTIDE AND CARBOHYDRATE AMPHIPHILES


## Abstract

We report on the co-assembly of aromatic carbohydrate and dipeptide amphiphiles under physiological conditions as a strategy to generate minimalistic proteoglycan mimics. The resulting nanofibers present a structural, fluorenylmethoxycarbonyl-diphenylalanine (Fmoc-FF) core and a functional carbohydrate (Fmoc-glucosamine-6-sulfate or –phosphate) shell. The size, degree of bundling and mechanical properties of the assembled structures depend on the chemical nature of the carbohydrate amphiphile used. In cell culture medium, these nanofibers can further organize into supramolecular hydrogels. We demonstrate that, similar to proteoglycans, the assembled gels prolong the stability of growth factors and preserve the viability of cultured cells. Our results demonstrate that this approach can be applied to the design of extracellular matrix (ECM) substitutes for future regenerative therapies.


---


*This chapter is based on the publication:*

**Brito, Alexandra;** Abul-Haija, Yousef M.; Costa, Diana S.; Novoa-Carballal, Ramon; Reis, Rui L.; Ulijn, Rein V.; Pires, Ricardo A.; Pashkuleva, Iva: "Minimalistic Supramolecular Proteoglycan Mimics by Co-assembly of Aromatic Peptide and Carbohydrate Amphiphiles", Chemical Science, vol. 10, pp. 2385 - 2390, doi:10.1039/c8sc04361b, 2019

## VI.1. INTRODUCTION

Molecular self-assembly is a versatile bottom-up approach for design and synthesis of functional biomaterials.[1-5] The main advantage of this approach is the possibility to create structural and functional biomimetics with simple and systemically customizable compositions.[3-5] As an example, bioactive peptide amphiphiles (PA) of varying complexity have been used as simple functional analogues of various proteins.[2-4] These building blocks can code specific biochemical information and transfer it to the surrounding (biological) environment. Glycosylation, the process of functional decoration of proteins with carbohydrates chains, is the most common post-translational modification that diversifies the proteins' roles by instructing their folding and by activating specific recognition events and different signaling pathways.[6] Attached carbohydrate chains can also have a protective role which contributes to the proteins' stability and activity.[6, 7] So far, these diverse roles of carbohydrates have received little attention, compared to peptides, in the design of molecular self-assembling blocks for the synthesis of functional supramolecular gels.[8-14]

Aiming to develop extracellular matrix (ECM) mimics, recent studies introduced the use of peptide amphiphile (PA) end-on functionalized with carbohydrate moieties.[8-11] Upon assembly of such amphiphiles, the carbohydrate units are exposed on the surface of the assembled fibre and are able to participate in multivalent biospecific interactions. While this approach seems straightforward for generating supramolecular mimics of proteoglycans, the introduction of the carbohydrate unit is challenging in terms of PA synthesis and assembly as it may disturb the delicate balance of forces governing the process of self-organization.[15, 16]

Multicomponent co-assembly offers a possibility to expand the chemical diversity and functional complexity of the supramolecular systems without to compromise the simplicity of the building blocks.[17] The feasibility of this approach has been demonstrated by combination of different PAs.[15-17] We hypothesized that a similar strategy can be also applied for co-assembly of simple carbohydrate amphiphiles (CAs, **3**) and their peptide analogue (**4**) and the result will be a synergistic system mimicking proteoglycans (Scheme VI. 1).

The range of carbohydrates found in biological systems provide a rich library of water soluble, chiral building blocks.[18] Simple carbohydrate amphiphiles (CAs) functionalized with aromatic moieties such as naphthalene and fluorenylmethoxycarbonyl (Fmoc) have been recently developed and shown to form self-assembled structures.[19-21] However, the amphiphiles bearing

naphthalene unit do not form gel and the ones functionalized with Fmoc require a heat-cool cycle or specific enzymatic stimulus to enable the formation of gels at physiological conditions.[19, 20]

Herein, we describe bi-component systems, in which the fluorenylmethoxycabonyl-diphenylalanine (Fmoc-FF) provides the structural component, while the Fmoc-carbohydrate is the solvent-exposed functional element, which can be systematically exchanged (Scheme VI.1). We demonstrate that these modular materials combine the simplicity of small molecules with the versatility and biofunctionality of glycans and proteins, respectively.

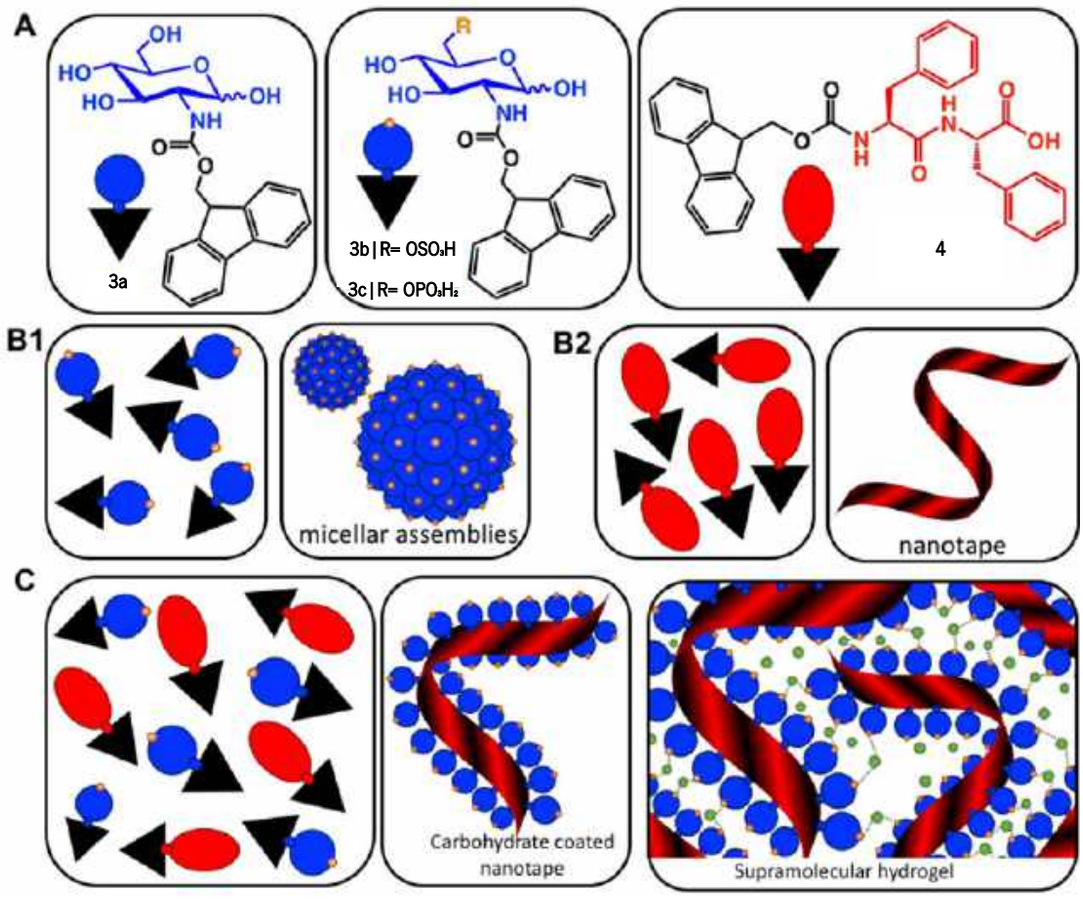


**Scheme VI.1. (a) Chemical structures of the carbohydrate amphiphiles (3) and the peptide analogue Fmoc-FF (4). (b) Schematic presentation of the assembly of the individual components (3) and (4) in water resulting in the formation of**

**micelles and nanotapes, respectively. (c) Co-assembly of (3) and (4) to form carbohydrate functionalized peptide nanotapes and supramolecular hydrogels. Green dots represent divalent cations.**

## VI.2. METHODS

### VI.2.1. Characterization of aromatic carbohydrate amphiphiles

The purity of the samples was determined by HPLC (KANUER, Germany) using a 250 mm x 4.6 mm reverse-phase C18 Atlantis column (Waters, UK), a flow of 1 mL/min, a UV detection wavelength at 280 nm and two buffers: A - water (with 0.1% trifluoroacetic acid, Sigma, Germany); and B - acetonitrile (VWR, with 0.1% trifluoroacetic acid). The HPLC runs comprised an initial step of 4 min under isocratic flow of 80% of buffer A, followed by a gradient to 80% of B at 31 min; this buffer composition (80% of B) was maintained for 5 min, followed by a gradient to 80% of A for 2 min and an isocratic elution (under 80% of A) during 4 min. $^{1}H$ and $^{13}C$ NMR spectra were recorded on Bruker Avance III spectrometer (Bruker, Gemrany) at 25 °C in $D_2O$. The chemical shifts are reported in ppm ($\delta$ units) downfield to the solvent signal. Duplicated signals observed for some protons and carbons correspond to the two anomeric forms. Mass spectra were acquired on an electrospray ionization (ESI) mass spectrometer (MS) Finnigan LXQ (Thermo Electron Corporation, USA) under negative-ion mode.

### VI.2.2. Self-assembly of aromatic carbohydrate amphiphiles (3) and Fmoc-FF (4)

Single component solutions were prepared by dissolving each of the components (**3** and **4**) in water. Fmoc-Glc (10 mM, **3a**) dissolved only upon temperature increase to 80 °C as previously reported.[19] Formation of translucent hydrogel was observed when the obtained solution was cooled down to room temperature. A transparent solution of Fmoc-FF (BiogelX, 10 mM, **4**) was obtained after rising the pH to 11-11.5 (0.5 M NaOH).[23] The pH of this solution was then adjusted to 8 (0.5 M HCl), filtered (0.8 μm syringe filters) and stored at 4 °C for 24 h. No additional adjustments were needed to dissolve Fmoc-GlcN6S (5 mM, **3b**) and Fmoc-GlcN6P (5 mM, **3c**). Each single component solution was characterized by atomic force microscopy (AFM).

Co-assembly of Fmoc-FF and Fmoc-Glc6X (X=S or P) was studied at room temperature. Samples were prepared by suspending Fmoc-FF (10 mM) and Fmoc-GlcN6X at different concentrations (2.5, 5 and 10 mM) in water. A complete dissolution was achieved for the systems obtained with 2.5 and 5 mM

Fmoc-GlcN6X by adding 0.5 M NaOH (pH 11) to the obtained suspension and then vortexing it (Fig. SVI.14). After decreasing the pH to 8 (0.5 M HCl), the solutions were filtered (0.8 μm syringe filters) and characterized by circular dichroism (CD) and fluorescence emission spectroscopy. All results described in the main manuscript were performed with the system Fmoc-FF (10 mM)/Fmoc-GlcN6X (5 mM).

### VI.2.3. Atomic force microscopy (AFM)

(3-Aminopropyl)triethoxysilane (APTES, 200 μL) was dropped on a fresh cleaved mica sheet and let for 30 min at room temperature. Then, the mica was rinsed with deionized water and dry under nitrogen flow. A drop of the above described solutions of CA, PA and CA/PA was deposited on the functionalized mica sheet. AFM images were acquired with a JPK Nanowizard 3 in air at room temperature under AC mode. The scans were acquired at 512 x 512 pixels resolution using ACTA-SS probes (k~37 N/m, AppNano, USA), a drive frequency 254 kHz, setpoint 0.5 V and a scanning speed 1.0 Hz. Images were analyzed using the JPK data processing software. The mechanical properties of the nanofibers were determined under JPK quantitative imaging mode using TAP525 probes (k~200 N/m, Bruker, Germany) calibrated by the contact free method. Approaching force curves were fitted using Hertz model to obtain the elastic modulus (E). The reported E is averaged over 30 measurements.

### VI.2.4. Zeta Potential

The zeta potential of pre-gelation solutions was measured by Nano ZS (Malvern Instruments, Malvern, UK). The mobility of nanostructures was measured and was converted to zeta potential by the software. Size of the assemblies generated from carbohydrate amphiphiles **3b** and **3c** (single component systems) was also determined using this equipment. The measurements were taken after 24 h of sample preparation.

### VI.2.5. Circular dichroism (CD)

40 μL of each amphiphile(s) solution were analyzed using a cuvette of 1 mm pathlength. CD spectra were acquired at 37 °C on a Jasco J-810 spectrometer within the range of 200-400 nm using a bandwidth of 1 nm. Each spectrum was obtained by accumulation of three acquisitions.

### VI.2.6. Fluorescence emission spectroscopy

Fluorescence emission spectra were recorded within the range 300-600 nm using a Jasco FP-6500 spectrofluorimeter. An excitation wavelength of 295 nm and a slit width of 3 nm was used. The data are presented as an average of three measurements.

### VI.2.7. Transmission electron microscopy (TEM)

Carbon-coated copper grids (200 mesh) were glow discharged in air for 30 s. The support film was touched onto the gel surface for 3 s and blotted down using filter paper. Negative stain (20 mL, 1% aqueous methylamine vanadate obtained from Nanovan; Nanoprobes) was applied and the mixture blotted again using filter paper to remove excess. The dried specimens were then imaged using a LEO 912 energy filtering transmission electron microscope operating at 120kV fitted with 14 bit/2 K Proscan CCD camera.

### VI.2.8. Fourier transform infrared spectroscopy (FTIR)

Spectra were acquired using a Bruker Vertex 70 spectrometer with a spectral resolution of 1 $cm^{-1}$. The spectra were obtained by averaging 25 scans per sample. Measurements were performed in a standard IR cuvette (Harrick Scientific), in which the sample was contained between two $CaF_2$ windows (thickness, 2 mm) separated by a 25 μm PTFE spacer. All sample manipulations were performed in a glove box to minimize interference from atmospheric water vapour. $D_2O$ (Sigma-Aldrich) was used as the solvent for all the infrared spectral measurements.

### VI.2.9. Preparation and characterization of the hydrogels

The single component Fmoc-FF hydrogel and its co-assemblies Fmoc-FF/Fmoc-Glc6S and Fmoc-FF/Fmoc-Glc6P were prepared using identical protocol. Briefly, the water solutions described above were mixed with a pipette carefully to homogenize them and to remove any air bubbles. 500 μL of each solution was pipetted into transwell cell culture insert (12 wells, Greiner Bio-one), placed into 12 wells culture plate and 1.5 mL of cell culture medium (Dulbecco's Modified Eagle's Medium, DMEM) was added into the well. The plate was placed in an incubator (37 °C, humidified atmosphere of 5% $CO_2$, 2 h) to complete

the gelation process. After this period, the medium was refreshed and additional 200 μL DMEM were gently pipetted on top of the gel.

As Fmoc-Glc is not soluble at room temperature the gels Fmoc-FF/Fmoc-Glc were prepared following a different procedure. A solution of Fmoc-FF (10 mM) in water was prepared as described above. Then, Fmoc-Glc (5 mM) was added to this solution, the temperature was raised to 80 °C and stirred for 1 h. The obtained clear solution was allowed to cool at room temperature and hydrogelation was assessed by inversion of the reaction vial.

### VI.2.10. Rheometry

The mechanical properties of the hydrogels were measured on a Kinexus Rheometer with an 8 mm/cone-plate geometry. The elastic (G') and viscous (G'') moduli of the hydrogels were recorded as a function of frequency between 0.01 and 10 Hz. A solvent trap was used to keep the sample hydrated and the temperature of the sample was maintained at 37 °C by an integrated temperature controller.

### VI.2.11. Interactions of supramolecular gels with basic fibroblast growth factors (FGF-2)

Among the growth factors, we have selected FGF-2 as it interacts specifically with sulfated glycosaminoglycans. Recombinant human FGF-2 (AF-100-18B) and human FGF-2 enzyme-linked immunosorbent assay development kit (ELISA, 900-K08) were purchased from Peprotech. FGF-2 Antibody (anti-FGF-2), clone bFM-2, 17.5 kDa was purchased from Milipore (05-118).

FGF-2 (1 μg/mL) was added to the solutions of Fmoc-FF, Fmoc-FF/Fmoc-Glc6S and Fmoc-FF/Fmoc-Glc6P prior to gelation. The FGF-2 containing solutions (500 μL) were dropped into transwell cell culture inserts (12 wells, Greiner Bio-one) and 1.5 mL of cell culture medium (Dulbecco's Modified Eagle's Medium, DMEM, Sigma) was added to the well and allowed gelation to occur (2 h). The culture medium was changed and this time point was set as 0. The release of FGF-2 was followed by taking aliquots at different time points (2 h, 24 h, 48 h, 72 h and 7 days) and analyzing the solutions by ELISA following the instructions of the supplier. FGF-2 remaining in the hydrogel was quantified by SDS-PAGE & Western Blot. The gels were frozen at -80 °C for 24 h. After this time, they were destroyed by mechanical force: pipetting up and down until a clear solution was obtained. An aliquot of 20 μL was taken from this solution and boiled in Laemmli buffer. The samples were electrophoretically resolved on 12.5% reducing SDS-PAGE. Proteins were transferred to nitrocellulose membranes (Amersham) using a Pierce Power Station

and blocked with 5% dry milk in TBS containing 0.1% Tween-20 (TBS-T). The membranes were then incubated at 4 °C with the FGF-2 antibody overnight, followed by alkaline phosphatase-conjugated goat anti-mouse IgG (Vector) for 1 h. After each antibody incubation, the membranes were washed with TBS-T. Signals were developed with the Novex AP chromogenic substrate (Invitrogen).

The distribution of the FGF-2 within the gels was visualized by confocal laser scanning microscope (Leica TCS SP8, Leica Microsystems). The hydrogels were permeabilized with Triton (1%), washed (PBS) and then incubated with anti-FGF-2 (1:200, 1 h, room temperature). After washing (PBS), the gels were stained with AlexaFluor 488 anti-mouse goat (1:500, 1h, room temperature), washed (PBS) and observed under the microscope.

### VI.2.12. Determination of thermal stability of FGF2 by enzyme-linked immunosorbant assay (ELISA)

The stability of FGF2 in culture medium at 37 °C was assessed by a human FGF2 standard ABTS ELISA development kit (PreproTech, UK), according to the manufacture's protocol. Briefly, 100 µL/well of 1 µg/mL antiFGF2 was immobilized on a 96-well polystyrene plate (E&K Scientific, Campbell, CA) by incubation at room temperature overnight. The plate was then washed 4 times with phosphate buffer saline (PBS) with 0.05% Tween-20 using 300 µL/well. Next, we added 300 µL/well of block buffer (PBS with 1% Bovine serum albumin) and incubated the plate for 1 h at room temperature, followed by washing with PBS. The FGF2 (4ng/mL) was dissolved in DMEM and incubated at 37 °C. Aliquots of 100 µL were taken at predetermined times, added to microtiter plate and incubated at room temperature for 2 h. After washing, 100 µL/ well of biotinylated Rabbit anti-human bFGF supplemented with D-mannitol was added and incubated for another 2 h. The plate was washed and 100 µL of avidin-anti-bFGF were added to each well and incubated for 30 min. After washing, 100 µL of ABTS substrate solution (Sigma) was added to each well, and incubated at room temperature for color development. The plate was then read at 405 nm with wavelength correction set at 650 nm. The obtained values were used to calculate the concentration of the bioactive FGF2 from a standard curve.

### VI.2.13. Cytotoxicity of the supramolecular gels

The cytotoxic effect of the gels was evaluated by two different protocols for 2D and 3D cell culture. Under each protocol we assayed three cell lines, namely the fibroblast cell line L929 that is recommended by

ISO 109993-5 for testing in vitro cytotoxicity of medical devices; the chondrogenic cell line ATDC5 as we envision soft tissue engineering as possible application of the developed gels; and HeLa as a model for cancer cells. Each cell line was cultured (5% $CO_2$ incubator at 37 °C) on tissue culture polystyrene (TCPS) using the recommended medium (DMEM Low Glucose for L929; DMEM-F12 for ATDC5; and DMEM High Glucose for HeLa) supplemented with 10% fetal bovine serum and 1% Antibiotic/Antimycotic. Upon reaching confluence, the cells were detached from the TCPS with TrypLe (ThermoFisher Sci), centrifuged, and resuspended in the respective medium.

2D cell culture: The cell media and pregelation solutions were heated (water bath) to 37 °C. The gels were formed as described in S4. After gelation the DMEM was replaced by the specific medium (DMEM Low Glucose, DMEM-F12, or DMEM High Glucose) supplemented with 10% fetal bovine serum and 1% Antibiotic/ Antimycotic). This process was repeated 3 times during 24 h to ensure total replacement of the medium. After this period, the top medium from the insert was replaced with a suspension of the respective cell line (L929, ATDC5 or HeLa) at a concentration of $10^5$ cells/gel). The medium was exchanged after 24 h of culture. After 48 h in culture, gels were washed with PBS and incubated with Calcein-AM (Life Technologies) and Ethidium Homodimer-1 (EthE-1, Sigma) in PBS for 10 min. The samples were washed and observed using confocal laser scanning microscope (Leica TCS SP8) with 488 nm (green, Calcein AM) and 633 nm lasers (red, EthE-1).

3D cell culture: Pregelation solution (500 μL) was pipetted into transwell cell culture insert, placed into 12 wells culture plate and 1.5 mL of specific cell culture medium (DMEM Low Glucose, DMEM-F12 or DMEM High Glucose) was added in the well (i.e. no medium was added directly to the pregelation solution). The plate was placed in an incubator (5% $CO_2$, 37°C) for 15 min. After this period, the pregelation solution in the insert was mixed (pipetting up and down several times) and the media from the plate was replaced. This process was repeated 3 times. Cell suspension (150 μL, $2.5\times10^5$ cells/gel) was then added into the insert (pipetting up and down several times to mix well) and the plate was incubated again. After gelation (2 h) the media from the bottom of the insert was replaced and 200 μL of fresh medium was added on top of the gel. The medium was exchanged after 24 h of culture. After 48 h in culture, the gels were processed as described above for the 2D culture.

Cell viability: The cell viability was quantified with CellProfiler image analysis software (version 3.0) using the confocal images (at least three per sample) of a live/dead staining. Live cells (green signal) and dead cells (red signal) were separated from the background using Otsu threshold method and the clumped cells were separated by shape. Cells that were stained simultaneously in green and red were counted as death cells. The cell viability is presented as percentage of live cells from the total of number of cells.

## VI.3. RESULTS AND DISCUSSION

### VI.3.1. Self-assembly of aromatic carbohydrate amphiphiles (3) and Fmoc-FF (4)

The amphiphiles Fmoc-glucosamine-6-phosphate (Fmoc-Glc6P, **3c**) and Fmoc-glucosamine-6-sulfate (Glc6S, **3b**) and were obtained from the respective glucosamines in a single-step reaction using an excess of Fmoc chloride (details on the synthesis and chemical characterization of the amphiphiles are provided in the SI, Fig. S VI.1-S13). Fmoc-Glc (**3a**) is not soluble in water at room temperature. Upon temperature rising (80 °C), it dissolves and organizes spontaneously into nanofibers that, at room temperature, form a highly hydrated scaffold (Fig. VI. 1a).[19] On the other hand, Fmoc-FF (**4**) dissolves in water only at basic pH (~11) and self-assemble upon pH decrease.[24-26] The assembly of 4 is controlled by peptidic hydrogen bonds that results in the formation of β-sheet-like structures that are further stabilized by aromatic π-π interactions, whilst the organization of **3a** is driven by a combination of CH-π and π-π (T-shape) stacking interactions.[19, 23, 25]

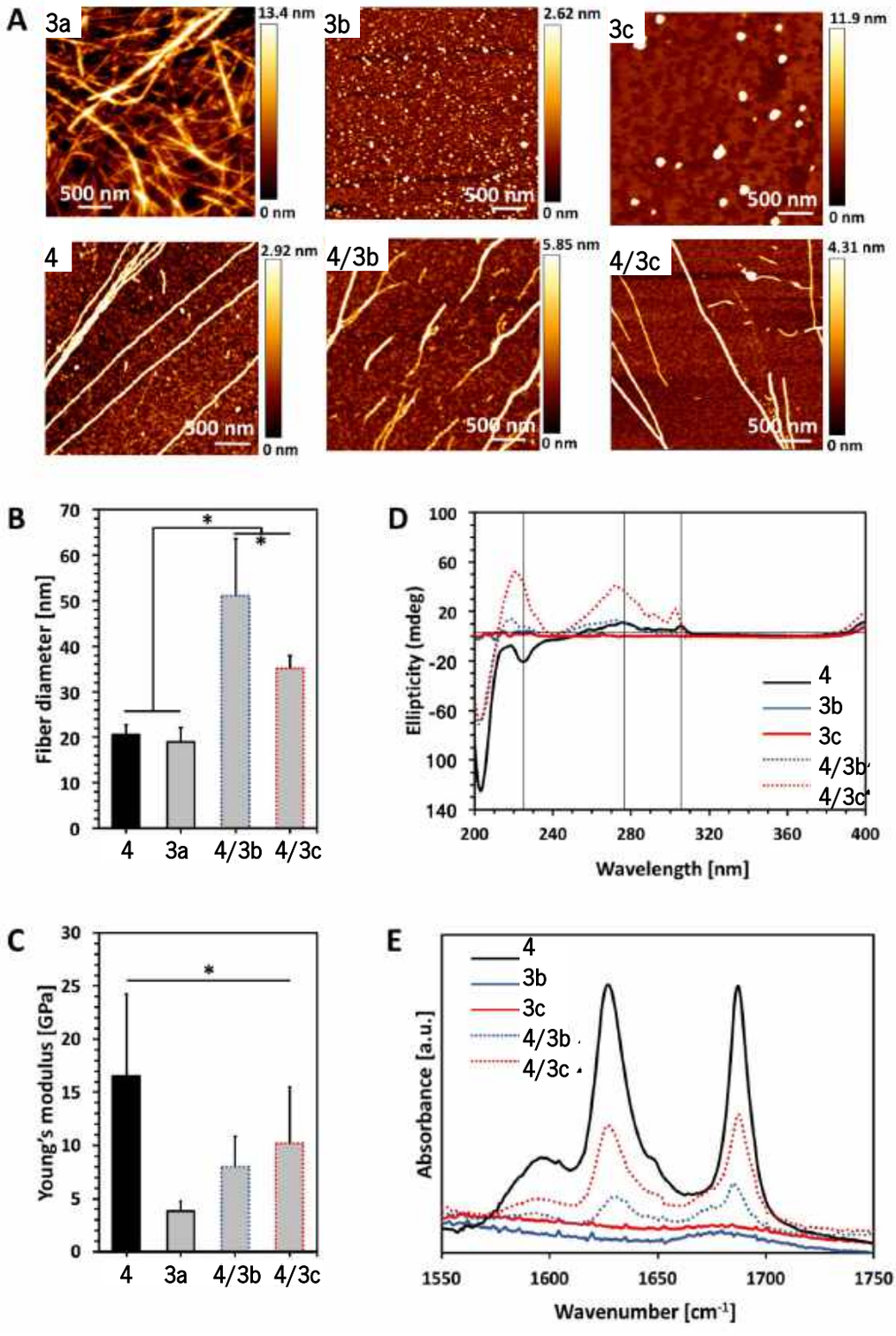


Figure VI.1. Characterization of single (10 mM) and bi-component (ratio PA:CA 2:1) assemblies: (a) AFM images; (b) Fibre diameter and (c) Young's modulus of the assembled fibres measured by AFM; (d) CD spectra of the PA Fmoc-FF (4, its CA analogues Fmoc-Glc6S (3b) and Fmoc-Glc6P (3c), and the respective co-assemblies; (e) FTIR spectra of the precursor amphiphiles and their co-assemblies. Statistically significant difference ($p < 0.01$) are marked with (*). Of

**note, Fmoc-Glc (3a, 10mM) was dissolved at 80 °C and the solution gels upon its cooling to room temperature and thus, AFM analysis was performed on a gel.**

We compared the properties of the formed assemblies by AFM (Fig. VI.1b, c, black outlines) and found that the fibres have similar size but their Young's moduli are significantly different: the PA 3 assembles in very rigid fibres (~16 GPa) that have 4-fold higher modulus than the ones obtained from the carbohydrate analogue **3a** (~4 GPa).

The co-assembly of **4** and **3a** is challenging as both compounds have limited solubility in water and dissolve at different conditions. We functionalized **3a** with polar groups aiming to improve the solubility and to impart relevant functionality. Sulphate groups (**3b**) were chosen because of their biological relevance: most ECM glycosaminoglycans are sulphated and they interact specifically with other biological entities (involved in cell-cell and cell-ECM interactions) depending on their sulphation patterns.[6] On the other hand, carbohydrates internalized by cells are activated *via* their functionalization with phosphate groups and thus, we have also chosen this functionality (**3c**). As expected, incorporation of these functional groups resulted in improved solubility and affected the assembly of Fmoc-Glc6S (**3b**) and Fmoc-Glc6P (**3c**): the introduced polar, negatively charged groups cause electrostatic repulsion between the modified CA thus, disturbing the unidirectional assembly observed for 3a. Such Coulomb forces favour self-assembled morphologies with high surface to volume ratio. Indeed, **3b** and **3c** form micellar assemblies with negative zeta potential (-112.0 ± 23.7 mV for 3c and -74.4 ± 5.3 mV for 3b), indicating that the sulphate group of **3b** and the phosphate group of **3c** are displayed on the surface of the micelles formed in water (Fig. II.1A). Of note, the micelles of **3c** are bigger (swollen) than the ones assembled from **3b** due to the different Coulomb forces (Fig. S VI.17). The circular dichroism (CD) analysis supports the AFM results: no signals were observed in the CD spectra of **1b** and **1c** (Fig. VI.1D).

Co-assembly of **4** with either **3b** or **3c** was performed in water at room temperature. The respective amphiphiles were dissolved at basic pH (~11) at different ratios (i.e. PA:CA of 2:0.5, 2:1, 2:2) but transparent solutions were observed only for the ratios 2:0.5 and 2:1 (Fig. S VI.14). The pH was then adjusted to 8 by drop-wise addition of HCl. CD spectra of these solutions were recorded 24 h after the pH adjustment and indicated formation of assemblies that clearly differ from **3** (Fig. VI.1D, S VI.18). The peak at 204 nm is associated with $\pi$-$\pi^*$ transition and is clearly observed for all systems that contain 3. Formation of a superhelical arrangement (n-$\pi^*$ transition) is shown by the signal at 225 nm in the spectrum of **4**.[23, 27] A blue shift of this peak, observed in

the mixed systems (217 nm for **4**/**3c** and 220 nm for **4**/**3b**), indicates changes in the superhelical structure.[28, 29] This shift was concomitant with polarity change upon addition of CAs and increased intensity especially for **4**/**3b**, indicating co-assembly of the CAs with **4**. Signals associated with the π-π* transition of the Fmoc groups (the signal with maximum at 278 nm and the peak at 306 nm in the spectrum of **4**, Fig. VI.1D) are also blue-shifted in the spectra of the mixed systems confirming co-assembly.[27]

TEM and AFM characterization corroborated the CD and fluorescence data. The co-assembled fibres differ from the single component fibres in several aspects: both **4**/**3c** and **4**/**3b** fibres are bundled (and appear branched), thicker and less stiff than the Fmoc-FF fibres (Figs. VI.1a-c and S VI.16, S20). Furthermore, the co-assembled fibres have higher Young's moduli compared to the single component CA (**3a**) fibres, *i.e.* the co-assemblies have intermediate mechanical properties when compared with the PA and CA single component fibres. FTIR spectroscopy was also performed to characterize the co-assemblies (Fig. VI.1e).[30, 31] Absorptions at 1625 and 1687 $cm^{-1}$ are associated with formation of H-bonding by Fmoc-peptide amide and carbamate groups.[32] As expected, these peaks are missing in the spectra of CA (**3b** and **3c**) solutions. On the other hand, the amide I peaks are clearly observed for the co-assembled systems (**4**/**3c** and **4**/**3b**) demonstrating that the β-sheet structure remains intact in the presence of the CA although the lower intensity of these peaks suggest that a degree of intercalation might have occurred.

Previously, different models for assembly of two-component systems have been proposed.[16, 17, 31] Our results (AFM; CD and FTIR spectra) indicate that **4** co-assembles with **3b** and **3c** into core-shell nanofibers with the carbohydrate moieties exposed on the surface. Such co-assembly would involve intercalation between the Fmoc moieties of the CA and PA on the formed fibre surface (Scheme VI.1b), thus shielding the hydrophobic Fmoc while exposing the carbohydrate unit.[31] We studied the surface charge of the formed nanofibers in order to confirm this organization (Table S VI.1). The value determined for **4** was -0.04 mV, which agrees with our previous work showing that the apparent $pK_a$ of the terminal carboxylic acid in **4** is substantially shifted due to the favoured self-assembly of the uncharged form.[24] The co-assembled systems **4**/**3c** and **4**/**3c**b have negative zeta potentials, -56.0 ± 1.5 mV and -55.4 ± 6.1 mV respectively. As expected, the absolute values are smaller than the ones of the precursor CAs due to the lower density of the functional groups on the co-assembled fibres as compared with the single component micelles. These results further

confirm our hypothesis for co-assembly resulting in the formation of systems with peptide-based core and carbohydrate shell.

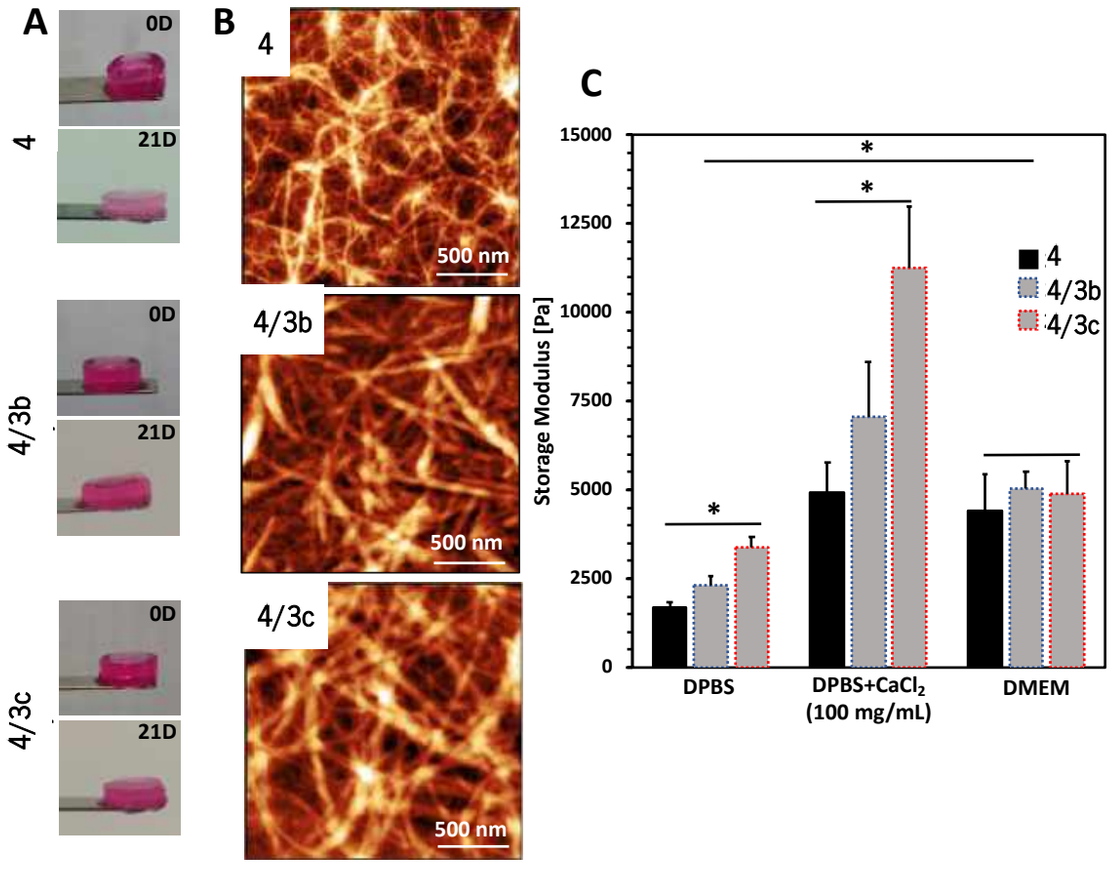


**Figure VI.2. Characterization of the formed gels: (a) Optical images showing gels macroscopic integrity after formation in cell culture medium (DMEM) at 37 °C (0D) and after immersion for 21 days at the same conditions (21D); (b) Tangled nanofibrous structures observed by AFM; (c) Mechanical properties of the gels determined by rheology. DPBS: Dulbecco's Phosphate-Buffered Saline (with no $Ca^{2+}$ and $Mg^{2+}$); DMEM: Dulbecco's Modified Eagle's Medium; DMEM was supplemented with 10% fetal bovine serum.**

### VI.3.2. Characterization of the supramolecular gels

Upon contact with cell culture medium (pH 7.4), the PA **4** and its co-assemblies with the CAs form self-sustained macroscopic gels (Fig. VI.2a).

We used AFM to analyse the gels and observed typical entangled fibrous network for all studied compositions (Fig. VI.2B, S VI.21). However, two major differences can be observed in the AFM images: fibres of **4** are thinner and more entangled compared to the ones generated by co-

assembly (**4**/**3c** and **4**/**3b**). These differences are also reflected in the viscoelastic properties of the gels: mixed systems form more robust gels in all studied media (Fig. VI.2c, S VI.23). Previous studies have demonstrated that gelation of similar PA systems can be either pH- or salt-triggered via formation of salt bridges between the anions exposed on the fibres surface. (Scheme VI.1c).[33] Our rheological studies confirmed such double-stimuli triggered gelation: upon reduction of the pH by adding Dulbecco's Phosphate-Buffered Saline (DPBS, pH 7.4, only monovalent cations), we observed formation of soft gels. The moduli of the formed gels increase significantly in the presence of divalent $Ca^{2+}$ cations (Fig. VI.2d, DPBS+$CaCl_2$). This difference depends on the anions exposed on the fibre surface and we observed the following order $HPO_4^{2-}/H_2PO_4^-$ (**4**/**3b**, 3.3-fold increase) > $SO_4^{2-}$ (**4**/**3c**, 3-fold increase) > $COO^-$ (3, 2.7-fold increase). These results confirmed that the carbohydrate units are exposed on the fibres' surface.

After confirming the exposure of the carbohydrate units on the fibre surface and their ability to form gels under physiological conditions, we evaluated the bioactivity of the generated co-assemblies by their ability to interact specifically with proteins. We designed two experimental setups to evaluate two fundamental roles of proteoglycans in the ECM: the ability of the assembled gels to protect growth factors and to host cells.

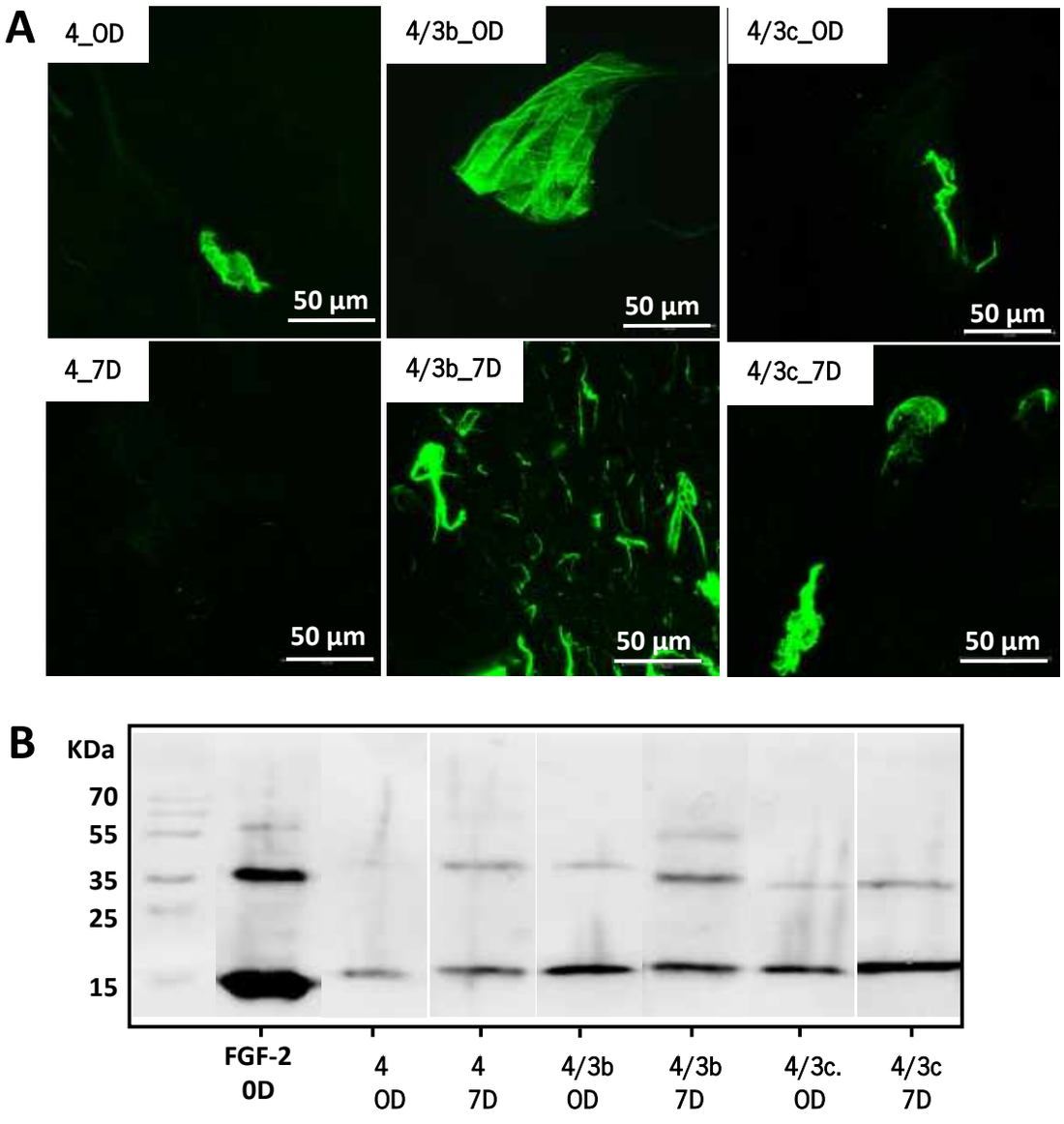


Figure VI.3. Interaction of one- and bi-component supramolecular hydrogels with FGF-2: (a) bioactive FGF-2 (green) distribution and stability within the gels demonstrated for 0 and 7 days by confocal imaging and immunostaining. Of

note, FGF-2 was not homogenised intentionally to facilitate the visualization of the growth factor by fluorescent microscopy; (b) SDS-PAGE analysis of FGF-2 entrapped (0D) and preserved in the hydrogel after 7 days.

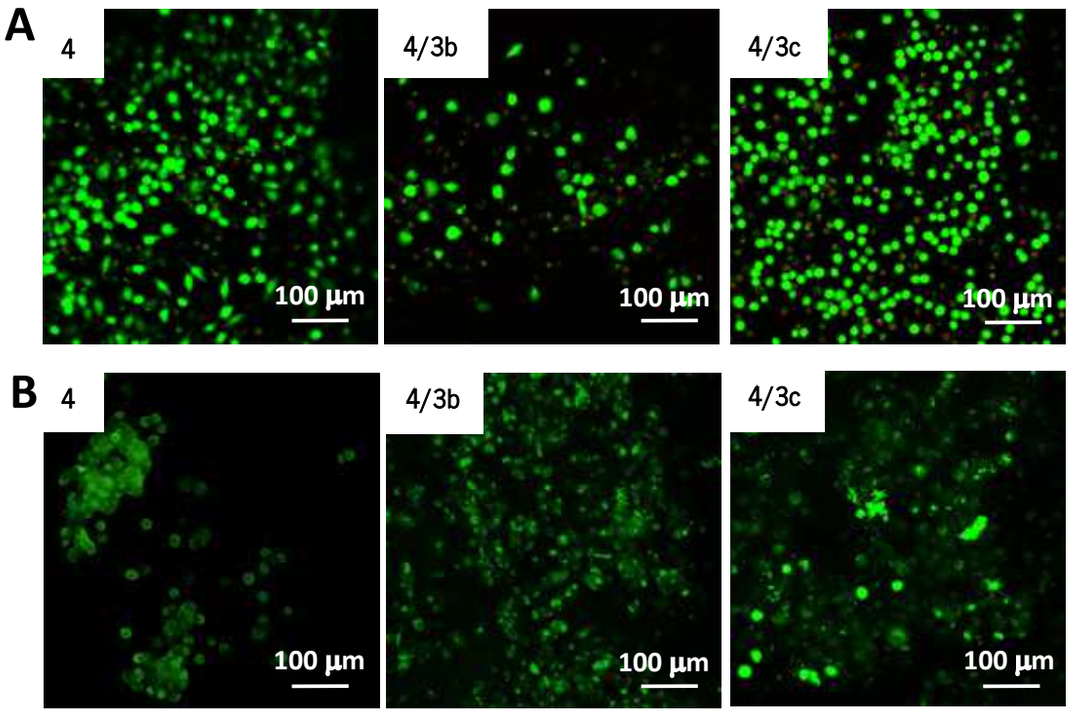


Figure VI.4. Live/dead assays for L929 cultured (a) on top of the gels or (b) encapsulated within the gels for 48 h. Dulbecco's Modified Eagle's Medium (DMEM) was used for these tests.

### VI.3.3. Interactions of the supramolecular gels with basic fibroblast growth factors (FGF-2)

Basic fibroblast growth factor (FGF-2) is a glycoprotein known for its thermal instability: it loses most of its activity after 24 h of incubation at 37 °C (Fig. S VI.24). In its native environment – the pericellular space – FGF-2 interacts specifically with cell surface proteoglycans functionalized with sulphated glycosaminoglycans as heparins/heparan sulphates and chondroitin sulphates, which protect it from degradation and aggregation.[6] Indeed, addition of heparin or heparan sulphate to the FGF-2 incubation media prolong its activity.[34-36] We therefore tested the developed systems for their capacity to protect FGF-2 and preserve its bioactivity (Fig. VI.3).[9] We encapsulated the growth factor in the gels without to homogenise it in order to facilitate the visualization of the bioactive FGF-2 by confocal microscopy (green staining is indication of bioactivity of the growth factor as it is generated upon specific binding of a labelled antibody to FGF-2). Our results demonstrated that mixed systems entrapped more FGF-2 in its bioactive form and protect it from degradation for at

least 7 days. ELISA tests did not show any release of the growth factor in the surrounding media for this period of time. The immunostaining and SDS-PAGE data revealed differences in the distribution and amount of the FGF-2 in **4**/**3c** and **4**/**3b**: stronger co-localization (Fig. VI.3a) and more protein (Fig. VI.3b) is visible for the FGF-2 loaded in the mixed systems.

### VI.3.4. Cytotoxicity of the supramolecular gels

Next, we tested the cytotoxicity of the gels. Initially, we used L929 cells that are recommended for standard *in vitro* cytotoxicity tests. Our results demonstrate that cells remain viable either when they are seeded on top of the gels (Figs. VI.4a, S VI.27) or when they are encapsulated inside the gels (Figs. VI.4b, S VI.27). Chondrogenic cell line ATDC5 (Fig. S VI.25) and epithelial HeLa cells (Fig. S VI.26) were also tested with the assembled materials to prove their versatility. In all the cases, we observed a majority of viable cells (Fig. S VI.27). The culture of these cell lines requires the use of media supplemented with proteins (10% fetal bovine serum, FBS) that can affect the mechanical properties of the gels.[37] Our results demonstrated that indeed the presence of proteins affect significantly the storage moduli of the gels: when DPBS supplemented with $CaCl_2$ was replaced with DMEM (same $Ca^{2+}$ concentration) supplemented with FBS we observed significant decrease of the storage moduli, especially for the co-assembled systems (Figs. VI.2c, S VI.23). Of note, the substitution of DMEM by DMEM/F12 does not induce any significant change in the mechanical properties of the gels (Fig. S VI.23). This data suggests that the proteins from the medium interact with the mixed systems and disrupt partially the ionic crosslinking bridges between different nanofiber segments. As the mechanical properties of the assembled gels at cell culture conditions are very similar, we suggest that the observed different number of adherent/encapsulated cells is due to the different chemistry of the generated supramolecular systems and their specific interactions with the cultured cells.

We have successfully designed and synthesized supramolecular, functional glycoprotein mimics by co-assembly of simple building blocks. In spite of the building blocks' simplicity, the proposed approach has several other advantages: the assembly is carried out under physiological conditions, the formed hydrogels are stable, non-cytotoxic and biofunctional. We also demonstrated that by changing the chemical design in a systematic way we are able to control the biofunctionality and mechanical properties of the supramolecular gels – features that are of key importance in the design of materials for biomedical and tissue engineering applications.

## VI.4. SUPPLEMENTARY INFORMATION

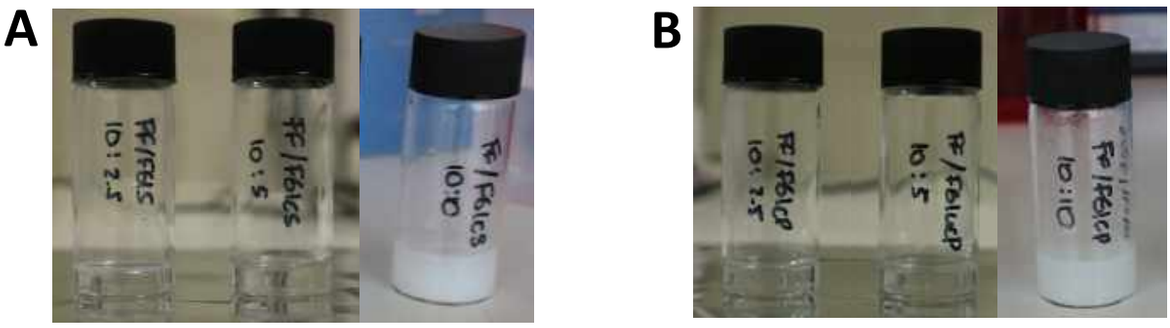


Supplementary Figure VI.1. Water solutions of 10 mM Fmoc-FF (4) with either (a) Fmoc-Glc6S (3b) or (b) Fmoc-Glc6P (3c) at concentrations 2.5, 5 and 10 mM.

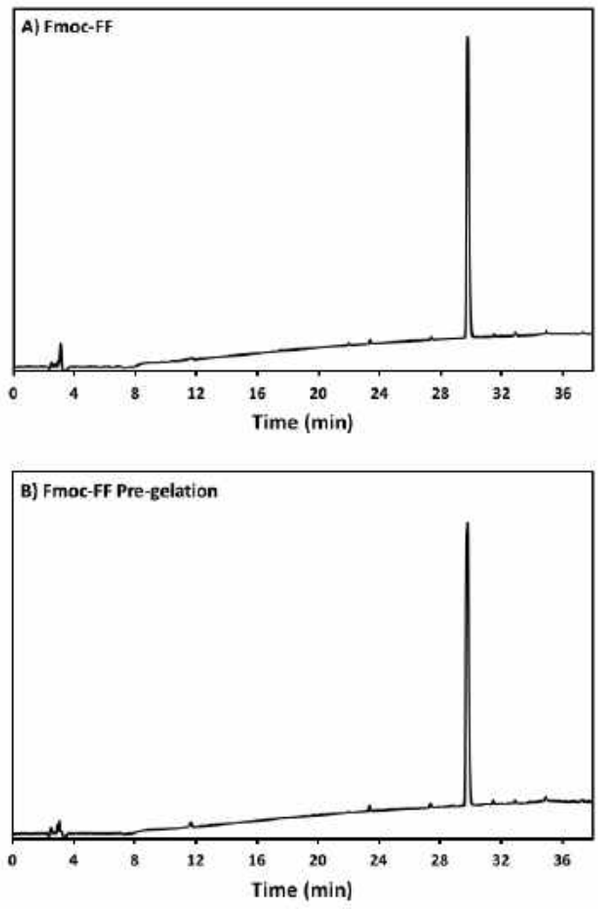


Supplementary Figure VI.2. HPLC runs of Fmoc-FF before (a) and after (b) solubilization in water using basic pH. No Fmoc cleavage was observed after the solubilization.

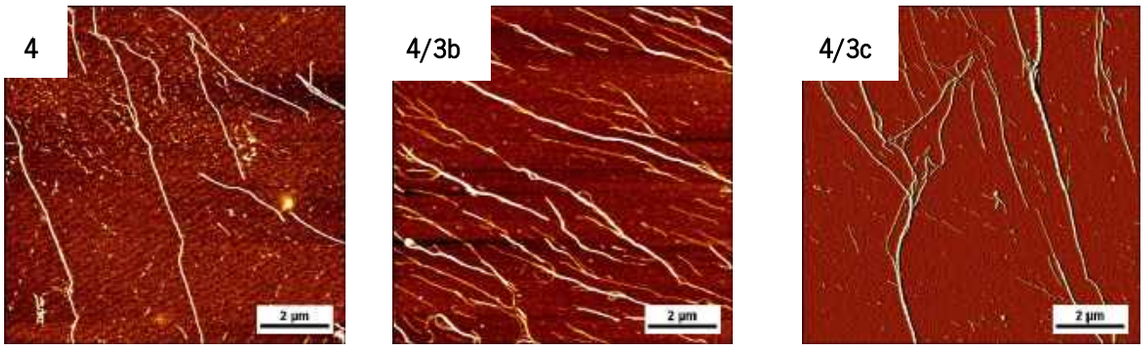


**Supplementary Figure VI.3. Supplementary AFM images for the studied systems. The used concentrations were 10 mM for (4) and 5 mM for (3b) and (3c).**

**Supplementary Table VI.1. Dimensions (determined by AFM) and zeta potential (determined by dynamic light scattering, DLS) of single and bi-component fibers**

| Components | Fiber height [nm] | Fiber width [nm] | ζ-Potential [mV] |
|---|---|---|---|
| Fmoc-FF | 2.8 ± 0.5 | 20.6 ± 2.2 | 0.0 ± 0.0 |
| Fmoc-Glc | 4.6 ± 1.3 | 19.0 ± 3.1 | –* |
| Fmoc-FF/Fmoc-Glc6S | 9.1 ± 1.1 | 51.1 ± 12.5 | -56.0 ± 1.5 |
| Fmoc-FF/Fmoc-Glc6P | 5.4 ± 1.2 | 35.1 ± 2.9 | -55.4 ± 6.1 |

* Limited solubility

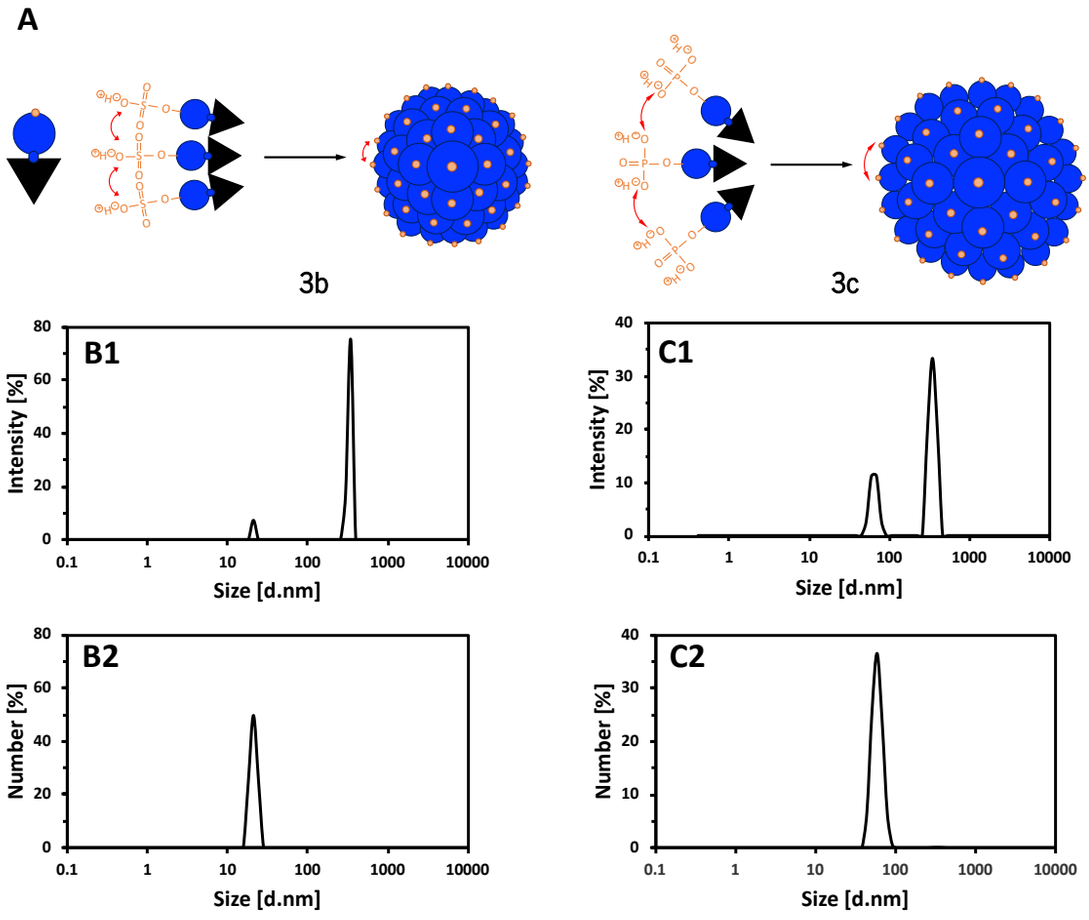


Supplementary Figure VI.4. Schematic presentation (a) and dynamic light scattering data about size for single component assemblies in water of 3c (b) and 3b (c) at concentration 10 mM. The intensity distribution (b1 and c1) showed presence of aggregates but the number distribution (b2 and c2) and the polydispersive index (PDI: 0.5 for 4b and 0.4 for 4c) indicated that their concentration is relatively low.

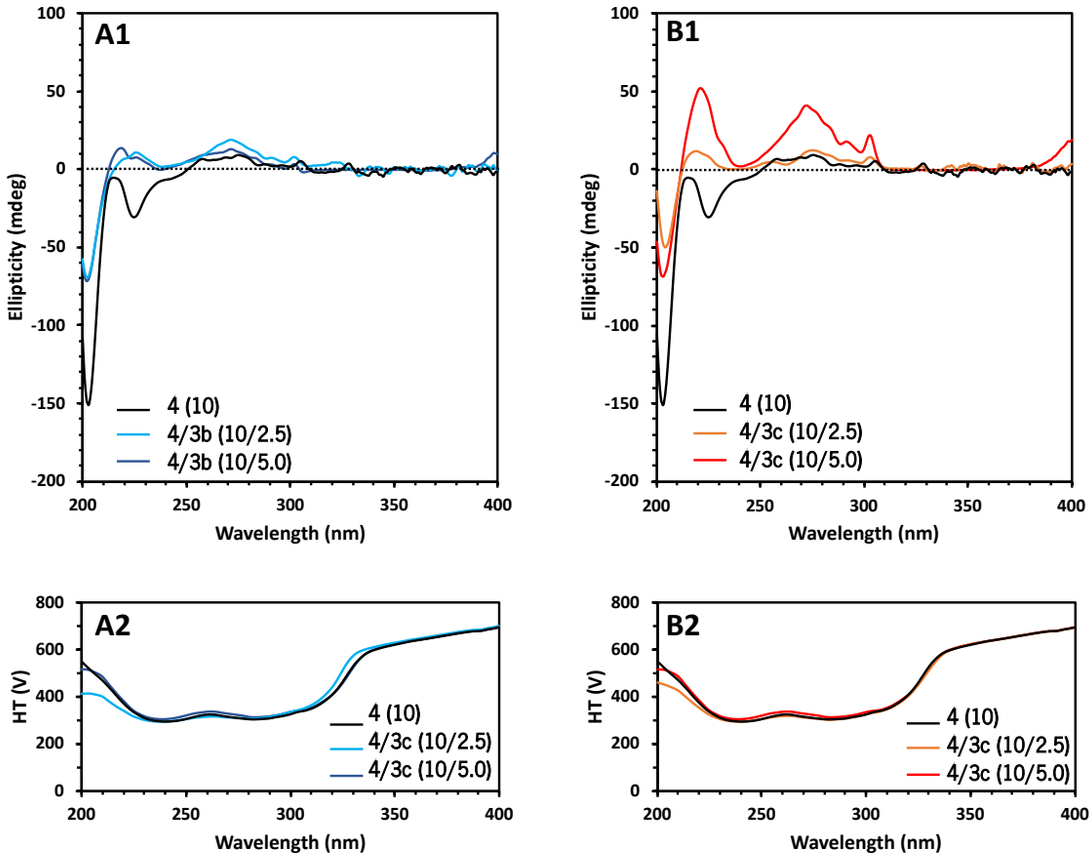


Supplementary Figure VI.5. CD (A1, B1) and HT (A2, B2) spectra of the peptide amphiphile Fmoc-FF (3, 10 mM) and its co-assemblies with carbohydrate analogues GlcN6S (4b) and GlcN6P (4c) at different ratios.

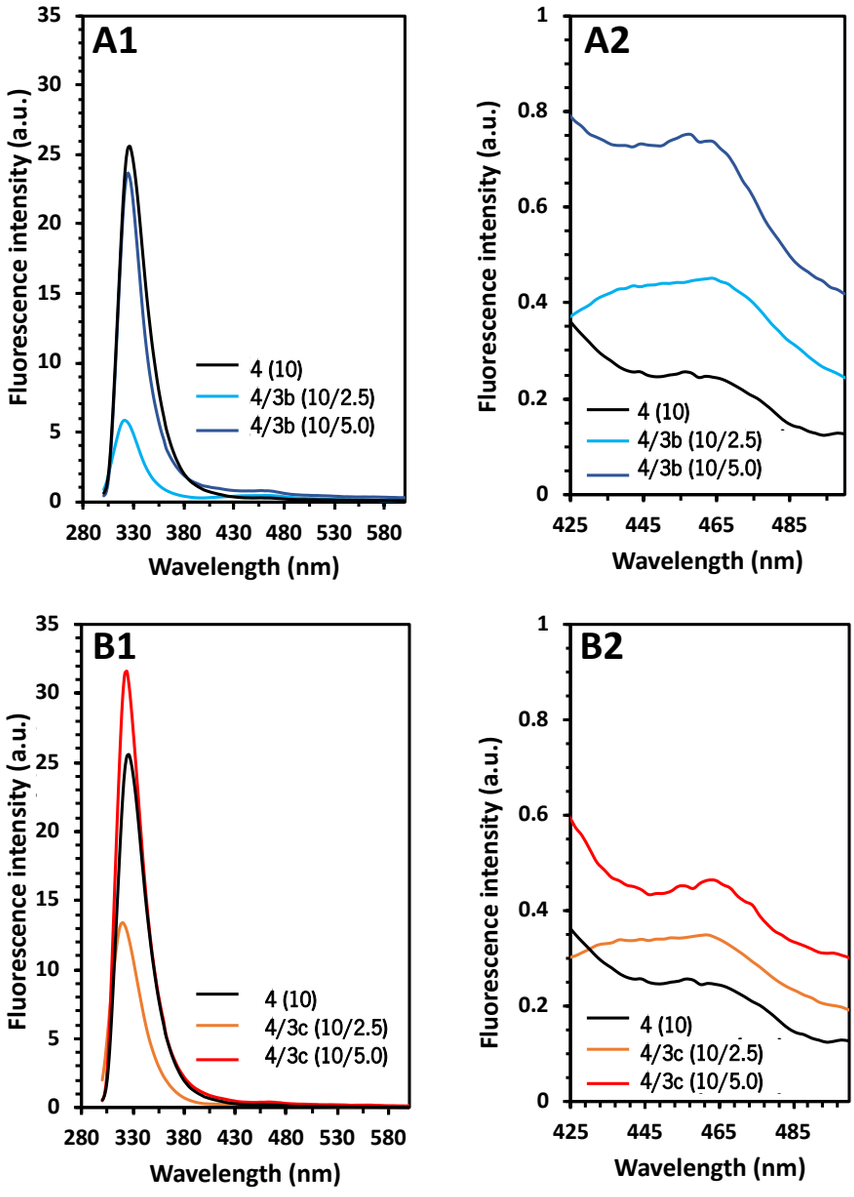


Supplementary Figure VI.6. Fluorescence spectra of solutions of Fmoc-FF (3, 10 mM) and its mixtures (a) Fmoc-FF/Fmoc-GlcN6S (4/3b) and (b) Fmoc-FF/Fmoc-GlcN6P (4/3c) at different ratios.

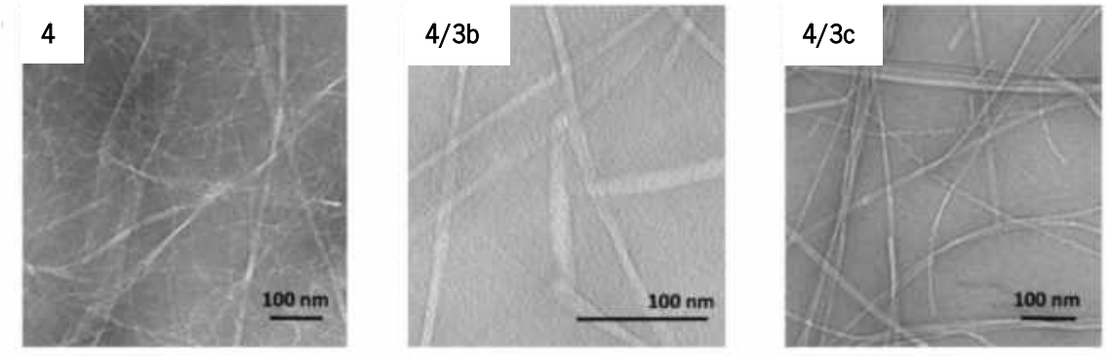

**Supplementary Figure VI.7. TEM images of the fibers obtained by self-assembly of the Fmoc-FF (4,** 10 mM**) and its co-assemblies with the carbohydrate amphiphiles Fmoc-GlcN6S (3b,** 5 mM**) and Fmoc-GlcN6P (3c,** 5 mM**).**

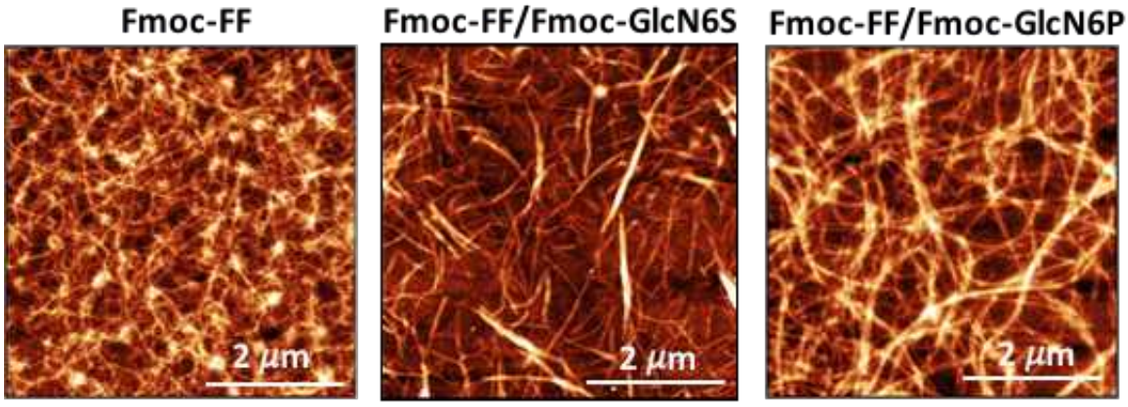


**Supplementary Figure VI.8. Supplementary AFM images for the supramolecular hydrogels obtained by assembly of Fmoc-FF (4, 10 mM), Fmoc-FF/Fmoc-GlcN6S (4/3b, 10 mM/5 mM) and Fmoc-FF/Fmoc-GlcN6P (4/3c, 10 mM/5 mM).**

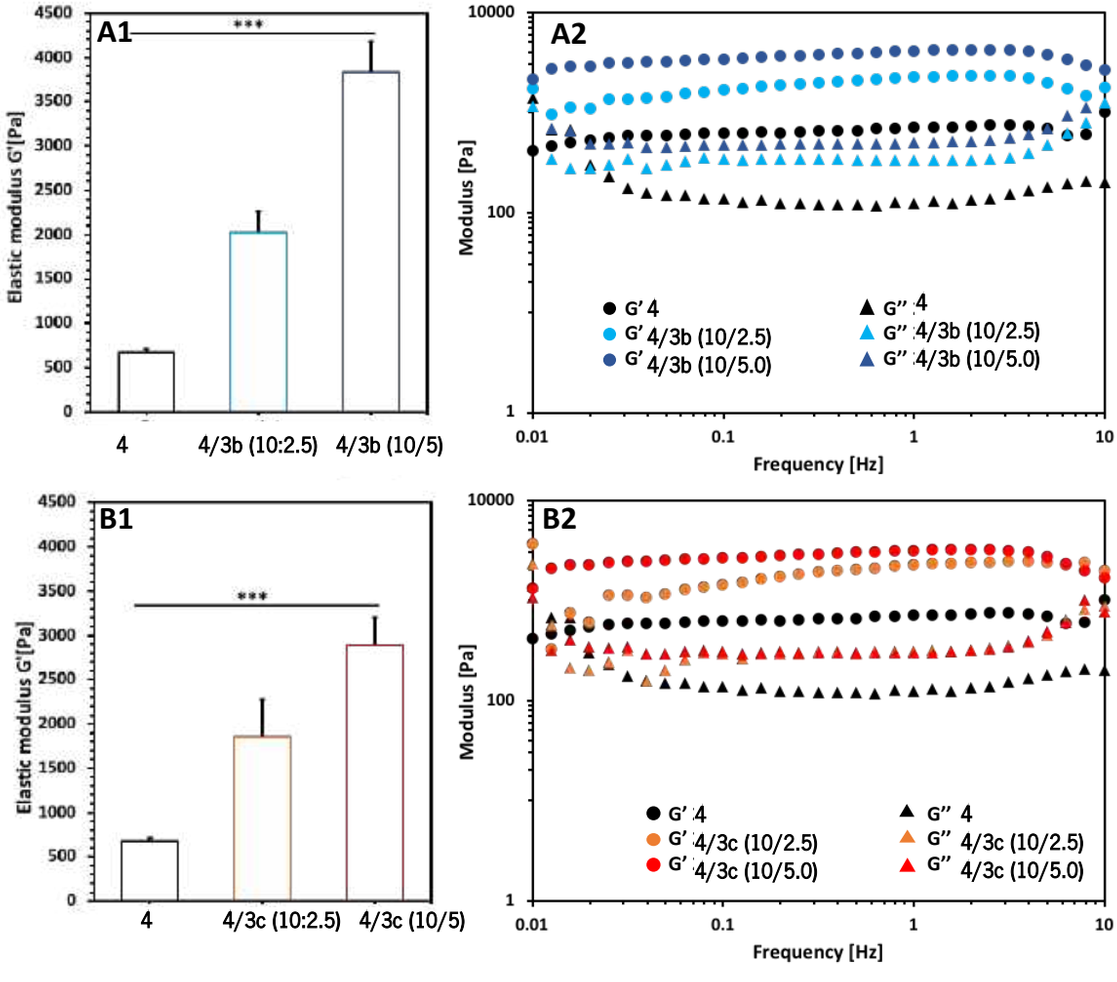

Supplementary Figure VI.9. Rheology data illustrating the effect of carbohydrate amphiphiles (a) Fmoc-GlcN6S (3b) and (b) Fmoc-GlcN6P (3c) on gel stiffness.

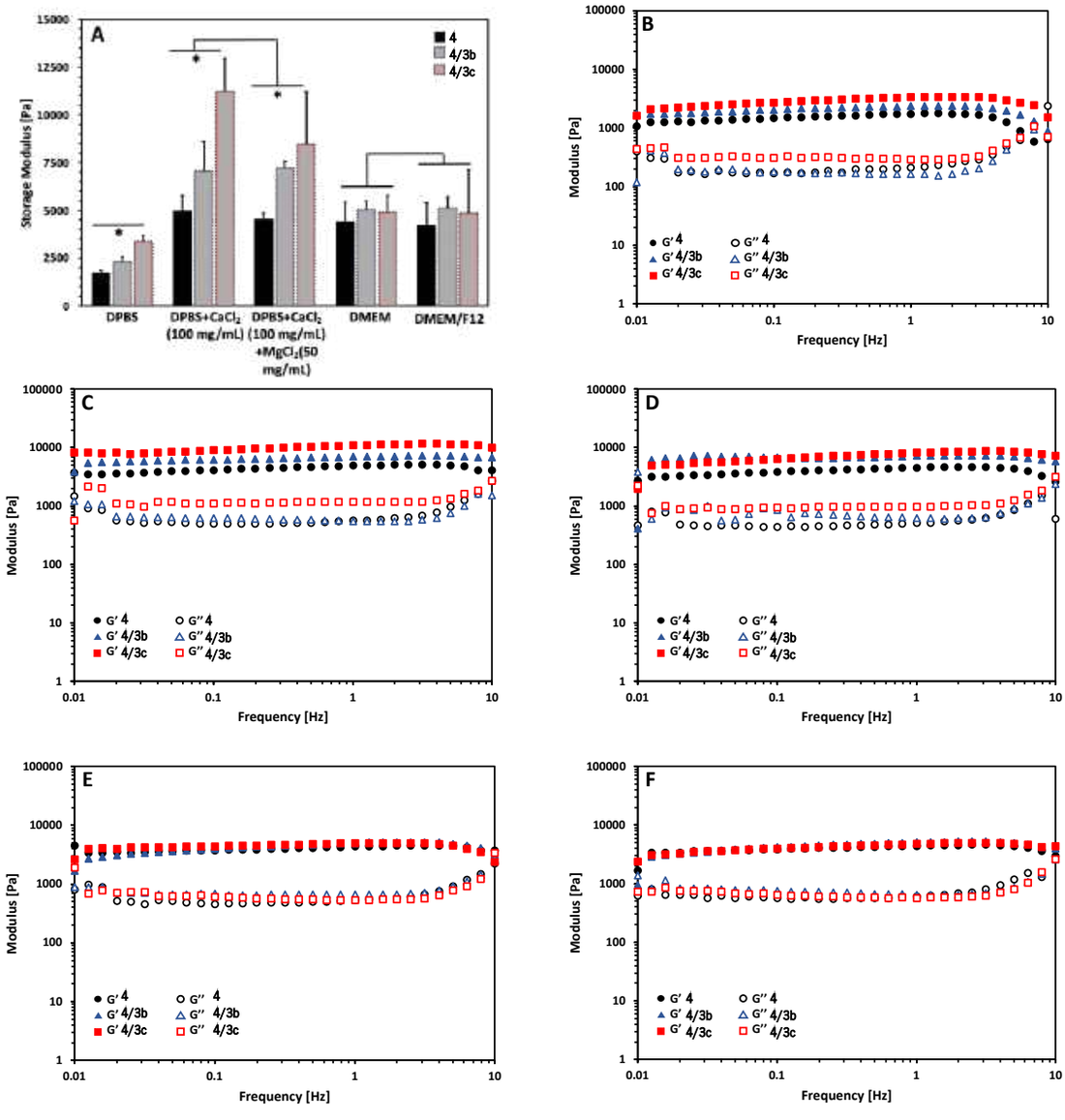


Supplementary Figure VI.10. Storage modulus of supramolecular gels obtained in different media (A) and representative rheological data for elastic (G') and viscous (G'') moduli in (B) Dulbecco's Phosphate Buffered Saline (DPBS); (C) DPBS supplemented with $CaCl_2$ (100 mg/mL); (D) DPBS supplemented with $CaCl_2$ (100 mg/mL) and $MgCl_2$ (50 mg/mL); (E) Dulbecco's Modified Eagle's Medium (DMEM) supplemented with Fetal Bovine Serum (FBS) at 10%; (F) DMEM-F-12 supplemented with FBS (10%). The same amphiphiles concentration, namely Fmoc-FF (4, 10 mM); Fmoc-FF/Fmoc-GlcN6S (4/3b, 10 mM/5 mM), and Fmoc-FF/Fmoc-GlcN6P (4/3c, 10 mM/5 mM) was used at all conditions. DPBS

was chosen because it does not contain divalent cations. The concentration of $CaCl_2$ and $MgCl_2$ was chosen based on the concentration of $Ca^{2+}$ and $Mg^{2+}$ in DMEM.

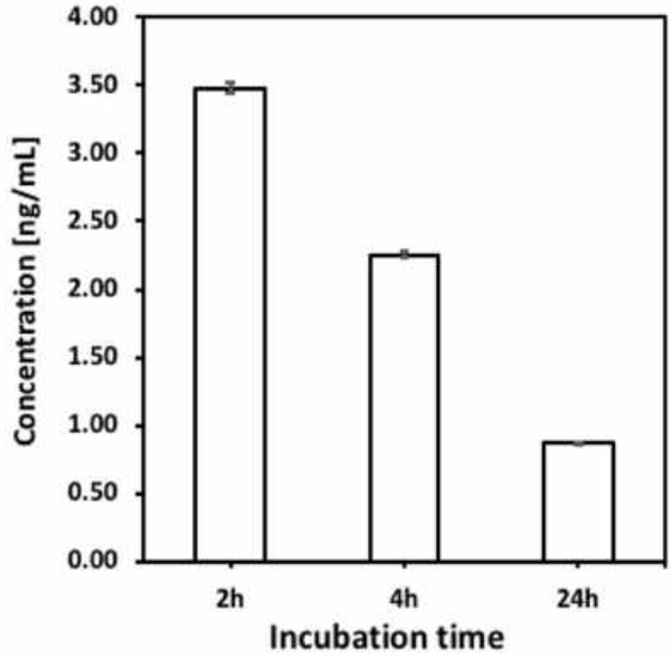


Supplementary Figure VI.11. FGF-2 is thermally instable and loses most of its activity 24h after incubation at 37 °C as demonstrated by ELISA assay.

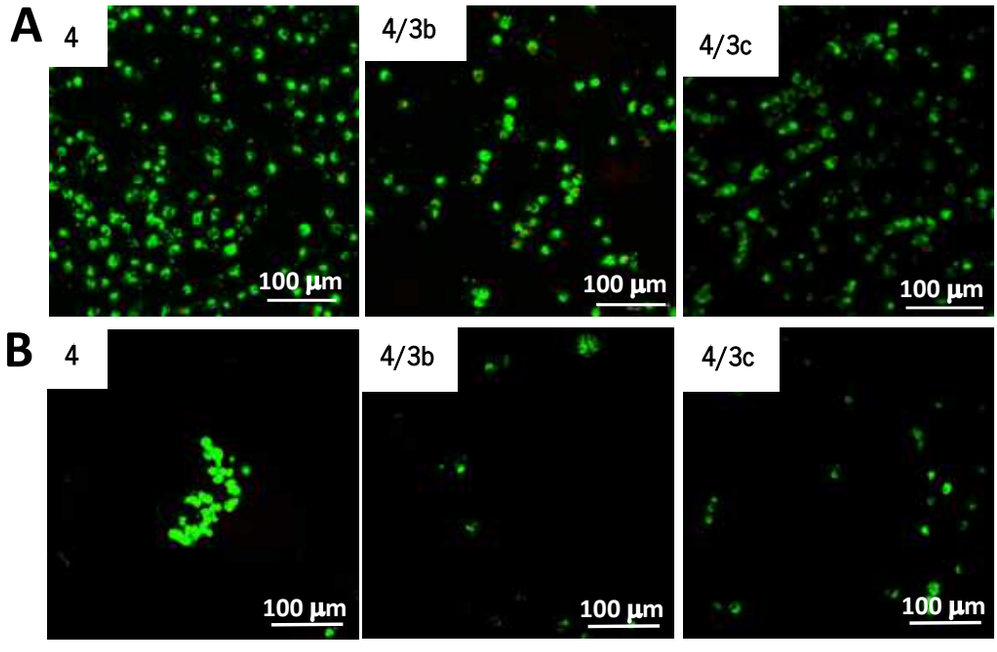

Supplementary Figure VI.12. Representative laser scanning confocal microscope images of ATDC5 cells cultured (A) on top or (B) encapsulated within the gels for 48 h. Live cells are stained in green and dead ones in red.

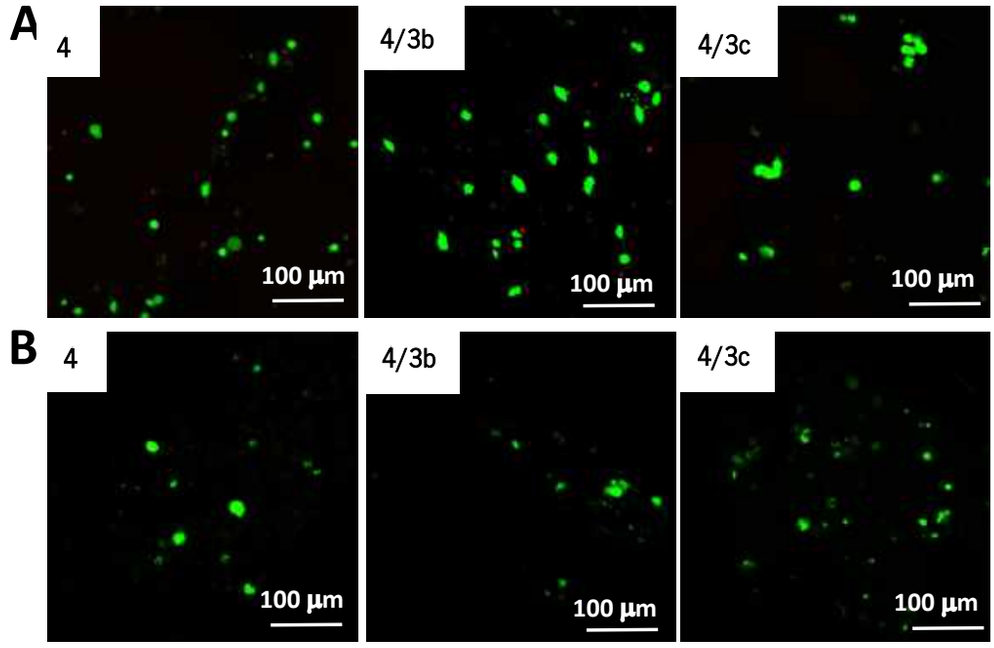


Supplementary Figure VI.13. Representative laser scanning confocal microscope images of HeLa cells cultured (A) on top or (B) encapsulated within the gels for 48 h. Live cells are stained in green and dead ones in red.

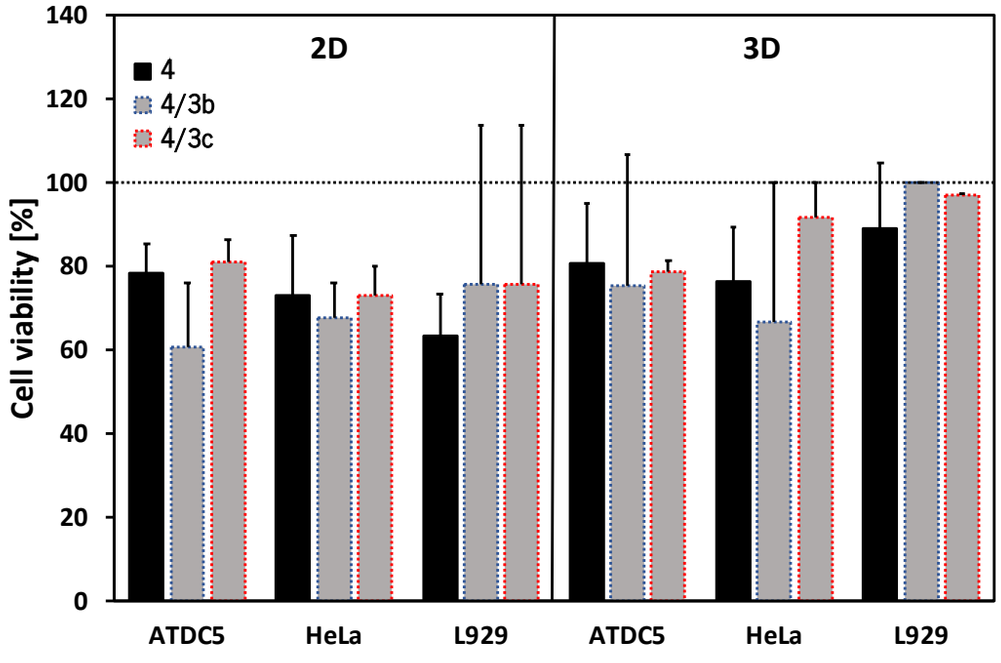


Supplementary Figure VI.14. Percentage of live cells cultured on top (2D) or encapsulated within the gels (3D) for 48 h.

## VI.5. REFERENCES

1. Amabilino, D. B.; Smith, D. K.; Steed, J. W., Supramolecular materials. Chem Soc Rev 2017, 46 (9), 2404-2420.

2. Boekhoven, J.; Stupp, S. I., 25th Anniversary Article: Supramolecular Materials for Regenerative Medicine. Adv Mater 2014, 26 (11), 1642-1659.

3. Du, X. W.; Zhou, J.; Shi, J. F.; Xu, B., Supramolecular Hydrogelators and Hydrogels: From Soft Matter to Molecular Biomaterials. Chem Rev 2015, 115 (24), 13165-13307.

4. Inostroza-Brito, K. E.; Collin, E.; Siton-Mendelson, O.; Smith, K. H.; Monge-Marcet, A.; Ferreira, D. S.; Rodriguez, R. P.; Alonso, M.; Rodriguez-Cabello, J. C.; Reis, R. L.; Sagues, F.; Botto, L.; Bitton, R.; Azevedo, H. S.; Mata, A., Co-assembly, spatiotemporal control and morphogenesis of a hybrid protein-peptide system. Nat Chem 2015, 7 (11), 897-904.

5. Webber, M. J.; Appel, E. A.; Meijer, E. W.; Langer, R., Supramolecular biomaterials. Nat Mater 2016, 15 (1), 13-26.

6. Costa, D. S.; Reis, R. L.; Pashkuleva, I., Sulfation of glycosaminoglycans and its implications in human health and disorders. Annu Rev Biomed Eng 2017, 19, 1-26.

7. Azevedo, H. S.; Pashkuleva, I., Biomimetic supramolecular designs for the controlled release of growth factors in bone regeneration. Adv Drug Deliver Rev 2015, 94, 63-76.

8. Du, X. W.; Zhou, J.; Guvench, O.; Sangiorgi, F. O.; Li, X. M.; Zhou, N.; Xu, B., Supramolecular Assemblies of a Conjugate of Nucleobase, Amino Acids, and Saccharide Act as Agonists for Proliferation of Embryonic Stem Cells and Development of Zygotes. Bioconjugate Chem 2014, 25 (6), 1031-1035.

9. Lee, S. S.; Fyrner, T.; Chen, F.; Álvarez, Z.; Sleep, E.; Chun, D. S.; Weiner, J. A.; Cook, R. W.; Freshman, R. D.; Schallmo, M. S.; Katchko, K. M.; Schneider, A. D.; Smith, J. T.; Yun, C.; Singh, G.; Hashmi, S. Z.; McClendon, M. T.; Yu, Z.; Stock, S. R.; Hsu, W. K.; Hsu, E. L.; Stupp, S. I., Sulfated glycopeptide nanostructures for multipotent protein activation. Nat Nanotech 2017, 12, 821-829.

10. Kim, B. S.; Hong, D. J.; Bae, J.; Lee, M., Controlled self-assembly of carbohydrate conjugate rod-coil amphiphiles for supramolecular multivalent ligands. J Am Chem Soc 2005, 127 (46), 16333-16337.

11. Zhou, J.; Du, X. W.; Chen, X. Y.; Xu, B., Adaptive Multifunctional Supramolecular Assemblies of Glycopeptides Rapidly Enable Morphogenesis. Biochemistry 2018, 57 (32), 4867-4879.

12. Lim, Y. B.; Park, S.; Lee, E.; Jeong, H.; Ryu, J. H.; Lee, M. S., Glycoconjugate nanoribbons from the self-assembly of carbohydrate-peptide block molecules for controllable bacterial cell cluster formation. Biomacromolecules 2007, 8 (5), 1404-1408.

13. Liu, J.; Sun, Z. L.; Yuan, Y. Q.; Tian, X.; Liu, X.; Duan, G. X.; Yang, Y. G.; Yuan, L.; Lin, H. C.; Li, X. M., Peptide Glycosylation Generates Supramolecular Assemblies from Glycopeptides as Biomimetic Scaffolds for Cell Adhesion and Proliferation. Acs Appl Mater Inter 2016, 8 (11), 6917-6924.

14. Yuan, D.; Shi, J.; Du, X.; Zhou, N.; Xu, B., Supramolecular Glycosylation Accelerates Proteolytic Degradation of Peptide Nanofibrils. J Am Chem Soc 2015, 137 (32), 10092-5.

15. Raeburn, J.; Adams, D. J., Multicomponent low molecular weight gelators. Chem Commun 2015, 51 (25), 5170-5180.

16. Buerkle, L. E.; Rowan, S. J., Supramolecular gels formed from multi-component low molecular weight species. Chem Soc Rev 2012, 41 (18), 6089-6102.

17. Makam, P.; Gazit, E., Minimalistic peptide supramolecular co-assembly: expanding the conformational space for nanotechnology. Chem Soc Rev 2018, 47 (10), 3406-3420.

18. Delbianco, M.; Bharate, P.; Varela-Aramburu, S.; Seeberger, P. H., Carbohydrates in Supramolecular Chemistry. Chem Rev 2016, 116 (4), 1693-1752.

19. Birchall, L. S.; Roy, S.; Jayawarna, V.; Hughes, M.; Irvine, E.; Okorogheye, G. T.; Saudi, N.; De Santis, E.; Tuttle, T.; Edwards, A. A.; Ulijn, R. V., Exploiting CH-pi interactions in supramolecular hydrogels of aromatic carbohydrate amphiphiles. Chem Sci 2011, 2 (7), 1349-1355.

20. Pires, R. A.; Abul-Haija, Y. M.; Costa, D. S.; Novoa-Carballal, R.; Reis, R. L.; Ulijn, R. V.; Pashkuleva, I., Controlling cancer cell fate using localized biocatalytic self-assembly of an aromatic carbohydrate amphiphile. Journal of the American Chemical Sociaty 2015, 137 (2), 576-9.

21. Yang, Z. M.; Liang, G. L.; Ma, M. L.; Abbah, A. S.; Lu, W. W.; Xu, B., D-glucosamine-based supramolecular hydrogels to improve wound healing. Chem Commun 2007, 0 (8), 843-845.

22. Pires, R. A.; Abul-Haija, Y. M.; Costa, D. S.; Novoa-Carballal, R.; Reis, R. L.; Ulijn, R. V.; Pashkuleva, I., Controlling cancer cell fate using localized biocatalytic self-assembly of an aromatic carbohydrate amphiphile. Journal of American Chemical Sociaty 2015, 137 (2), 576-9.

23. Jayawarna, V.; Ali, M.; Jowitt, T. A.; Miller, A. E.; Saiani, A.; Gough, J. E.; Ulijn, R. V., Nanostructured hydrogels for three-dimensional cell culture through self-assembly of fluorenylmethoxycarbonyl-dipeptides. Adv Mater 2006, 18 (5), 611-614.

24. Tang, C.; Smith, A. M.; Collins, R. F.; Ulijn, R. V.; Saiani, A., Fmoc-Diphenylalanine Self-Assembly Mechanism Induces Apparent pK(a) Shifts. Langmuir 2009, 25 (16), 9447-9453.

25. Smith, A. M.; Williams, R. J.; Tang, C.; Coppo, P.; Collins, R. F.; Turner, M. L.; Saiani, A.; Ulijn, R. V., Fmoc-Diphenylalanine self assembles to a hydrogel via a novel architecture based on pi-pi interlocked beta-sheets. Adv Mater 2008, 20 (1), 37-41.

26. Mahler, A.; Reches, M.; Rechter, M.; Cohen, S.; Gazit, E., Rigid, self-assembled hydrogel composed of a modified aromatic dipeptide. Adv Mater 2006, 18 (11), 1365-1370.

27. Zhang, Y.; Gu, H. W.; Yang, Z. M.; Xu, B., Supramolecular hydrogels respond to ligand-receptor interaction. J Am Chem Soc 2003, 125 (45), 13680-13681.

28. Chin, D. H.; Woody, R. W.; Rohl, C. A.; Baldwin, R. L., Circular dichroism spectra of short, fixed-nucleus alanine helices. P Natl Acad Sci USA 2002, 99 (24), 15416-15421.

29. Mondal, S.; Adler-Abramovich, L.; Lampel, A.; Bram, Y.; Lipstman, S.; Gazit, E., Formation of functional super-helical assemblies by constrained single heptad repeat. Nat Commun 2015, 6, 8615.

30. Abul-Haija, Y. M.; Roy, S.; Frederix, P. W.; Javid, N.; Jayawarna, V.; Ulijn, R. V., Biocatalytically triggered co-assembly of two-component core/shell nanofibers. Small 2014, 10 (5), 973-9.

31. Fleming, S.; Debnath, S.; Frederix, P. W. J. M.; Hunt, N. T.; Ulijn, R. V., Insights into the Coassembly of Hydrogelators and Surfactants Based on Aromatic Peptide Amphiphiles. Biomacromolecules 2014, 15 (4), 1171-1184.

32. Fleming, S.; Frederix, P. W.; Ramos Sasselli, I.; Hunt, N. T.; Ulijn, R. V.; Tuttle, T., Assessing the utility of infrared spectroscopy as a structural diagnostic tool for beta-sheets in self-assembling aromatic peptide amphiphiles. Langmuir 2013, 29 (30), 9510-5.

33. Chen, L.; Pont, G.; Morris, K.; Lotze, G.; Squires, A.; Serpell, L. C.; Adams, D. J., Salt-induced hydrogelation of functionalised-dipeptides at high pH. Chem Commun 2011, 47 (44), 12071-12073.

34. Chen, G.; Gulbranson, D. R.; Yu, P. Z.; Hou, Z. G.; Thomson, J. A., Thermal Stability of Fibroblast Growth Factor Protein Is a Determinant Factor in Regulating Self-Renewal, Differentiation, and Reprogramming in Human Pluripotent Stem Cells. Stem Cells 2012, 30 (4), 623-630.

35. Gospodarowicz, D.; Cheng, J., Heparin Protects Basic and Acidic Fgf from Inactivation. J Cell Physiol 1986, 128 (3), 475-484.

36. Saksela, O.; Moscatelli, D.; Sommer, A.; Rifkin, D. B., Endothelial Cell-Derived Heparan-Sulfate Binds Basic Fibroblast Growth-Factor and Protects It from Proteolytic Degradation. J Cell Biol 1988, 107 (2), 743-751.

37. Javid, N.; Roy, S.; Zelzer, M.; Yang, Z. M.; Sefcik, J.; Ulijn, R. V., Cooperative Self-Assembly of Peptide Gelators and Proteins. Biomacromolecules 2013, 14 (12), 4368-4376

# Chapter VII

# Effect of serine and threonine on the aggregation of short peptides and glycopeptides

# EFFECT OF SERINE AND THREONINE ON THE AGGREGATION OF SHORT PEPTIDES AND GLYCOPEPTIDES


## Abstract

We report on the self-assembly of tripeptides and their O-glycosylated analogues, in which the carbohydrate moiety is coupled to either serine or threonine positioned in the middle of the peptide sequence. We demonstrate that the replacement of serine with threonine affects the peptide stereochemistry and results in formation of assemblies with different morphology: serine containing tripeptide forms nano-tapes while threonine one aggregates into nanofibrils. O-glycosylation reduces the stiffness of the generated aggregates and increases their stability.


---


*This chapter is based on the publication:*

**Brito, Alexandra;** Dave, Dhwanit; Lampel, Ayala; Kroiss, Daniela; Reis, Rui L.; Tuttle, Tell; Ulijn, Rein V.; Pires, Ricardo A.; Pashkuleva, Iva: "Effect of serine and threonine on the aggregation of short peptides and glycopeptides", submitted.

## VII.1. INTRODUCTION

Proteins are key players in most cellular interactions. Their function depends on the intricate and distinct three-dimensional structure that is acquired *via* intramolecular self-assembly of the polypeptide chain - a process called folding (Scheme VII.1a).[1, 2] Cells have different mechanisms to control this process: misfolded proteins are detected by the cellular proteostasis and are either degraded or refolded correctly by different means such as chemical chaperons and post-translational modifications.[1, 3, 4] Loss of this control results in molecular aggregation *via* intermolecular self-assembly (Scheme VII.1a), which is the origin of a wide variety of pathological conditions.[1-3]

The propensity of a protein to aggregate is primarily coded by the intrinsic properties of the amino acids sequence but it also depends on multiple contributing influences from the crowded cellular milieu and post-translational modifications, *e.g.* glycosylation.[2, 4, 5] Because even the simplest protein is composed by many amino acids, the experimental studies and computational modelling of this process is challenging due to the associated combinatorial complexity.[6] Some years ago, Gazit proposed a reductionist biodesign, which uses intramolecular self-assembly of minimalistic (less than five amino acids) peptide sequences that can code specific protein bioinformation and transfer it to the assembled system (Scheme VII.1b).[7, 8] The developed structural and functional biomimics are simpler in composition, thus, allowing rational and systematic studies to establish connections between peptide sequence and supramolecular functionality.[6, 9, 10] Applying computation approaches to such short sequences, we have shown that mainly hydrophobic peptides and/or short sequences that contain aromatic amino acids are prompt to aggregation and that the morphology and stability of the aggregates depend on the order of the amino acids in the sequence.[6, 10, 11] Besides these findings, very few experimental results with minimalistic peptides prompt to aggregation are reported in the literature.[10] Herein, we report on a reductionist approach that uses tripeptides and their *O*-glycosylated analogues (Scheme 1c) to study the effect of serine (S) *vs* threonine (T) and their glycosylation on molecular aggregation.

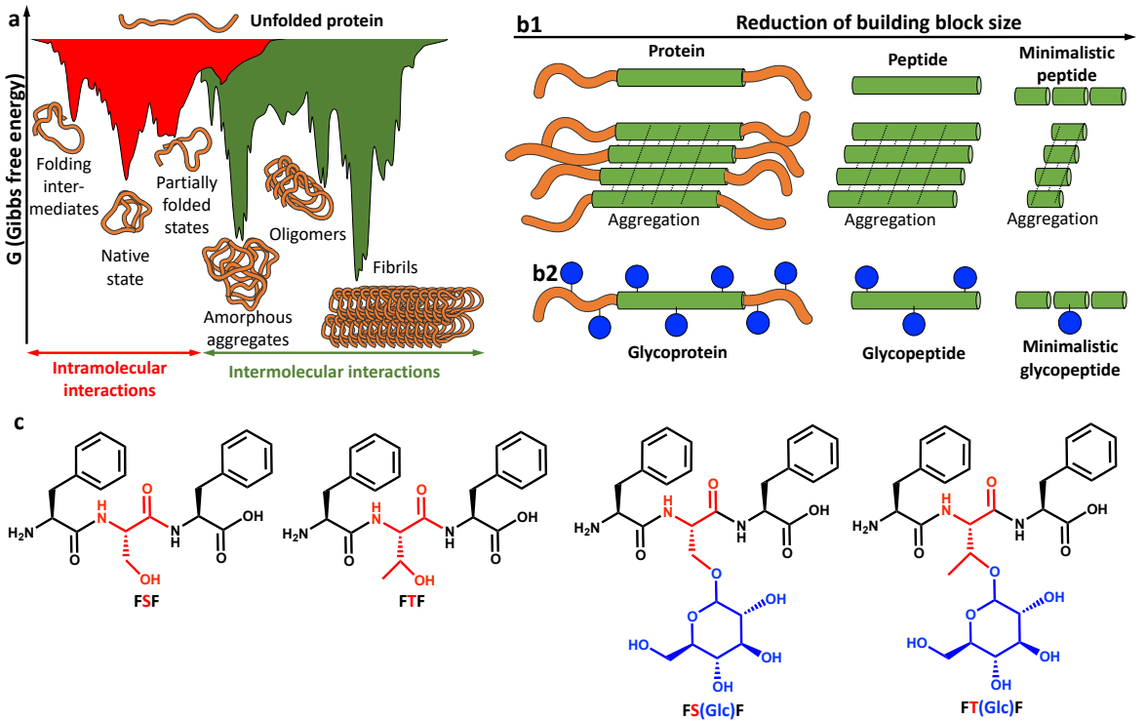


**Scheme VII.1. Schematic presentation of: (a) Proteins self-assembly: intramolecular interactions between different amino acids residues lead to protein folding (red), while intermolecular interactions between different protein chains result in protein aggregation (green); (b) Reductionist approach using (b1) short peptides as minimalistic analogues of proteins in aggregation studies or (b2) the proposed herein short glycopeptides as reductionist *O*-glycoproteins; (c) Chemical structure of peptides and glycopeptides used in this study.**

## VII.2. MATERIALS AND METHODS

### VII.2.1. Aggregation of peptides and glycopeptides

F(Glc)F and FS(Glc)F were dissolved in distilled water to 65 mM stock concentration. Then, diluted to 40 mM final concentration and incubated for 24 h at room temperature. FTF and FSF peptides were dissolved in distilled water to 40 mM and incubated for 24h. All characterization was done after this period.

### VII.2.2. Atomistic Molecular Dynamics Simulations

Tripeptide structures were generated using Avogadro (v 1.2.0) [27] and the CHARMM36 [28] force-field was used. GROMACS 2020.1 [29] implementation of CHARMM [30] was used for the simulations. First, the 50

peptide molecules were randomly placed in a 7 x 7 x 7 $nm^3$ box (=0.24M) and this box was solvated with TIP3P water. These systems were then relaxed for 50000 steps using the steepest descent integrator. This box was then subjected to *NVT* and *NPT* equilibration for 100ps each using a 2fs timestep while holding the peptides with a position restraint. The position restrains were released for the production runs where the systems were equilibrated for 500ns in triplicate runs for statistical analysis. The LINCS constraint algorithm was used to constraint bonds and PME was used for electrostatics. Temperature was set to 300K using the modified Berendsen thermostat (V-rescale) and the pressure coupling was achieved using the Parinello-Rahman algorithm with a reference pressure of 1.0 bar. Some simulations were rerun for 2000ns to ensure equilibration of self-assembled structures. The glycosylated tripeptide structures were generated using CHARMM-GUI [31-34] and the identical protocol as above was used for the simulations. The trajectories generated were visualized using VMD.[35] Hydrogen bonding, Solvent-Accessible Surface Area (SASA) and radial-distribution function (RDF) analysis was also carried out using inbuilt GROMACS tools.

### VII.2.3. Transmission electron microscopy (TEM)

5 μL of the sample solution in water (24 hrs after dissolving to allow self-assembly) was dropped onto a carbon-coated grid (Electron Microscopy Sciences) and incubated for one minute. The excess of solution was removed using filter paper (blotting), followed by staining with 5 μL of 2 % (w/v) uranyl acetate solution, for 30 sec. The excess staining was removed by blotting and the grid was left to dry in air at room temperature. Sample was then imaged in a FEI TITAN Halo TEM operating at 300 kV and images were recorded using a FEI CETA 16M camera.

### VII.2.4. Scanning electron microscopy (SEM)

A drop of a solution of the self-assembled systems was deposited onto a silicon wafer and left to dry in air at room temperature. Dried samples were coated with platinum (Leica ACE600 sputter coater) and imaged using a FEI Helios Nanolab660 Dualbeam FIB-SEM, recorded at 5 kV.

### VII.2.5. Atomic Force Microscopy (AFM)

A fresh cleaved mica sheet was functionalized with 200 µL of (3-Aminopropyl)triethoxysilane (APTES) for 30 min at room temperature. The mica was rinsed with deionized water and dried under nitrogen flow. A drop of the self-assembled sample was added on the functionalized mica sheet. All AFM images were acquired with a JPK Nanowizard 3 in air at room temperature. The morphological features and mechanical properties of the nanofibers were assessed under JPK quantitative imaging mode using RTESPA-525 probes (k~200 N/m, Bruker, Germany), calibrated by the JPK contact free method. All approaching force curves were fitted using Hertz/Sneddon model to obtain the Young's modulus. The reported Young's moduli are averaged over 30 measurements.

### VII.2.6. Circular dichroism

28 µL of each sample (7.5-15 mM) in water were placed in a 0.1 mm demountable quartz cuvette and spectra were measured on a JASCO J-1500 spectrometer (2 s integration, a step size of 1 nm, single acquisition with a slit width of 1 nm). The temperature was maintained at 20 °C for all the measurements. Continuous ramp temperature measurements were performed for the stability studies.[23] The samples (7.5-15 mM self-assembled glycopeptides and peptides in water) were added to a cuvette placed in a temperature controlled module. Spectra were collected as a function of temperature starting from 25 °C and increasing to 90 °C (2 °C steps) and then decreasing back to 25 °C (5 °C steps) for a complete cycle. The intensity of the signal at ~220 nm was measured and it is presented as a function of the temperature in the main manuscript (Fig. VII.2d).

### VII.2.7. Wide-angle-X-ray Powder Diffraction (XRD)

Glycopeptides and peptides were dissolved in water (40 mM) 24 hrs prior to the measurements and maintained at room temperature. The formed assemblies were freeze-dried and the obtained powder was placed on a quartz substrate. X-ray intensity data were recorded on a PANalytical X'Pert Pro Powder Diffraction instrument with an x-ray source of 3 kW and working at a wavelength of 1.5405 Å.

## VII.3. RESULTS AND DISCUSSION

Glycosylation is a common post-translational modification that effectively enriches the protein repertoire beyond the bioactivities coded by the amino acids sequence and alter the energy landscape associated with the protein folding and aggregation.[4, 12-15] However, the exact mechanism of this process is poorly understood and mainly based on *in silico* models.[4] In eukaryotic cells, *O*-glycosylation takes place at the endoplasmic reticulum, where a monosaccharide (usually *N*-acetylgalactosamine but also fucose and glucose) is coupled to the hydroxyl of S or T of newly synthesized polypeptides.[4, 13, 15] We designed and synthesized tripeptides that contain phenylalanin (F) - aromatic amino acid that can promote peptide aggregation by π-stacking, and S or T. Of note, the hydrophilic amino acid is introduced in the middle of the peptide sequence. The *O*-glycosylation of these short peptide chains at S or T generated the minimalistic *O*-glycopeptides (Scheme VII.1c) that differ from previously described self-assembling glycopeptides that are end-on glycosylated.[16, 17]

The aggregation of the obtained tripeptides and the respective glycopeptides was studied in water. The peptides differ only by a methyl group (Scheme VII.1c, FSF *vs* FTF) but this subtle difference affects tremendously the morphology of the generated aggregates: FSF forms nano-tapes while nanofibrils are visible for FTF (Fig. VII.1).

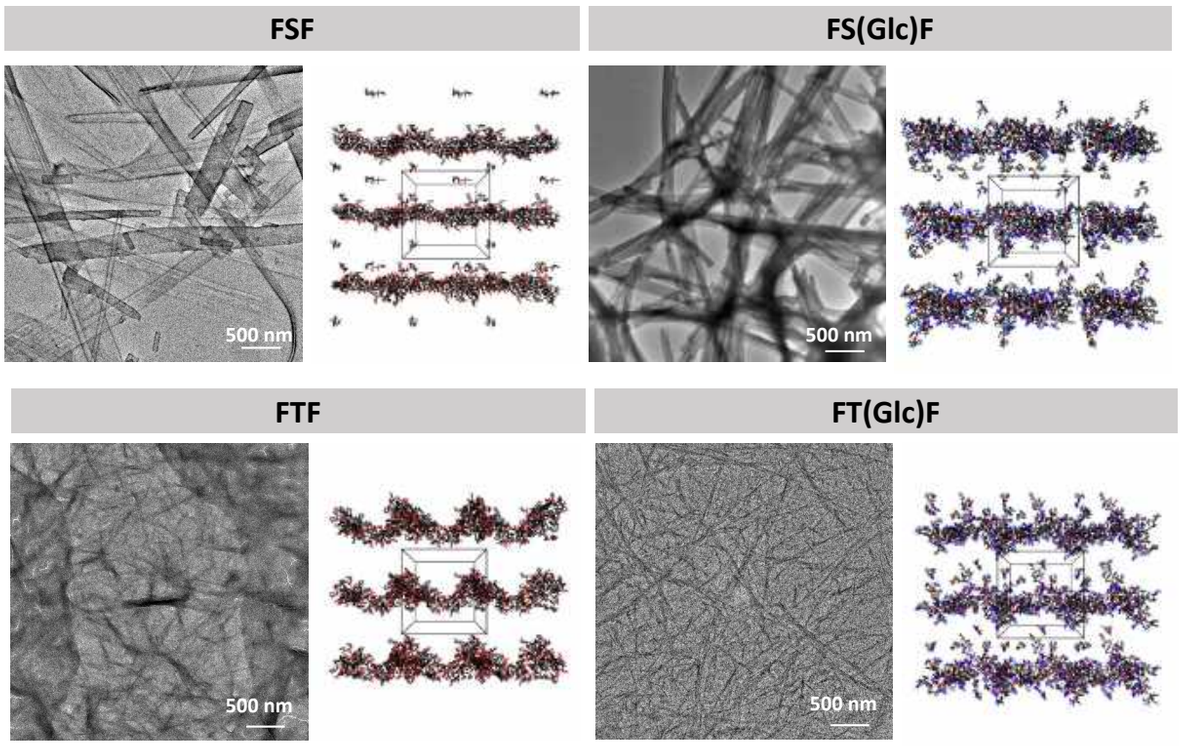


**Figure VII.1. Transmission electron microscopy (TEM) images of the peptides and glycopeptides aggregates formed in water (40 mM, room temperature, 24 hrs) and the respective models obtained by atomistic molecular dynamic simulations (F: black, Glc: blue, and S/T: red).**

These results agree with previous data about Fmoc-dipeptides showing formation of planar structures for Fmoc-SF-OMe and an extended network of twisted fibers for Fmoc-TF-OMe.[18] Atomistic molecular dynamic simulations showed a substantial decrease of solvent-accessible surface area (SASA) for the aromatic F groups overtime (Fig. VII.2a, black), indicating that these groups participate in the aggregation and are mostly hidden in the aggregates core. The SASA for S and T changed significantly less as compared to F (Fig. VII.2a, red), suggesting greater exposure of these amino acids on the surface of the aggregates. A comparison between S and T revealed some differences: S has higher propensity to form hydrogen bonds (Fig. VII.2c), while T has a higher tendency to interact with F *via* CH-π interactions (Fig. VII.2d, S VII.Fig.14 radial distribution peak at 4.5 Å). These propensity differences can be augmented during the aggregation process due to an induced stereochemical fit of the peptides chains and explain the different morphology of FSF and FTF aggregates (Fig. VI.2d).[18]

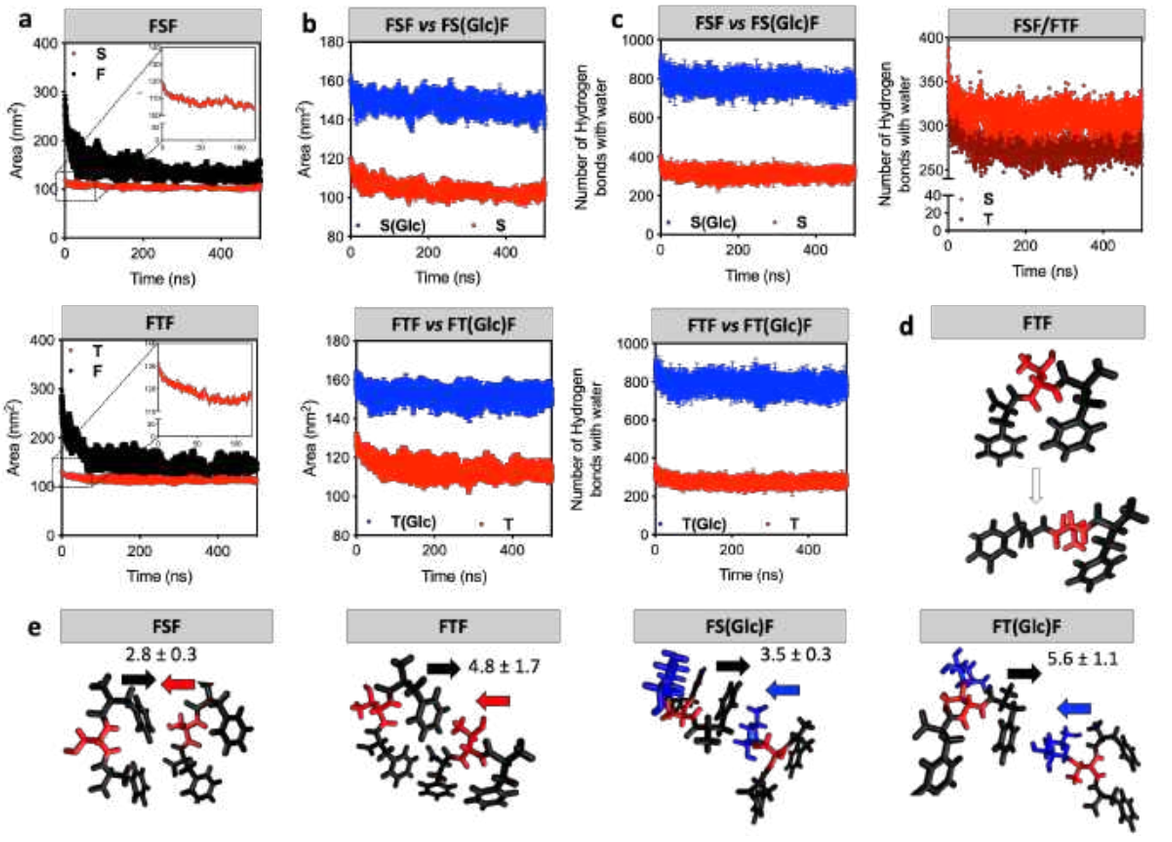


**Figure VII.2. Computational modelling studies showing (a, b) solvent-accessible surface area (SASA) analysis, (c) number of hydrogen bonds with the solvent, (d) start and end conformation of FTF during assembly and (e) the propensity of CH-π interactions between S, T, S(Glc) or T(Glc) and the aromatic F (the distance limit was set to 0.45 nm).**

Circular dichroism (CD) and X-ray powder diffraction (XRD) supported the computational data. The CD spectra of the peptides have an intensive, positive signal at ~220 nm for the n-π* transition (Fig. VII.3b).[19, 20] In the FTF spectrum there is an additional positive peak at ~200 nm that was assigned to aromatic π-π* stacking and confirms that the methyl group of T induces conformational changes that affect the relative spatial orientation of F and thus, the supramolecular interactions and the aggregation process.

The *in silico* models showed lower aggregation propensity for *O*-glycosylated analogues (Table S VII.1). Experimentally, we did not observe morphological differences between the aggregates of the peptides and the respective glycopeptides but the glycosylation affected aggregates size, mechanical properties, and stability (Figs. VII.1 and VII.3). Native *O*-glycoproteins have a high capacity to capture water, which is essential for their viscoelastic properties and physiological functions. At the molecular level, hydration can cause high steric bulk and prevent

β-sheet formation.[21] Thus, the decreased Young's modulus of *O*-glycopeptides (2 fold as compared with the tripeptides) might be due to the increased hydration capacity and/or structural changes caused by the conformational distortions and supramolecular forces, such as H-bonding and π interactions,[22] impaired by the introduced glucose moiety. Because the assembly was performed in water, it is expected that the carbohydrate moiety will be exposed on the surface of the assemblies contributing to their increased hydration when compared with the respective tripeptides. The computational results showed that indeed, the glycosylated peptides have higher SASA (Fig. VII.2b) and propensity to form hydrogen bonding with water (Fig. VII.2c). However, the results also indicated the presence of the carbohydrate moieties in the core of the aggregates (Fig. 2d), suggesting their involvement in the aggregation beyond simple hydration. The glycosylation led to a ~1.2-fold increase of the propensity of CH-π interactions (Fig. VII.2d), which in turns affect the π-π stacking (Fig. VII.3b). This rebalance of the π-interactions was confirmed by X-ray diffraction (XRD, Fig. VII.3c) where a crystalline-amorphous transition is visible for the glycopeptides and by the CD spectra, where a decrease of the 220 nm signal intensity for both glycopeptides was observed. The introduction of the bulky carbohydrate group at S has a similar stereochemical effect as the T's methyl group (FS(Glc)F *vs* FTF in Fig. VII.3b) shown by the appearance of the π-π* signal in the FS(Glc)F spectrum (FSF *vs* FS(Glc)F in Fig. VII.3b).

In the case of the S analogue, the performed *O*-glycosylation also affected the thermal stability of the aggregates (Fig. VII.3d). Upon heating, the aggregates of the glycosylated FS(Glc)F were more stable than the FSF ones.[23] Such difference was not well pronounced for the FT(Glc)F/FTF couple. These results are in agreement with previous studies with glycoproteins showed that the glycosylation generally improves the thermal stability of the proteins and the magnitude of this effect depends on the size of the carbohydrate chain, the position of glycosylation and the protein crystallinity.[24-26]

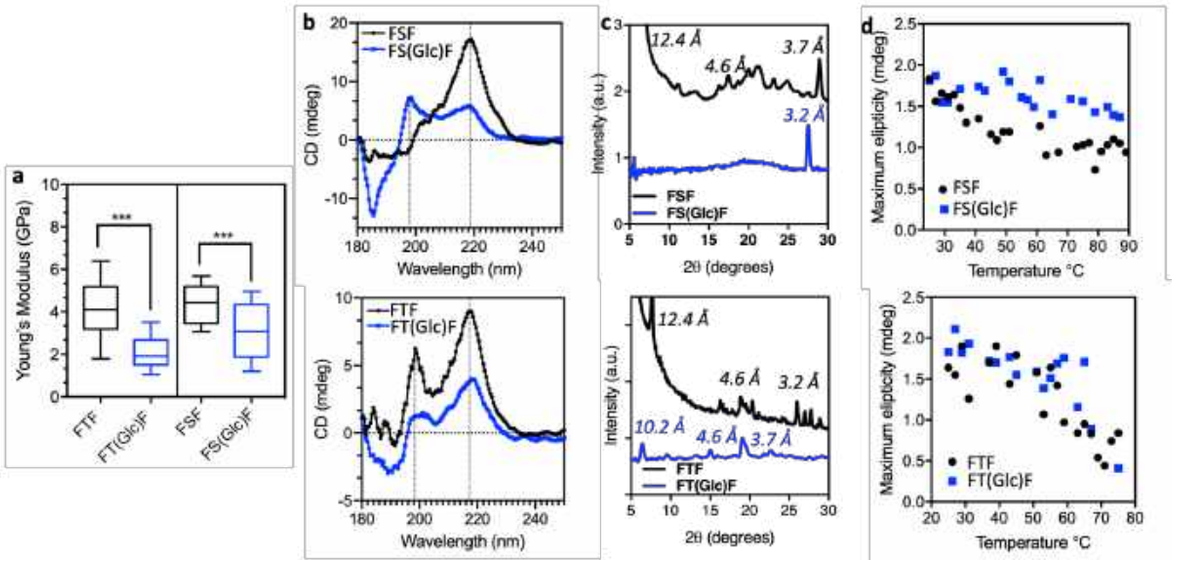


**Figure VII.3. Effect of glycosylation on the aggregation: (a) Youngs modulus of the aggregates determined by atomic force microscopy; (b) circular dichroism (CD) spectra; (c) X-ray diffraction (XRD) patterns and (d) thermal stability of the generated aggregates obtained from the CD spectra (intensity of the signal at ~220nm) at different temperatures.**

Finally, we also studied the aggregation of mixtures of peptides and the respective glycosylated analogues at different molar ratios (1:0, 3:1, 1:1, 1:3, and 0:1) to mimic the native scenario in which proteins and glycoproteins co-exist.

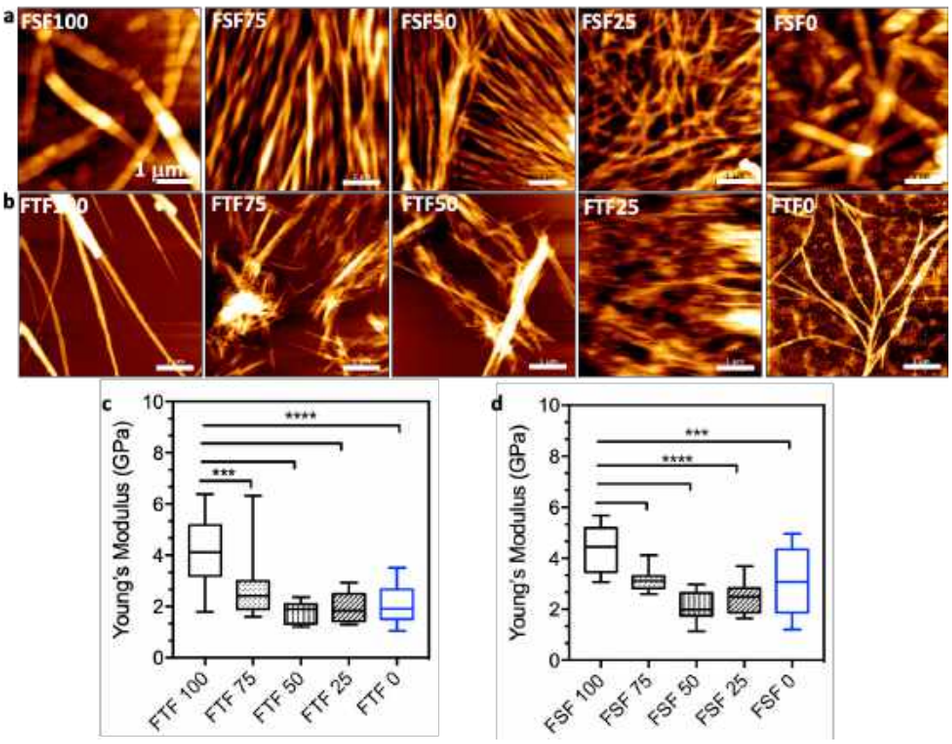


**Figure VII.4. Aggregation of peptide/glycopeptide mixtures at different ratios: (a, b) Atomic force microscopy (AFM) images of assemblies obtained from FXF:FX(Glc)F mixtures at different ratios and (b, d) Young's modulus for these assemblies measured by AFM: (a,c) X=S and (b,d) X=T. FXF100 (FXF:FX(Glc)F=1:0); FXF75 (FXF:FX(Glc)F=3:1); FXF50 (FXF:FX(Glc)F=1:1); FXF25 (FXF:FX(Glc)F=1:3); FXF0 (FXF:FX(Glc)F=0:1).**

The morphology of the assemblies obtained from the mixtures was different from the single-component systems and we observed the formation of entangled nanofibers for all mixtures (Fig. VII.4a, b). The Young's modulus gradually decreased upon addition of the glycopeptides, reached a minimum at ratio 1:1 and further enrichment of the mixtures with O-glycopeptides does not affect the modulus significantly (Fig. VII.4c, d). These results are compatible with co-assembly and indicate that in a crowded environment glycosylation affects not only the aggregation of the protein to which the carbohydrate unit is bound but also to the close neighbours.

Our results demonstrate that the described short glycopeptides are an excellent reductionist model for elucidation of the glycosylation involvement in supramolecular interactions driving the protein aggregation. Using these models and in similarity with the native glycoproteins, we showed a distinct role of S, T, and Glc in the glycopeptides stereochemistry and consequently in the characteristics of the generated assemblies. Such interactions are often challenging for quantification because they are usually hidden in big, native glycoproteins but are crucial for

protein synthesis, trafficking, and function. The introduced glycosylation did not avoid the aggregation but distort the assembly giving rise to more amorphous and weaken structures, due to the introduction of CH-π interactions. These changes were more pronounced for T analogues as compared with S ones.

## VII.4. SUPPLEMENTARY INFORMATION

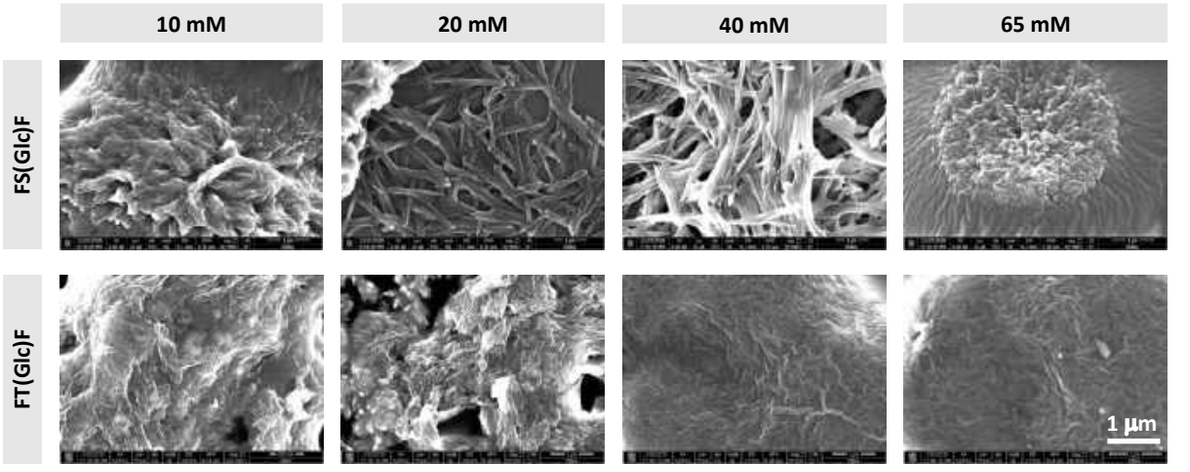


Supplementary Figure VII.1. Scanning electron microscopy images of the aggregates generated at different concentrations of glycopeptides

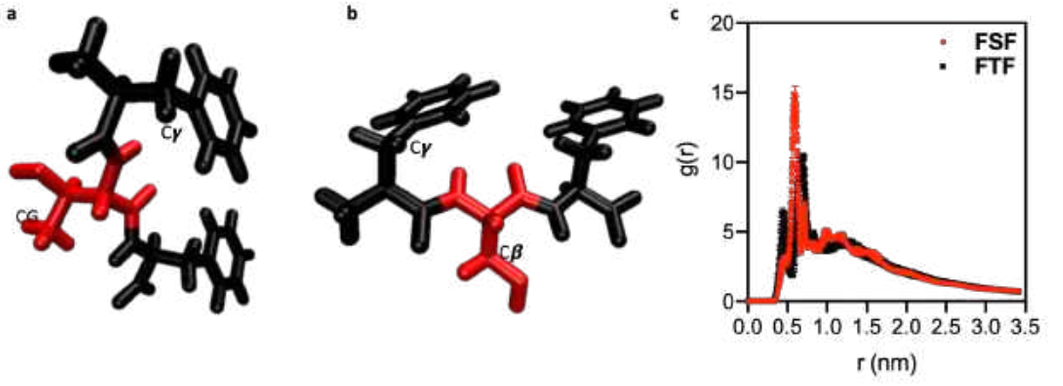


Supplementary Figure VII.2. Molecular structure of FTF (a) and FSF (b), the definition of the studied carbons; (c) Radial distribution function between Ser/Thr and Phe.

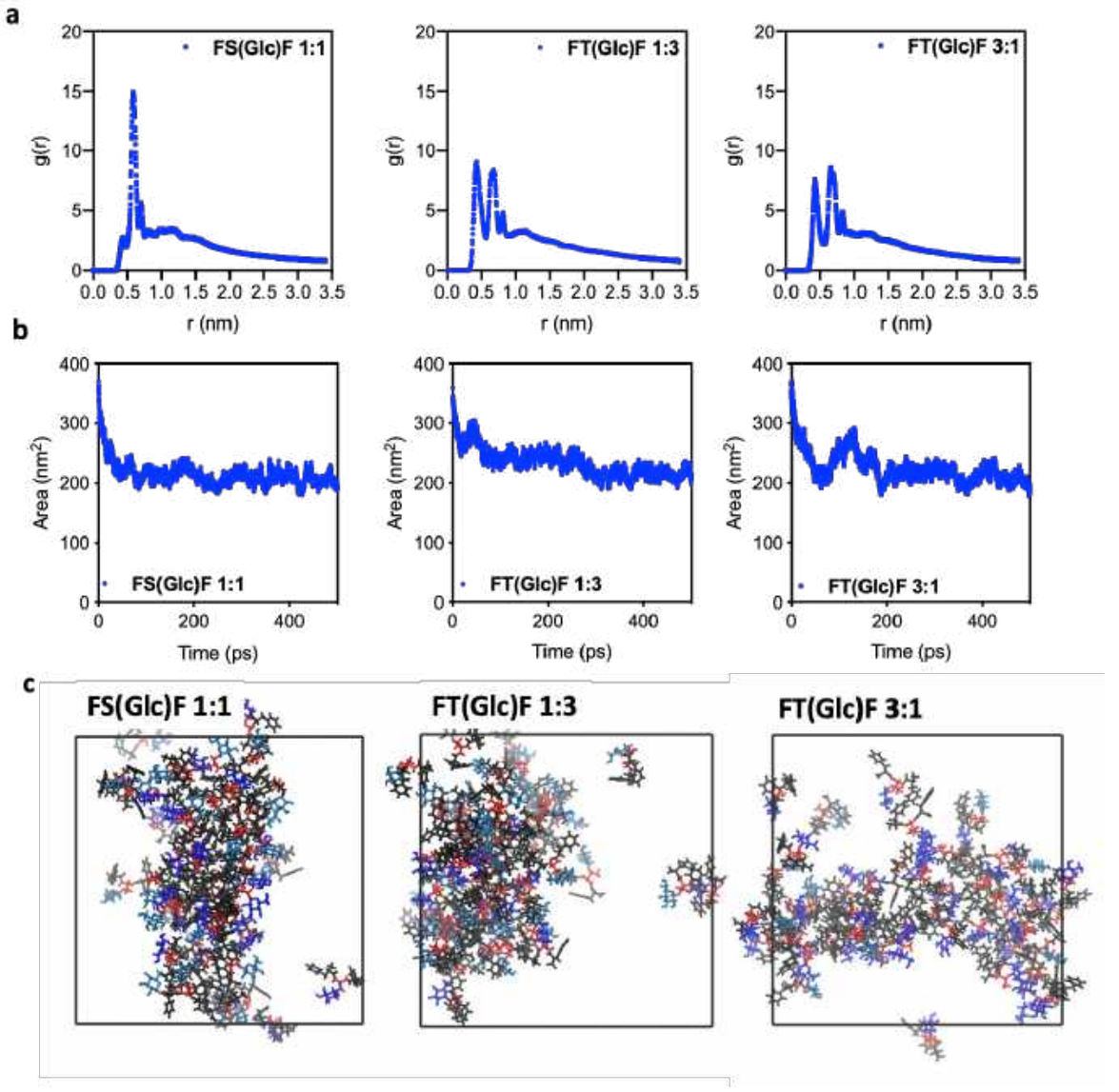


Supplementary Figure VII.3. Characterization of the glycopeptide monomer mixture assembly (a) Radial distribution function between Ser/Thr and Phe; (b) Solvent accessible surface area (SASA); (c) screenshot at 500 ns of the simulation.

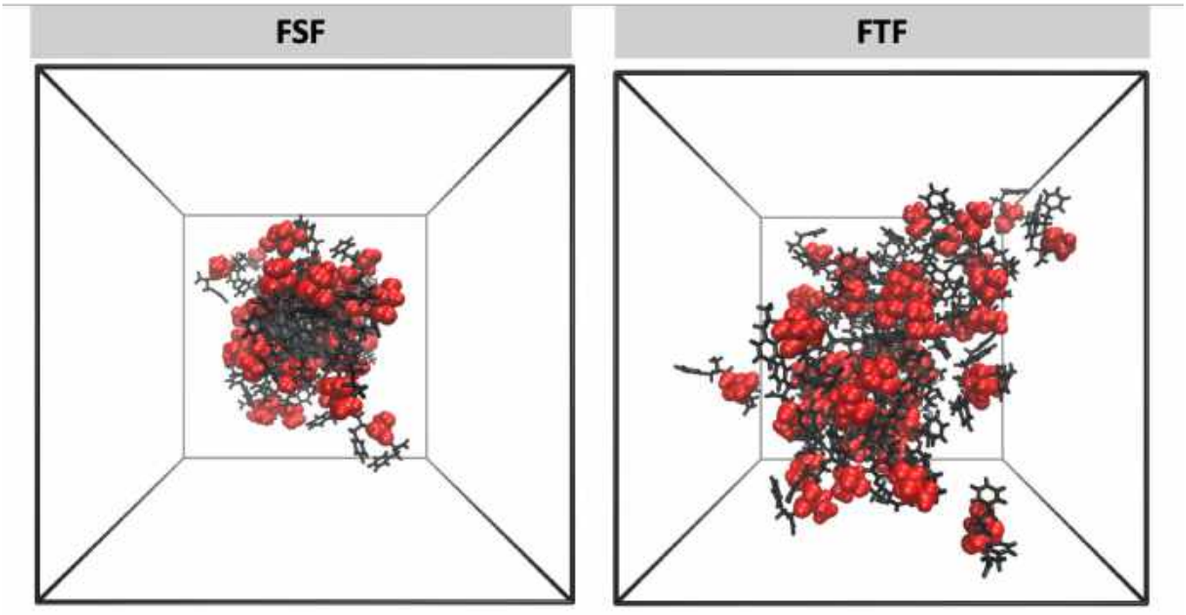


Supplementary Figure VII.4. Screenshot of the assembly of FSF and FTF, showing mainly S (red) on the surface of the assembled structure and in FTF, T, in the core of the assembly.

Supplementary Table VII.1. Peptide and glycopeptide aggregation propensity

| Peptide/Glycopeptide | Aggregation Propensity* |
|---|---|
| FSF | 2.23 ± 0.26 |
| FSGlcF | 1.90 ± 0.14 |
| FTF | 2.18 ± 0.05 |
| FTGlcF | 1.62 ± 0.08 |

*Average of three 500 ns runs

Supplementary Table VII.2. Glycopeptide anomers mixture aggregation propensity

| Peptide/Glycopeptide | Aggregation Propensity* |
|---|---|

| | |
|---|---|
| FS(Glc)F 1:1 (α:β) | 1.97 ± 0.10 |
| FTGlcF 1:3 (α:β) | 1.46 ± 0.16 |
| FT(Glc)F 3:1 (α:β) | 1.83 ± 0.20 |

*Average of three 500 ns runs

**Supplementary Table VII.3. Radial distribution function denotated by g(r), which defines the probability of Ser-Glc and Thr-Glc in glycopeptides mixtures, of finding Phe group at 0.45 nm distance, for CH-π interactions. Cβ: carbon beta; CG: carbon methyl; Cγ: carbon gama.**

| Peptide/Glycopeptide | g(r)* at r=0.45 nm for Ser(Cβ)/Thr(CG) – Phe(Cγ) |
|---|---|
| FS(Glc)F 1:1 (α:β) | 3.0 ± 0.4 |
| FTGlcF 1:3 (α:β) | 6.9 ± 1.0 |
| FT(Glc)F 3:1 (α:β) | 6.1± 0.4 |

*Average of last 200 ns from three 500 ns simulations

## VII.5. REFERENCES

1. Hartl FU, Hayer-Hartl M. Converging concepts of protein folding in vitro and in vivo. Nat Struct Mol Biol. 2009;16(6):574-81.

2. Vendruscolo M, Zurdo J, MacPhee CE, Dobson CM. Protein folding and misfolding: a paradigm of self-assembly and regulation in complex biological systems. Philos T R Soc A. 2003;361(1807):1205-22.

3. Gazit E. The "Correctly folded" state of proteins: Is it a metastable state. Angewandte Chemie-International Edition. 2002;41(2):257-9.

4. Shental-Bechor D, Levy Y. Effect of glycosylation on protein folding: A close look at thermodynamic stabilization. Proceedings of the National Academy of Sciences of the United States of America. 2008;105(24):8256-61.

5. White DA, Buell AK, Knowles TPJ, Welland ME, Dobson CM. Protein Aggregation in Crowded Environments. Journal of the American Chemical Society. 2010;132(14):5170-5.

6. Pappas CG, Shafi R, Sasselli IR, Siccardi H, Wang T, Narang V, et al. Dynamic peptide libraries for the discovery of supramolecular nanomaterials. Nature Nanotechnology. 2016;11(11):960-7.

7. Brahmachari S, Arnon ZA, Frydman-Marom A, Gazit E, Adler-Abramoyich L. Diphenylalanine as a Reductionist Model for the Mechanistic Characterization of beta-Amyloid Modulators. Acs Nano. 2017;11(6):5960-9.

8. Gazit E. Reductionist Approach in Peptide-Based Nanotechnology. In: Kornberg RD, editor. Annual Review of Biochemistry, Vol 87. Annual Review of Biochemistry. 872018. p. 533-53.

9. Yoshida M, Hinkley T, Tsuda S, Abul-Haija YM, McBurney RT, Kulikov V, et al. Using Evolutionary Algorithms and Machine Learning to Explore Sequence Space for the Discovery of Antimicrobial Peptides. Chem-Us. 2018;4(3):533-43.

10. Frederix PWJM, Scott GG, Abul-Haija YM, Kalafatovic D, Pappas CG, Javid N, et al. Exploring the sequence space for (tri-) peptide self-assembly to design and discover. Nature chemistry. 2015;7(1):30-7.

11. Lampel A, McPhee SA, Park HA, Scott GG, Humagain S, Hekstra DR, et al. Polymeric peptide pigments with sequence-encoded properties. Science. 2017;356(6342):1064-8.

12. Brito A, Abul-Haija YM, da Costa DS, Novoa-Carballal R, Reis RL, Ulijn RV, et al. Minimalistic supramolecular proteoglycan mimics by co-assembly of aromatic peptide and carbohydrate amphiphiles. Chemical Science. 2019;10(8):2385-90.

13. da Costa DS, Reis RL, Pashkuleva I. Sulfation of Glycosaminoglycans and Its Implications in Human Health and Disorders. Annual Review of Biomedical Engineering. 2017;19:1-26.

14. Xu CC, Ng DTW. Glycosylation-directed quality control of protein folding. Nat Rev Mol Cell Bio. 2015;16(12):742-52.

15. Dobson CM. Protein folding and misfolding. Nature. 2003;426(6968):884-90.

16. Pratt MR, Bertozzi CR. Synthetic glycopeptides and glycoproteins as tools for biology. Chemical Society Reviews. 2005;34(1):58-68.

17. Restuccia A, Seroski DT, Kelley KL, O'Bryan CS, Kurian JJ, Knox KR, et al. Hierarchical self-assembly and emergent function of densely glycosylated peptide nanofibers. Communications Chemistry. 2019;2.

18. Lee SS, Fyrner T, Chen F, Alvarez Z, Sleep E, Chun DS, et al. Sulfated glycopeptide nanostructures for multipotent protein activation. Nature Nanotechnology. 2017;12(8):821-9.

19. Corzana F, Busto JH, Jimenez-Oses G, de Luis MG, Asensio JL, Jimenez-Barbero J, et al. Serine versus threonine glycosylation: The methyl group causes a drastic alteration on the carbohydrate orientation and on the surrounding water shell. Journal of the American Chemical Society. 2007;129(30):9458-67

20. Naganagowda GA, Gururaja TL, Satyanarayana J, Levine MJ. NMR analysis of human salivary mucin (MUC7) derived O-linked model glycopeptides: comparison of structural features and carbohydrate-peptide interactions. Journal of Peptide Research. 1999;54(4):290-310.

21. Hughes M, Frederix PWJM, Raeburn J, Birchall LS, Sadownik J, Coomer FC, et al. Sequence/structure relationships in aromatic dipeptide hydrogels formed under thermodynamic control by enzyme-assisted self-assembly. Soft Matter. 2012;8(20).

22. Kramer JR, Onoa B, Bustamante C, Bertozzi CR. Chemically tunable mucin chimeras assembled on living cells. Proceedings of the National Academy of Sciences of the United States of America. 2015;112(41):12574-9.

23. G. Cheng, V. Castelletto, C. M. Moulton, G. E. Newby and I. W. Hamley, Hydrogelation and Self-Assembly of Fmoc-Tripeptides: Unexpected Influence of Sequence on Self-Assembled Fibril Structure, and Hydrogel Modulus and Anisotropy. Langmuir. 2010, 26(7): 4990-4998.

24. S. Marchesan, C. D. Easton, K. E. Styan, L. J. Waddington, F. Kushkaki, L. Goodall, K. M. McLean, J. S. Forsythe and P. G. Hartley, Chirality effects at each amino acid position on tripeptide self-assembly into hydrogel biomaterials, Nanoscale, 2014, 6(10): 5172-5180.

25. Micsonai, A.; F. Wien, L. Kernya, Y. H. Lee, Y. Goto, M. Refregiers and J. Kardos, Accurate secondary structure prediction and fold recognition for circular dichroism spectroscopy, Proceedings of the National Academy of Sciences of the United States of America, 2015, 112(24): E3095-3103.

26. E. Eanes, G. J. J. o. H. Glenner and Cytochemistry, 1968, 16, 673-677.26. Chen WT, Enck S, Price JL, Powers DL, Powers ET, Wong CH, et al. Structural and Energetic Basis of Carbohydrate-Aromatic Packing Interactions in Proteins. Journal of the American Chemical Society. 2013;135(26):9877-84.

27. Hanwell MD, Curtis DE, Lonie DC, Vandermeersch T, Zurek E, Hutchison GR. Avogadro: an advanced semantic chemical editor, visualization, and analysis platform. Journal of cheminformatics. 2012;4(1):17.

28. Best RB, Zhu X, Shim J, Lopes PE, Mittal J, Feig M, et al. Optimization of the additive CHARMM all-atom protein force field targeting improved sampling of the backbone $\phi$, $\psi$ and side-chain $\chi 1$ and $\chi 2$ dihedral angles. Journal of chemical theory and computation. 2012;8(9):3257-73.

29. Abraham MJ, Murtola T, Schulz R, Páll S, Smith JC, Hess B, et al. GROMACS: High performance molecular simulations through multi-level parallelism from laptops to supercomputers. SoftwareX. 2015;1:19-25.

30. Bjelkmar P, Larsson P, Cuendet MA, Hess B, Lindahl E. Implementation of the CHARMM force field in GROMACS: analysis of protein stability effects from correction maps, virtual interaction sites, and water models. Journal of chemical theory and computation. 2010;6(2):459-66.

31. Jo S, Kim T, Iyer VG, Im W. CHARMM-GUI: a web-based graphical user interface for CHARMM. Journal of computational chemistry. 2008;29(11):1859-65.

32. Brooks BR, Brooks III CL, Mackerell Jr AD, Nilsson L, Petrella RJ, Roux B, et al. CHARMM: the biomolecular simulation program. Journal of computational chemistry. 2009;30(10):1545-614.

33. Lee J, Cheng X, Swails JM, Yeom MS, Eastman PK, Lemkul JA, et al. CHARMM-GUI input generator for NAMD, GROMACS, AMBER, OpenMM, and CHARMM/OpenMM simulations using the CHARMM36 additive force field. Journal of chemical theory and computation. 2016;12(1):405-13.

34. Park S-J, Lee J, Qi Y, Kern NR, Lee HS, Jo S, et al. CHARMM-GUI Glycan Modeler for modeling and simulation of carbohydrates and glycoconjugates. Glycobiology. 2019;29(4):320-31.

35. Humphrey W, Dalke A, Schulten K. VMD: visual molecular dynamics. Journal of molecular graphics. 1996;14(1):33-8.

# SECTION 6

# GENERAL CONCLUSIONS

# Chapter VIII

# General Conclusions and Future Perspectives

# GENERAL CONCLUSIONS AND FUTURE PERSPECTIVES

This thesis studies the design, synthesis, and supramolecular polymerisation of carbohydrate amphiphiles in physiological milieu. We developed carbohydrate self-assembling blocks and showed that:

(i) Biofunctional supramolecular systems involving carbohydrates can be assembled in physiological media using different approaches such as co-assembly and biocatalytic self-assembly (BSA);

(ii) These systems extend the prospects for generating functional and structural complexity beyond the diversity offered by amino acids sequence;

(iii) Supramolecular carbohydrate assemblies can be used to manipulate different biochemical processes and signaling cascades that ultimate determined cell fate and pathological conversion;

(iv) The developed systems can be used either as multifunctional responsive biomaterials or in dynamic experimental modelling to obtain valuable qualitative and quantitative information of carbohydrate-protein interactions and thus, about the carbohydrates involvement in different physiological and pathological process;

(v) Among the different approaches applied in this thesis, BSA systems generated substantial interest and we believe that the provided new insights lay out a paradigm change especially in the field of cancer management. New insights on the mechanism of action of carbohydrate amphiphiles may lead to the design of more efficient chemotherapeutics;

Beside these breakthroughs, there are number of challenges that remain:

(i) The supramolecular complexes prepared in this thesis are based on the simplest and widely abundant monosaccharide - glucose. Keeping in mind that the cells are surrounded by complex polysaccharides, novel concepts that create supramolecular assemblies with complex carbohydrate must be developed.

(ii) Most of the developed systems are established by copycatting the assembling principles established for structurally different blocks, *e.g.* polymers and peptides, and specific interactions such as carbohydrate-carbohydrate (CCI) ones are not explored. We still know very little about these interactions and about their physiological importance since most of the currently available systems target or exploit

only carbohydrate-protein interactions (CPIs). Thus, important breakthroughs can come up from studies involving CCIs.

(iii) Chirality abundance of carbohydrates is also underexploited. Further developments of the chiral systems developed under this thesis present opportunities for expansion and diversification of supramolecular systems at functional and structural level by mimicking the biological control of structure and function through the carbohydrate chirality.

(iv) Finally, glycopeptides are a class of materials that can be further exploited as minimalistic models to study the effect of glycosylation on the kinetics and thermodynamics of the protein aggregation. Such results would have significant impact on our understanding on the role of the protein aggregation in different physiological and pathological processes and can suggest different meanings to control this process.